Designing a Hybrid Inkjet and Laser Manufacturing System for the Digital and Non-Contact Fabrication of Emerging Nanotechnology Based Devices.

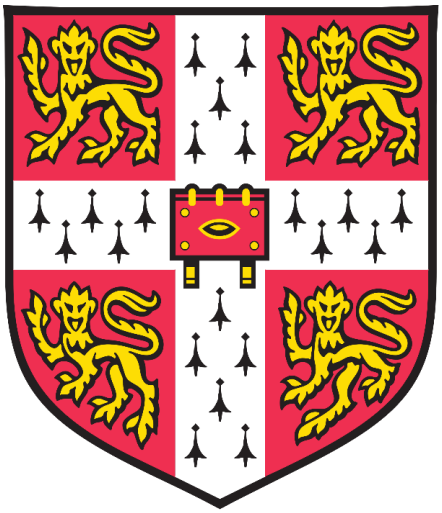

Yoanna Shams

Newnham College

Institute for Manufacturing,

Department of Engineering,

University of Cambridge

September 2018

This dissertation is submitted for the degree of Doctor of Philosophy

Abstract

Designing a Hybrid Inkjet and Laser Manufacturing System for the Digital and Non-Contact Fabrication of Emerging Nanotechnology Based Devices

Yoanna Shams

Though many VA-CNT based applications have recently been developed, there is still a research gap in the scalable manufacture of VA-CNT applications in industry. In this research, a hybrid additive and subtractive direct-write digital fabrication platform has been developed to deposit and pattern catalyst for VA-CNT Growth. Inkjet printing has been explored as the ***additive technology*** for depositing magnetite nanoparticles as catalyst, and laser ablation has been studied as a ***subtractive technique*** to pattern the catalyst for growing VA-CNT structures, using chemical vapour deposition as an ***assistive growth procedure***. The research was conducted in three phases. In the ***feasibility phase*** the CVD growth conditions were established and a comparison was made using SEM and AFM analysis. A variation in size between the annealed nano-islands formed from the nanoparticle film and the PVD deposited iron film was identified. The magnetite ink properties were then characterised for inkjet printing. In the ***specification phase*** inkjet printing and laser patterning experiments were conducted. It was determined that VA-CNTs can be grown by printing 2.19 $\%_{w/w}$ ink concentration on UV treated 10 nm alumina coated substrates at a droplet spacing of 45 µm. SEM analysis identified that even though the nano-islands formed from the inkjet printed catalyst are larger in size than those formed from the PVD deposited catalyst, VA-CNTs were successfully grown. In the laser patterning experiments a femtosecond laser fluence range between 0.48 J/cm^2 and 0.64 J/cm^2 was found to successfully pattern the nanoparticle catalyst. Varying laser fluence resulted in a change in the annealed catalyst nano-island size, giving varying growth trends. In the ***conceptualisation phase***, an industrially scalable laser system by M-Solv Ltd was successfully demonstrated for patterning the catalyst. Gas sensing experiments were also conducted proving a response of the VA-CNTs to changes in nitrogen dioxide.

To my Parents

For their unrelenting dedication, love, and faith,
That has brought me this far,
And will continue to take me forward.

Declarations

This dissertation is the result of my own work and includes nothing which is the outcome of work done in collaboration except as declared in the Preface and specified in the text. It is not substantially the same as any that I have submitted, or, is being concurrently submitted for a degree or diploma or other qualification at the University of Cambridge or any other University or similar institution. I further state that no substantial part of my dissertation has already been submitted, or, is being concurrently submitted for any such degree, diploma or other qualification at the University of Cambridge or any other University or similar institution. The length of this dissertation is under 65000 words and 150 figures, and thus not exceeding the prescribed word limit for the Department of Engineering Degree Committee.

Yoanna Shams
September 2018

Acknowledgements

The completion and success of this academic journey is owed to the support and guidance of many people, without the acknowledgement of which this thesis would be incomplete. I would like to express my foremost gratitude, respect and appreciation for my Supervisor Dr. Ronan Daly, and for the patience with which he has always guided and supported me these past four years. The Fluids in Advanced Manufacturing Group began with group meetings of three, and has now grown to fifteen members. Despite having more responsibilities, Dr. Daly has consistently through his notable scientific insight helped me direct my research, and encouraged me to always aim for that extra edge. I must also extend my appreciation towards my advisor Dr. Claire Barlow and her support, particularly in my final year. I would also like to thank the FIAM group members for their constant encouragement during the writing phase, and for always providing a positive and enjoyable work environment. In particular, I would like to thank Dr. Etienne Rognin, Dr. Niamh Fox and Qingxin Zhang with whom I began my doctoral journey, for their technical help with the rheology and high speed imaging experiments. I would also like to Thank Dr. Cristina Rodriguez Rivero, who has become a dear friend over these years, and Alice Gregory for being the administrative backbone of our group.

This PhD would not have been possible without the support of the EPSRC Ultra Precision CDT, where I have met so many inspiring individuals, and grown personally and professionally. I would like to thank Dr. Bill O'Neill for giving me the privilege of being part of this distinguished institute, and Sophie Fuller for her remarkable organisation. I am also grateful for the CDT for giving me life-long friends; Dr. Clare Collins, Chris Wright and Jason Ten who have made my years at Cambridge so enjoyable. I would like to particularly thank Jason Ten, for all his help on the days the Satsuma laser didn't behave, for his technical input into the laser experiments, and for five years of friendship and support.

The support of M-Solv Ltd. and The Centre of Science Technology and Innovation policy has been vital for this research, and I would like to thank Dr. Phil Rumsby, Dr. Adam Brunton, Dr. David Myles, Dr. Eoin O'Sullivan, and Dr. Charles Featherston for aiding in expanding the horizon of my work. I would also like to express my gratitude for Prof. Ian Hutchings and his contributions to the field of Inkjet and the Institute for Manufacture, without which my work would not be possible. The laser patterning experiments were

conducted at the Centre of Industrial Photonics, for which I would like to thank Dr. Martin Sparkes. Working at the Nanoscience Centre has been essential towards the completion of this research, and I would like to express my utmost gratitude to Dr. Colm Durkan for his scientific input in the AFM research conducted in this thesis. I would also like to thank Dr. Stephen Hodge and Tahmida Huq at the Cambridge Graphene Centre for their help with the gas sensing equipment. The CVD growth experiments have been made possible with the support of the NanoManufacturing Group, and I would like to express my appreciation for Dr. Michael De Volder, Dr. Davor Copic, Dr. David Beesley, Dr. Hsin-Ling Liang and Dr. Hadi Modarres for their scientific input and guidance. I must also acknowledge and thank the hard work of all the technical and administrative staff at the Institute for Manufacture, Nanoscience Centre, Graphene Centre, Department of Materials, Maxwell Centre and Cavendish Laboratory, who enable the smooth functioning of the departments and our research.

On a more personal note I must acknowledge the immense role Newnham College has played in my years at Cambridge. It has been a true home where I have found some of the happiest memories and lasting friendships which have shaped me and my future aspirations. I would like to extend a special acknowledgement for Dr. Kate Fleet for always keeping her door open, and for the personal support and guidance she has provided. My friends at Cambridge particularly, Corina, Becky, Robynne, Edwin and KC have been a source of unwavering support, and I have great gratitude towards them for always hearing me and helping me believe in myself.

Last but not least I would like to thank my family. My parents for the sacrifices they have made for me to come to Cambridge, for the faith that they have in me which has enabled me to achieve things I didn’t think possible, and for always having my back. I must also thank a new addition to my family, my Fiancé Seán. My journey at Cambridge has become more special because I have shared it with him. I must thank him for all his patience and coffee during the late night writing sessions, for giving me the support and motivation to take my time to enjoy this journey, and for being my rock.

Table of Contents

Glossary of Abbreviations

2D	2 Dimensional
3D	3 Dimensional
10ASW	10 nm Alumina Coated Silicon Wafer
AFM	Atomic Force Microscopy
CI	Confidence Interval
CIJ	Continuous Inkjet Printing
CNT	Carbon Nanotube
CVD	Chemical Vapour Deposition
DFM	Design for Manufacture
DLS	Dynamic Light Scattering
DMP	Dimatix Materials Printer
DNA	Deoxyribosenucleic Acid
DOD	Drop on Demand
DPS	Diode Pumped Solid State
DW	Direct Write
DWCNT	Double Walled Carbon Nanotube
ED	Electron Diffraction
E-beam	Electron Beam
EELS	Electron Energy Loss Spectroscopy
EDX	Energy Dispersive X-Ray Spectroscopy
ETEM	Environmental Transmission Electron Microscopy
EUSPEN	European Society for Precision Engineering and Nanotechnology
FC-CVD	Floating Catalyst Chemical Vapour Deposition
FET	Field Effect Transistor
F_{High}	High Fluence
F_{Low}	Low Fluence
F_{Med}	Medium Fluence
FIB	Focused Ion Beam
FSLI	Function and Length Scale Integration
FTIR	Fourier Transform Infrared Spectroscopy
GI-SAXS	Grazing Incidence Secondary Angle X-Ray Scattering
GI-XRD	Grazing Incidence X-Ray Diffraction
HAZ	Heat Affected Zone
HIC	High Ink Concentration
HIS	High Speed Imaging
INN	International Institute for Nanotechnology
IPA	Isopropanol
IR	Infrared
LCVD	Laser Assisted Chemical Vapour Deposition
LIC	Low Ink Concentration
LEEP	Laser Enhanced Electroless Plating

MEMs	Micro Electronic Mechanical Systems
MIC	Medium Ink Concentration
MRI	Magnetic Resonance Imaging
MRL	Manufacturing Readiness Level
MWCNT	Multi Walled Carbon Nanotube
Oh	Ohnesorge Number
PDS	Product Design Specification
PE-CVD	Plasma Enhanced Chemical Vapour Deposition
POC	Point of Care
PVD	Plasma Vapour Deposition
QFD	Quality Function Deployment
Re	Reynolds Number
R&D	Research and Development
RP	Rapid Prototyping
SD	Standard Deviation
SEM	Scanning Electron Microscopy
S_{ID}	Individual Droplets
SIMS	Secondary Ion Mass Spectroscopy
SMI	Scanned Mask Imaging
S_o	Overlapping Droplets
SPA	Shots per Area
S_{PO}	Partially Overlapping Droplets
SWCNT	Single Walled Carbon Nanotube
T-CVD	Thermal Chemical Vapour Deposition
TEM	Transmission Electron Microscopy
TRL	Technology Readiness Level
UV	Ultraviolet
VA-CNT	Vertically Aligned carbon Nanotubes
VOC	Voice of Customer
VOE	Voice of Engineer
We	Weber
XPS	X-Ray Photoelectron Spectroscopy
XRD	X-Ray Diffraction
XRR	X-Ray Reflectivity
Z	Inverse Ohnesorge Number

Chapter 1

INNOVATION STRATEGY FOR DIGITAL MANUFACTURE OF VA-CNTS

Although the first examples of certain stable nanomaterials, such as carbon nanotubes and cementite nanowires, can be traced back 600 years to ancient India, in the steel of Damascus blades, the discovery and emergence of these functional materials and the foundation of nanotechnology as a scientific discipline has only existed since the 1970s [1]. What is more, the development of manufacturing techniques to exploit the exceptional properties of these nanomaterials has only truly propelled in the last 10 years. Nanotechnology has been defined by Whatmore (2001) as, *"the study, development and processing of materials, devices and systems in which structure definition on a dimension of less than 100 nm is essential to obtain the required functional performance"*[2]. With the increasing emergence of multifunctional and compact high-tech devices, manufacturing specialists are required more than ever to deliver high quality and reliable products that contain nanomaterials, with minimised carbon footprint [3]. Many programmes, across at least 30 countries have been initiated to focus on the development of nanotechnology [4]. Some of these programmes have been specifically dedicated to developing nano-manufacturing tools [2], [5]–[8]. These include:

- The Scalable Nano-manufacturing Programme, The National Science Foundation, USA
- The European Society for Precision Engineering and Nanotechnology EUSPEN, Cranfield University, UK

- International Institute for Nanotechnology (INN), Northwestern University, USA
- The Manufacturing Engineering Centre, Cardiff, UK

Most often for micro-electromechanical devices lithography is the predominant nano-manufacturing tool to produce micro and nano size features. However, it has been widely deemed an unsuitable technique for the high throughput fabrication of miniaturised devices that require high aspect ratio features on multiple materials [8]. It is also very costly when used with low-volume manufacturing. Therefore, new manufacturing methods need to be developed to achieve this function and length scale integration (FSLI) for the development of niche miniaturised devices [9]. This need leads to the convergence of an additive inkjet fabrication technology and ultra-precision laser machining into a direct-write platform technology, which is developed and studied in this manufacturing research thesis. This chapter introduces the direct-write technologies and nanomaterials studied in this thesis, and the challenges associated with their scale-up. With the scale-up challenges identified, a hybrid inkjet printing and laser patterning manufacturing platform for nanomaterial based devices is introduced, and the research framework identifying the various phases of development presented. Initial literature analysis is conducted to understand the maturity levels of the technologies studied as a knowledge base before experiments are conducted.

1.1 Direct-Write Technologies

Recently direct-write (DW) technologies have become more prominent in nano-manufacturing, enabling fabrication of two and three dimensional objects without the need for a mask or mould [10]. Many definitions have been formulated to define DW technologies. However, as identified by Hon (2008) these definitions have failed to

distinguish DW technologies from rapid prototyping (RP) processes, giving a new definition to these techniques as:

"*A group of processes which are used to precisely deposit functional and/or structural materials on to a substrate in digitally defined locations. DW is distinguished from conventional RP processes due to the following characteristics:*

- *The track width ranges from sub microns to millimetres*
- *The range of materials deposited can include metals, ceramics and polymers, electronically and optically functional materials as well as biological materials including living cells.*
- *The substrate is an integral part of the final product."* [3]

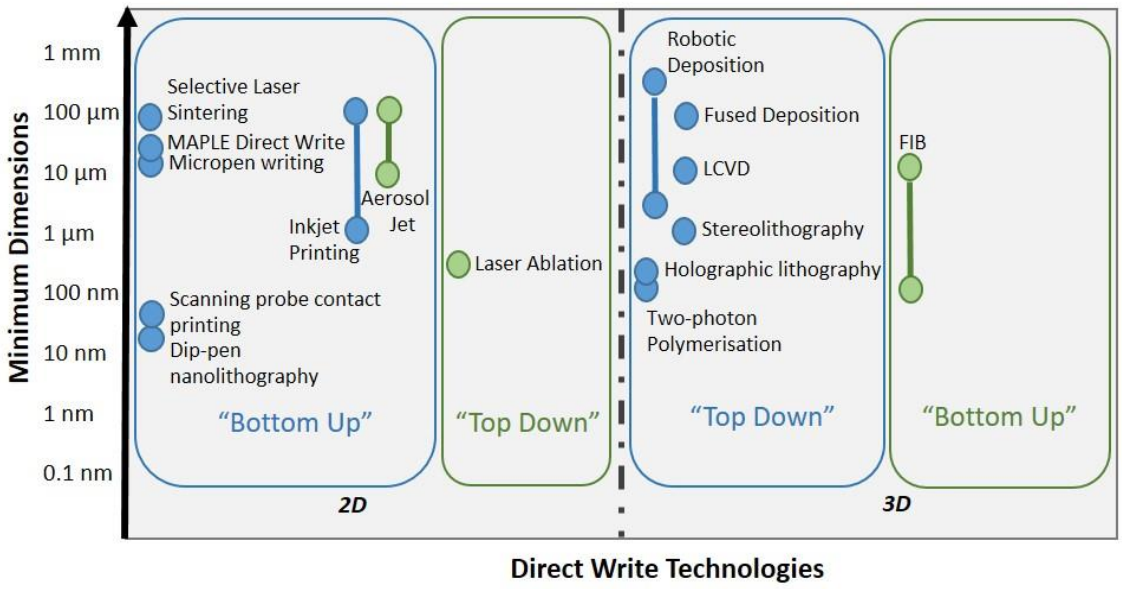

Figure 1: *Direct-write technologies scale map identifying top down and bottom-up approaches (data obtained from Lewis, J. 2004 [11])*

With the printed electronics market alone being forecasted as a US $55 billion industry by 2020, it is essential to develop DW technologies for nanomaterial-based device fabrication [12]. Figure 1 shows some of these technologies characterised into *Top-Down* and *Bottom-Up* methodologies. As defined by the Royal Society and Royal Academy of Engineering (2004), top-down techniques involve the milling or etching down of material,

and bottom-up techniques involve the building up of material from smaller sub-units into desired shapes [13]. While DW fabrication techniques still need to overcome some challenges, the advantages of this approach are listed in Table 1. Inkjet printing and laser-writing techniques are two of the most developed DW techniques for processing functional materials [3].

Inkjet printing relies on the deposition of colloidal nanoparticle or organic based inks to create layered structures by either a drop on demand (DOD), or continuous inkjet printing (CIJ) approach, achieving feature resolutions on the order of 20 µm at industrial scale [11]. However, smaller features have been achieved in recent research [14]–[16]. Laser writing relies on creating patterned materials through ablation, selective sintering, or reactive processes, and can achieve feature resolutions of 400 nm at industrial scale [17]. Feature sizes below this resolution have been achieved at research level [18]. Although there are many laser writing technologies for depositing materials, such as laser assisted chemical vapour deposition (LACVD), laser enhanced electroless plating (LEEP), and laser induced forward transfer (LIFT), laser milling can be used as a subtractive technique for material removal in conjunction with other additive DW technologies [3]. Laser milling involves using laser energy to remove material through ablation, and can machine feature sizes down to 40 µm for a wide range of materials [8]. Ablation mechanisms can be distinguished by the laser pulse lengths used, from ultra-short femtosecond pulses through to microsecond pulses [19]. Laser milling at shorter pulse lengths allows for direct sublimation of the exposed material with negligible thermal conduction into the substrate, and thus resulting in almost no heat-affected zone (HAZ), where the material chemistry is normally modified through thermal effects [8].

DW techniques, such as inkjet printing and laser ablation, allow for a rapid and smooth transition between a computer model and the physical realisation of a product [20]. This allows for flexibility of design and production of unique objects with customised specifications for each product. However, there are a range of challenges to this approach, as noted in Table 1, which will be tackled in this thesis. As identified by Pitkethly (2004), the constant development of nanomaterials has increased the number of applications across medicine, pharmaceuticals, communication technologies and agriculture. CNTs have emerged as an ideal material for a wide range of applications, such as micro-electronic-mechanical systems (MEMs), field emission displays, chemical and biological sensors and energy storage devices [21]. For this reason, the exploration of DW tech in this thesis will focus on micro and nano fabrication of CNT based devices to bridge the gap between the highly desirable electrical properties of CNTs and the length scale of bulk engineering materials [22]

Table 1: *Advantages and challenges faced by current DW fabrication techniques* [3]

Challenges	Advantages
• In depth understanding of process parameters • Improvements in adhesion, surface finish and resolution • Integration issues for microsystem applications • Post processing evaluation of functional materials • Process modelling and optimisation	• Digital patterning • On demand deposition • Process chain simplification • Reduced production time and cost • Multiple material compatibility (biological, nano and functional materials) • Multiple substrate compatibility • Non-contact reducing contamination • Minimal waste • Length scale from nanometres to millimetres.

1.2 Carbon Nanotubes for Devices

Carbon Nanotubes (CNTs) have been under discussion for the past 20 years for electronic applications, including sensors [23]. This has resulted in the commercial incorporation of CNT powders into micro-electronic devices by companies, such as Fujitsu, IBM and Eikos [24]–[26]. DW technologies are mostly used to explore deposition of CNTs for transparent, flexible and stretchable circuits is now emerging [12]. Companies, such as Eikos and Unidym are incorporating traditional printing methods for the fabrication of CNT films for solar, touch screen, e-paper and OLED applications [27]. However, the production of CNT inks is costly as the purification and dispensing of CNTs is complex, resulting in commercial dispersions costing in excess of £5000 per litre (Sigma Aldrich 791490 – 100ML) [28], [29]. Vertically aligned CNTs on the other hand have a larger surface area in comparison to thin films, and thus provide a cost effective scale-up of bulk CNT properties [30]–[32]. However, there is a limited understanding of what affects their properties during synthesis, how these factors can be controlled to maintain selectivity, and how such structures can be made by DW patterning [33].

Chemical Vapour Deposition (CVD) is one of the most common methods for production of vertically aligned CNTs (VA-CNTs) directly on a substrate, using a transition metal as catalyst [32], [34]. The yield and quality of CNTs synthesised by CVD are greatly influenced by the growth parameters, including: catalyst particle size, catalyst concentration, pressure, growth time and gas flow rates. [35], [36]. Therefore, the controlled growth of carbon nanotubes is vital for the full scale realisation of many proposed VA-CNT applications [37]. As industrial scale production of VA-CNT devices is yet to be achieved, efforts are currently directed towards developing novel methods for VA-CNT fabrication [38]–[41]. Lithographic techniques are being developed for achieving

mass production of nanostructures with benefits of minimal defects and large spacial resolutions. However, such approaches generate significant waste products or incorporate multiple fabrication stages, rendering their incorporation into automated systems difficult [42]. Patterning of VA-CNT structures in particular poses significant scale-up problems. Therefore, there is a need for DW technologies to be explored for the direct deposition and patterning of catalyst for VA-CNT growth.

1.3 Selecting Technology to Scale-Up

Studies into DW processes for VA-CNT have focused on individual techniques, such as laser patterning of CNTs [43], laser assisted CVD growth [44], [45] or inkjet printing of catalyst for CNT growth [46]–[48]. However, these manufacturing techniques have yet to be combined for VA-CNT device fabrication. Biosensors and lab-on-a-chip devices are good examples of a need for functional and length scale integration, as they require a combination of functional, biological and nano materials in microfluidic channels, set within a macroscale user interface [49]. Designing processes and process chains is more suitable than designing products for emerging technologies [50]. Therefore, to develop these process chains the need for technology convergence requires top-down and bottom-up nanotechnology synthesis, a field currently of interest to many researchers [2], [9]. Combining DW technologies specifically, gives the potential to converge ultra-precision and micro-manufacturing processes to build cost effective process chains. [8][9]. Therefore, it is essential to examine the trends and maturity levels of these technologies through analysis of existing literature at each development stage. This analysis can aid in identifying implementation and commercialisation risks so that an effective research direction can be defined. Many different methodologies for scalable manufacturing have

been proposed, but they are specific to particular combinations of materials and manufacturing techniques [50]–[54] . Therefore, as concluded by Brousseau (2010);

"… Future hybrid production platforms should rely on and integrate material deposition and refinement processes with material removal technologies." [8]

With over 150 processes available for bottom-up fabrication and many more available for top-down fabrication, there are many challenges associated with defining a suitable manufacturing methodology [53]. Some of the challenges associated with achieving a desired product output and appropriate metrics have been defined by Cooper (2017) and shown in Table 2. These manufacturing challenges form the basis of the research questions answered in this thesis. Lithographic production of VA-CNT devices poses production scalability, affordability, efficiency and repeatability limitations whereas, the final VA-CNT performance and functionality is dependent on the placement of the catalyst, feature size, resolution and nanostructure density. All these challenges are required to be tackled when developing manufacturing process chains for producing VA-CNT based devices.

Table 2: *Manufacturing Challenges* [53]

Desired Outcomes	Appropriate Metrics
• Product Quality • Durability • Process Repeatability • Process Reliability • Production Scalability • Production Affordability • Production Efficiency • Yield • Product Performance • Product Functionality	• Precision of Placement • Feature Size • Resolution • Overlay Registration • Nanostructure Density • Nanostructure Complexity • Nanostructure Rate of Forming

The following conclusions can be drawn for the opportunities and challenges associated with developing scalable micro and nano manufacturing processes [8], [9], [50], [51]

- Development of innovative process chains is vital to meet demands for miniaturised electronic devices.
- A tool box of technologies already exists for designing miniaturised products for specific materials and designing process chains to satisfy functional and technical requirements
- Trends towards technology convergence and top-down/ bottom-up synthesis necessitate research into process-material interactions to understand new scalability standards and tolerances
- Determining the best manufacturing route is difficult when selecting from a vast collection of technologies. Therefore design for manufacture knowledge needs to be addressed
- Integration of technologies with varying processing rates and operating conditions into a hybrid system is difficult.

These challenges identified have been considered when determining the feasibility of combining inkjet printing and laser patterning as a hybrid technology for VA-CNT growth. Details of the hybrid manufacturing process chain are defined in the next section.

1.4 Inkjet Printing and Laser Fabrication of VA-CNT Devices

Recently, inkjet printing has been identified by Ameloot (2017) as, *"an excellent tool to integrate catalyst and/or support layer"* with research efforts being devoted to printing catalysts as thin films or combinatorial arrays [10]. VA-CNT devices have greater potential for higher device sensitivity in comparison to those incorporating printed CNTs [55][56]. By utilising low cost magnetite nanoparticles Fe_3O_4 as catalyst (£173.00 per litre Ferrotec MSGW11), in combination with additive and subtractive manufacturing techniques of

inkjet printing and laser patterning, we propose a digital DW technology for growing VA-CNTS, for sensing applications, as shown in Figure 2. Techniques such as sintering, annealing or chemical treatment are defined as assistive techniques as they are a secondary process to assist the main processing techniques [57]. Therefore, CVD growth is an assistive technique in the fabrication methodology.

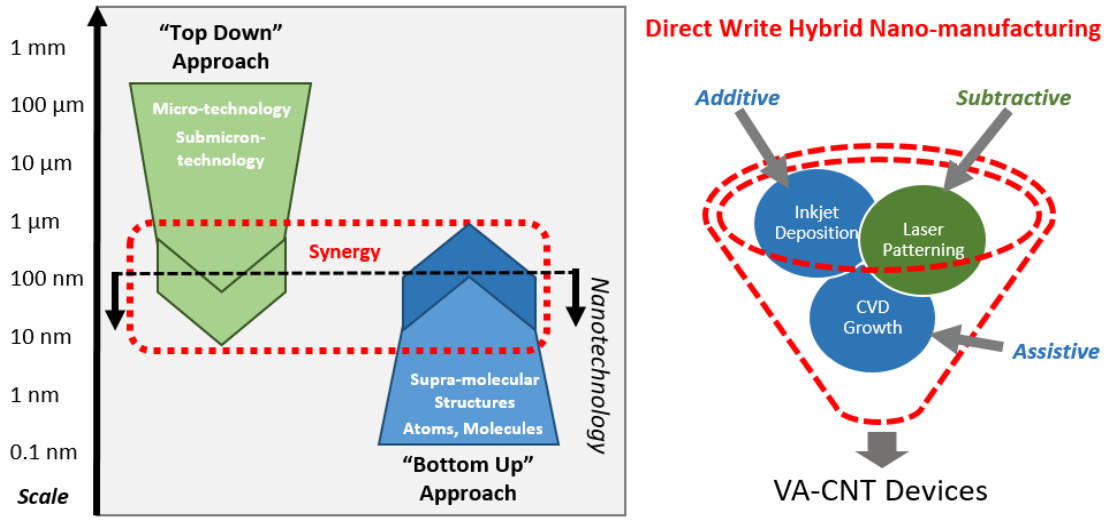

Figure 2: *Graph representing the target scale area where synergy between top-down and bottom-up approaches can be achieved* ***(left)*** *(adapted from the Royal Society and Royal Academy of Engineering* [58][13]*. The union of inkjet printing (additive), laser patterning (subtractive) and CVD (assistive) growth as a hybrid manufacturing platform, for the development of VA-CNT devices* ***(right).***

1.5 Research Methodology

Knowledge transfer between academic research and industry has traditionally occurred in the form of a hardware prototype, scientific paper and other written communication [59]. Many experts have deemed the technique inadequate and have identified that in order to compete commercially, the ability to exploit knowledge is a key factor, and thus making the role of universities even more important in innovation [60]. Roco (2001) identified that for nanotechnology research to develop it is important to enhance communication, networking and development of R&D partnerships internationally, with a joint vision for

increased productivity and sustainable development [4]. Industries, governments and universities are working more closely than ever before, taking up different roles at different stages of the innovation process [60]. Nanotechnology provides a natural experiment for evaluating the relationship between innovation policy and entrepreneurship, as when a technology is first developed the infrastructure for entrepreneurship is under developed [61].

In the past few years many strategy and development practices for innovation technology have been presented. Schoen (2005) demonstrated a complex multiple spiral innovation model that argues innovation is not a step by step process, but a combination of individual innovation and invention processes driven by market pull and technology push forces [62]. Nanotechnology specifically is a process based innovation where process and product innovation is tightly coupled. Any changes to the manufacturing process can result in significant change in the end product during any phase of the product life cycle [63]. Islam *et al*. (2009) identified that the boundary between scientific fields is blurring with researchers from various scientific disciplines promoting nanoscience fusion by working in parallel attracting the interest of policy makers. Therefore, the successful implementation of nanotechnology system innovation requires researchers, industrialists and policy makers from multi-disciplinary backgrounds to come together and facilitate building of a network for exchanging nano expertise or knowledge [64]. Therefore, this research has been conducted with collaborations across industry and academia to ensure the gap from lab research to industry is minimised by identifying scale-up risks early.

This project has been sponsored by M-Solv Ltd. and the Centre for Science Innovation and Technology Policy. M-Solv is a company based in Oxford that specialises in the manufacture of micro-electronics and photovoltaics using laser micro-machining tools. They have industrial scale combinations of additive and subtractive processes to

interconnect devices and have a laser and inkjet hybrid for conductive track fabrication. Collaborating with M-Solv is beneficial as it not only enables communication with industry, but allows opportunity for scaling the research findings. To further aid this translation, a framework was developed and adopted to help prompt the right scale-up related question at a stage as early as possible during the research phase. This was created by joining design methodology with technology risk management techniques. Design has been described as the first step in manufacturing, and consequently since the 1980s many techniques have been introduced to guide designers towards easy to manufacture products [65]. The introduction of design for manufacture (DFM) has enabled the development of products through the systematic identification of materials and manufacturing processes required to develop a product, based on its capabilities and limitations [66]. However, when developing a new technology many other factors have to be taken into consideration, such as its disassembly, recyclability, and environmental impacts. Therefore, many innovation and design models have been presented over the years as reviewed by Adams (2015) [67].

Stuart Pugh observed that academic teaching of design was aloof from industrial practice and that industrial practice lacked self-reflective structuring [68]. Thus, he developed a design methodology known as Total Design, in which the complexity of design is tackled through a systematic framework capturing both technology specific methods and technology independent methods [67], [69]. Pugh defines six distinctive steps to in this methodology: feasibility, specification, conceptualisation, detail design and manufacture and sell (Appendix A, Figure A 1) [70]. Each phase has a range of techniques to provide a wholesome operational strategy that can be applied to not only product design, but also innovation strategy in academic research. Techniques such as a product design specification (PDS), quality function deployment (QFD), Voice of the Customer vs Voice of the Engineer Analysis (VOE/VOC) and a concept selection matrix can be helpful tools

in defining specific requirements of an emerging technology [71]. The phases are not linear and require a thorough exchange of feedback to ensure consistent re-evaluation and application of development strategy. With a similar approach, the U.S DoD has outlined technology readiness levels and manufacturing readiness levels to help manage decision making in the development of technology and manufacturing chains [72].

It was previously discussed that for emerging technologies, especially nanotechnologies, the processes and products have to be developed side by side. In Appendix A, Table A 1 and Table A 2 show the TRLs and MRLs as defined by the U.S DoD. TRL 1 to TRL 3 are more focused towards developing the concept which is then validated with laboratory experimentation at TRL 4 and TRL 5. Beyond TRL 5 the technological components are required to be tested in simulated environments to construct a prototype and eventually develop the technology commercially. Similarly, MRL 1 to MRL 4 are focused towards the development of technology in the laboratory with experimentation and analysis of scientific principles. Beyond TRL 5 the manufacturing processes are developed in controlled environments and developed to an operational manufacturing chain.

In this thesis, considerations of TRL and MRL stages have been incorporated with Pugh's six stages of design to construct a strategy for nanotechnology development. A schematic demonstrating the methodology can be seen in Figure 3. The TRLs and MRLs have been defined in synergy with Pugh's stages of design. At the beginning of the development phase knowledge from the different scientific disciplines being tested is gathered. Each process and material, is analysed and tested appropriately. The laboratory research can only be conducted until the conceptualisation phase, with challenges associated with the technology and manufacturing levels established up until TRL 4 and MRL 4. Prototyping is conducted at the embodiment stage, where industry input is essential as the

manufacturing and technology processes have to be developed and integrated in a relevant environment.

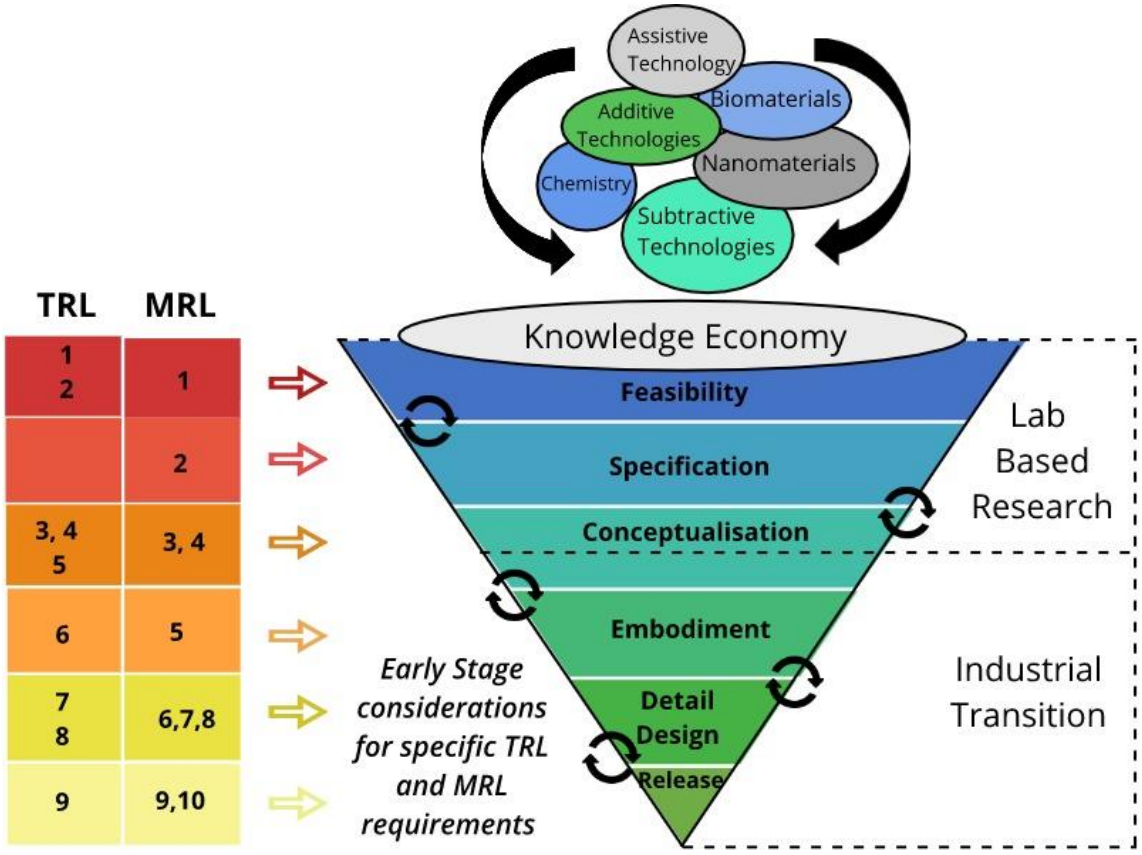

Figure 3: *Proposed design methodology for processing nanotechnology*

The research presented in this thesis has only been conducted until the conceptualisation phase. Details of the three phases of research can be seen in Figure 4. In the feasibility phase of the research the assistive technique and the material specifications are defined. The CVD growth conditions are optimised, and the catalyst ink formulation characterised. In the specification phase the additive inkjet printing technique and subtractive laser patterning technique are defined and verified for VA-CNT growth, using magnetite nanoparticles. The conceptualisation phase looks at the development of a test sensor and the incorporation of industrial technologies in the manufacturing process chain. However, before the innovation phases can be determined, knowledge of the nanomaterials and

subtractive and additive techniques being researched is required, to understand the questions required to be answered at each development phase.

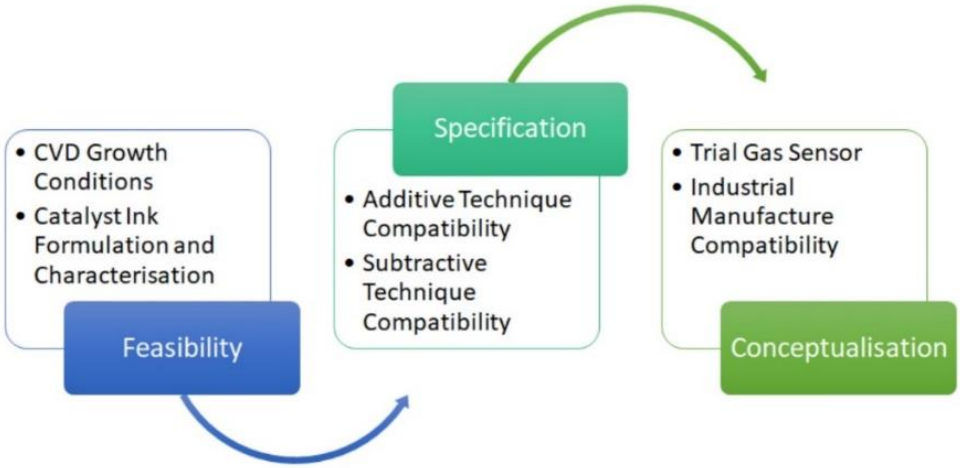

Figure 4: *Steps to achieve Research Phases*

1.6 Current Research Trends

With the target materials technology and process technology defined, this chapter now introduces the overarching trends in research for VA-CNTs, inkjet printing and laser patterning in the nano-manufactured sensor sector. A more detailed and focused review of techniques and materials behaviours is presented in each appropriate chapter, to identify specific research needs.

1.6.1 Aligned Carbon Nanotubes

Chen *et al*. (2010), Lan *et al*. (2011) and Kang (2017) give comprehensive reviews on some of the latest developments on VA-CNT fabrication and application [73]–[75]. VA-CNTs can be used in a range of devices, such as drug delivery, sensing, water purification, supercapacitors, field emission displays and energy storage [73], [76]–[78]. However, CNTs have recently gained a lot of interest in sensing applications, where they are being used as the active sensing material by maintaining the overall sensor signal over a large area, while reducing the size of the electrode [79], [80]. Just like carbon based electrode

material, carbon nanotubes can be applied to chemical and biosensors to obtain miniature, high sensitivity, and high speed detection [81], [82]. Functionalisation or chemical modifications to the VA-CNTs allows for new properties that can improve the interaction between VA-CNTs and their environment [83], [84]. Hooijdonk *et al*. (2013) discusses that VA-CNTs can be modified through either chemical modification or dry chemical modification of the CNT tips [85]. They can be functionalised, doped or coated with metals, oxides, enzymes and polymers to amplify their response in various sensing applications [83], [86].

The high electron mobility of CNTs can give high speed real time results which are highly suitable for POC diagnostics and environmental monitoring [79], [87], [88]. The absorption of gas results in a charge transfer or capacitance change in VA-CNTs, and thus making them an ideal material for developing gas sensors [88]. This capability is used by Penza *et al*. (2010) to demonstrate a multiple array land fill gas monitoring system made with VA-CNT films sputtered with platinum, ruthenium and silver [89]. Wei *et al*. (2006) has developed a chemical vapour sensor for detecting ethanol and cyclohexane using aligned carbon nanotubes and polymer composites [90]. Reviews by Yang *et al.* (2015), Lamberti *et al*. (2011) and Balasubramanian *et al*. (2006) have identified that CNTs on account of their high aspect ratios, high mechanical strength and high surface areas, with excellent chemical and thermal stability and rich electronic and optical properties, can also be used for many biosensing applications [91]–[94]. Glucose sensors have already been extensively researched for CNTs on account of their similar dimensions to redox proteins, making them effective connectors with redox enzymes [95]–[97]. As demonstrated by Lin *et al*. (2004), glucose oxidase can be covalently immobilised on CNT electrodes for the detection of glucose. Thus, eliminating the need for artificial electron mediators and selective membranes, and simplifying sensor design and fabrication procedure [98]. This

methodology can be applied to other enzyme based sensors, and as a result to devices for cholesterol, DNA, dopamine, uric acid and cancer detection have been reported [93], [99]–[101]. The electrochemical properties of CNTs makes them a desirable material for developing lab-on-a-chip devices, especially as they can be grown on multiple substrates via CVD [102]. Hence, enabling their integration into current microfluidic systems [102], [103]. Microfluidic integrated CNT arrays have already been demonstrated for nucleic acid concentration and a platform lab-on-a-chip device manufactured using traditional lithographic processes [49], [79]. Although many sensing applications using VA-CNTs have been reported, there are few that measure the reproducibility of fabricating these devices in industrial settings, which is a key factor for commercial scalability.

Banerjee *et al.* (2008) identified the quality challenges of CNT interconnects, such as defects, contact to substrate and their diameter and size is dependent on the manufacturing technology, and so making it essential to develop robust fabrication processes that minimise variations [24]. For testing CNTs, gas sensing FET or resistors measuring resistance changes of CNTs are the most commonly used sensor structures [88]. Therefore, when developing VA-CNT devices with new fabrication technologies, testing the VA-CNTs for gas sensing applications first is a simple yet commercially relevant path. The platform technology can then be used to develop further sensing architectures. Therefore, we need to look at the inkjet printing and laser patterning effects on catalyst deposition and patterning. The resulting VA-CNT growth can be studied in detail to establish the functionality and complexity of the VA-CNTs structures, and thus device architectures possible. However, before this can be achieved the VA-CNT growth procedure has been reviewed and the growth conditions established in **Chapter 2**, by comparing the catalytic nano-island formation during growth for a magnetite nanoparticle film and a PVD deposited iron film.

1.6.2 Inkjet Printing

Inkjet printing has been evolving as a widely used technique for depositing biological and nanomaterials [104]–[106]. Although there are multiple types of inkjet printing, piezoelectric DoD fabrication is of most interest for this research [107]. Inkjet printing has the advantage of flexibility to manipulate designs for customised applications to create complex shapes. For CNT based applications, inkjet printing has been almost entirely used for the direct deposition of CNT inks [108]–[111]. However, limited research has been conducted for the direct deposition of catalyst for CNT growth. Mansoor *et al*. (2010) utilised nickel based catalytic inks for growth, but upon CVD growth, alignment of CNTs was not achieved [46]. Chatzikomis (2012) demonstrated inkjet printing of iron salts as catalyst for CNT growths, where alignment of CNTs was again unsuccessful [47]. Commercial magnetite nanoparticles have been demonstrated as a suitable catalyst source for grown VA-CNTs [112]. Beard *et al.* (2013) inkjet printed magnetite nanoparticle suspensions for the successful growth of VA-CNTs [48]. However, the effects of inkjet printing parameters to achieve patterns of VA-CNT forests have not yet been explored in detail.

For the successful printing of any material some critical parameters have been identified by Lim (2012) and include; surface modification or treatment, before or after printing, to avoid problems such as the coffee stain effects, and other interaction problems that might occur [113]. Detailed morphology and rheology analysis are required to understand the ink and its behaviour pre and post processing [114]. One of the main difficulties with inkjet printing is not the printing procedure itself, but the preparation of inks. The inks that are deposited using piezoelectric inkjet printers are required to be of a particular viscosity, surface tension and density, otherwise clogging can occur, or the piezoelectric will fail to push the liquid out of the nozzles [115], [116]. Printer factors such as nozzle size, droplet

size, dot density, and lateral resolution of printer head determine the feature size [117], [118]. All the parameters defined can be altered to deposit catalyst layers with varying thickness, and so are studied in detail through literature analysis and experimentation in **Chapter 3**.

1.6.3 Laser Patterning

Laser micromachining is a highly precise, fast and contactless technique that does not require clean-room facilities or lithography, making it a suitable alternative to classical machining or patterning [119]. The main technical advantages of laser micromachining is the ability to control beam shaping properties and laser beam energy for localised materials processing [120]. Laser machining can be used in combination with other techniques or on their own for macro and microscale structuring, drilling, fine cutting, joining and surface modification. Su *et al.* (2003) and Lim *et al.* (2013) have reported using lasers to prune already grown VA-CNTs forests [121], [122]. However, this patterning technique could result in undesirable airborne CNTs. Terrones *et al.* (1997) and Grobert *et al.* (2000) demonstrated that the direct laser patterning of deposited iron, nickel and cobalt catalyst films results in improved VA-CNT growth [123], [124]. Therefore, combining inkjet printing and laser technology allows the deposition and removal of catalyst on a single hybrid machine before CVD growth [125]. Ko *et al.* (2005),(2007) and (2008) present the integration of low temperature subtractive laser processing of inkjet printed gold nanoparticles for flexible electronics [126]–[128]. This hybrid fabrication technique is feasible for nanoparticle patterning and can be applied to magnetite nanoparticles. Therefore, laser patterning effects on the catalyst are studied in detail through literature analysis and experimentation in **Chapter 4.**

1.7 Research Aim and Objectives

The literature reviewed shows that VA-CNTs can be harnessed for a plethora of applications. Research interest in the inkjet printing of catalyst for VA-CNT growth and laser patterning of VA-CNT forests is also clearly evident from the literature reviewed. This demonstrates a demand for innovative fabrication strategies for VA-CNT devices. Therefore the aim of this research is to explore a new hybrid fabrication technique using inkjet printing and laser patterning for growing VA-CNTs for sensing applications. In order to achieve this aim a set of objectives have been formulated.

- Determine feasibility of using magnetite nanoparticles as catalyst during CVD growth of VA-CNTs.
- Define and characterise printability of magnetite nanoparticles using inkjet printing for VA-CNT growth.
- Determine the compatibility of using laser ablation to pattern magnetite nanoparticles for growing VA-CNT structures.
- Explore the commercial and industrial scalability of this hybrid manufacturing technique through gas sensing experiments and exploration of already existing industrial lasers.
- Analyse the findings and determine the next set of steps required to translate research to industry.

The objectives defined above give an overview of the research targets. The research has been split into three phases as defined in the research methodology presented in section 1.5. Therefore, detailed aims and objectives will be defined for each research phase.

1.8 Thesis Outline

This section represents a detailed outline of how the three phases of development; feasibility, specification and conceptualisation will be tackled. With a base knowledge economy founded, *Chapter 2* will present results verifying the **feasibility phase** of the research. Operating procedures for CVD growth will be determined and the magnetite ink properties defined. *Chapters 3* and *Chapter 4* present results from the **specification phase**. *Chapter 3* will look at detailed analysis of the printability of the magnetite ink selected, and the printing parameter specifications to achieve VA-CNT growth. *Chapter 4* will explore effects of laser patterning on the functionality of the magnetite nanoparticle film. *Chapter 5* presents findings from the **conceptualisation phase** which looks at the development of a first principle gas sensing application, and the feasibility of using other industrial laser patterning techniques. Detailed theoretical and literature knowledge will be built throughout each research phase. The research findings have been summarised and directions for future work outlined in *Chapter 6.*

Chapter 2

CHEMICAL VAPOUR DEPOSITION – ASSITIVE MANUFACTURE AND CATALYST SOURCE

CVD is the most commercially utilised technique for CNT synthesis [129]. Before beginning to optimise the additive and subtractive techniques, it is important to understand the fundamentals of the CVD process, and to better define how the transition from vacuum deposited catalyst to DW deposition will change growth behaviour. As many lab-based CVD systems are custom made, it is essential to understand the optimum conditions and parameters under which VA-CNTs can be grown to underpin later research. This study is conducted to establish the non-variable operating conditions for the CVD growth process, and the toolset required to compare VA-CNT forests and catalyst evolution upon alteration of deposition and patterning techniques. Therefore, the aim of the chapter is to determine the feasibility of using CVD growth mechanism and magnetite nanoparticles for VA-CNT growth, and has four objectives:

- Identifying conditions necessary for the growth of VA-CNTs on a catalyst layer deposited using conventional methods in a custom designed CVD system, and analysing the quality of the forest grown.
- Establishing a toolset for analysing VA-CNT growth.
- Characterise the magnetite nanoparticle catalyst ink and determine its effect on CNT growth.
- Compare catalyst evolution during annealing for PVD deposited iron and magnetite nanoparticle ink films.

However, before beginning any experiments, it is essential to build up a theoretical understanding of the state-of-the-art CVD growth process.

2.1 Theoretical Knowledge

This section analyses literature defining the CVD process technology and catalyst evolution for CNT growth.

2.1.1 CNT Synthesis and Characterisation

CNT synthesis techniques can be divided into three main categories; laser ablation, arc-discharge and CVD [130]. Methods such as arc-discharge and laser ablation techniques suffer disadvantages of high operating temperatures (> 3000 ° C), significant levels of impurities, and difficulty in scale-up as a carbon source has to be evaporated for CNT growth [131], [132] . In contrast, CVD synthesis is a technically advanced, yet simple large-scale technique for CNT growth requiring only an oven, tubular reactor and mass flow controllers. It has advantages of lower processing temperatures (550 – 1000 ° C), lower cost, fewer product impurities, and simple installation and usage [133], [134]. Three main types of CVD techniques exist [32]:

- Floating catalyst (FC-CVD)
- Plasma enhanced (PE-CVD)
- Thermal (T-CVD).

The catalyst precursor can be delivered as a solid, liquid or gas [135]. The synthesis can be carried out as a single step process with catalyst directly fed via flow, or as a double step process where a substrate is pre-coated with catalyst via solution based spin coating or physical vapour deposition (PVD) [32], [135], [136]. PE-CVD or T-CVD, with catalyst deposited on a substrate using PVD, is the most commonly used procedure to grow VA-

CNTs (self-supported arrays of CNTs, commonly referred to as forests). Van der Waal forces, over-crowding effects and mechanical leaning have been used to describe this parallel alignment of CNTs [137]. Sometimes, T-CVD can be assisted with a laser to grow localised structures [138], [139]. Although PE-CVD enables the growth of CNTs on a varied catalyst layer thickness, high equipment costs make this technique less attractive [140]. Therefore, in this research we use T-CVD owing to its simplicity of use and lower cost.

A hydrocarbon source, such as methane, ethylene or acetylene is fed into the chamber, where it comes in contact with the hot catalyst source and breaks it into its reactive species; carbon and hydrogen [88], [136]. The catalyst surface assists the carbon atoms from the hydrocarbon feed to dissolve onto the catalyst and upon supersaturation precipitate and crystallize in the form of a cylindrical network called a CNT [33], [131]. This understanding is based on the tip and base growth model proposed by Baker *et al*. (1973), shown in Figure 5, and the theory developed by Wagner & Ellis (1964), that describes the growth of silicon whiskers through a vapour-liquid-solid mechanism [141], [142]. The model suggests that during CNT growth, when a substrate catalyst interaction is strong, the catalytic nano-island stays at the base (base growth model), whereas when the interaction is weak the catalytic nano-island is lifted up by the growing nanotube (tip growth model) [131].

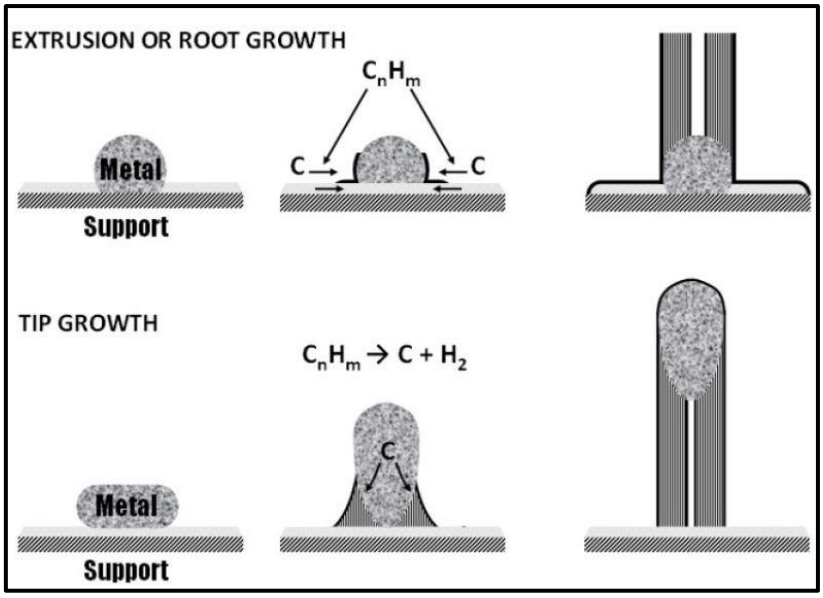

Figure 5: *Base growth and Tip Growth of Carbon Fibres According to the VLS model* [133]

2.1.2 Catalyst Layer Thickness

An increased development in potential applications of VA-CNTs has stimulated work on large area chemical vapour deposition growth methods. However, catalyst deposition techniques still need further development. The catalytic layer is typically deposited on the substrate through sputtering or evaporation. The disadvantages include the need for a high vacuum requirement and limitations to particle uniformity and density imposed by thin film dewetting. This common deposition technique is also unsuitable for niche, low-volume manufacturing scale-up [143]. Transition metal nanoparticles such as iron, nickel and cobalt have proven to be the most efficient catalysts for CNT synthesis on an industrial scale [34]. Albeit, in comparison to nickel and cobalt, iron has higher crystallinity and is usually chosen as the preferred catalyst [144], [145].

Bulk iron does not favour CNT growth. Therefore, prior to growth the iron film is annealed in a controlled environment, where internal stresses and defects in the catalyst film cause it to form particles or nano-islands through a process called dewetting [143], [146]. Well

dispersed catalyst nano-islands favour CNT growth, and are primarily responsible for controlling the properties of the CNTs such as wall number, diameter, chirality, yield and alignment, which directly correspond to their conductive properties [147], [148]. As each CNT is grown on a single nano-island controlling the size and density of these catalyst nanoparticles on the substrate is important to achieve the desired CNT properties [149] [144], [150]. It has been suggested by Bronikowski (2006) that catalyst activity switches on for a catalyst thickness between 1.5 nm to 6 nm [151]. For VA-CNT growth a < 1nm thick layer of iron is conventionally deposited on a support layer of alumina (10-100 nm thick) [152].

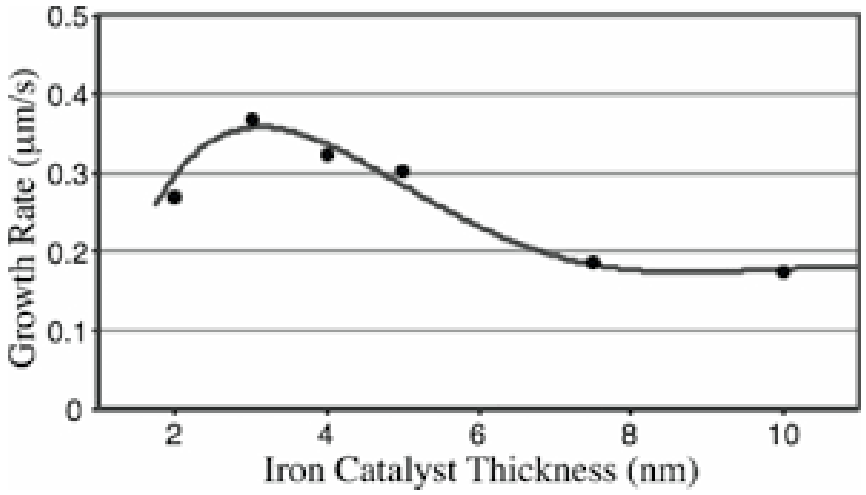

Figure 6: *Growth rates for varying iron layer thickness as found by Moulton et al. (2012)* [153].

As the deposited catalyst film thickness increases, it yields larger catalyst islands on which carbon precipitates, whereas thinner catalyst films result in the formation of smaller catalyst islands with lower areal coverage [151], [153], [154]. The annealed nano-islands typically have a lateral size range of 10-100 nm and this variance in particle size results in a distribution of growth activation behaviour [150]. Moulton *et al.* (2012) graphically presented data that as catalyst film thickness is increased maximum VA-CNT growth rate occurs at a specific thickness as shown in Figure 6 [153]. Anything below or above this thickness value can result in a decrease in growth rate. As a result it is determined that

aligned growth can occur within a specific range of iron catalyst thickness. For catalyst thickness below this range, low catalyst nano-island density leads to sparse growth of nanotubes, with weak Van der Waals forces to support them [145]. Consequently, the growth rate is dependent on iron availability and Van der Waal forces preventing the CNTs from growing at varying growth rates, and thus resulting in an even forest height [140]. However, for the thicker catalyst films during annealing a critical size of nano-islands is reached beyond which carbon encapsulation deactivates their functionality [33], [155]. Therefore, the growth rate of the CNTs is also limited by the gas phase diffusion of hydrocarbon radicals and the diffusion rate of carbon in and across the catalyst nano-island [156]–[158]. The formation of carbon structures on the catalyst surface will poison the catalyst particle, and thus serving as a limiting factor [159]. As the catalytic layer thickness increases, the mechanism of growth transitions from base to tip growth owing to a weak substrate catalyst interaction [153].

2.1.3 Support Layer and Catalyst Evolution

During growth, the iron film can interact with the silicon substrate and form iron silicide, and thus exhausting the iron catalyst source available for the formation of nanotubes. Therefore, an inert oxide support layer is used as a barrier to limit diffusion between the catalytic film and the silicon substrate by minimising Ostwald ripening and inhibiting the silicification of the catalyst. Hence, preventing catalyst poisoning [35], [160], [161]. Although many materials can be used as a buffer layer to support CNT growth, such as oxidized silicon substrates, silica, alumina, quartz, sapphire, zeolites and magnesium oxide, alumina (Al_2O_3) is the most common for VA-CNT growth owing to its strong substrate catalyst interaction [152], [162]. During CVD growth, reduction in CNT alignment leads to growth termination. Therefore, during the annealing phase of the growth process,

maximising growth height and alignment is dependent on controlling the buffer layer and catalyst interaction to achieve catalyst islands with suitable sizes and density [152].

In the case of VA-CNTs it has been shown that alumina may restrict the mobility of the iron. For smaller catalyst nano-islands (< 20 nm) surface diffusion is the main transport mechanism whereas for larger catalyst nano-islands (>100 nm) this is by bulk diffusion [163]. During the initial phase of hydrogen annealing, Ostwald ripening (the growth of large particles at the expense of smaller ones) causes larger catalyst clusters to undergo sub-surface diffusion into the alumina support, while the remaining catalyst forms small nano-islands [35], [37]. This is evidenced by a broadening of particle size distribution during the initial phases of annealing followed by a narrowing of the distribution during the latter phase [159]. An illustration by Bedewy (2017) demonstrates the evolution of an iron film as catalyst during CNT growth as shown in Figure 7 [164]. The opposing mechanisms of surface diffusion and Ostwald ripening result in a uniform assembly of small catalyst particles and are critical factors for CNT growth. This means that any iron compound can potentially serve as a catalyst such as salts, nanoparticles and buckyferrocene [35]. The support layer plays a critical role in balancing the opposing effects of Ostwald ripening and sub-surface diffusion, and thus promoting nano-island formation of a critical size range outside of which carbon encapsulation results in termination of catalytic activity [33], [35], [156]–[159], [165].

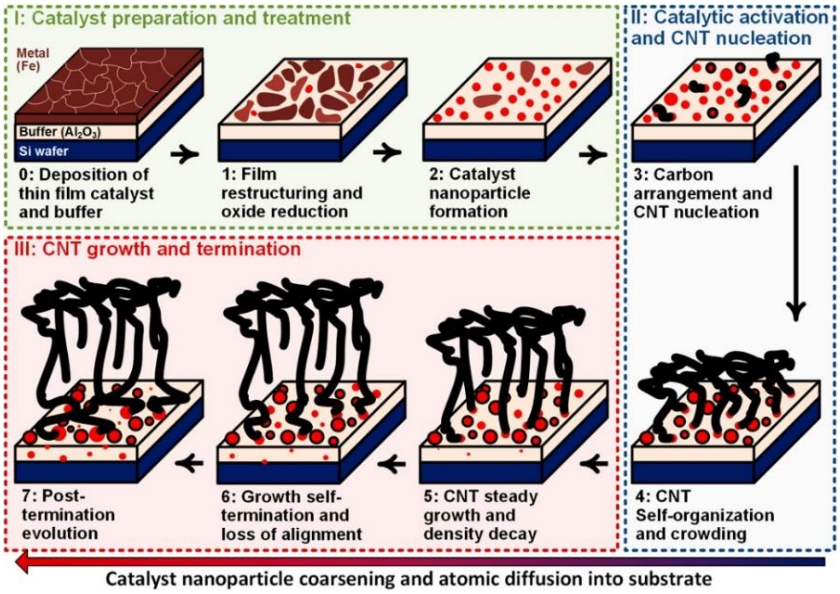

Figure 7: *Illustration by Bedewy (2017) showing the successive stages of CNT growth* [164]

Sakurai *et al.* (2012) demonstrated a model to describe how subsurface diffusion and Ostwald ripening have to be balanced in catalyst formation for single-walled CNT forest growth as shown in the equation below [33].

$$\frac{dr}{dt} = -\frac{A_s}{r^3}\left(1 - \frac{r}{r_c}\right) - C$$

Where, A_s is the rate coefficient for Ostwald ripening, r is the size of the catalyst, r_c is the critical size of Ostwald ripening and C is the constant for sub-surface diffusion. This model was further verified by Sakurai *et al.* (2013), where it was demonstrated that any iron compound supported on AlOx and treated with hydrogen can serve as catalyst for CNT forest growth when the effects of subsurface diffusion and Ostwald ripening balance out [166]. However, these models are still being verified and require specialist analytical techniques such as electron energy loss spectroscopy (EELS), X-ray photoelectron spectroscopy (XPS) and secondary ion mass spectroscopy (SIMS). Prof. John Hart's Mechanosynthesis group, at the University of Michigan is also looking at developing catalyst growth models and *in situ* analysis techniques for understanding catalyst evolution

for VA-CNT growth. They use an *in situ* grazing-incidence small angle X-ray scattering (GI-SAXS) to show particle dewetting dynamics, X-Ray diffraction (GI-XRD), electron diffraction (ED) to monitor the catalyst phase change dynamics, X-ray photoelectron spectroscopy (XPS) to reveal the changes in chemical states during catalyst carbon interactions, Z-contrast scanning transmission electron microscopy and optical reflectivity for real-time characterisation of CNT nucleation density and height kinetics [167]–[170].

The alumina (Al_2O_3) and iron (Fe) interaction during the initial heat treatment leads to the formation of Fe_2O_3 [161]. The oxidised catalyst is then reduced to a metal, and upon subsequent treatment with hydrogen is further reduced into nano-islands with a narrow particle size distribution, that act as nucleation sites for VA-CNTs to grow [145], [171]. The active catalyst nano-islands where the CNTs are grown are in their crystalline metallic form, as no graphitic structures are found on oxidised iron [155]. Wirth *et al.* (2012) suggests that for γ – rich iron catalyst the active phase for CNT growth is metallic iron, whereas for α – rich iron catalyst the active phase is a carbide (Fe_3C) [172]. Therefore, complicated kinetic effects control the catalyst and the exact mechanism of the iron phase evolution once CNT growth starts is still under research. Upon the growth of CNTs, amorphous carbon or graphitic build up on top of the CNTs reduces the growth rate of the CNTs over time by depleting the iron catalyst sites due to the formation of carbides [153], [171] . This build-up of amorphous carbon can be etched away and reduced by the introduction of hydrogen or water vapour in the reaction chamber during synthesis [143], [161]. As is clear from the review above, there is no specific recipe for the growth of CNTs as variations in particle size and the support layer and catalyst configurations affect the catalytic activities of the nano-islands for CNT growth [174].

2.1.4 Iron Oxide Nanoparticles as Catalyst

Hofmann *et al.* (2009) found that for an Al_2O_3 buffer layer and Fe catalyst configuration, both Fe^{2+} and Fe^{3+} interface states were present [155]. Magnetite iron oxide nanoparticles (Fe_3O_4) can be used as catalyst for VA-CNT growth as they consist of different ions like Fe^{2+} and Fe^{3+} [175]. Magnetite is not very stable and is sensitive to oxidation, and thus transforms into maghemite (γFe_2O_3), a more thermodynamically stable phase of Fe_2O_3 [176]. As previously stated the activation phase for γ-rich iron catalyst is metallic. Therefore it can be deduced that magnetite is reduced into metal films during the high temperature CVD growth process, and thus is suitable for CNT growth. However, an efficient substrate and buffer layer is still required to prevent them from agglomerating into nano-islands of monodisperse diameters as a result of Ostwald ripening [177], [178]. Controlling the spread and thickness of the nanoparticle layer on the substrate is important, as when the nanoparticles entirely cover the substrate as a film, CNTs are grown as a continuous carpet whereas when the nanoparticles are not enough to completely cover the surface, they form small nano-islands on which bundles of CNTs can form [112]. Three types of carbon nanostructures have been previously observed as sparse, tangled CNTs and VA-CNTs [143]. In order to achieve a more uniform distribution of CNT diameters, it is important to select a suspension with nanoparticles of a controlled size range [146]. Many researchers have reported the growth of VA-CNTs using iron oxide nanoparticles, and as a result commercially available nanoparticles can be used for this research [48], [143], [178]–[181]. Beard *et al.* (2013) in their paper demonstrating VA-CNT growth from inkjet printed iron oxide nanoparticles have put emphasis on the importance of a catalyst monolayer to achieve VA-CNTs. They have presented the only model known at time of writing for determining the number of inkjet droplets required for a given printer, ink concentration

and substrate wettability to achieve a printed monolayer of catalyst for VA-CNT growth, as shown in the equation below [48].

$$n = \left(\frac{3\beta^2 \xi h}{2D_o f}\right)^3$$

Where β is the substrate contact angle, ξ is the packing efficiency of the particles ($\pi/3\sqrt{3}$) for a single layer of closely packed spherical nanoparticles), h is the diameter of the nanoparticles, D_o is the nozzle size of the printhead and f is the percentage volume fraction of nanoparticles in a given suspension. However, this model does not take into consideration many inkjet printing parameters including droplet spacing and coffee ring effects, and Beard *et al.* (2013) found it to underestimate the required number of droplets in experimental data.

Ferrofluids are widely used in MRI contrast enhancement, drug delivery and cell separation, and thus are available in large volumes at low cost [143], [182]. They are colloidal suspensions of approximately 10 nm magnetic particles, coated with a surfactant (SFF) or ionic coating (IFF) to prevent agglomeration in oil or water based media [183]. Several types of cationic, anionic or non-ionic surfactants can be used depending on the medium selected [182]. Ferrofluids are known to behave as Newtonian fluids when suspended at low concentrations in Newtonian solvents [47], [184], [185]. From the literature reviewed it can be concluded, that the greatest advantage of using nanoparticle layers as catalyst is improved control over particle size distribution prior to deposition by careful selection of the nanoparticle size and varying ink concentration. Thus, a commercial ferrofluid, can be procured, analysed and tested as a suitable catalyst for CNT growth.

2.1.5 Iron Oxide Nanoparticle and CNT Characterisation

The morphology and structure of the iron oxide nanoparticle can be characterised using a host of techniques. The phase of the nanoparticle and particle size can be determined by Transmission Electron Microscopy (TEM) or X-Ray diffraction using Scherer's equation [186].

$$D_p = \frac{0.94\lambda}{\beta_{1/2} \cos\theta}$$

Where D_p is the average crystallite size, λ is the x-ray wavelength, β is the line broadening radius and θ is the bragg angle [187]. Dynamic Light Scattering (DLS) can also be used to calculate the nanoparticle size where a monochromatic laser beam is passed through the nanoparticle suspension and the frequency change in the scatter light known as the Doppler shift is studied [188]. The precision of DLS is still not completely understood as factors such as particle concentration, scattering angle and shape of the nanoparticles is neglected [189]. When measuring particle size using DLS, the hydrodynamic radius is calculated which also takes into account the surfactant layer on the nanoparticle and particle aggregation in water [182]. Therefore, the particle size obtained from DLS is generally greater than that determined by TEM micrographs which show the true radius of the nanoparticle as small molecular size organic compounds generally used as a surfactant layer such as (oleic acid and oleyalmine) are electron transparent, and thus not visible [189], [190].

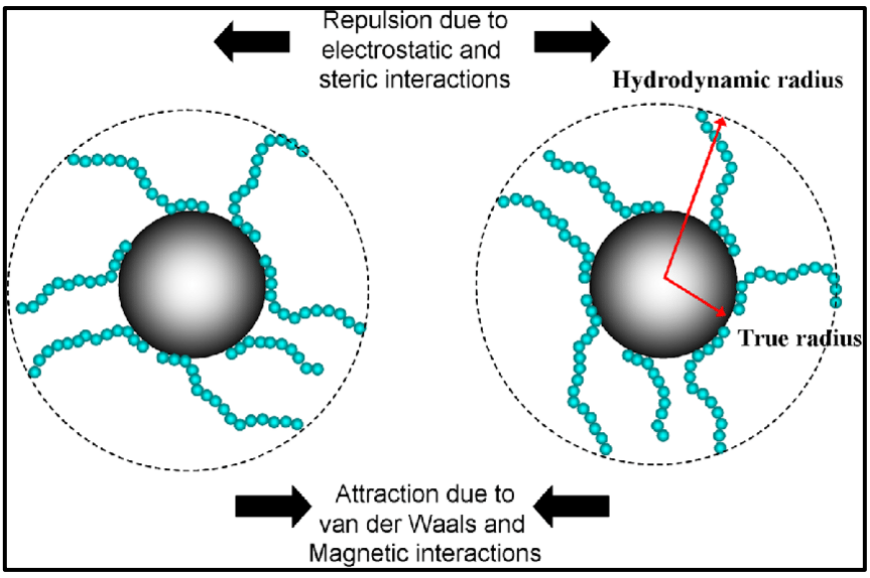

Figure 8: *Illustration by Lim et al (2013) showing magnetic nanoparticles and the major interactions involved between them that dictate the colloidal stability of the suspension* [190]

Fourier Transform Infrared Spectroscopy (FTIR) can be used to analyse the surface coating of the nanoparticles in order to determine the surfactants presence on the surface [182]. A combination of the aforementioned techniques is generally employed to characterise the iron oxide nanoparticles being studied, as one technique is not enough to carry out a complete structural analysis of the nanoparticles. CNTs can be analysed using Raman spectroscopy. By calculating the ratio of the peaks occurring at the graphitic structure derived G-band and the defect derived D-band, normally found at 1590 cm^{-1} and 1350 cm^{-1}, we can determine the quality of the nanotubes [191], [192]. Hodkiewicz *et al.* (2010) summarises the expected Raman spectra range for SWCNTs, DWCNTs and MWCNTs, as shown in Figure 9 [191]. Atomic Force Microscopy (AFM) is often used to examine CNTs once they are deposited onto a flat surface as individual tubes or a sparse network [193] . SEM is used to look at the VA-CNT forests as it can reveal the overall forest structure and detailed interaction between individual CNTs without any damage and AFM is used to look at the catalyst structure.

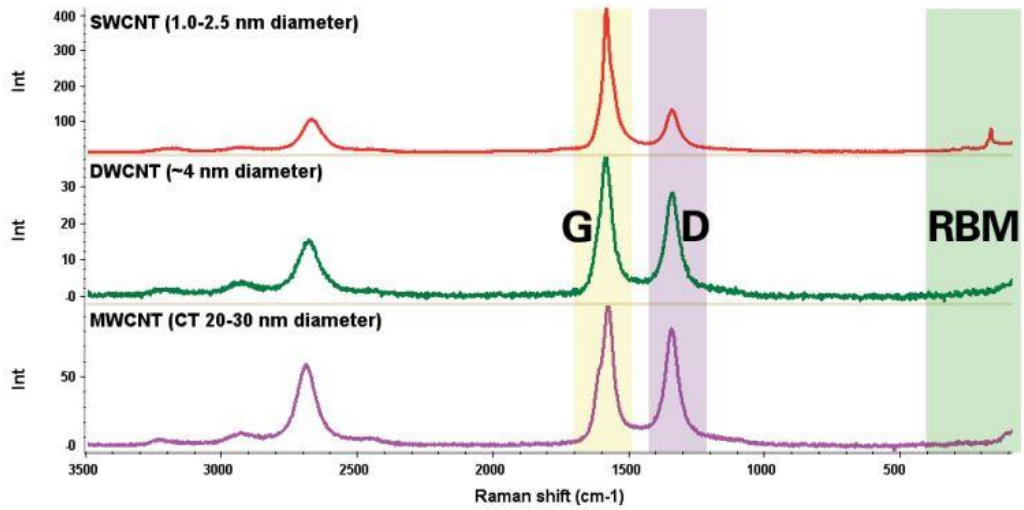

Figure 9: *Comparison of Raman spectra of SWCNTs, DWCNTs, and MWCNTs* [191]

From the literature analysed was determined that multiple catalyst sources can be used for VA-CNT growth, The greatest advantage of using nanoparticle layers as catalyst is improved control over particle size distribution and coverage prior to deposition, by careful selection of the nanoparticle size and varying ink concentration. Thus, a commercial ferrofluid can be procured, analysed and tested as a suitable catalyst for CNT growth. However, prior to optimising deposition conditions the magnetite nanoparticle ink should be characterised and the CVD growth conditions optimised. As noted in section 2.1.2 and 2.13, post annealing catalyst nano-island size distribution and coverage are important factors in determining alignment, and hence can be analysed. As loss of alignment results in growth termination, the VA-CNT height can be compared to understand differences between the catalyst variations. Therefore, in this chapter a new magnetite ink suspension has been characterised and compared to PVD deposited catalyst via analysis of catalyst nano-island formation during annealing, as it has previously not been explored. The VA-CNT growth conditions are defined for PVD deposited catalyst and a new analytical methodology for studying the evolution of varying catalyst sources during annealing is demonstrated. The next section outlines the experimental methodology.

2.2 Experimental Methodology

(100) Silicon wafers of diameter 100 mm and thickness 500 µm were procured from University Wafers [194] .

2.2.1 Plasma Vapour Deposition

The wafers were coated with a 10 nm alumina layer and a 1 nm iron layer using a LEV – Lesker PVD 75, four crucible e-beam evaporator. The silicon wafers after coating were scored with a diamond-tipped scribe into approximately 10 mm by 10 mm chips and transferred to the CVD process.

2.2.2 CVD

The CVD deposition for growing CNTs was carried out in the ambient pressure quartz tube furnace manufactured by Vecstar Ltd and customised by Dr. Davor Copic, Nano-manufacturing group, Department of Engineering, University of Cambridge. The quartz tube was cleaned using acetone and isopropanol (IPA) and baked for 2 hours at each section (inlet, middle and outlet) to ensure that any residue in the tube was removed. The schematic in Figure 10 shows how the CVD system works. The conditions described are recommended as standard operating conditions as designed by Dr. Davor Copic for this particular CVD system. A conditioning cycle of ten individual growths was carried out to stabilise flow of the gases on the internal surface of the quartz in order to ensure repeatable growths. All samples were cleaned prior to growth by sonication in acetone (480 s) and IPA (480 s). The samples were dipped in water and dried using a pressurised air gun.

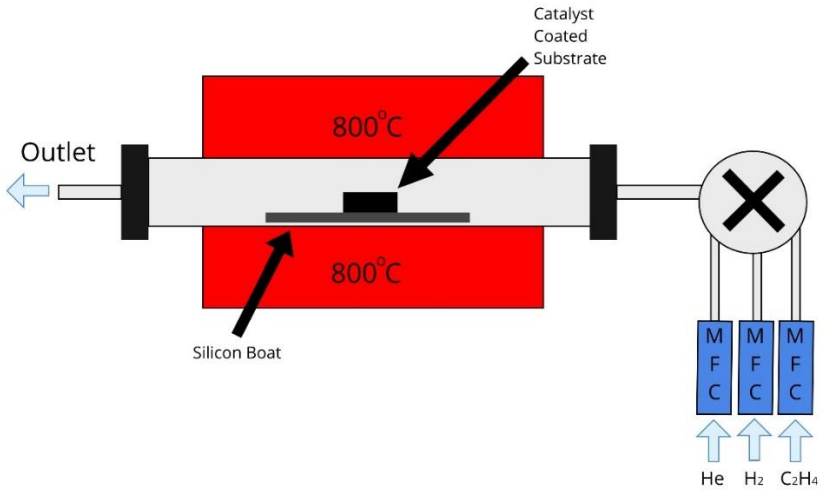

Figure 10: *Chemical Vapour Deposition Mechanism*

Three gases are used for the CNT growth: helium, hydrogen and ethylene. The furnace is preheated to 800 ºC and the tube baked for 30-45 minutes in order to clear the remaining material from the previous growth by keeping only the outlet flow tube attached. After the baking is complete, the outflow tube is removed and the upstream tube is attached for the inlet gases to flow and the growth programme initiated. The system is flushed with helium (450 sccm) for ten minutes, during which the sample boat is loaded into the tube and the outlet flow tube attached. A gas change then occurs for 1 minute during which the tube is slid into the furnace under the flow of helium (100 sccm) and hydrogen (400 sccm). The annealing step is then carried out for 14 minutes with a mixture of helium (100 sccm) and hydrogen (400 sccm). After annealing, another gas change step for 1 minute under the flow of helium (400 sccm) and hydrogen (100 sccm) following which the 30 minute CNT growth procedure is commenced under the flow of helium (400 sccm), hydrogen (100 sccm) and ethylene (100 sccm). Upon completion of the growth step, a 5 minute cooling cycle is carried out during which the tube and the samples are pulled out and removed under the flow of helium (450 sccm).

2.2.3 CNT Characterisation

The techniques used to analyse the iron oxide catalyst before growth and the CNTs after growth are described below:

- **AFM**

A catalyst and buffer layer coated silicon chips were annealed in the CVD and removed before the growth step in order to analyse the size of the catalyst nano-islands formed using an Atomic Force Microscope (Model CN6000, by CambridgeNano). The PVD deposited iron catalyst was analysed using the Tap 300 AI-G tips by Budget Sensors with a resonant frequency of 300 kHz and a force constant of 40 N/m [195]. The iron oxide nanoparticle catalyst was analysed using the Hi Res-C14/Cr-Au tips by µMasch with a resonant frequency of 160 kHz and a force constant of 5 N/m. Both tips are suitable for tapping mode and intermittent contact. The analysis was carried out in tapping mode.

- **SEM**

Images of the catalyst were taken using a Leo Gemini 1530VP FEG-SEM system with an InLens detector. Images of all the VA-CNT forests grown were taken using a Zeiss Crossbeam with an SE2 detector (contrast imaging) and InLens detector (topography imaging). All imaging was carried out at an accelerating voltage of 5 kV. Increasing the tilt value rotates the sample holder about the x axis. The samples are placed such that CNT forests are parallel to the y axis and the tilt angle θ is applied about the x axis. Therefore height h of the VA-CNTs is calculated using the following equation [196]:

$$h = \frac{d}{\sin\theta}$$

Where d is the apparent height in the image and θ is the tilt about the axis.

- **Raman**

The CNT quality was analysed using a Renishaw inVia Raman microscope with a 532 nm (green) diode with an 1800 I/mm grating. The laser power was set at laser power of 5 %, exposure time of 10 s and 1 accumulation. Raman analysis was conducted in three locations on a sample and the average calculated.

2.2.4 Ferrofluid MSGW10 Magnetite Ink characterisation

Ferrofluid MSGW10 was obtained commercially from Ferrotec. This ink was selected as it has been successfully blade-casted as a thin film for CNT growth and uses water as a carrier fluid, which is compatible with most printing systems. The ink specifications can be found in the table below.

Table 3: *MSGW10 Ferrotec Ferrofluid Specifications.*

Composition % (by volume)	Magnetite 2.8-3.5% Dispersant 2-4% Water 92.5 – 95.2%
Appearance	Black fluid
Carrier liquid	Water
Nominal Particle Diameter	10nm
Particle Concentration %v/v	3.6
Nominal pH	10.5
Saturation Magnetisation	185 Gauss
Density	1.19 x 10^3 kg/m^3
Viscosity	<5cP
Nominal Surface Tension	40mN/m

The nanoparticles as procured are dispersed in water and surfactant. The surfactant was analysed using a Perking Elmer Frontier FTIR system. 8 dilutions were made using deionised water to ensure the carrier fluid and volatility were kept constant. The solutions after mixing were sonicated for 30 minutes. The viscosity and surface tension of 3 dilutions were measured to give an indication of ink behaviour upon dilution with water. The viscosity and the surface tension of the solutions were measured with the portable electronic

Hydramotion Viscolite 700 viscometer and the bubble pressure tensiometer SITA pro line t15. The rheology measurements were conducted using an Anton Paar rheometer. Three techniques were employed to analyse the structure and morphology of the nanoparticles. The particle size was verified by examining the particles with an FEI Philips Tecnai 20 TEM and an Anton Paar Litesizer 500 DLS. The particle morphology was verified using Bruker D8 XRD and the particle size calculated using Scherrer's Equation.

$$D_p = \frac{0.94\lambda}{\beta_{1/2} \cos\theta}$$

Where D_p = average crystallite size, λ is the Cu Kα, β is the full width at half maximum (FWHM) in radians and θ is one half of the XRD peak position in radians [197].

2.3 Results and Discussion

The results are reported in three sections. The first section looks at the optimisation of the CVD system and its performance on PVD deposited catalyst, as a control, analysing the forest heights and quality. The second section presents characterisation data for the magnetite ink. The section also looks at the effect of growing CNTs from PVD deposited iron in the presence of the magnetite ink. The final section explores the difference between the annealed nano-islands formed from a 1 nm layer of PVD deposited iron and a layer of magnetite ink suspension. This comparison will enable us to determine the size of the nano-islands formed from the magnetite ink suspension layer and set the premise for the research in Chapter 3 to optimise the required magnetite layer thickness for VA-CNT growth. These findings will shed light on the ongoing argument of the importance of catalyst nano-island size during annealing for VA-CNT growth as highlighted in 2.1.2 and 2.1.3.

2.3.1 PVD Deposited Catalyst CNT Growth

The optical image in Figure 11.a shows the silicon wafer chip coated with a catalyst/buffer layer configuration of 10 nm alumina and 1 nm iron. Figure 11.b shows an optical image taken of the silicon wafer coated with iron and alumina post CVD growth. The black appearance of the silicon wafer after CVD growth is indicative that a carbon based material has grown on the substrate. The samples were analysed at a 45° tilt using an SEM to measure the height of the forests. For each height measurement, an average of ten measurements was taken using ImageJ. SEM micrographs of the VA-CNTs can be seen in Figure 11.c and d. The height of the forest in Figure 11.d was calculated to be 265.1 ± 0.5 µm.

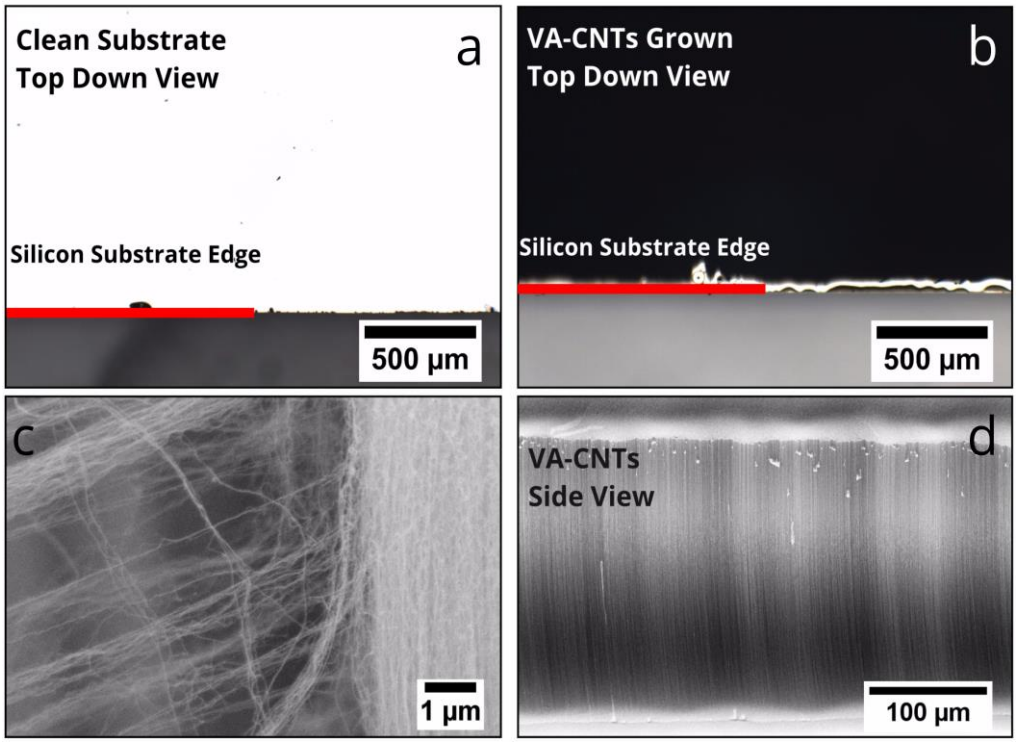

Figure 11*: Optical micrograph showing (a) silicon wafer chip coated with 1 nm iron catalyst and 10 nm alumina buffer layer before growth and b) silicon wafer chip after VA-CNT growth. SEM micrograph show c) the individual CNTs and d) the overall forest.*

As noted in Section 2.2.2, the quartz tube is conditioned to ensure repeatable VA-CNT growth. Three of the ten conditioning samples can be seen in Figure 12.a, b and c representing the beginning, middle and end of the conditioning cycle. The annotations on

the micrographs indicate the apparent height of the forest as viewed and the adjacent tables list the actual heights calculated. For the first growth of the conditioning cycle a maximum forest height of 330.9 ± 2.5 µm was achieved. As the conditioning cycle was continued the forest height dropped to 203.2 ± 1.1 µm and by the end increased to 317.2 ± 2.6 µm. A total height variation of approximately 127 µm was observed across the conditioning cycle.

Although a conditioning cycle was run, subsequent samples grown continued to show height variations, but of a smaller margin. Growth samples can be found in Appendix B, Figure B 1 where the average height range for the VA-CNT forests grown from PVD deposited catalyst film for the particular CVD found to be between 250 µm – 320 µm. While this range is narrower than that achieved during the conditioning cycle, this variation in forest height indicates that the CVD process is not completely stable. The CVD set-up is placed on a work bench shared with other equipment. Small vibrations result in gas flow disturbances resulting in variations in growth conditions. These errors may be reduced by using a commercial CVD system. However, for the purpose of this research these minor variations in VA-CNT forest height are not significant.

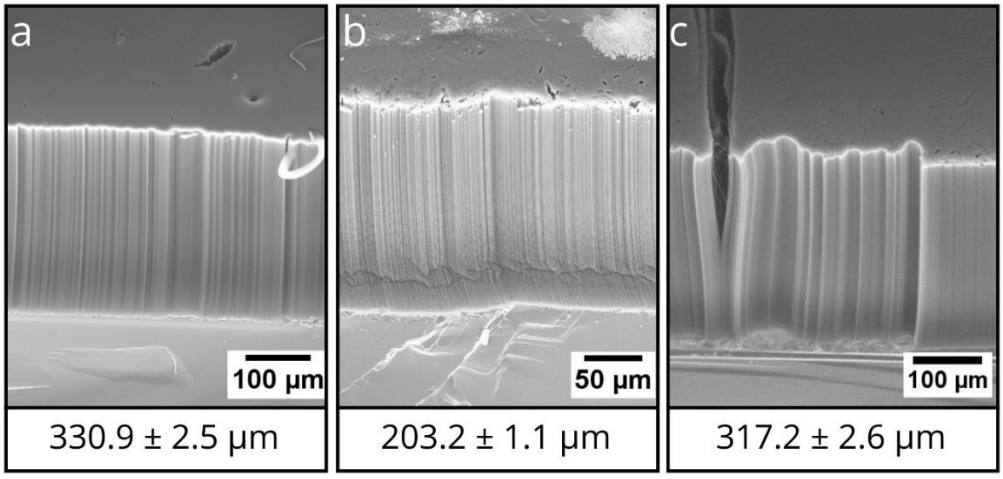

Figure 12: *SEM micrographs showing VA-CNTs on conditioning samples representing a) beginning b) middle and c) end of the conditioning cycle with VA-CNT heights listed as calculated from the SEM micrographs with tilt angle corrections. The height of the VA-CNTs and standard error have been reported below each image.*

Raman spectroscopy is used to identify and evaluate the quality of CNTs based on the ratio of the tangential G-band (1589 cm^{-1}) and the defect induced D-band (1335 cm^{-1}) as explained earlier in section 2.5 [152]. The G/D ratio is used to quantify the quality of CNTs by evaluating the amorphous components or amount of defects present. SWCNTs, have higher G/D ratios (>20) than MWCNTs (<10) indicating that SWCNTs have lower defects than MWCNTs [198]. The quality of the CNTs is highly dependent on the CVD system. Most high quality CNTs are obtained via arc ablation or laser ablation growth mechanisms whereas, for large scale growth of aligned CNTs, CVD systems are normally used, resulting in mostly MWNTs with defects [199]. For the CVD used in this research, VA-CNTs are usually grown with a maximum G/D ratio of 5. The suitability of using G/D ratios to determine the quality of CNT conductivity or strength is still under discussion [198]. However, it is a widely used technique to identify the presence of CNTs. Figure 13 shows a representative Raman spectra taken in the centre of one of the samples grown. A G/D ratio of 3.5 was calculated from the graph shown. VA-CNTs of similar quality were observed for the other samples.

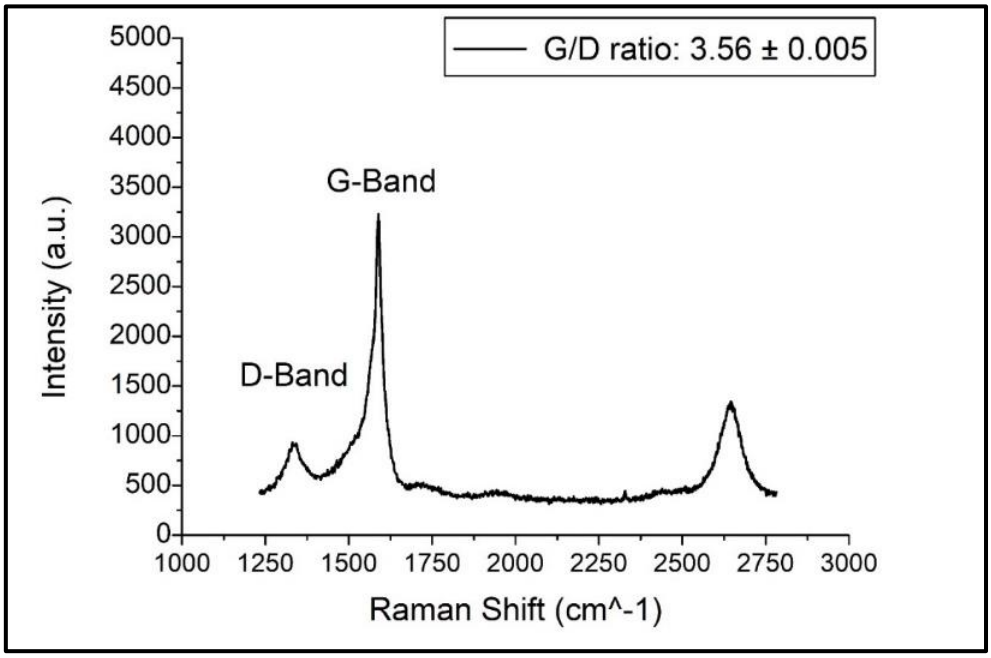

Figure 13: *Raman spectroscopy graph of VA-CNT forest grown from a 1nm iron catalyst and 10nm alumina buffer layer coated silicon wafer chip.*

2.3.2 Magnetite (Fe_3O_4) Ink Characterisation and CNT Growth

With the CVD conditions optimised for growing VA-CNTs with PVD deposited iron films, in this section the magnetite ink is characterised and diluted to achieve varying magnetite concentrations. As seen in Table 3, although the volume percentage of the magnetite and the overall density of the suspension are listed in the specifications provided by the supplier, the density of the magnetite particles in the suspension is unknown. The magnetite density in the procured suspension is important to estimate the weight percentage of the ink when diluted. The 'as-procured' ink was measured to have a magnetite concentration of 14.59 % $_{w/w}$ magnetite from which seven dilutions were made: 0.72 % $_{w/w}$, 1.46 % $_{w/w}$, 2.19 % $_{w/w}$, 4.42 % $_{w/w}$, 6.57 % $_{w/w}$, 8.71 % $_{w/w}$ and 10.93 % $_{w/w}$. The calculations can be found in Appendix B, Table B 1 and Table B 2. The 'as-procured' magnetite ferrofluid had a viscosity of 2.3 ± 0.05 cP. The surface tension measurements were taken for representative dilutions 2.19 % $_{w/w}$, 6.57 % $_{w/w}$ and 14.59 % $_{w/w}$, and the results can be seen in Figure 14. It can be seen in the graph that as concentration increases the viscosity increases and surface tension decreases. However, the surface tension measurements for all three inks dilutions demonstrate a dynamic behaviour where the surface tension for each ink concentration drops with increasing bubble life time. This trend is synonymous with aqueous surfactant solutions, where the surfactant around the surface of a bubble cause changes in the bubble rising motion, leading to a variation of surface tension across the bubble surface [200]. The results shown in Figure 14 indicate a reduction in surface tension as bubble lifetime is increased, resulting in the solution appearing more viscous with increasing lifetime [201].

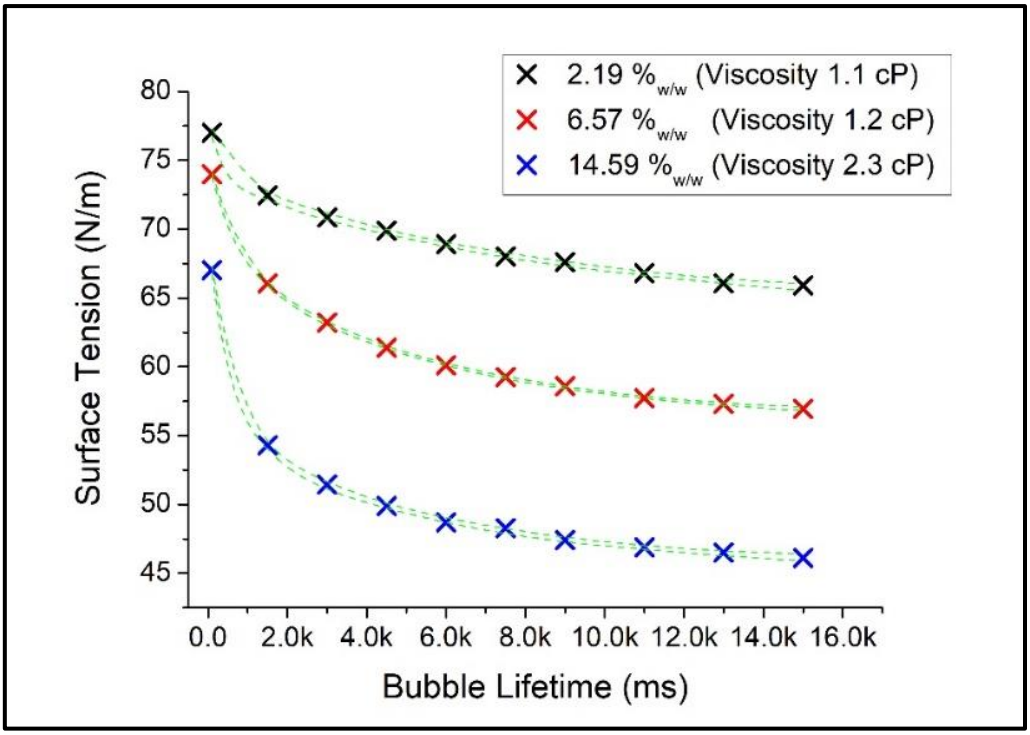

Figure 14: *Graphic representation of surface tension measurements and viscosity values for ink concentrations 2.18 %w/w, 6.57 %w/w and 14.59 %w/w. The green dotted lines represent a 95% CI of ± 0.3 N/m .*

However, to fully understand the behaviour of an ink it is essential to determine its rheological properties which define the ink as a Newtonian or non-Newtonian fluid. Water based magnetite suspensions are expected to display Newtonian characteristics. Therefore, rheology measurements were conducted to determine the effect of varying shear rate (1/s) on the viscosity (cP) of ink dilutions 2.19 %w/w (LIC), 6.57 %w/w (MIC) and 14.59 %w/w (HIC), as shown in Figure 15. Although during inkjet printing, liquids face she shear rates of up to 10^6 s^{-1}, standard rheometers, such as the one used in this work, can give errors when measuring beyond 500 s^{-1} as a result of an unstable torque. Consequently, measurements were not taken beyond a shear rate of 500 s^{-1} as the measured viscosity values were not accurate.

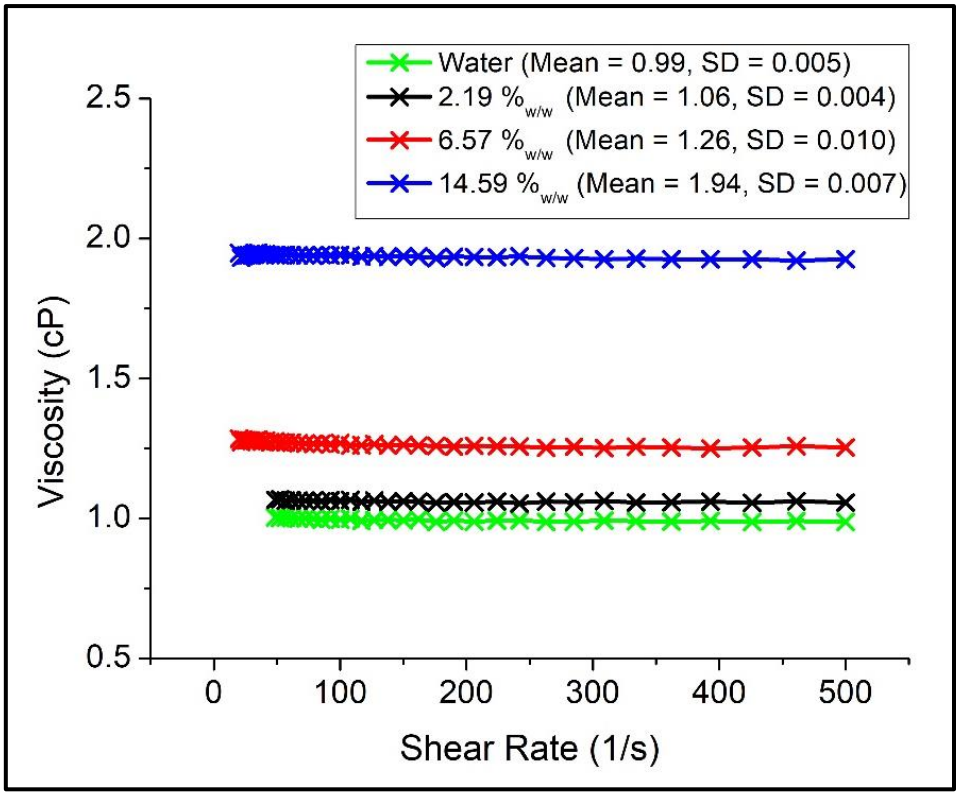

Figure 15: *Graph representation of rheological properties viscosity (cP) against shear rate (1/s) for water and magnetite concentrations 2.19 %w/w, 6.57 %w/ and 14.59 %w/. With a 95% CI, the average viscosities for LIC, MIC and HIC are calculated as 1.06 ± 0.001, 1.27 ± 0.003 and 1.94 ± 0.002.*

The results shown in Figure 15 confirm that the 'as-procured ink' concentration 14.59 %w/w behaves as a Newtonian fluid for shear rates up to 500 s^{-1}. Diluting the ink reduces the average viscosity, while still maintaining the inks Newtonian behaviour. Therefore, no viscoelastic and extensional flow behaviour characterisation was required. The average viscosities calculated for LIC, MIC and HIC are 1.06 ± 0.001 cP, 1.27 ± 0.003 and 1.94 ± 0.002 cP. The viscosity measurements calculated for the LIC and MIC via the rheometer have a low variance of 0.1 % and 0.2 % respectively in comparison to previously measurements conducted with the viscometer in Figure 14. On the other hand HIC has a higher variance of approximately 6% from its previously calculated value. The standard error and variance of the viscosity calculations made from the rheometer readings are low, and can henceforth be used for further calculations.

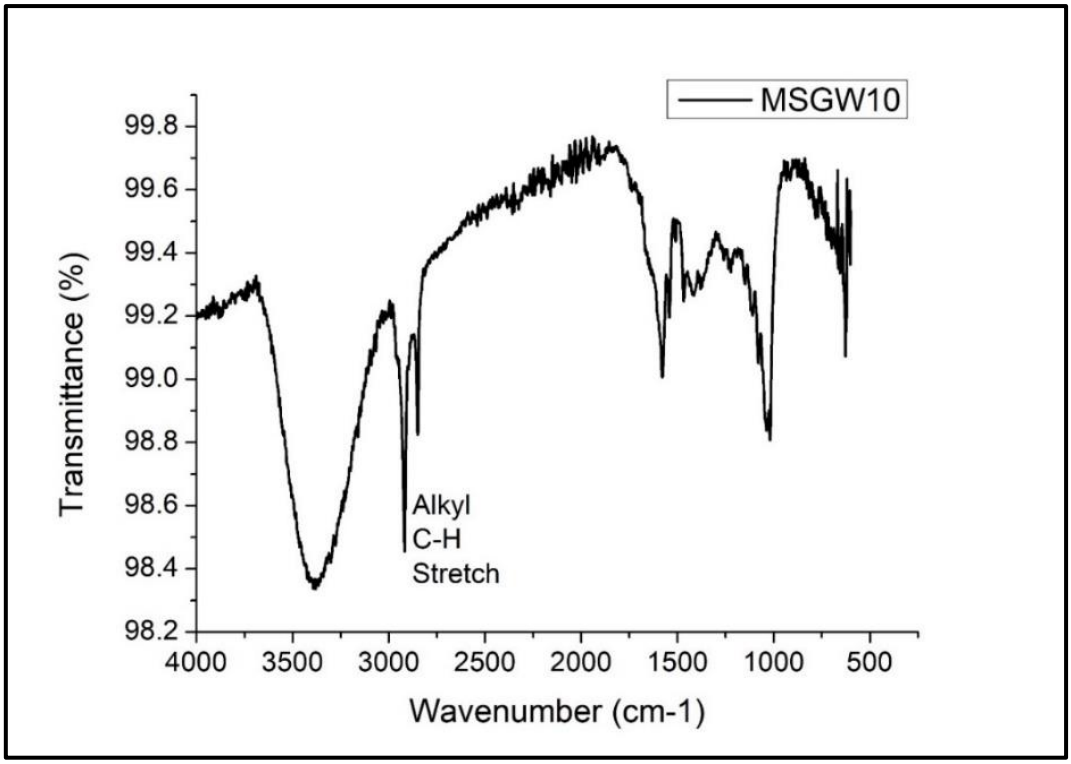

Figure 16: *Graph showing FTIR spectrum of the as procured iron oxide nanoparticle suspension*

It is also important to also consider the nanoparticles themselves. The FTIR spectrum in Figure 16 show antisymmetric and symmetric vibration of CH_2 chains at 2916 cm^{-1} and 2849 cm^{-1}. The broad peak between 3100 cm^{-1} and 3600 cm^{-1} indicates the presence of exchangeable protons from alcohol, amine, amide or carboxylic groups [202]. Peaks in the finger print region below 2000 cm^{-1} are difficult to identify and need comparison with other spectra. The exact composition of the surfactant is not known as it is a proprietary material from Ferrotec, but the FTIR spectra reveal the presence of a surfactant. TGA was attempted to determine the exact nature of the surfactant, but measurement was not possible on account of low surfactant concentration. This is not critical in this case, as successful growths of VA-CNTs have been previously reported using this ink [143].

DLS measurements were taken to determine size of the magnetite nanoparticles. A hydrodynamic radius of approximately 49.5 ± 0.5 nm was calculated using the DLS. The product specification reports the nanoparticles to have an average particle diameter of

10 nm. Therefore, XRD and TEM were employed to verify the structure and morphology of the nanoparticles.

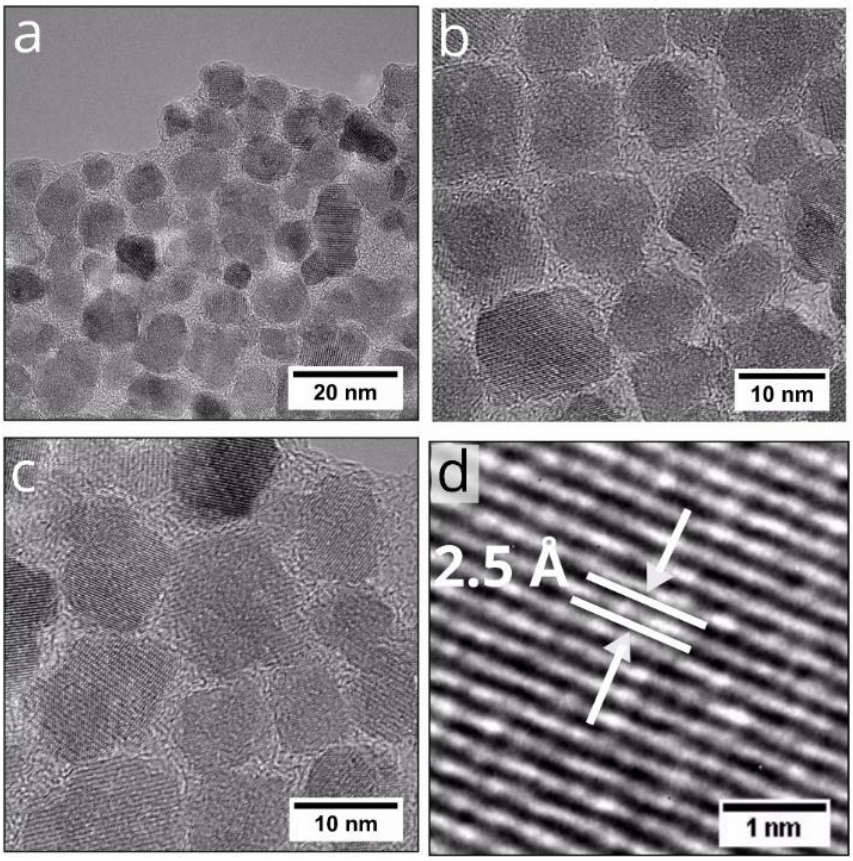

Figure 17: a) b) c) *TEM micrographs of the nanoparticles and d) interplanar lattice spacing measured at 2.5 ± 0.1 Å. Errors have been calculated as a 95% CI.*

TEM micrographs in Figure 17.a, b and c show the surfactant layer around the nanoparticles as seen in. A mean interplanar spacing of 2.5 ± 0.1 Å with a 95% CI was calculated from the TEM micrographs shown in Figure 17.d and is synonymous with the magnetite structure of the nanoparticles [187]. TEM micrograph analysis using ImageJ calculated the average diameter of the iron oxide nanoparticles to be 9.3 ± 0.6 nm with a 95% CI, verifying the approximate < 10nm particle size reported by the suppliers and allowing us to estimate that the additional 40 nm identified in DLS was due to the effect of surfactant on the hydrodynamic radius.

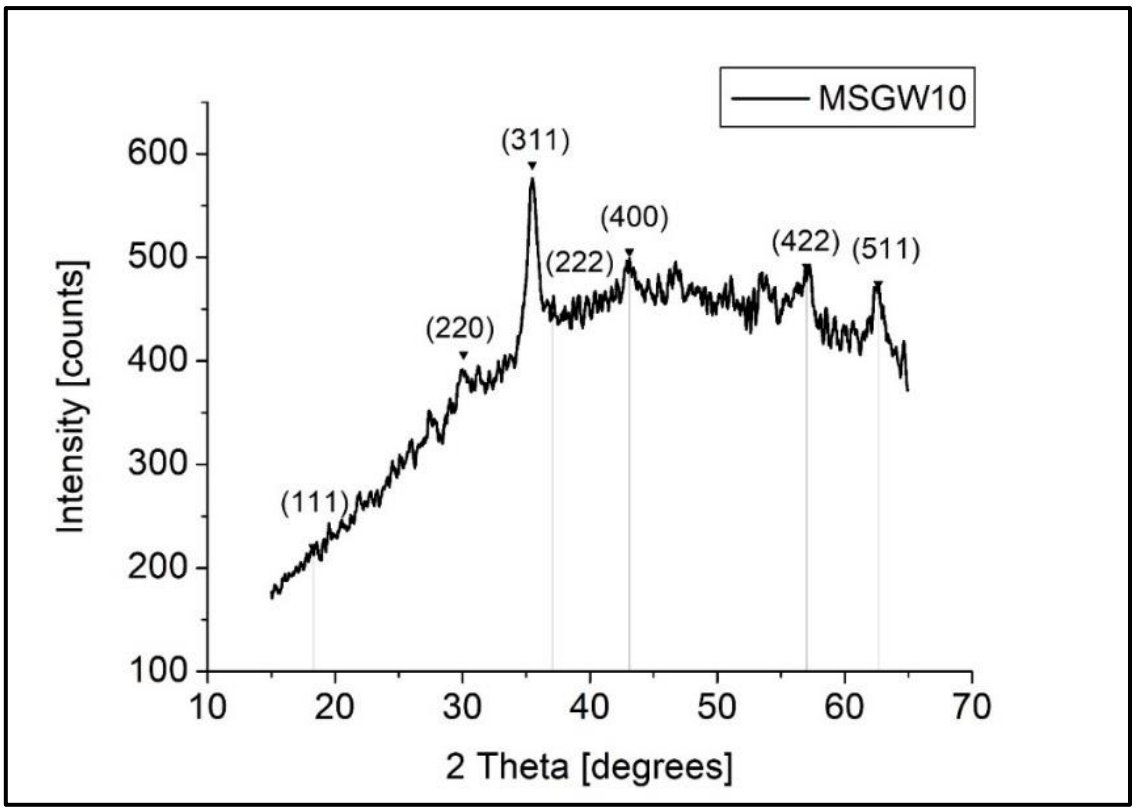

Figure 18: *XRD graph with peaks identifying a magnetite structure of the procured ink when drop casted and dried.*

Peak analysis of XRD data also verified this magnetite structure of the particles as seen in Figure 18. Scherer's equation was used to calculate the crystallite size as approximately 14 ± 0.5 nm as seen in Table 4. To ensure enough material was available for XRD analysis, the magnetite nanoparticles were drop casted on a silicon wafer chip. However, the films were found to crack and displace upon drying. As XRD is mostly used for large area analysis of homogeneous samples, the gaps occurring on account of the films cracking and displacing during analysis can affect measurements [203]. This is further evidenced by the noise observed in the XRD spectra in Figure 18. TEM on the other hand gives a visual analysis of sample homogeneity in localised areas, and thus was concluded as the more suitable approach in this case for analysing the magnetite nanoparticles and identifying the correct particle size [204]. Standard XRDs are not suitable for analysing the phase of the annealed nanoparticles as upon removal from the quartz tube, exposure to air causes changes in the catalyst film rendering it unrepresentative of the catalyst nano-island phase.

The thickness of the catalyst film also determines the morphology and phase of the nanoparticle film during annealing. In order to understand how the phase of the nanoparticles changes during the annealing phase of CVD growth, in situ EELS, XRD, XPS, SIMS and environmental transmission electron microscopy (ETEM) are required, but were out of the scope of this study [167]–[170][172].

Table 4: *XRD peak analysis data, calculating particle diameter using Scherrer's Law.*

Dp (nm)	**Cu Kα (Å)**	**Peak position 2θ (°)**	**FWHM 2θ (°)**	**Interplanar Spacing (Å)**
14.77	1.54	35.45	0.59	2.53

It is not clear if the inclusion of surfactants will be detrimental to the CVD process when using magnetite inks. As an initial test, PVD deposited catalyst samples were grown alongside samples with drop casted magnetite ink. Upon SEM height analysis it was observed that the height of the forests grown on the PVD samples were shorter than when grown without the drop casted samples. The SEM micrographs can be seen in Figure 19.a and b where the forest heights are calculated as 139.1 ± 1.3 µm and 99.2 ± 2.6 µm. All errors have been calculated to a 95% CI. The CVD growth process is conducted at high temperatures, which will cause ink components such as surfactants to evaporate from the catalyst film. The vaporised component can react with the gases flowing through the quartz tube, and thus may be responsible for altering the growth environment leading to early growth termination.

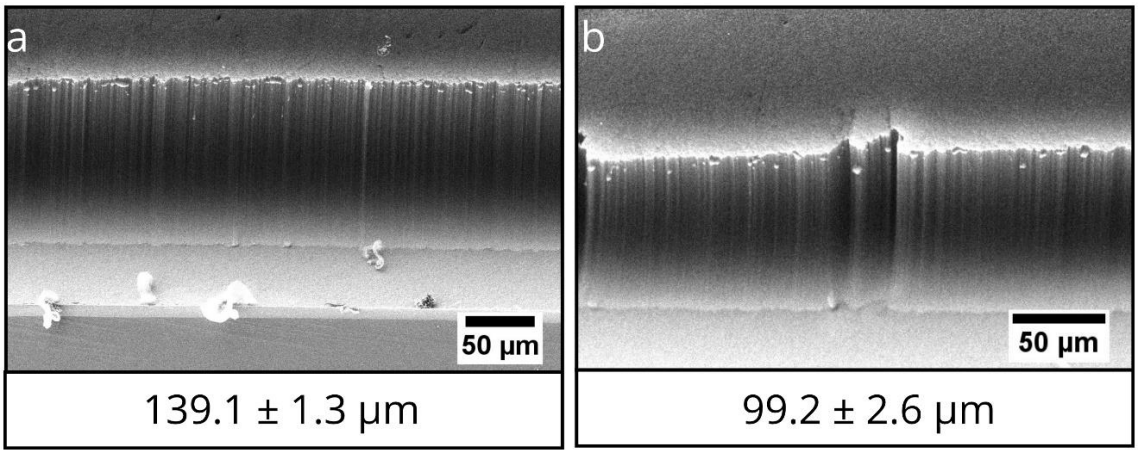

Figure 19: *SEM micrographs showing samples 1 a) and 2 b), showing VA-CNTs grown in the presence of magnetite ink on PVD deposited catalyst with VA-CNT heights listed as calculated from the SEM micrographs with tilt angle corrections. All errors calculated as a 95% CI.*

2.3.3 Comparison between PVD Deposited Iron and Iron Oxide Nanoparticles

As discussed in section 2.3, catalyst films during the annealing phase reorganise into active nano-island sites upon which CNTs are grown. The source and thickness of the catalyst determine the size of the nano-island sites formed. As in-situ XRD techniques are not available on the CVD set-up being used, comparing the size of the nano-islands visually is another technique to compare the effect of different catalyst sources and film thickness on CNT growth. PVD deposited iron is compared directly with inkjet deposited magnetite nanoparticles, to understand the difference in nano-island formation behaviour. Specifically, a 1 nm PVD iron layer was compared to a printed line of diluted ink concentration (2.19 $\%_{w/w}$). Both were applied on a 10 nm alumina coated silicon wafer. It is important to note that additional, more detailed analysis of inkjet printing of catalyst will be addressed in Chapter 3.

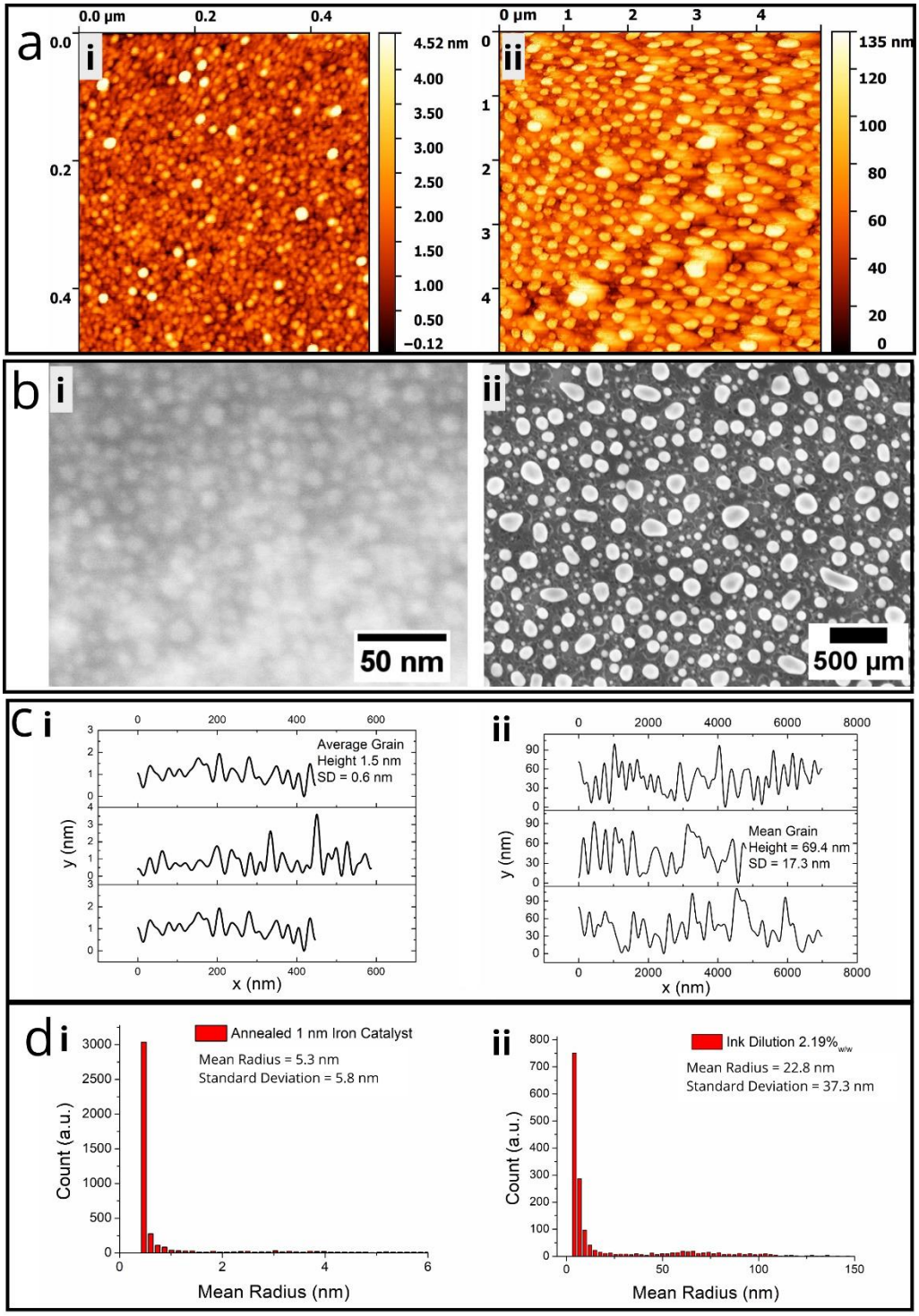

Figure 20: *Comparison of the post annealed catalyst nano-islands formed from* ***i)*** *PVD deposited iron film and* ***ii)*** *layer of magnetite nanoparticle ink.* ***a)*** *AFM micrograph and* ***b)*** *SEM micrographs show microstructure of nano-islands formed post annealing. Graphical representation show* ***c)*** *height profiles and* ***d)*** *mean grain size distributions of the annealed nano-islands..*

Starting with the PVD coated layer, AFM analysis of an annealed silicon substrate coated with 1 nm iron and 10 nm alumina revealed that after annealing the iron film melts, and through a complex Ostwald ripening and surface diffusion mechanism, reorganises into

nano-islands of a mean height of 1.5 ± 0.1 nm mean grain size of 5.3 ± 1 nm as seen in Figure 20.a, e and g. All errors have been calculated as a 95% CI. It is important to note that owing to oxidation of the catalyst upon removal of samples from the oxygen-free annealing environment, the size of the nano-islands may have changed from the original size. The nano-islands were also analysed under an SEM as seen in Figure 20.c. However, in this case the resolution was insufficient for accurate analysis to be carried out.

The annealed coating of iron oxide nanoparticles were studied using AFM, but the particles had poor adherence to the substrate, resulting in distortions and stretching of the image, as seen in the micrograph in Figure 20.b. SEM analysis proved a more suitable technique to analyse annealed magnetite ink particles as they are clearly visible as seen in Figure 20.d. It can be seen that the nano-islands formed from the magnetite catalyst are larger than those formed from the PVD deposited iron catalyst. A mean nano-island height of 1.5 ± 0.2 nm and grain size of 5.3 ± 1 nm was calculated for the PVD deposited iron layer, whereas a mean nano-island height of 69.4 ± 6 nm and a mean grain size of 22.8 ± 7 nm were calculated for the magnetite catalyst layer (Figure 20.a and b). This showed that a combination of SEM and AFM is required for analysis of post annealed catalyst nano-islands as their size and substrate adherence can vary depending on thickness of catalyst layer deposited, as highlighted in sections 2.1.2 and 2.1.3. As identified in section 2.1.4, the model presented by Beard *et al.* (2013) is not suitable for detailed printing applications on account of it not taking into consideration key inkjet printing parameters and conditions. The model is only demonstrated for droplets deposited in a single location. Therefore, inkjet printing parameters need to be investigated to understand whether patterns of iron oxide nanoparticle catalyst layers can be achieved with a layer thickness suitable for VA-CNT growth. The findings will be compared to those indicated by the model presented by

Beard *et al.* (2013) and optimised to achieved maximum growth rate, and hence VA-CNT height.

2.4 Conclusions

Development of the subtractive and additive components of the proposed hybrid manufacturing technology is not feasible without defining the non-variable operating conditions for the assistive component and the magnetite ink properties. This chapter forms the basis of all future CVD growth analysis and has successfully identified the key techniques required to analyse CNTs grown during the course of the lab based research and during scale-up. Key findings from this chapter are highlighted below:

- VA-CNT growth is highly dependent on the CVD quartz tube conditions, catalyst thickness and material composition.
- Conditioning of the tube improved process repeatability. However, other flow changes and variations can result in minute height variations for each growth cycle. Therefore, commercial CVD systems are required for scale-up.
- Early catalyst activation occurs for PVD deposited iron catalyst when grown in the presence of magnetite ink was observed, and is attributed primarily to changes in the growth environment caused by surfactant evaporation.
- Upon comparison of the annealed PVD deposited catalyst and magnetite nanoparticle films, it was observed that the magnetite ink films formed larger catalyst nano-islands during annealing than those formed with PVD deposited iron films

The findings highlighted above give a new insight into the mechanism of CVD growth of VA-CNTs. It can be predicted that on account of the surfactant present in the magnetite

ink suspension, alignment of CNTs is possible if the right catalyst layer thickness, and hence size of the annealed nano-islands is achieved. However, the VA-CNTs grown are expected to be of a shorter height than those grown from PVD deposited iron films. Characterisation of the commercial magnetite ink was conducted to not only verify the supplier provided specifications, but also determine its behaviour during inkjet printing. When transitioning from iron films to magnetite nanoparticles as catalysts the printed catalyst layer thickness needs to be modified carefully to ensure smaller nano-islands can be formed during annealing. This knew knowledge sets up the premise for the experiments to be conducted in the next chapter where inkjet printing will be utilised to deposit layers of iron oxide nanoparticles as a catalyst for VA-CNT growth. The size of the nano-islands formed from the inkjet printed catalyst during annealing can be modified by controlling the amount of catalyst deposited in a given area. The behaviour of the catalyst can then be compared to the models defined in section 2.1.

The chapter defines a new methodology of characterising and comparing annealed nanoparticles to those formed from PVD deposited iron films. In terms of characterisation techniques, Raman spectroscopy will be used to compare CNT quality in future. While AFM analysis is a suitable technique for determining particle size distribution of annealed catalyst nano-islands for PVD deposited iron catalyst, it is not suitable for analysing large nano-islands formed by thick magnetite ink layers, on account of poor adherence to the substrate. Therefore, a new analysis technique using SEM was employed and proved more suitable for analysing annealed nano-islands formed from magnetite ink. In order to compare the phase changes and catalyst evolution during the CVD growth process, in-situ XRD, XRR and ETEM technology are required. However, the lack of these techniques is not detrimental to the next phases of research as other techniques can be used to characterise VA-CNT growth. In-situ analysis of catalyst evolution can be incorporated at industrial

scale pilot facilities for detailed optimisation of fabrication parameters. In the next chapter, detailed analysis will be conducted to determine whether magnetite nanoparticles can be inkjet printed as catalyst for VA-CNT growth. With this new knowledge of the CVD procedure, catalyst evolution during the annealing phase, and varying VA-CNT growth rates, the research can now move onto the specification phase. The CVD growth conditions determined in this chapter will be kept constant for all future growths.

Chapter 3

INKJET PRINTING – ADDITIVE MANUFACTURING WITH MAGNETITE CATALYST FOR VA-CNT GROWTH

In conventional printing systems such as lithography, gravure and screen printing, rolls, plates or screens are used as the medium to transfer a pattern onto a substrate via direct or indirect contact [205]. Inkjet printing is a digital, non-contact, and additive fabrication process that builds up the pattern directly on a substrate by depositing suspensions and solutions [48]. The current global printing industry accounts for more than U.S. $900 billion [205]. Conventional patterning techniques such as photolithography have been shown to produce feature sizes as small as 15 nm; whereas, inkjet printing renders feature sizes between 1 µm to 100 µm [11], [206]. Albeit its larger feature size, inkjet printing can be used as a complimentary tool to conventional device fabrication techniques, for higher and more precise throughput [207][208][209].

Although printing of CNT dispersions has been reported in the past, the direct inkjet printing of CNTs poses many problems. Homogeneous dispersions of CNTs are difficult to achieve, ink viscosity increases rapidly with increasing CNT concentration, causing nozzles to block [47], [108]. Wetting limitations on hydrophobic substrates also reduces CNT film and substrate adhesion [46]. Researchers have recently attempted the growth of CNTs by inkjet printing of catalyst for CNT growth, but for many only tangled nanotubes of mats have been grown and reported [46], [47]. The growth of VA-CNT with inkjet printed catalyst has been only reported by Beard *et al.* (2013), where short pillars of VA-CNTs were grown by inkjet printing Fe_3O_4 nanoparticles of size 10 nm suspended in

toluene [48]. Toluene is a carcinogenic solvent requiring specialist handling procedures and respiratory equipment when used in bulk [210]. Therefore, it is not ideal for large scale inkjet printing. Water based nanoparticle suspensions are more suitable. All research on inkjet printing of catalyst for CNT growth previously reported, has not fully explored the effects of digital patterning of catalyst for scale-up. Although limited research has been conducted on the effects of varying catalyst ink concentration on CNT growth, a comprehensive study on the effect of varying inkjet parameters and substrate surface conditions, is still missing. In Chapter 2, the CVD growth conditions were established for VA-CNT growth with PVD deposited iron catalyst and the ferrofluid MSGW10 characterised. It was concluded that in order to understand the effect of the magnetite ink concentration on the vertical alignment of the CNTs, it is essential to study catalyst nano-island formation during the annealing phase of the CVD growth process. In literature published to date, detailed analysis of the transformation of the inkjet printed ink during the annealing phase of CVD growth is yet to be explored.

Inkjet printing parameters and substrate surface wettability control the catalyst layer spread and thickness on the substrate, and hence catalyst nano-island formation during the annealing step. Daly (2015) reports the process steps that must be considered when defining the characterisation techniques for any application of inkjet printing as pre-jetting surface quality, drop impact behaviour, delivery of function, final surface and long term behaviour [211]. When developing a scalable methodology for printing catalyst it is necessary to determine the ink behaviour at each of these process steps. This chapter is aimed at determining the feasibility of inkjet printing magnetite catalyst for growing VA-CNT structures. The chapter has five main objectives:

- To quantify how the ink properties affect the jetting and drop impact behaviour of the magnetite ink, by mapping its printing and spreading regimes.

- To investigate the correlation between the experimental and theoretical outcomes of the printing behaviour of the ink.
- To determine and study effects of varying ink concentration, printing parameters and substrate surface conditions to understand effects on catalyst deposition, spread and functionality for VA-CNT growth.
- To verify the characterisation tools identified in Chapter 2 for studying and quantifying the effects of varying the above parameters on catalyst nano-islands formed post annealing by studying the catalyst surface.

3.1 Theoretical Knowledge

In Chapter 2 a thorough research analysis was conducted to understand how the catalyst layer affects CNT growth. In this section it is important to consider the fundamental principles behind inkjet printing, and the parameters that should be studied when depositing the catalyst. There are two methods for inkjet depositing material; Continuous inkjet printing (CIJ) and drop on demand (DOD). In a CIJ system, a continuous stream of drops is generated from a nozzle and broken into individual droplets as a result of surface tension, and each drop is steered individually to land on a substrate [205]. On the other hand in DOD systems, an array of nozzles are individually controlled using a transient pressure pulse in the nozzle chamber [3]. Thermal and piezoelectric actuators are used to eject droplets from the printhead [10]. In this thesis we are focused on piezoelectric DOD printers where pulses of electric fields are used to generate pressure waves that change the internal volume of the cartridge cavity to eject a droplet [3], [10].

3.1.1 Dimensional Analysis, Jetting and Impact Behaviour

Ink characterisation is important as factors such as ink surface tension, rheological properties and particle concentration directly impact the formation of drops and ligaments [3], [212]. It is also important to ensure that the particles being printed are 100 times smaller than the nozzles to prevent clogging [10]. Ink viscosity and the pressure in the ink reservoir have to be low enough to allow filling of the ink chamber without dripping, and hence preventing ink drying around the nozzles [113] . The surface tension of an ink also contributes its printing behaviour such that; inks with higher surface tensions tend to have shorter filaments and more spherical droplet formations during printing whereas, inks with lower surface tensions form droplets with longer filaments that can result in satellite droplets [213]. Surfactants can be used to control the surface tension of the ink as when a bubble rises in aqueous surfactant solutions, or when droplets are created at the nozzle during printing, the surfactant is moved from the front of the droplet/bubble to the rear [200]. This phenomenon occurs on account of Marangoni flows in the droplet, leading to a variation of surface tension along the surface, causing tangential shear stress on the surface [201]. This change in surface tension is a dynamic process as the molecules first diffuse to the surface of the droplet/bubble from the bulk and then orient themselves at the interface [214], [215]

An ejected droplet falls under the influence of gravity and air resistance until it impacts the substrate surface where it spreads, driven by surface tension and viscosity of liquid, and substrate wettability [209], [216], [217]. Gravity has a negligible effect for most drop-on-demand printing, due to the small size of the drops. Upon impact, there are six possible surface substrate interactions possible as outlined by Rioboo *et al.* (2001); deposition, prompt splash, corona splash, receding breakup, partial rebound and complete rebound

[218]. According to Rioboo *et al.* (2001) deposition is only considered when a droplet upon impact attaches to the surface without any breakups. Images of the different morphologies can be found in Figure 21 The spreading of the ink upon impact can be divided into four phases: kinematic, spreading relaxation and wetting/equilibrium [219], [220]. Jung (2011) defines these phases in detail [221]. In the kinematic stage, the initial shape of the region of the drop remains unchanged until the contact diameter reaches the original drop diameter [219], [222]. In the spreading phase that follows, the contact line expands radially [223], [224]. The fluid properties, substrate wettability and impact conditions govern this phase [221]. Upon reaching maximum spread relaxation oscillation of shape or receding contact line occurs. On hydrophobic surfaces receding contact lines are observed whereas, on hydrophilic surfaces oscillation at the contact line is visible after which the droplet spreads until an equilibrium state is achieved [218], [219], [221].

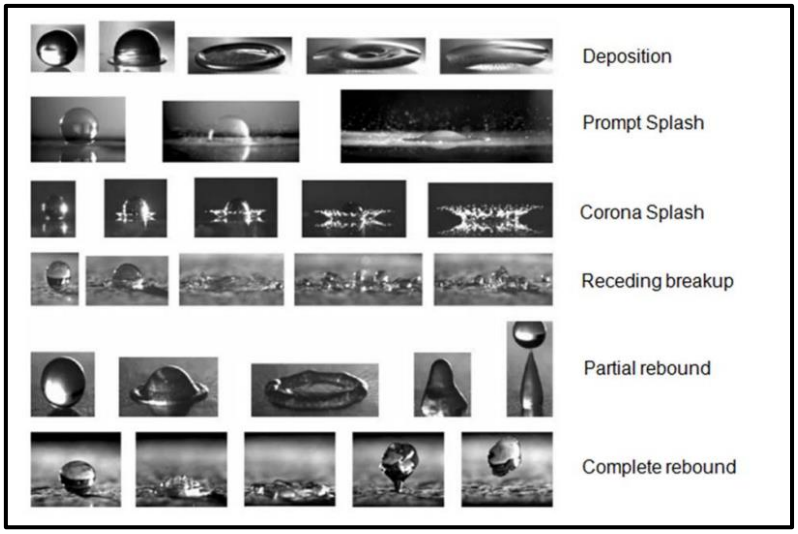

Figure 21: *Morphologies of liquid drop impacts on a dry surface* [218]

The flow properties of a Newtonian ink can be defined by non-dimensional numbers; the Reynolds (*Re*), Weber (*We*) and Ohnesorge (*Oh*) incorporating the drop diameter, velocity, density, surface tension and viscosity [223]–[226]. The *Re*, *We* and *Oh* values can be calculated and the operation and impact regimes mapped using the equations below [205].

$$Re = \frac{\rho V d}{\eta}$$

$$We = \frac{\rho V^2 d}{\gamma}$$

$$Oh = \frac{\eta}{\sqrt{\gamma \rho d}}$$

Where $\boldsymbol{\rho}$ is the density, V is velocity, η is the viscosity, d is the nozzle diameter and $\boldsymbol{\gamma}$ is the surface tension of the ink. The *Oh vs Re* values has been mapped to determine the operating regime of the printing process as shown in Figure 22 [227], [228]. Schiaffino and Sonin (1997) have identified that the impact regime can be mapped in four regions (as shown in Figure 22.b) defined by *We vs Oh* values [226]. Both graphs show an optimum printing regime for DoD printing to occur for an *Oh* range of 0.1 to 1, also recommended by Reis *et al.* (2005) [113], [229].

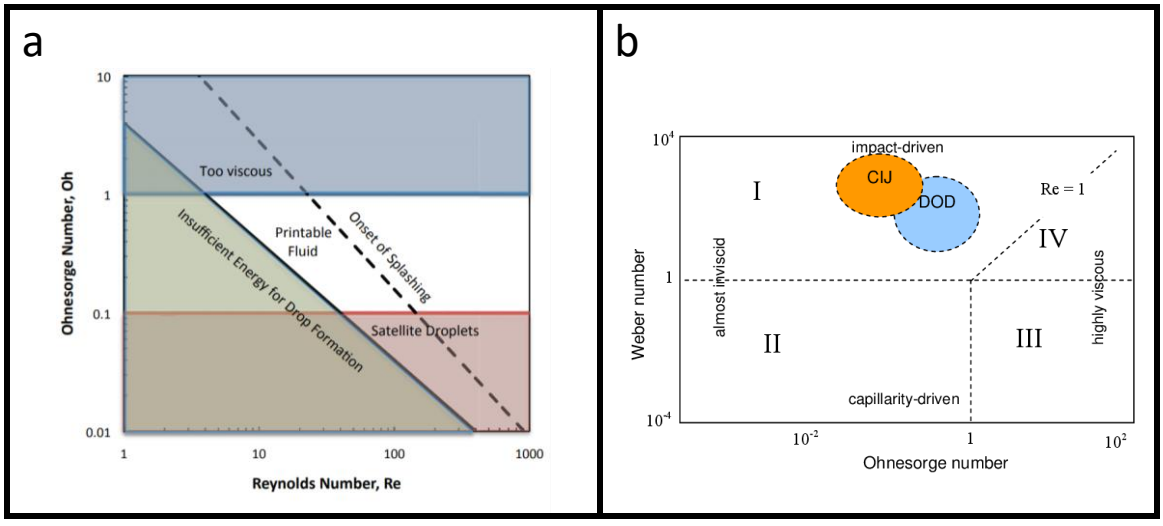

Figure 22: a) *Operating regime of stable operation of DOD inkjet printing* [227]. ***b)*** *Droplet impact behaviour regime based on values of Weber and Ohnesorge Numbers* [221][226] .

During inkjet printing droplet formation involves phases of ejection, stretching of the fluid, necking, rupture and recoil of the fluid, and formation and recombination of a single droplet and a satellite, as defined by Jang *et al.* (2009) [212]. They also explore a range of ink properties and conclude that for inks to be printable their *Oh* must lie in a narrower range

of 0.07 and 0.25 which is narrower from the earlier *Oh* range of 0.1 to 1. Schulkes (1996) was the first to present a detailed model of a contraction of liquid filaments, which was further developed by Notz *et al.* (2004) and state that the conditions under which a liquid filament will break into drops is dependent on a critical range of the filament aspect ratio ($L_{o,c}$), which is calculated by dividing the filament length ($2L_o$) by the filament diameter ($2R_o$), and the *Oh* number (Oh_c) [230], [231]. These models have been verified by Castrejón-pita *et al.* (2012) through experimental data where they found that the critical *Oh* value when the break up transition occurs lies between 0.05 and 0.7 [232]. Therefore, variations in the recommended *Oh* values for printing, as highlighted by Castrejón-pita *et al.* (2012) can occur on account of computational factors, differences in theoretical modelling and experimental conditions. DoD deposition entails impact-driven spreading as shown in the graph in Figure 22.b. Viscosity inhibit drop spreading at high *Oh* values, and surface tension inhibits spreading at low *Oh* values [212], [221]. Therefore, ink and printing properties need to be carefully controlled to ensure satellite droplets and splashing can be minimised. In this work we will demonstrate this by controlling the rheological properties of the ink and printing waveform and voltage.

3.1.2 Substrate Surface Wettability

In order to achieve optimal resolutions between 25 µm to 100 µm, it is essential to optimise fluid and substrate interactions, by changing the contact angle and/or shape of the substrate, for controlled spreading of the ink droplets [10]. The printed ink dries through evaporation, and in some cases coffee-staining effects have been observed and is detrimental for applications requiring uniform deposition of nanoparticles [233]–[235]. Coffee-staining defines the preferential build-up of particles at the edge of the drop, on account of faster evaporation on the outer rim of the droplet [47], [235]. Multiple interactions such as solvent drying, changes in ink viscosity, transport of particles and substrate/ink surface interactions

cause coffee-staining, and the thickness of the coffee-ring is proportional to the ink concentration [209]. Surface wettability can be varied to control coffee staining. Lim (2012) stated that the contact angle defined between the ink droplet and substrate can be defined as a pinned contact angle for hydrophilic substrates and a constant contact angle for hydrophobic substrates [113]. On hydrophilic surfaces, differences in evaporation fluxes on account of Marangoni flows occur between the centre and edge of the printed line carrying particles to the edge [228], [236] Whereas, hydrophobic surfaces, the evaporation rates are similar across the printed layer [236], [237] The evaporation mechanism can be seen in Figure 23. Increasing substrate temperature also increases the evaporation resulting in more prominent coffee-staining [113].

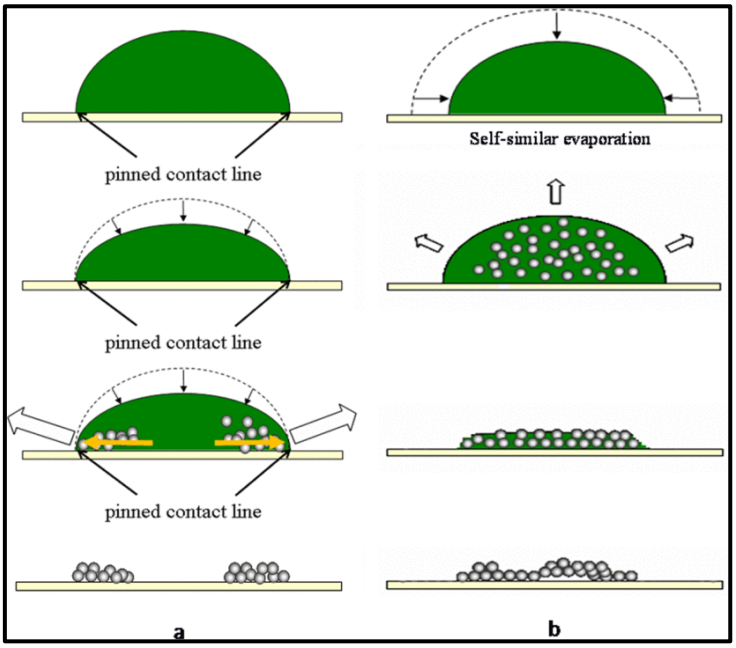

Figure 23: *Evaporation Mechanism for* ***a)*** *pinned contact line (hydrophillic surfaces) resulting in coffee-staining and* ***b)*** *constant contact angle (hydrophobic surfaces) leading to relatively uniform deposits* [237].

As the coffee-ring effect is related to the contact angle of the ink on the substrate, it is important to understand surface wettability changes on coffee-staining as demonstrated by Zhang *et al.* (2013) [234]. UV/Ozone treatments are used for cleaning contaminated

substrates via oxidation of functional groups residing on a surface and have been demonstrated to increase substrate wettability [238]–[240]. Plasma cleaning can also be used to increase wettability through the collision of gas molecules resulting in chemical etching of the substrates surface [241]. The substrate/ink interaction should be such that when individual droplets are deposited on the substrate to form a pinning contact line, stable lines can be achieved by depositing overlapping coalescing droplets [242]. Overlapping droplets can result in five basic morphologies as defined by Soltman *et al.* (2008); individual drops, scalloped line, uniform line, bulging lines and stacked coins [237], [243]. Therefore, droplet spacing has to be varied to achieve the desired morphology [242].

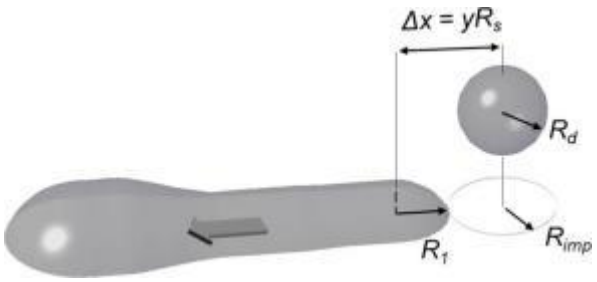

Figure 24: *Liquid bead formation model* [244]

When two droplets are brought together and coalescence begins a bridge of high surface curvature is formed which draws the fluid from the droplets into the necking region, until the droplets become one, and an equilibrium is reached [243]. At smaller drop spacings, the droplets form tracks on the substrate despite mobility of contact line. Whereas, as droplet spacing is increased the droplets do not bridge the gap due to contact line retraction resulting in track discontinuities [243]. Soltman *et al.* (2010) describes a model to predict line stability and has been verified through experimental data by Hsiao *et al.* (2014) [240], [241]. The model states that if drops with radius (R_d) combine to form a cylindrical

liquid bead on a surface (as illustrated in Figure 24) the radius (R_1) of the resultant bead can be defined as:

$$R_1 = \sqrt{\frac{8}{3}\left(\frac{{R_d}^3\Psi}{\Delta x}\right)}$$

Where, Ψ is a geometric function of the static contact angle θ and calculated as:

$$\Psi = \frac{\pi}{2}\left(\frac{\sin^2\theta}{\theta - sin\theta cos\theta}\right)$$

With the resultant radius of the bead calculated as R_1, the maximum contact radius (R_{imp}) to which a newly landing droplet can spread before contact an existing bead can be calculated as:

$$R_{imp} = \Delta x - R_1$$

As droplet spacing $\Delta x$is increased, R_{imp} increases and R_1 decreases. Therefore for a given ink and nozzle size, R_{imp} can be calculated at a range of different droplet spacings and the point after which scalloped lines can possibly occur can be determined when R_{imp} is greater than R_1. As the substrate and ink interaction is critical to deposition of material, it is essential to analyse the surface pre and post deposition using high speed imaging (HIS) optical microscopy, AFM and SEM techniques [211].

The literature presented evidences the complex fluid interactions that need to be controlled during printing. In the experiments to follow it is essential to ascertain whether the ink properties are suitable for DoD inkjet printing by mapping the operation and impact regimes, using the *Oh*, *We* and *Re* values. The jetting behaviour of the ink can be analysed using HSI. The impact behaviour of the ink can be analysed using HIS, optical microscopy, AFM, interferometry and SEM analysis. As previously explained in Chapter 2, catalyst

thickness and uniformity is critical for VA-CNT growth. The literature demonstrates difficulty with coffee-staining occurring when printing nanoparticles, and so substrate wettability is a key factor in controlling ink spreading, and achieving uniform layers of catalyst. In this research varying droplet spacing combined with substrate wettability changes is essential to achieve uniform lines of catalyst. Ink concentration can also be varied to control amount of nanoparticles deposited in a given region.

3.2 Experimental Methodology

This section describes the equipment and experimental procedures used.

3.2.1 Inkjet Printing

The Dimatix Materials Printer by Fujifilm, DMP 2800 series was used to print the inks. The printer is a piezoelectric inkjet printer that uses disposable cartridges for ink delivery. Ink is loaded in maximum volumes of 1.5 ml into the cartridges using a syringe. The cartridges have a row of 16 nozzles of diameter 21.5 µm placed 254 µm apart. The print cartridge is inserted and carried on the Z stage of the printer that is attached to the X stage of the printer. The platen with dimensions 210 mm by 260 mm is attached to the Y stage. The platen has a vacuum that holds the substrate in place and can be heated up to 60 º C [246].

The droplet formation is controlled by the wave form which in turn is controlled by the voltage. The waveform is divided into three segments: fill, print and recovery. A negative voltage is first applied to fill the cartridge, a positive voltage is then used to dispense the droplet and no voltage is applied in the recovery phase to allow the cartridge to return to its original shape. The starting point for formatting the waveforms is to adjust a voltage for the nozzles used such that a maximum number of droplets are ejected. Droplet formation

is viewed in the drop watcher. Ejection through all 16 nozzles is not usually achievable. Therefore, a number of nozzles where droplet ejection is observed are selected, and the waveform adjusted for optimum droplet formation. The maximum voltage possible for the Dimatix printer is 40 V. The voltage and pulse length are adjusted to get maximum droplet velocity. Once a suitable droplet velocity is obtained, the waveform is matched to the acoustics of the piezoelectric. All segments of the waveform can be controlled by varying the amplitude, slew rate and segment duration. The slew rate relates to the bending of the chamber membrane and the duration for which it is maintained in that position. Changing the slew rate or duration of the liquid intake and printing greatly effects drop formation. Magnetite nanoparticles can block the nozzles. Therefore, cleaning cycles are run during prints in order to maintain nozzle functionality.

3.2.2 Substrates and Surface Wettability

Silicon and fused silica wafers of diameter 100 mm and thickness 500 µm were procured from University Wafers. Three types of substrates were used.

- As procured silicon wafers
- 10 nm alumina coated silicon wafers (10ASW)
- Fused silica wafers

All alumina was deposited using an e-beam. The deposition procedure can be found in Chapter 2. All samples were cleaned using ultrasonication for 5 minutes with acetone, 5 minutes with IPA and then dried with compressed air followed by a 60 minute curing time in an oven at 80 °C to remove any water before printing. After printing, the samples were again dried in the chamber at 60 °C for 30 minutes to remove any water remaining, which could affect growth. The procedure was carried out for all samples. Two different techniques were used to change the wettability of the substrates:

- The Femto Diener Plasma Vapour System was used to strike an oxygen plasma, which reacts with the surface to give a surface with close to perfect wetting.
- Bioforce Nanosciences UV-Ozone cleaning system was used to create ozone that reacted with the surface to give near-perfect wetting.

Exposure time was varied in both cases to understand the effects of plasma treatment or UV-Ozone treatment on substrate wettability. All contact angle images were taken using an in-house camera setup built by Dr. David Beesley and Dr. Hsin-Ling Liang. All contact angle measurements were made using ImageJ.

3.2.3 Catalyst and VA-CNT Characterisation

All high speed imaging was carried out using an in-house set up by Qingxin Zhang. The high speed imaging rig consists of a Phantom v7.3 camera operated using the Phantom PCC software, a Microfab nozzle of size 80 µm controlled by the MicroFab Jetdrive III Controller with samples mounted on a Parker MX80L TO2MS stage. The growth and annealing conditions for the CVD can be referred to in Chapter 2. The AFM, SEM and Raman methodologies and equipment details can be found in Chapter 2. Optical images were taken using an Olympus BX51 with ProgRes C10 plus camera. Focused ion beam milling was carried out on the Zeiss Auriga Crossbeam. Printed ink profiles were analysed using white light interferometry system (Wyco NT3300 white light interferometer by VEECO).

3.3 Results and Discussion

Experiments were conducted in three phases. As the rheological properties of the ink were already determined in Chapter 2, the **first phase** of experiments were conducted to understand the jetting and impact behaviour of the ink. The section is also focused on identifying the parameters required to be controlled, in order to achieve catalyst films

suitable for VA-CNT growth. The **second phase** of experiments were conducted to understand the effects of varying the selected printing parameters, substrate surface conditions and ink concentration on the CNTs grown. The **third phase** focused on an in-depth understanding of how the selected parameters impact the magnetite catalyst upon printing and during the annealing phase. Previously, as described in Chapter 2 section 2.1.4, literature to date has only focused on using inkjet printing to deposit catalyst at a single spot to grow pillars of VA-CNTs with no in depth study into the effects of varying inkjet printing parameters, substrate conditions or ink concentration on catalyst evolution during annealing. The approach described will enable new detailed knowledge to be added for inkjet printing patterns and arrays of VA-CNT structures with varying substrate, ink concentration and print conditions. This will be achieved by defining the printing and impact regimes of the ink for scale-up, and the catalyst thickness and catalyst nano-island formation required for VA-CNT growth.

3.3.1 Jetting and Impact Behaviour of Magnetite (Fe_3O_4) Ink

This section investigates the jetting and impact behaviour of the magnetite ink in order to determine which parameter should be selected to vary magnetite ink deposition for VA-CNT growth. Ink concentrations tested link to those in Chapter 2, i.e. the low, medium and high ink concentrations (LIC, MIC and HIC). Initial printing was carried out on a 10ASW substrate to determine droplet velocity. All the inks were printed with the same waveform at 20 volts with 3 jets, and demonstrated similar droplet formation. The waveform is shown in Figure C 1. Figure 25 shows representative optical micrographs of a droplet ejected for ink concentration 2.19 $\%_{w/w}$ (LIC), at varying times from ejection to droplet formation. The images were taken via the inbuilt drop watcher at a strobe delay of 30 µs and a firing frequency of 30 kHz.

Droplets with long tails are observed at ejection. It can be clearly seen in Figure 25 that the fluid flowing through the nozzle is stretched, with viscous forces resisting the drive of surface tension to break into droplets. The ligament breaks into a spherical droplet and a second ligament, which can either retract into a separate droplet and merge with the main droplet, or remain separate as a satellite droplet. While satellite droplets were occasionally observed, they either merged with the leading droplet before impact or shortly after impact. It was identified in section 3.1.1, that dimensional analysis can be used to define how surface tension, viscosity and rheological properties of an ink affect its jetting and impact conditions or in other words its printability. Surface tension, viscosity and rheology measurements for the magnetite ink were reported in Chapter 2. Therefore, the jetting behaviour of the ink can be quantified by calculating the dimensionless Reynolds (*Re*), Weber (*We*) and Ohnesorge (*Oh*) numbers.

The calculations for the non-dimensional numbers can be found in Appendix C, Table C 1. When looking at droplet formation, the importance of surface tension and viscosity can be defined by the *Oh* number, as identified in its equation presented in section 3.1.1. The *Oh* number for the three ink concentrations was measured as 0.03 for LIC, 0.03 for MIC and 0.05 for HIC and are below the recommended printing *Oh* range of 0.1 to 1. Therefore, the droplet formation behaviour is in line with that modelled and tested by Jang *et al.* (2009) and Castrejón-Pita *et al* (2012) [212], [232]. The droplet formation signifies that at low viscosity fluids droplet ejection is easier without any significant viscous dissipation. High kinetic energy and surface tension detach the filament from the primary droplet head resulting in the formation of a satellite droplet, as shown in Figure 25.

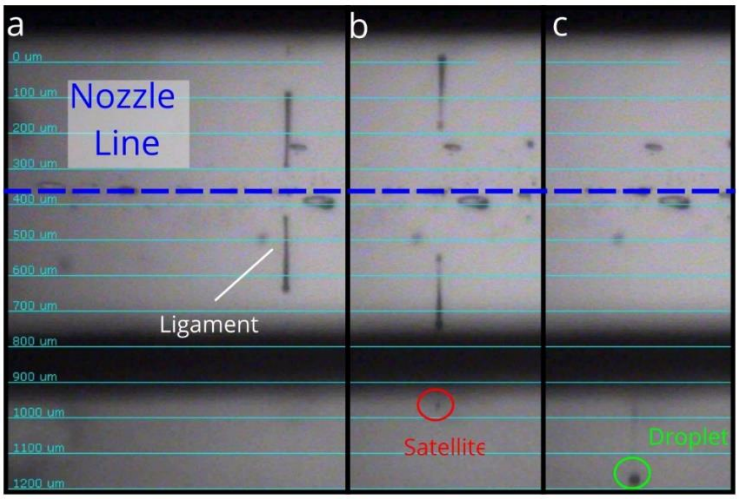

Figure 25: *Snapshots from the Dimatix software showing droplet formation in the Dimatix Printer for ink concentrations 2.19 %$_{w/w}$.*

As the drop watcher in the Dimatix does not have a high resolution, HSI was attempted for analysing the jetting behaviour of ink concentration 2.19 %$_{w/w}$ using an 80 µm Microfab nozzle. The images are shown in Figure 26. It can be seen in the images that droplet ejection is unstable with extensive breaking of the filament into multiple droplets. The shape of the primary droplet is not uniform and spinning was observed. This increase in instability can be explained by a change in the printing parameters. It was previously explained in section 3.1.1 that droplet ejection is dependent on the *Oh, Re and We* numbers and the filament aspect ratio. As the nozzle diameter is increased from 21.5 µm to 80 µm, the filament aspect ratio is also increased, resulting in a slightly different behaviour observed than that observed in the Dimatix drop watcher. The printing was also conducted at a voltage of 120 V for the Microfab which is a lot higher than a voltage of 20 V used for the Dimatix, resulting in an increase in droplet velocity. This increase in droplet velocity and nozzle diameter results in an increase in the *Re* and *We* numbers, and a decrease in the *Oh* number (see equations in 3.1.1) causing an increased likelihood of satellite drops and splashing. Therefore, it is evident that droplet ejection is heavily dependent on the ink properties and printing parameters (nozzle size, jetting voltage and waveform). By choosing, a suitable combination of ink and printer, suitable droplet ejection can be achieved. However, for the

purpose of this study detailed study of the ink droplet formation cannot be studied with the Microfab as it is not representative of the droplet ejection in the Dimatix. Therefore, a new HSI set-up is required to study droplet formation in the Dimatix printhead, which is outside the scope of this research.

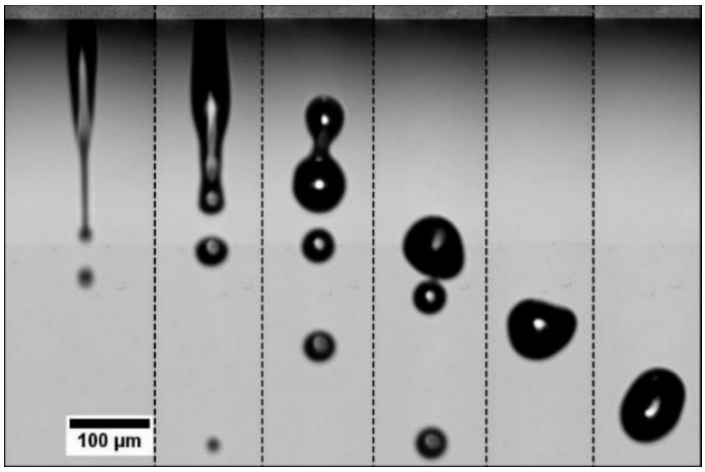

Figure 26: *High speed imaging of ink concentration 2.19 $\%_{w/w}$ jetting behaviour using an 80 µm Microfab nozzle jetting at 120 volts.*

The operation and impact regimes of the selected ink concentrations can be seen in Figure 27. Figure 27.a shows the printing regime for stable operation of DOD inkjet printing with the boundary conditions highlighted for printable fluid in section 3.1.1. It can be seen that the *Oh* and *Re* values of the ink concentrations printed, place them in the theoretically defined printable fluid region, but with expected satellite droplets. Satellite droplets were observed when printing the different ink concentrations and subsequently establish an agreement between the jetting behaviour observed and the theoretical printing regime mapped. Droplet spreading is inhibited at high *Oh* values as a result of viscosity and at low *Oh* values as a result of surface tension, whereas at high *We* droplet spreading occurs as a result of impact-induced inertia and at low *We* droplet spreading is inhibited as a result of capillary forces [221].

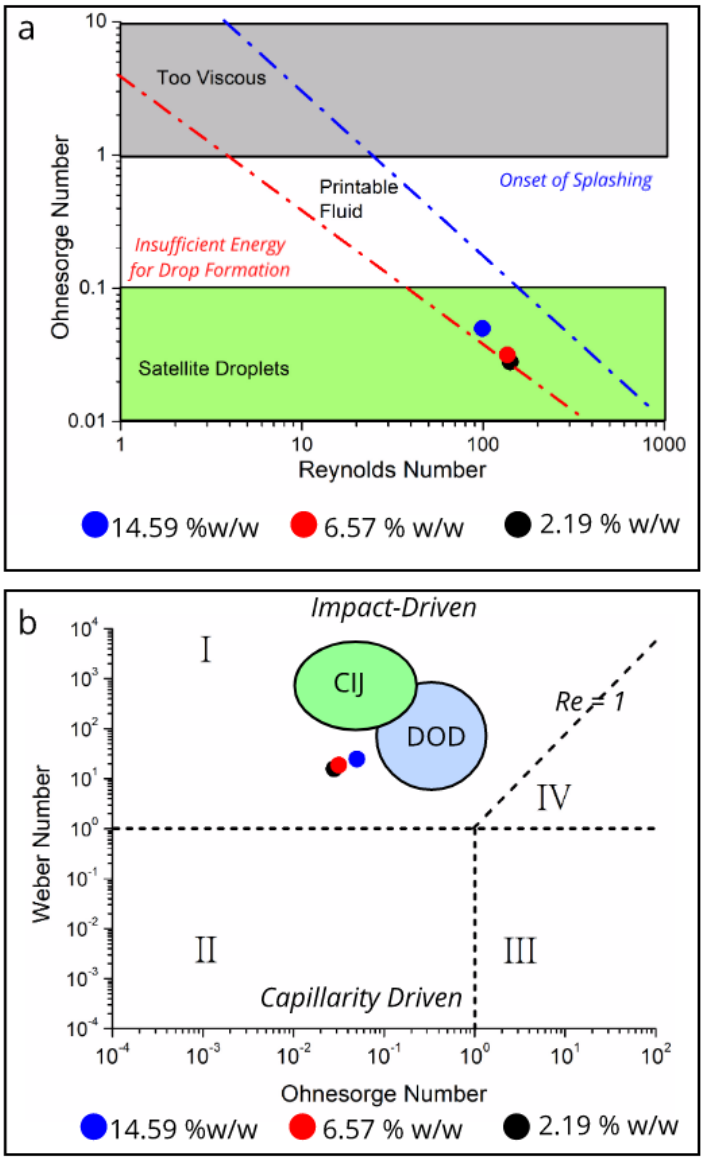

Figure 27: *Schematic diagrams of* ***a)*** *the printing regime (adapted from Jung (2011)) and* ***b)*** *the spreading regime of magnetite ink concentrations 14.59 %w/w, 6.57 %w/w and 2.19 %w/w (adapted from Mckinley et al. (2011))* [221][227].

Figure 27.b shows the four spreading regimes for an ink upon impact and the typical values for inks suitable for printing using CIJ and DOD systems. *We* and *Oh* values have been defined to characterise the driving and resistive forces in droplet spreading. In order to achieve the desirable patterns and spreading of the catalyst it is important to optimise the droplet impact conditions [247]. It can be seen in Figure 27.b that for LIC, MIC and HIC, the *We* and *Oh* are slightly offset, but lie within the same regime as those for ideal CIJ and DOD deposition. The ink spread is driven by the impact pressure and resisted by inertia

[247]. Viscosity effects during the initial spreading are weak, but are expected in the final stage of the spreading [226].

As all representative ink concentrations have the same printing and spreading regimes, LIC 2.19 $\%_{w/w}$ was printed on an untreated 10ASW substrate to visually ascertain the jetting and impact behaviour of the ink via HSI. Micrographs shown in Figure 28 clearly show that majority of the spreading occurs in a short time span of 67 µs. Receding of the liquid can be seen thereafter as shown by the 134 µs frame until a satellite droplet is observed at the 268 µs frame. The ink does not spread farther as the contact line advancement is slowed due to viscous effects dampening the oscillations. The droplet then dries and a coffee ring can be observed in the frame showing the final state. The micrographs show accordance between the jetting and droplet impact behaviour experimentally observed and the theoretically mapped printing and spreading regimes.

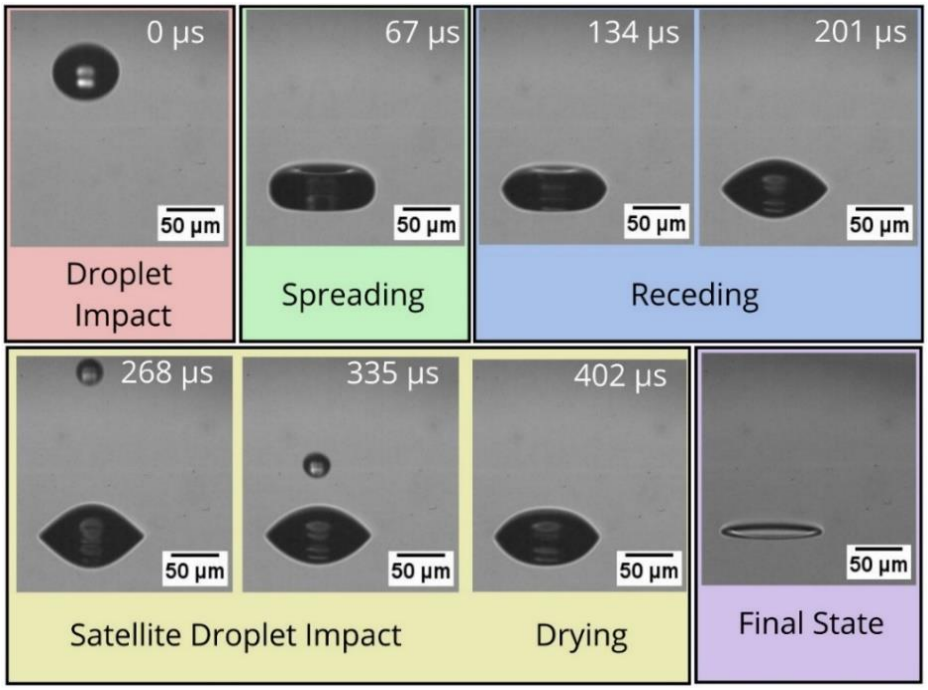

Figure 28: *High speed imaging of the impact, drying and final state of magnetite ink concentration 2.19 $\%_{w/w}$ droplet when printed on an untreated 10 nm alumina coated silicon wafer.*

The dimensional analysis and experimental data have indicated that along with the ink properties and jetting parameters, substrate surface parameters are equally important to achieve uniform patterns for printing. The catalyst and substrate interaction are required to be controlled such that that homogeneous deposition of catalyst patterns can be achieved. Therefore, further investigation is required to understand how the shape of the droplet upon impact and spreading can be controlled by varying substrate material and wettability.

3.3.1.1 Varying Substrate Surface Conditions

It is important to ensure that the substrate wettability is such that homogeneous and repeatable lines of catalyst can be achieved for patterning, while maintaining a catalyst layer thickness suitable for VA-CNT growth. As a result, the next set of experiments look at defining the substrate parameters that need to be controlled for printing homogeneous lines of magnetite catalyst. As described in section 3.1.2, air plasma treatment or UV/Ozone treatment can be used to vary substrate wettability by essentially generating oxygen-containing functional groups on the surface. Effects of increasing air plasma exposure time on surface wettability were investigated by printing lines of 1 layer of 60 % water/glycerol formulation at a droplet spacing of 5 µm and jetting voltage of 25 V. Optical micrographs of the printed ink at varying air plasma exposure times can be seen in Figure 29.a. The micrographs reveal that when printing on untreated silicon substrates, the printed liquid does not coalesce to form a film, but assembles as droplets. As the exposure time for plasma treatment is increased the surface wettability increases and the droplets coalesce to form a layer. The results evidence an increase in substrate surface wettability, and hence propagate ink spreading and minimise Rayleigh instabilities.

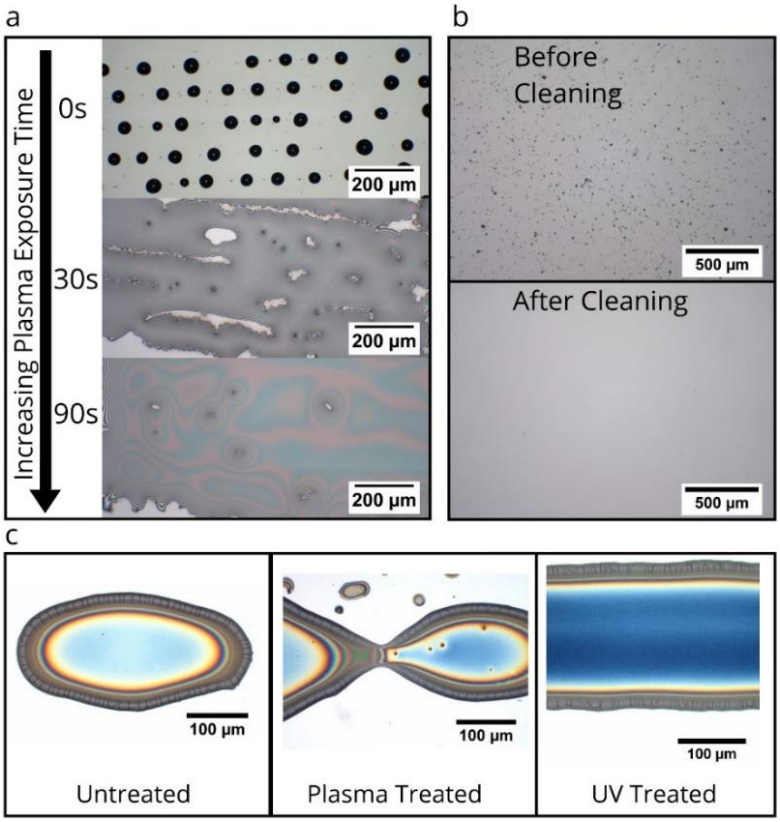

Figure 29: a) *Optical micrographs of 60% Glycerol water ink printed at a droplet spacing of 5 µm on glass slides showing effects of increasing plasma exposure time on substrate wettability and* ***b)*** *before and after cleaning images of the substrate.* ***c)*** *Optical micrographs of 2.19 $\%_{w/w}$ ink concentration printed on untreated, 60 s plasma treated and 600 s UV treated 10ASW substrates.*

When looked at closely, pinning effects can be observed in Figure 29.a and can cause increased spreading with undesirable coalescence of patterned lines. Therefore, in order to avoid any particulate contamination, surface treatment alone is not sufficient. Cleaning of the samples with acetone, IPA and water removes the particulates from the substrate giving a clean surface for printing as shown in Figure 29.b. Henceforth, all substrates were cleaned before printing to avoid any pinning effects and limit undefined instabilities or variations in the printed catalyst layers. Although air plasma exposure has been reported to increase surface wettability significantly with lower exposure times, UV treatment, while requiring longer exposure times, has been reported to be more repeatable. [248]. Yang *et al.* (2014) demonstrated that plasma treatment can have an etching effect on the alumina support layer, resulting in its densification and oxidation [249]. This improves catalyst and support layer

interaction, and thus improves VA-CNT alignment and height when growing from e-beam deposited iron catalyst [249]. However, the effects of plasma treatment of the support layer on magnetite nanoparticles as catalyst is not known. Therefore, experiments were conducted to understand how both plasma and UV treatment affect the magnetite ink interaction with the support layer, and hence VA-CNT growth.

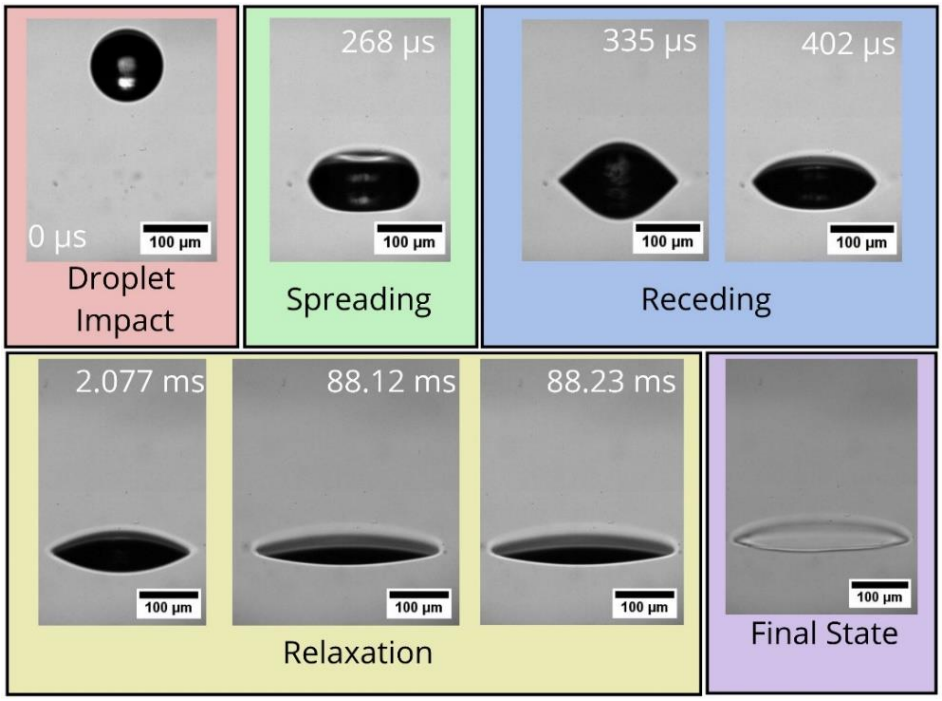

Figure 30: *High speed imaging of the impact, drying and final state of magnetite ink concentration 2.19 $\%_{w/w}$ when printed on a 600 s UV treated 10ASW substrate.*

LIC 2.19 $\%_{w/w}$ was printed at a droplet spacing of 5 µm on untreated, 60 s plasma treated and 600 s UV treated 10ASW substrates. It can be seen in the optical micrographs shown in Figure 29.c that a straight line was observed when printing on UV treated substrates whereas uneven printing was observed on plasma treated substrates. Droplet impact on UV treated samples was analysed through HSI micrographs taken using the Microfab nozzle. It can be seen in the micrographs shown in Figure 30 that ink spreading is much greater than that observed when printing on untreated substrate, and occurs over a longer period of time.

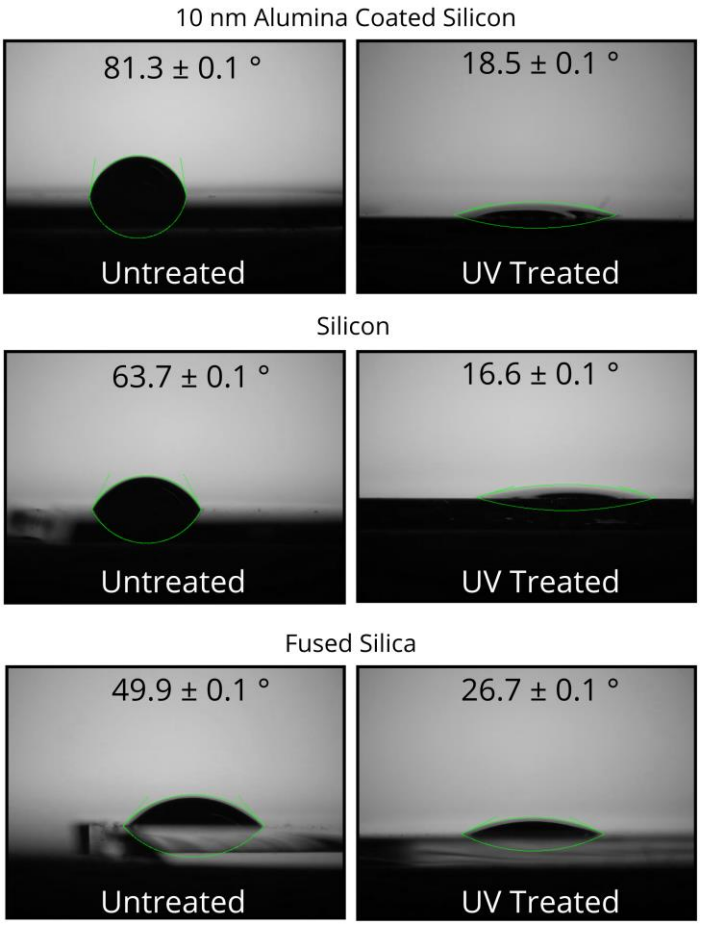

Figure 31: *Optical images showing the droplet impact of ink concentration 2.19 %w/w on untreated (left) and UV treated (right) 10 nm alumina coated silicon wafers (top), silicon wafers (middle) and fused silica chips (bottom). The standard error has been reported.*

To understand the extent of the increase in wettability when printing on UV treated substrates, ink concentration 2.19 $\%_{w/w}$ was drop casted on untreated and UV treated 10ASW, silicon and fused silica substrates. Optical micrographs in Figure 31 show how the contact angle varies for each substrate material before and after UV treatment. Before UV treatment, fused silica was observed to have the smallest contact angle of 49.9 ± 0.1 ° denoting highest wettability. Whereas, 10ASW substrates were observed to have the largest contact angle of 81.3 ± 0.1 °, denoting lowest wettability. Upon UV treatment the greatest wettability change was observed for droplets deposited on 10ASW substrates, with contact angle reduced to 18.7 ± 0.1 °. Silicon substrates were found to have the highest wettability

post UV treatment with a contact angle of 16.5 ± 0.1 ° whereas, fused silica underwent the least wettability change with the largest contact angle of 26.7 ± 0.1 °. Even though plasma and UV treatments both increase substrates surface wettability, the mechanism with which the wettability is increased can have an effect on the CNTs grown. The wettability of the substrate and ink surface tension are governing factors in achieving suitable catalyst layers and patterns. Therefore, it is important to investigate the effects of plasma and UV treatments on catalyst deposition in conjunction with varying printing parameters for detailed understanding of catalyst concentration impact on CNT alignment and growth.

3.3.1.2 Varying printing parameters

From the previous section, it is seen that the substrate wettability can be controlled to achieve improved spreading of the catalyst. To ensure the correct thickness, the initial concentration of catalyst delivered to a given area on the substrate must also be controlled. This is achieved by modifying the ink concentration and number of droplets delivered to a given area. Varying the spacing between each droplet and the number of layers can be used to control the desired film thickness and particle concentration. A single layer of LIC 2.19 $\%_{w/w}$ was printed on 60s plasma treated 10ASW substrates at droplet spacing varied between 5 µm to 60 µm at 5 µm increments. The formation of continuous lines of catalyst upon printing is dependent on the appropriate coalescence of droplets at a critical droplet spacing. It can be seen in Figure 32 that homogeneous lines of catalyst can be achieved by varying the droplet spacing given the appropriate surface interaction conditions. Using a nozzle diameter of 20 µm printing at low droplet spacings results in the coalescence of overlapping printed droplets, forming large thick layers of catalyst with an evident coffee ring effect. Upon increasing the droplet spacing, a critical point is reached, where the bulging effects are minimised by reducing the overlapping of individual droplets giving

smooth continuous lines. Further increase beyond this critical spacing, leads to scalloping effects and the eventual discontinuity of the line into individual droplets

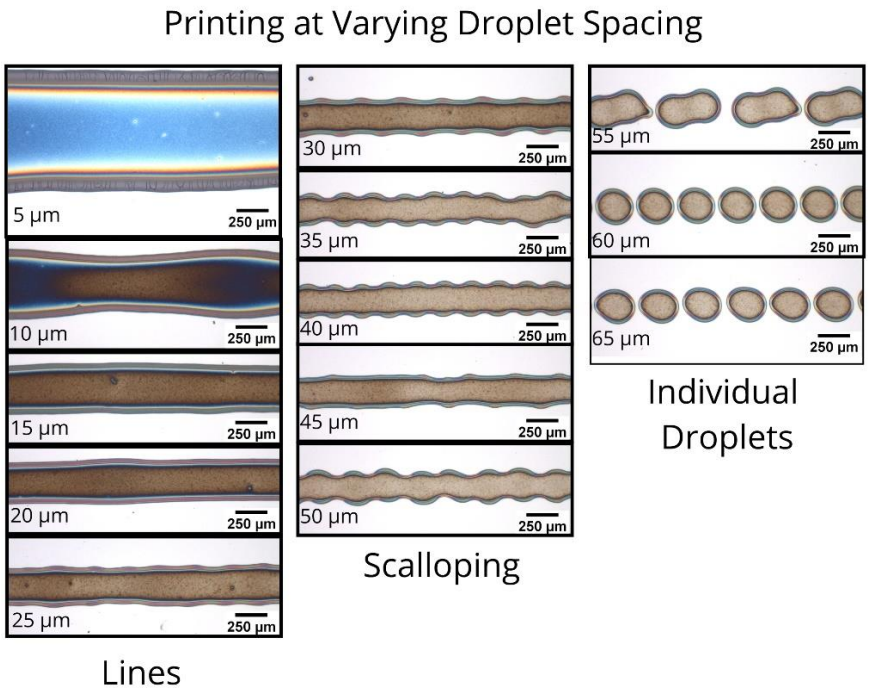

Figure 32: *Optical micrographs of magnetite ink concentration 2.19 $\%_{w/w}$ printed at varying droplet spacing on a plasma treated 10 nm alumina coated silicon substrate.*

Scalloping occurs at a droplet spacing of 30 µm in Figure 32. However, with a surface contact angle of 81.3°, an estimated droplet diameter of 21.5 µm and using the model presented in section 3.1.2, the theoretical droplet spacing after which scalloping should occur is 10 µm. This is the point where theoretically the maximum contact radius of a newly landed drop R_{imp} is greater than the end radius of the resultant bead R_1 (all calculated values shown in Table C 2). This result demonstrates that though the model can predict the droplet spacing after which scalloping effects can occur, it does not give an exact droplet spacing at which stable lines with minimum layer thickness can be achieved. Therefore, the results demonstrate the importance of extensive experimental data to determine optimum printing parameters.

The quantity of magnetite delivered to a given area were calculated when varying droplet spacing and ink concentration. These calculations have been made by measuring the average volume delivered per droplet for three representative LIC, MIC and HIC shown in Table C 3. Given a specific droplet spacing, the number of overlapping droplets and the volume per metre deposited per metre can be calculated. Knowing the average volume delivered per metre and the densities of the ink dilutions, the approximate mass of magnetite delivered in a given cross-sectional area of the printed layer can be calculated. The complete calculations can be found in Table C 4, while a graphical representation of the data can be seen in Figure 33 which shows that as ink concentration is increased and droplet spacing decreased, a larger quantity of magnetite is delivered to a given area.

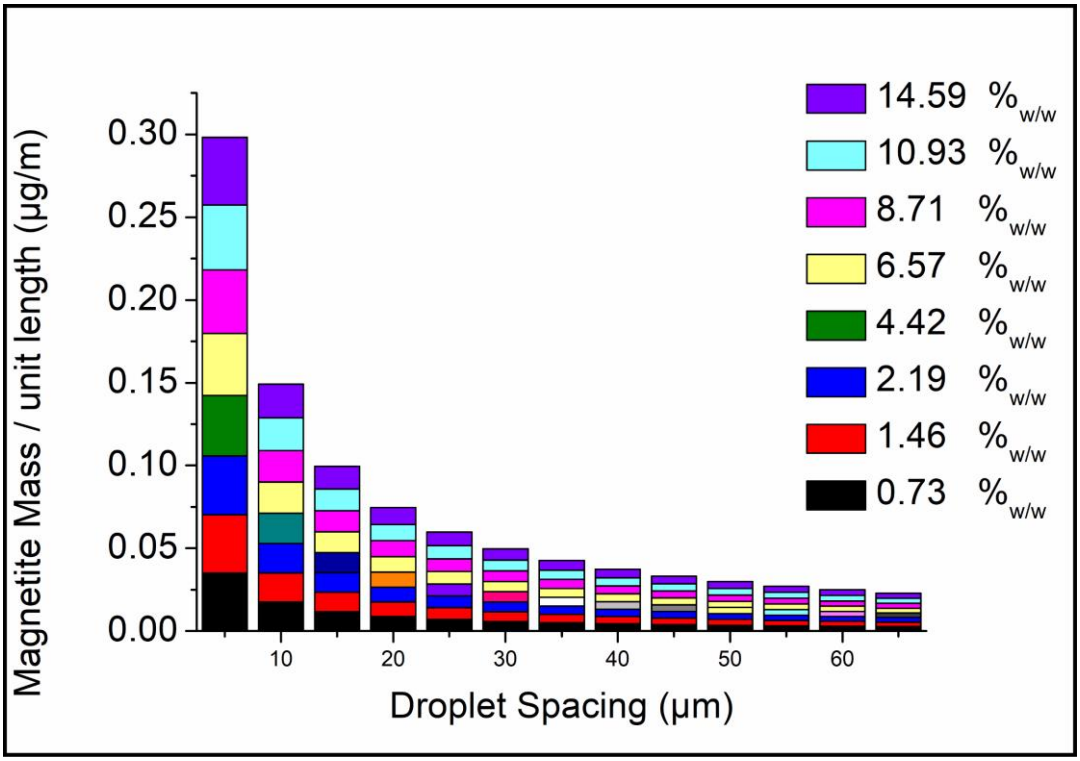

Figure 33: *Graphic representation of magnetite mass/unit length (µg/m) vs. droplet spacing (µm) for varying ink dilutions.*

The amount of magnetite delivered can also be increased by printing more layers of catalyst. Single and double layers of HIC 14.59 $\%_{w/w}$ were printed at a droplet spacing of 10 µm on glass slides. It can be seen in Figure 34.a.i that when printing with a high ink concentration

of magnetite particles, cracking at the edge of the printed line can be seen. When the concentration of particles in the printed line is further increased by printing three layers of catalyst, this results in further cracking and delamination of the ink as seen in Figure 34.a.ii. Cracks are dependent on the particle size and initial volume fraction of the film [116]. Residual stress release from the film during evaporation causes an abrupt volume reduction of the film resulting in cracking [250]. As an increase in cracking was observed for printing with multiple layers, varying magnetite catalyst with this technique is not suitable. Single layer lines of catalyst are more suitable for printing the magnetite catalyst.

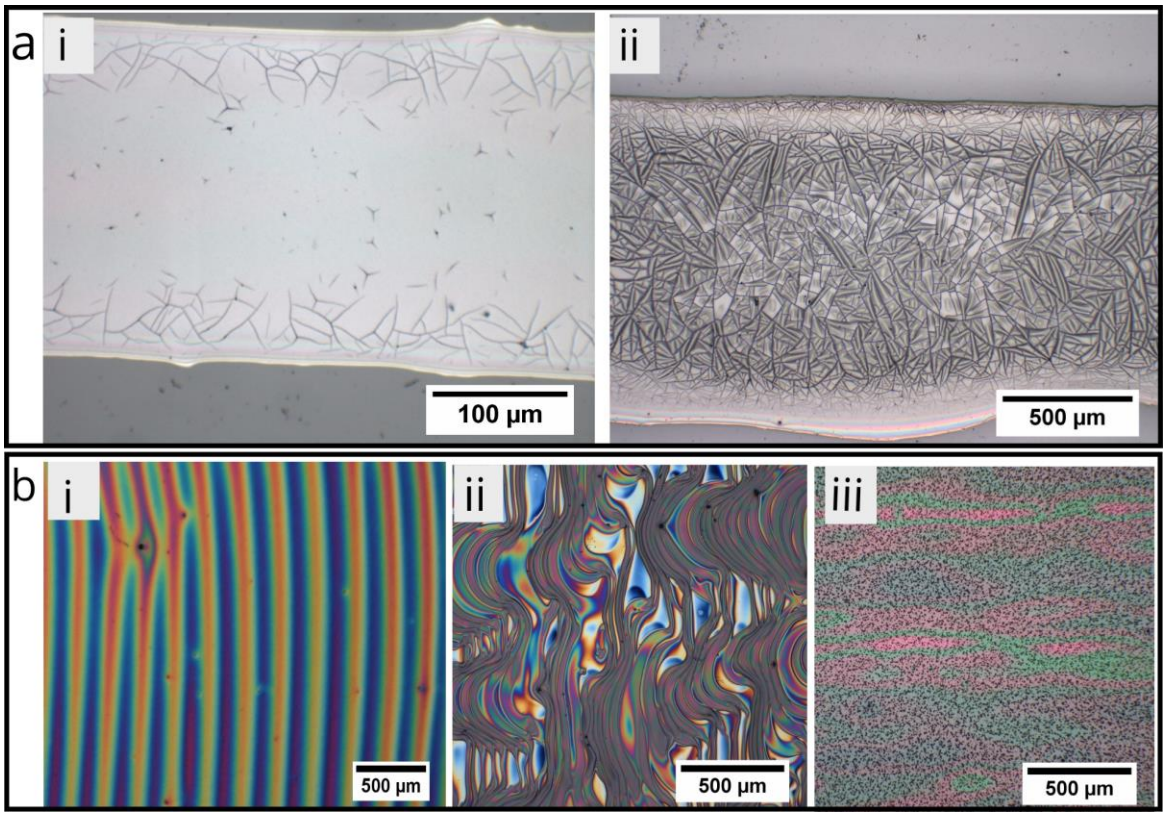

Figure 34: a) *Optical micrographs of* ***i)*** *1 layer and* ***iii)*** *3 layers lines of ink concentration 14.59 %$^{w/w}$ printed at a droplet spacing of 10 µm on glass slides.* ***B)*** *Optical micrographs of 1 layer of 10 by 10 mm box of magnetite ink concentrations* ***a)*** *2.19 %$_{w/w}$,* ***b)*** *4.42 %$_{w/w}$ and* ***c)*** *14.59 %$_{w/w}$ printed at a droplet spacing of 5 µm on 10ASW substrates plasma treated for 60 s.*

The droplet spacing controls the space between the droplets in the x and y direction. 10 x 10 mm boxes were printed with a droplet spacing of 5 µm to see if homogeneous films of catalyst can be deposited on larger areas of substrate, results for which can be seen in

Figure 34.b. Optical micrographs in Figure 34.b show that for LICs 2.19%$_{w/w}$ and 4.42 %$_{w/w}$ uneven layers are achieved evidenced by the fringe patterns. Patterns are printed with the Dimatix printer travelling in lines along the x axis first and incrementally moving down the y axis. The lines of the fringe pattern follow the movement of the Dimatix cartridge. The lines dry at different rates and do not coalesce, resulting in the fringe patterns. Increasing the ink concentration to 14.59 %$_{w/w}$ cracking is observed. When printing on larger areas substrate minute surface variations such as dust, surface roughness and pinning effects can have an impact on the print quality.

3.3.1.3 Selection of Parameters

It can be concluded from the results in this section that all magnetite ink concentrations can be printed with the Dimatix inkjet printer. A wide range of a parameters can be varied to control the amount of catalyst delivered to a printed area. However, it is important to limit the number of parameters to those with most impact on catalyst jetting and spread upon impact. Below is a summary of the findings from the results above

- *Catalyst and Substrate*

The magnetite ink will be printed on 10ASW substrates for all detailed analysis as it is conventionally used as the substrate on which iron catalyst is deposited via e-beam deposition. This ensures that the nature of the catalyst is the only variable affecting VA-CNT growth. Ink concentration can be varied to directly control the amount of magnetite ink delivered to a given substrate.

- *Dimatix Waveform.*

The experimental and theoretical analysis confirmed that all magnetite ink concentrations can be printed via inkjet and the waveform for printing the inks has been determined.

- *Substrate Surface Wettability*

Both air plasma and UV ozone surface treatments were found to cause extensive variation in substrate wettability. Therefore, both parameters will be studied in detail.

- *Printing Parameters*

As the amount of magnetite delivered to the substrate can already be varied with ink concentration and substrate wettability, the number of printing parameters to be varied should be kept to a minimum. Lines of width 0.005mm should be printed along the x axis, separated by a 0.5 mm gap to ensure no overlap occurs. Larger printed areas of catalyst are not desirable as the purpose of the study is to find the optimum printing and substrate conditions to achieve patterns of VA-CNT forests with minimum feature size. Therefore, varying droplet spacing and printing single droplet width lines can provide a more reproducible and controlled deposition of catalyst. It can be concluded that the three main parameters to be investigated for depositing magnetite for VA-CNT growth are: ***ink concentration, droplet spacing and substrate wettability.***

3.3.2 Printing Continuous and Homogeneous Catalyst Films for VA-CNT Growth

After determining the most important parameters for controlling the amount of catalyst deposited via inkjet printing, the results in this section report the effects of varying the selected parameters; ink concentration, droplet spacing and surface wettability on VA-CNT growth.

3.3.2.1 Varying Ink Concentration for VA-CNT Growth

The first set of experiments were conducted to investigate the effects of varying ink concentration on VA-CNT growth by printing at a constant droplet spacing and surface wettability. The entire range of ink concentrations formulated: 0.73 $\%_{w/w}$, 1.46 $\%_{w/w}$, 2.18 $\%_{w/w}$, 4.42 $\%_{w/w}$, 6.56 $\%_{w/w}$, 8.71 $\%_{w/w}$, 10.92 $\%_{w/w}$ and 14.59 $\%_{w/w}$. were printed on

untreated 10ASW wafers at a droplet spacing of 20 µm. As the orifice size of the nozzle is 21.5 µm a droplet spacing of 20 µm was selected to have the minimal droplet overlap and stable printed lines.

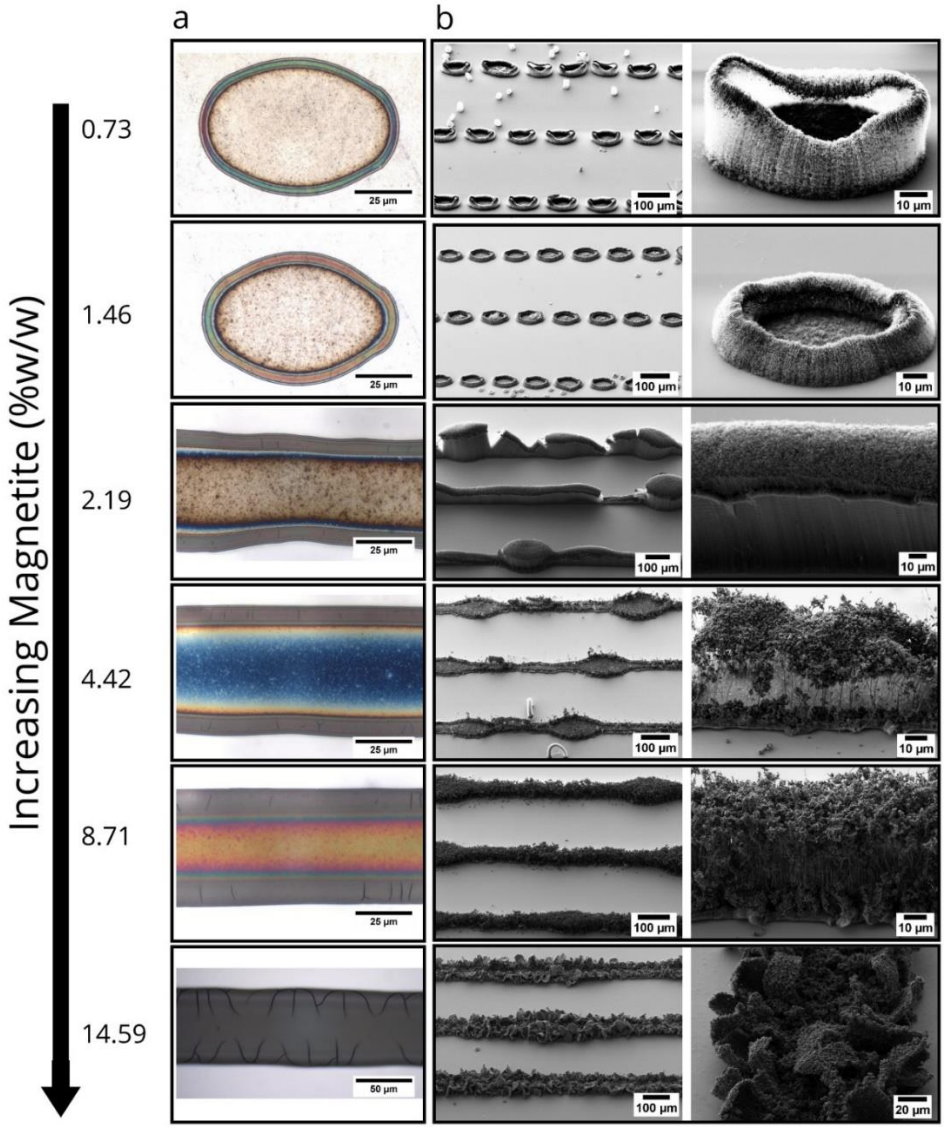

Figure 35: a) *Optical microscopy images of decreasing concentrations of magnetite ink printed at 20 µm droplet spacing.* ***b)*** *SEM micrographs of overall CNT growth* ***(left)*** *and individual structures* ***(right)*** *for printed magnetite concentrations 0.73 %w/w, 1.46 %w/w, 2.19 %w/w, 4.42 %w/w, 8.71 %w/w and 14.59 %w/w.*

It was found that upon drying, a unique colour variation attributing to the coffee ring effect was observed across the printed lines via optical microscopy for each concentration printed, as shown in Figure 35.a. As concentration decreases the coffee ring phenomenon becomes more prevalent, evidenced by an increase in the number of interference fringes (indicating

a greater variation in thickness), their narrowing and migration towards the edge of the printed region. This inhomogeneity of the catalytic film thickness occurring as a result of coffee-staining can impact CNT growth as it will affect the formation process of catalyst nano-islands during the annealing phase of CVD growth.

Upon CVD growth, for HIC of 14.59 $\%_{w/w}$, flake like structures were observed as shown in the SEM micrographs in Figure 35.b. The SEM micrographs reveal that as ink concentration is decreased, alignment of CNTs across the cross section of the printed region is increased with maximum aligned CNTs observed between ink concentrations 8.71 $\%_{w/w}$ and 2.19 $\%_{w/w}$. For concentrations higher than this range, graphitic carbon growth was seen in the coffee ring region of the printed lines. Uniform alignment is achieved across the entire printed cross section when the concentration is reduced down to 2.19 $\%_{w/w}$. However, further reduction in concentration results in loss of particle density in the centre of the printed region, as observed for 1.46 $\%_{w/w}$, where a short CNT carpet can be seen in the centre with aligned growth occurring at the edges of the printed droplets. The variation in growth across the printed region is evidence of a varying morphology and size of the catalytic nano-islands formed during the annealing step of CVD growth [167], a direct result of having insufficient thickness of catalyst in the centre of the printed area. Although aligned growth was observed when printing with 2.19 $\%_{w/w}$ ink concentration, printing at a droplet spacing of 20 µm resulted in irregular and discontinuous lines. Therefore, further exploration of the droplet spacing and surface wettability is required to achieve consistent and repeatable patterns of catalyst.

3.3.2.2 VA-CNT growth by Printing on Untreated and Air Plasma Treated Substrates

This section presents results from experiments conducted to understand how varying ink concentration and droplet spacing on untreated and plasma treated surfaces affects

homogeneity of the printed catalyst film. Three inks representing low, medium and high concentrations were selected: 2.19 $\%_{w/w}$ (LIC), 6.56 $\%_{w/w}$ (MIC) and 14.59 $\%_{w/w}$ (HIC). The inks were then printed on untreated and 60 s plasma treated 10ASW substrates, at droplet spacings varied between 5 µm and 60 µm at 5 µm interval. The droplet spacing range gives lines characterised as follows:

- < 15 µm - overlapping droplets (S_o)
- 15 µm > and < 55 µm - partially overlapping droplets (S_{PO})
- > 55 µm - individual droplets (S_{ID})

Full length optical micrographs of the printed inks can be found in the appendices, with Figure C 2 showing results for printing on untreated samples, and Figure C 3 for plasma treated samples. The samples thereafter were subjected to CVD growth and CNTs analysed via SEM.

- *Low Ink Concentration – 2.19 $\%_{w/w}$*

The printing and growth results for LIC can be seen in Figure 36. Previously lines of catalyst with bulging were observed when printing LIC 2.19 $\%_{w/w}$ at a droplet spacing of 20 µm on untreated samples. However, when printed again on new untreated samples, the droplets do not coalesce to form a line at any droplet spacing, as seen in Figure 36.a. The different surface wettability can be as a result of a combination of high surface tension of the ink and variation in the substrate surface tension as a result of inconsistencies and contaminations in the silicon wafer batch or during e-beam deposition of the alumina layer. Plasma treatment can be used to increase the surface wettability. It can be seen in Figure 36.b that after plasma treatment, the droplets partially coalesce when printed with S_o. Lines are achieved when printed with S_{PO} up until a droplet spacing of 35 µm after

which scalloping effects and discontinuities in the lines were observed. When printing with S_{ID}, insufficient overlapping of the droplets results the deposition of individual droplets.

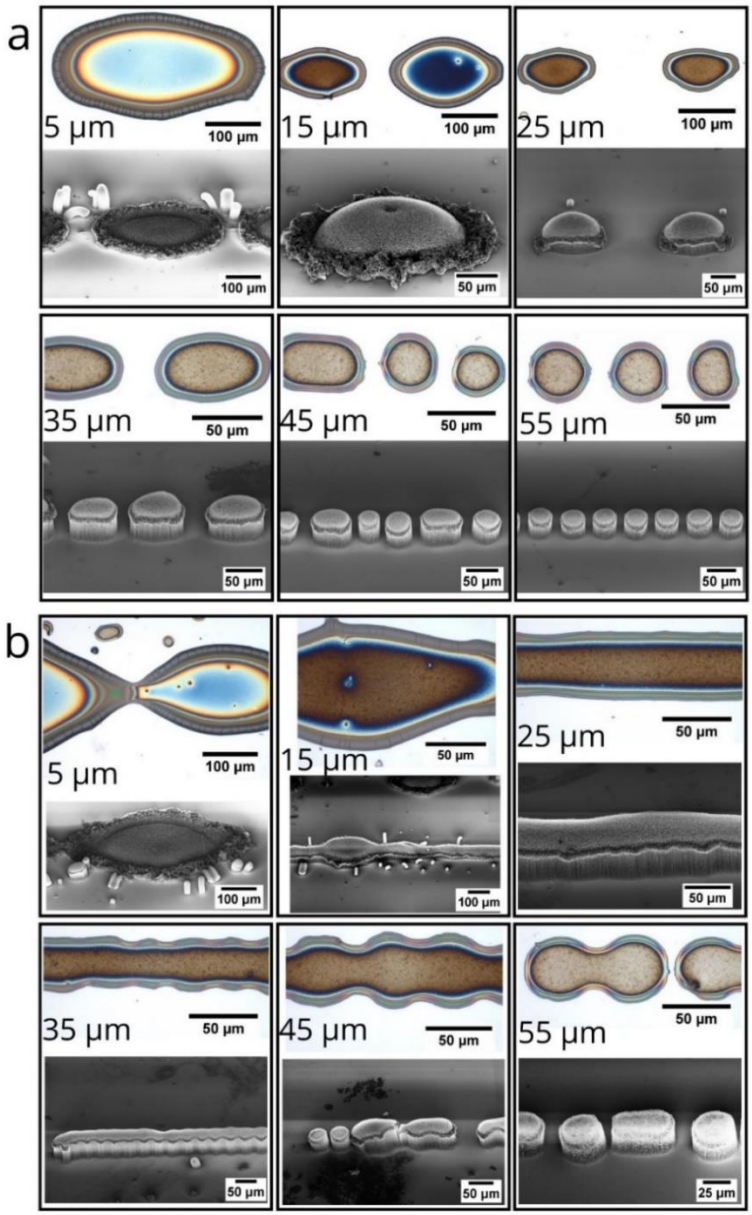

Figure 36: *10 nm alumina coated silicon wafers* ***a)*** *untreated and* ***b)*** *60 s plasma treated printed with magnetite ink concentration 2.19 %w/w at varying droplet spacings. Optical micrographs (top) show printed ink before CVD growth and SEM micrographs* ***(bottom)*** *show results post CVD growth.*

After CVD growth a short carpet of amorphous and crystalline structures intertwined with CNTs was observed when printing with S_o on both untreated and plasma treated substrates. Printing with S_o, results in maximum overlapping of droplets and largest magnetite concentration delivered to the substrate, subsequently resulting in growth termination on

account of excess catalyst. When printing with S_{PO} and S_{ID}, fewer droplets overlap, causing a thinning effect on the catalytic layer as the amount of magnetite delivered to a given area is reduced. This enables alignment of CNTs and short VA-CNT pillars can be seen for catalyst printed with S_{PO} on untreated substrates, whereas lines of forest were grown for catalyst printed on plasma treated substrates. The domed shape of the VA-CNT pillars encircled with a graphitic crust-like structure grown on the untreated substrates, mimic the coffee staining observed in the optical images taken prior to growth.

- *Medium Ink Concentration – 6.57 $\%_{w/w}$*

The printing and growth results for MIC can be seen in Figure 37. When printing on untreated samples thick bulging lines are observed when printing with S_o, and individual droplets when printing with $S_{ID.}$ On the other hand, smooth lines and a relatively uniform colour pattern across the central region is observed when printed with $S_{PO.}$ Similar results were observed when printing on plasma treated substrates. However, the colour of the printed catalyst recorded by optical microscopy varied indicating variation in catalyst film thickness as a result of substrate wettability changing.

Upon CVD growth, a short carpet of amorphous and crystalline structures intertwined with CNTs was observed when printing on both untreated and plasma treated samples with droplet spacing range S_o, as a result of growth termination from excess catalyst. Alignment is achieved when printing with S_{PO} and S_{ID} on untreated samples. A high degree of fidelity is observed between the shape of the forest grown and inkjet printing as seen in Figure 37, where, the forest growth closely mimics the shape of the continuous line, scalloping lines and individual drops. In comparison to LIC, printing with MIC achieves greater alignment and height of the VA-CNTs grown on the untreated substrates as seen in Figure 37.a. However, when printing on plasma treated substrates, graphitic flake like structures were observed for all droplet spacings.

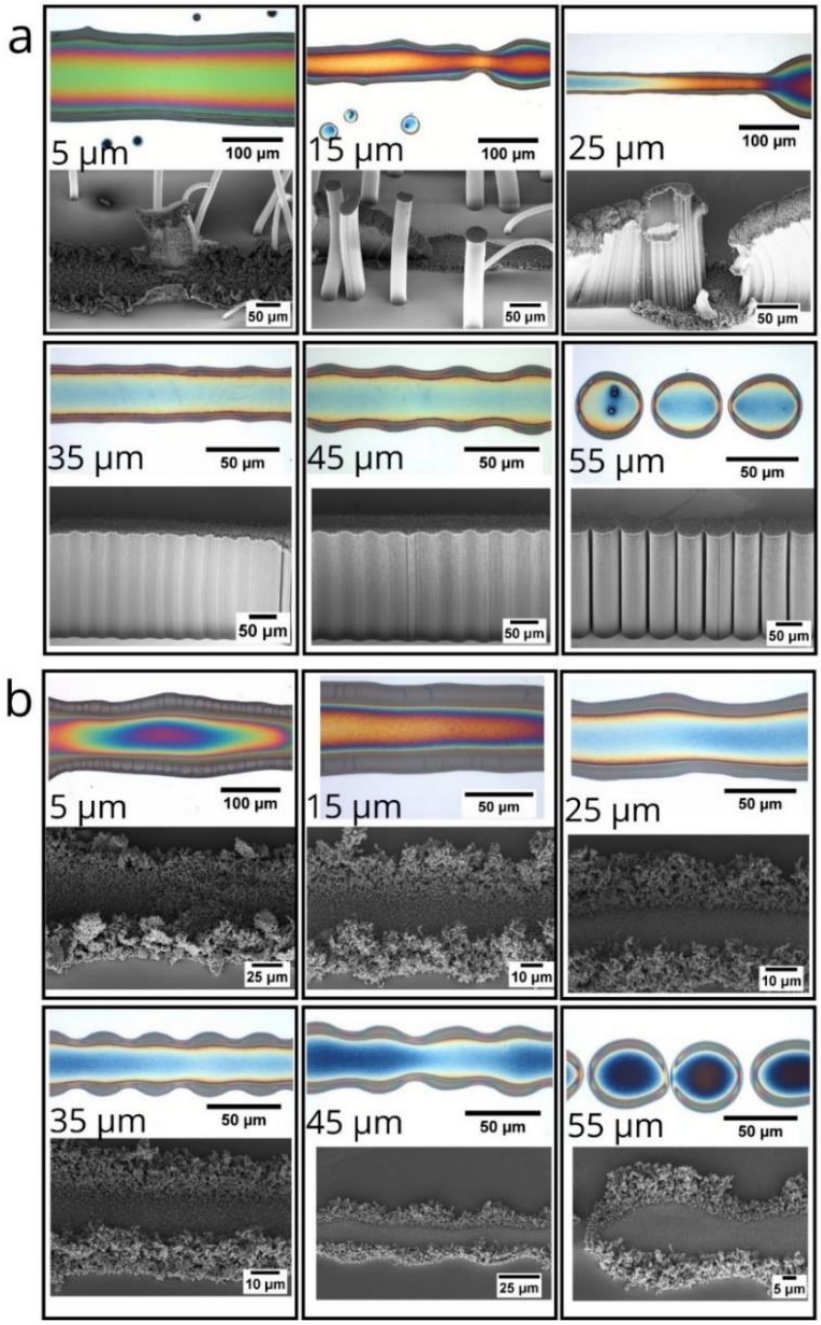

Figure 37: *10 nm alumina coated silicon wafers* ***a)*** *untreated and* ***b)*** *60 s plasma treated printed with magnetite ink concentration 6.57 %w/w at varying droplet spacings. Optical micrographs* ***(top)*** *show printed ink before CVD growth and SEM micrographs* ***(bottom)*** *show results post CVD growth.*

- *High Ink Concentration – 14.59 $\%_{w/w}$*

Figure 38 shows the printing and growth results for HIC. Thick bulging lines and individual droplets are observed when printed with S_o on both untreated and plasma treated samples.

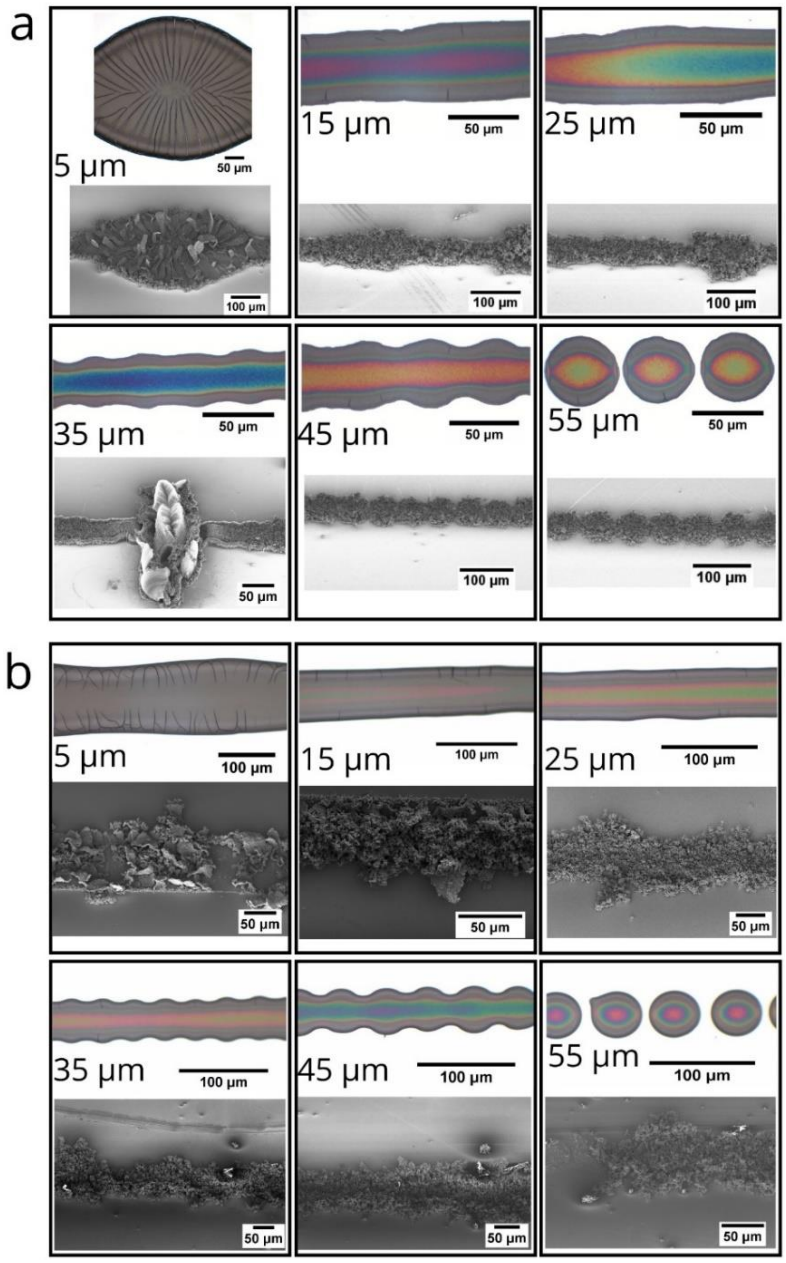

Figure 38: *10 nm alumina coated silicon wafers* ***a)*** *untreated and* ***b)*** *60 s plasma treated printed with magnetite ink concentration 14.59 %w/w at varying droplet spacings. Optical micrographs* ***(top)*** *show printed ink before CVD growth and SEM micrographs* ***(bottom)*** *show results post CVD growth.*

When printing with S_{PO}, owing to the higher surface tension of the ink, lines were achieved on both untreated and plasma treated substrates. However, a large coffee ring was observed. When printing with S_{PO} on untreated samples, bulging and breaks in the lines as the high particle density of the ink causes the dried films to crack. However when printing with S_{PO} on plasma treated samples, straight lines of catalyst were achieved. As droplet spacing was increased within the S_{PO} range, the transition from straight lines to scalloping lines was

observed. Eventual fragmentation of the line into individual droplets was seen when printing with S_{ID}. Upon CVD growth, no homogeneous lines of forest were grown for all droplet spacings on both untreated and plasma treated. When printing with S_{PO} on untreated substrates, the thinning effect observed with LIC and MIC is inhomogeneous in the case of HIC, resulting in regions of thick catalyst giving a combination of carpet growth mixed with sporadic regions of aligned CNT structures. However, when printing with S_{PO} on plasma treated substrates, no regions of alignment were observed.

- *Determination of Ink Concentration, Droplet Spacing and Surface Wettability for Scale-Up*

From the results presented in Figure 36, Figure 37 and Figure 38, a complex interplay between particle density, droplet surface tension, droplet spacing and substrate surface wettability can be seen. These parameters need to be optimised to achieve uniform and repeatable printing. Although VA-CNTs were achieved when printing LIC on both untreated and plasma treated substrates, the full length optical micrographs of the printed lines show discontinuities and scalloping (Figure C 2 and Figure C 3). Uniform lines of forest were only grown when printing MIC on untreated substrates, but printing on untreated substrates is not repeatable as a result of irregularities in the silicon wafer batch and alumina coating deposition. Optical micrographs as seen in Figure 39 show MIC printed on three different untreated substrates. For all three samples printing at droplet spacings less than 30 µm resulted in bulging lines with uneven layer thicknesses identified by the coloured fringes. Printing at droplet spacings greater than 30 µm resulted in scalloping and eventual break up of lines into individual droplets. Though lines were achieved at a droplet spacing of 30 µm for samples 1 and 2 the printing was not repeatable on sample 3. Bulging and extensive colour variation was observed across the length of the printed line on sample 3 indicating an uneven catalyst layer. As a result of this observed uneveness of layers and unprepatable print behaviour printing MIC on untreated samples

is not suitable for scalable VA-CNT growth. Printing MIC on plasma treated samples did not result in any VA-CNT growth. No growth was observed for all droplet spacings when printing HIC on both untreated or plasma treated substrates. It can be concluded that plasma exposure did not result in improved height and alignment of forests. This indicates that possible plasma etching effects in the alumina support layer do not allow for suitable formation of catalyst nano-islands with magnetite nanoparticles and other techniques for altering surface wettability should be studied.

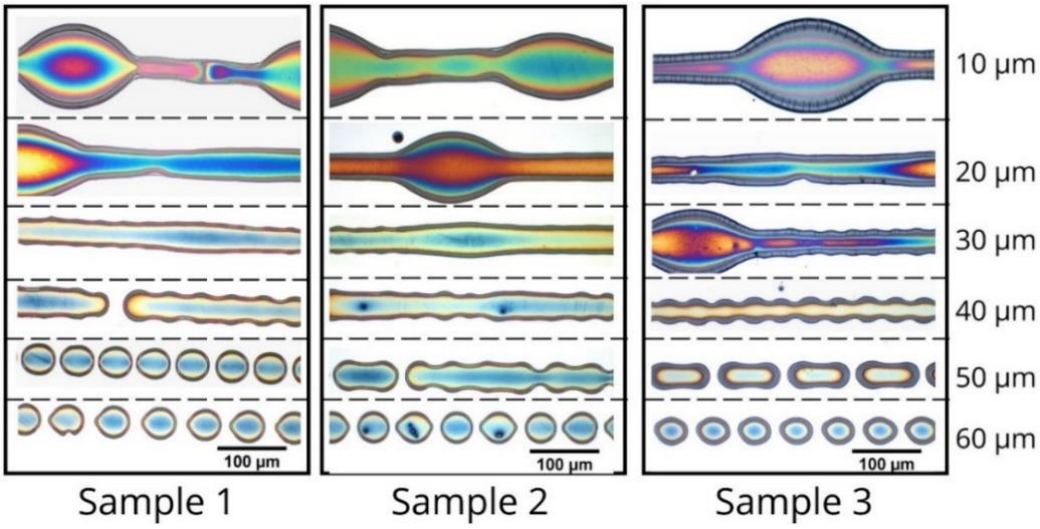

Figure 39: *Optical micrographs of ink concentration 6.57 $\%_{w/w,}$ printed on three untreated 10 nm alumina coated silicon wafers at varying droplet spacings.*

- *Raman Characterisation of Structure Grown.*

CNTs can be analysed by calculating the G/D ratio from their Raman spectra as previously shown in Chapter 2. The varying growth structures such as the flakes and VA-CNTs shown in the SEM micrographs can be compared via Raman spectroscopy to ascertain whether the differences in structures could be quantified by calculating the G/D ratio. Raman spectra for growths from all three concentrations printed on plasma treated substrates was analysed and the results shown in Figure 40.a. The graph shows a mildly higher G/D ratio for the

flake like structures grown from MIC and HIC than for the VA-CNTs grown from LIC. A similar trend was observed when comparing structures grown from MIC printed on untreated and plasma treated substrates, it can be seen in Figure 40.b that the G/D ratios calculated for the growth on plasma treated samples were higher than those calculated for growth on untreated samples. The higher G/D ratio of the graphitic flake structures grown on the plasma treated substrates could be on account of intertwined CNTs giving a higher signal upon interaction with the Raman laser, than the top crust of the VA-CNTs grown on untreated substrates. Comparison of the growths from LIC printed on untreated and plasma treated substrates revealed almost negligible variation as seen in Figure 40.This result is expected as the height and alignment of the VA-CNTs grown upon inspection via SEM appear similar on both substrates for all droplet spacing.

From the Raman data and SEM micrographs of the samples we can deduce that, while alignment does not necessarily increase the quality of the individual CNTs grown, the number of CNTs packed in a given area increases. Raman spectra comparing growth from LIC printed on untreated and plasma treated can be found in Figure C 4.a and b. Raman spectra comparing growths from LIC, MIC and HIC printed on plasma treated substrates at droplet spacing range $S_{o,}$ S_{OD} and S_{ID} can be seen in Figure C 4.c and d. The Raman spectra and G/D calculations do not show an evident quantitative trend between the different structures of growth observed. While Raman spectroscopy is a great tool for identifying the presence of CNTs, SEM analysis is required to analyse in detail the alignment and height of the forests grown. Air plasma treatment can change the surface of the alumina support layer such that no VA-CNTs can be grown. Therefore, the effects of

UV treatment on substrate wettability are investigated as it is a less reactive technique than plasma treatment. As no growth was observed for HIC, further study investigating the effects of UV treatment on the alignment of CNT growth was conducted for LIC and MIC only. The representative LIC and MIC ink concentrations; 2.19 $\%_{w/w}$ and 6.57 $\%_{w/w}$ are used for all further studies.

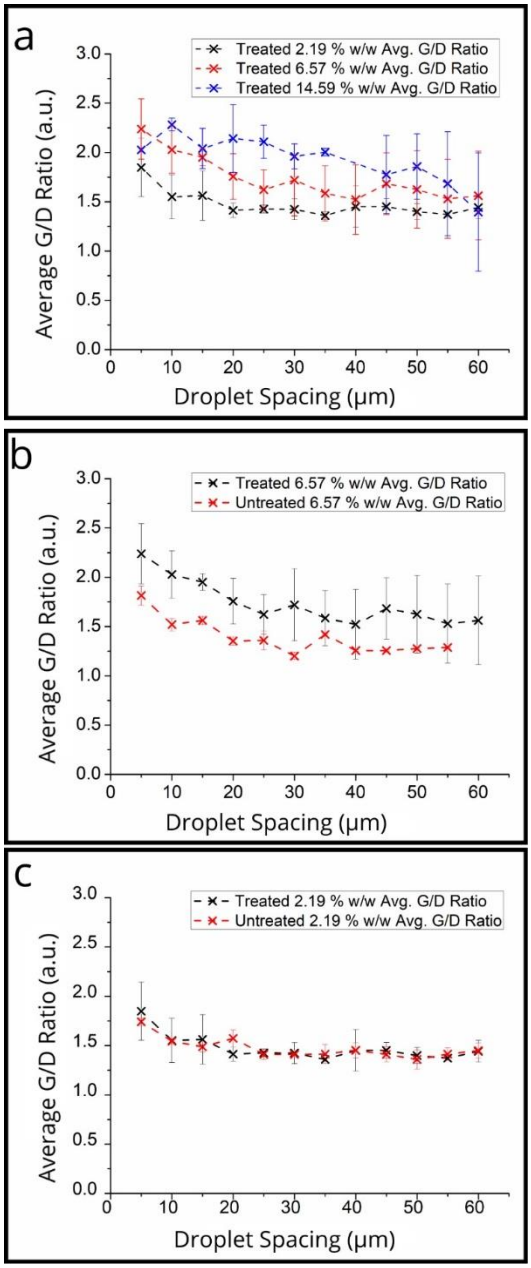

Figure 40: *graphical representation of G/D ratio vs droplet spacing comparing CNT growth from* ***a)*** *ink concentrations 2.19 $\%_{w/w}$ 6.56 $\%_{w/w}$ and 14.59 $\%_{w/w}$ printed on plasma treated substrates,* ***b)*** *ink concentration 6.57 $\%_{w/w}$ printed on untreated and 60 s plasma treated substrates and* ***c)*** *ink concentration 2.19 $\%_{w/w}$ printed on untreated and 60 s plasma treated substrates. All errors have been calculated as a 95% CI.*

3.3.2.3 VA-CNT growth by Printing on Untreated and UV Ozone Treated Substrates

UV treatment was found to increase the wettability of 10ASW substrates by reducing the contact angle by approximately 62 ° as calculated in section 3.3.1. This section explores the effects of varying surface wettability via UV Ozone. Ink concentrations 2.19 $\%_{w/w}$ and 6.57 $\%_{w/w}$, are printed on untreated and 600 s UV treated 10ASW substrates, and at droplet spacings varied between 5 µm and 60 µm varied at 5 µm increments. The alignment and height of the VA-CNTs grown is analysed via optical microscopy and SEM. Raman spectroscopy is not shown as it gave almost negligible quantitative variation between structures grown in the previous section.

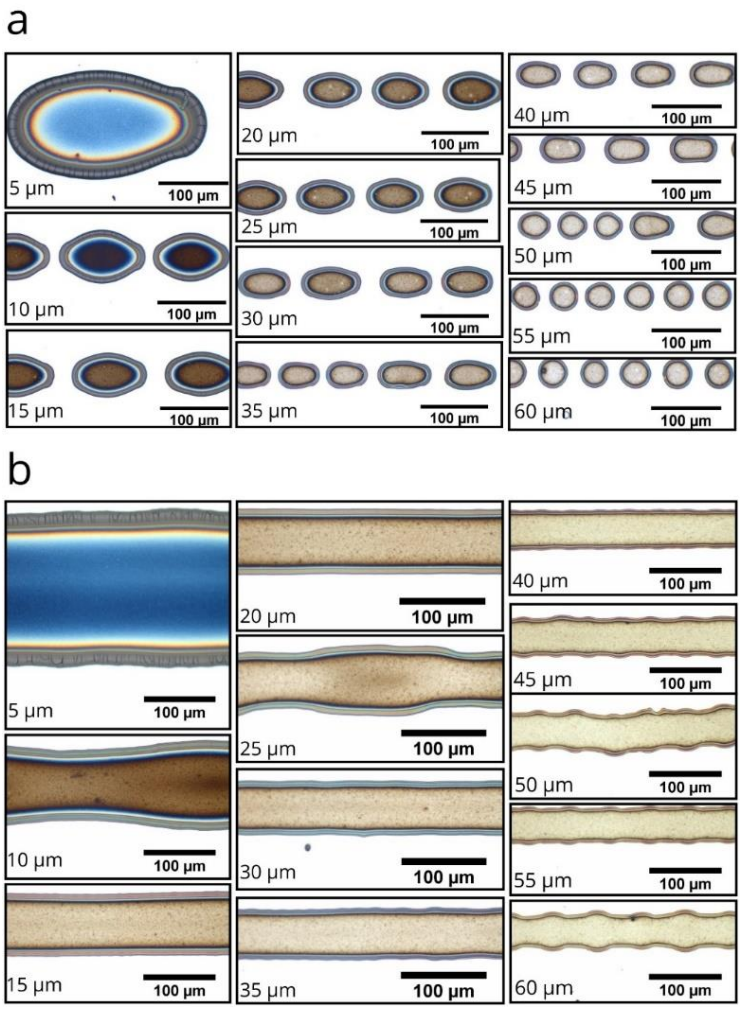

Figure 41: *Optical micrographs of magnetite ink concentration 2.19 $\%_{w/w}$ printed on* ***a)*** *untreated and* ***b)*** *600 s UV treated 10 nm alumina coated silicon wafers.*

Figure 41 shows optical micrographs comparing LIC printed on untreated and UV treated substrates. It is evident from the micrographs that UV treatment has a far more significant effect on substrate wettability than plasma treatment. It can be seen in Figure 41.a and b that here no ink coalescence was achieved when printing LIC on untreated substrates, printing on UV treated substrates resulted in lines of catalyst visible across all droplet spacings. The homogeneity of the lines printed is evidenced by the even colour of the printed lines seen in Figure 41.b.

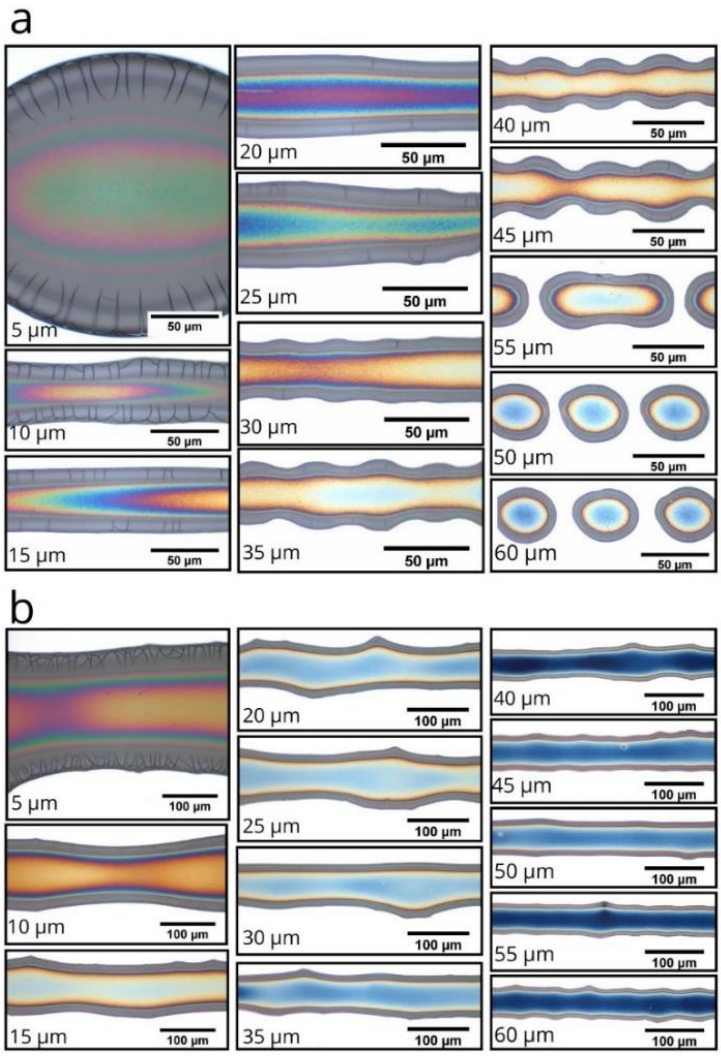

Figure 42: *Optical micrographs of magnetite ink concentration 6.57 %$_{w/w}$ printed on* ***a)*** *untreated and* ***b)*** *600 s UV treated 10 nm alumina coated silicon wafers.*

Optical micrographs in Figure 42.a reveal that upon repeating printing of MIC on untreated substrates, inhomogeneous spreading of the ink was seen as previously observed.

Homogeneous lines of catalyst were achieved when printing on surfaces treated with 600 s UV, similar to those observed when printing LIC. UV treatment allows uniform lines to be printed with both ink concentrations across the entire droplet spacing range as seen in the full length optical micrographs shown in Figure C 5. The result indicate that UV-Ozone treatment is a more suitable method of achieving lines of printed catalyst than plasma treatment.

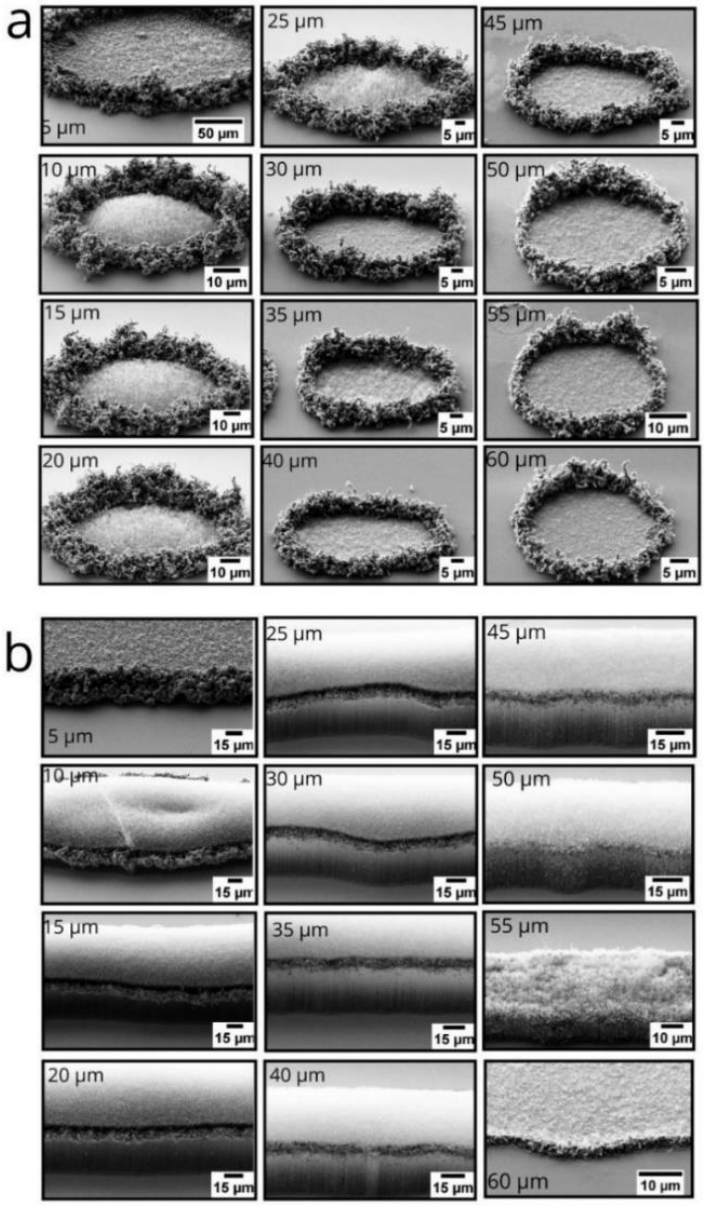

Figure 43: *SEM micrographs of grown CNTs from magnetite ink concentration 2.19 %$_{w/w}$ printed on* ***a)*** *untreated and* ***b)*** *UV treated 10 nm alumina coated silicon wafers.*

SEM micrographs in Figure 43.a show results of CVD growth for LIC printed on untreated substrates. The micrographs reveal that no VA-CNTs were grown for LIC printed on untreated substrates, even though pillars of VA-CNTs were previously observed. Instead, graphitic structures in the shape of nests were grown for all droplet spacings. These results further substantiate the unpredictability and irreproducibility of printing on untreated substrates. Additional SEM micrographs showing this unpredictable growth behaviour can be found in Figure C 6. SEM micrographs in Figure 43.b show results of CVD growth for LIC printed on UV treated substrates. Lines of forest can be seen when LIC is printed at droplet spacing range S_{OD}. Catalyst overloading results in the growth of graphitic flake structures when printed at $S_{O,}$ whereas catalyst scarcity leads to a short CNT carpet when printing at S_{ID}.

SEM micrographs in Figure 44.a show results of CVD growth for MIC printed on untreated substrates and reveal similar graphitic flake structures observed when printing LIC on untreated substrates. Although VA-CNTs were grown from printing MIC on untreated substrates in the previous section, no growth of VA-CNTs for this experiment supports that printing on untreated substrates is not feasible for scale-up on account of irregular results. UV treatment of the substrate also proved unsuccessful in the homogeneous growth of VA-CNTs as seen in Figure 44.b.

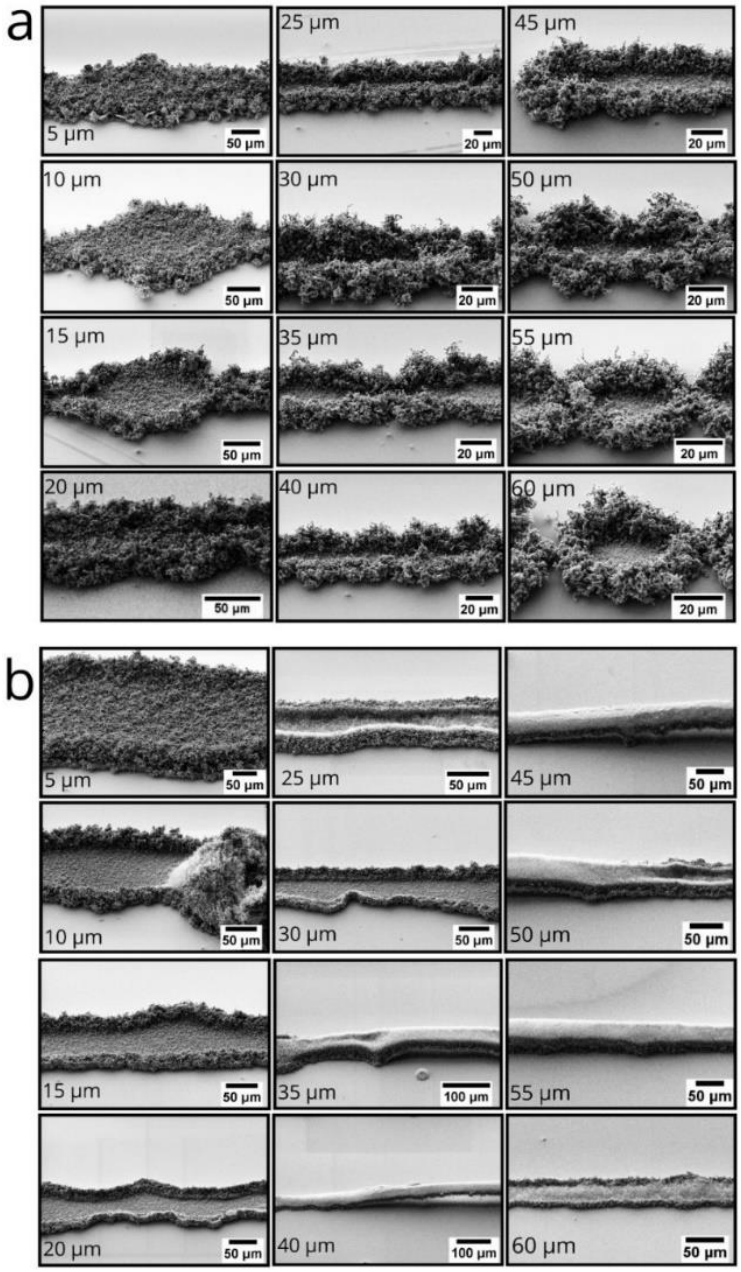

Figure 44: *SEM micrographs of grown CNTs from magnetite ink concentration 6.57 %w/w printed on* ***a)*** *untreated and* ***b)*** *UV treated 10 nm alumina coated silicon wafers.*

The results conclude that VA-CNT structures can be successfully grown by printing ink concentration 2.19 $\%_{w/w}$ on UV treated substrates at droplet spacing range S_{OD} as catalyst. The droplet spacing range can be further narrowed to a single value by measuring the height of the forest grown at each droplet spacing within this range. However, the height of the forest grown in Figure 44 is not very high. Up until this point all growths have been

conducted in the same quartz tube condition in Chapter 2. The quartz tube in the CVD has a lifetime after which shortening of the VA-CNTs can be seen. The functionality of the quartz tube can change as a result of variation in catalyst and build-up of material in the tube over time. Therefore, a new tube was conditioned for growing CNTs from only ink concentration 2.19 $\%_{w/w.}$ Figure 45.a shows SEM micrographs and height measurements of VA-CNTs grown in the new conditioned tube from ink concentration 2.19 $\%_{w/w}$ printed on UV treated substrates at varying droplet spacings. The height measurements ascertain that as the droplet spacing is increased, the height of the VA-CNT forest also increases up until a droplet spacing of 45 µm. Increasing droplet spacing further resulted in a reduction in VA-CNT height. This trend can be seen in the graph presented in Figure 45.b.

The height of the forest is dependent on the growth rate, as previously discussed in section 2.1. In section 2.1.2 data from Moulton *et al.* (2012) was presented (Figure 6) where a similar trend was observed that as iron film thickness increases the VA-CNT growth rate increases up until an ideal thickness of 3 nm after which the growth rate drops [153]. This trend is reflective of changes in the Ostwald ripening and subsurface diffusion effects on the catalyst nano-island formation. Similarly, in the graph presented in Figure 45.b maximum growth rate or VA-CNT height is observed at a droplet spacing of 45 µm. Anything below or above this thickness value can result in a decrease in growth rate. Therefore, detailed nano-island analysis is required to understand effects of varying catalyst layer thickness on VA-CNT growth.

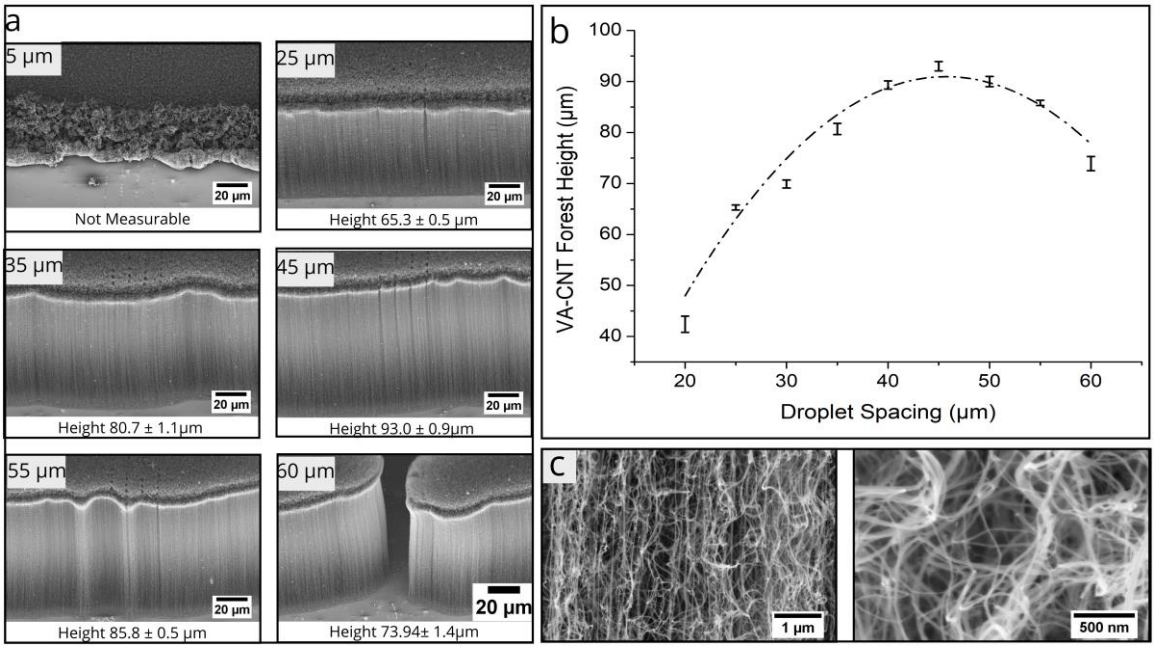

Figure 45: a) *SEM micrographs showing height variation of VA-CNTs grown from magnetite ink concentration 2.19 %$_{w/w}$ printed on UV treated 10 nm alumina coated silicon wafers at varying droplet spacings.* ***b)*** *Graphical representation of VA-CNT forest height vs. Droplet spacing. Error bars have been calculated as a 95% CI.*

A model by Beard *et al.* (2013), discussed earlier in section 2.1.4, can be used to determine the number of inkjet droplets required for a given printer, ink concentration and substrate wettability to achieve a monolayer of catalyst for VA-CNT growth [48]. According to the model when printing with spherical 10 nm sized magnetite nanoparticles suspension of concentration of 2.19 %$_{w/w}$, on a substrate with a contact angle of 18.46 °, using a nozzle of diameter 21.5 µm, 0.05 droplets give a monolayer suitable for VA-CNT growth. When an ink concentration of 2.19 %$_{w/w}$ is printed using a nozzle diameter of 21.5 µm, a droplet spacing of 45 µm ensures that multiple droplets are not deposited in a given area and the droplet spreads. However, it is difficult to determine what percentage of the droplet is in a given area. As previously discussed this model has limitations as it does not take into consideration coffee staining effects, giving underestimates. Therefore, catalyst layer thickness analysis and annealed nano-island size is required as a more definitive measure of determining catalyst suitability for VA-CNT growth. In, section 3.3.3 the catalyst layer

thickness, coffee-ring effects and annealed nano-island will be studied to understand the varying growths trends observed in this section.

Figure 45.c shows a close-up of the CNTs grown when printing the ink at a droplet spacing of 45 µm where the CNTs intertwine and support each other into a forest. However, as these SEM micrographs are taken at the edge of the printed catalyst, where a coffee ring effect is prevalent, the alignment of the VA-CNTs is not representative across the entire printed catalyst film. Therefore, the thickness of the film and catalyst nano-island formation at the edge of the printed line is also not demonstrative of that in the central region of the printed film. After finding the optimum ink concentration of 2.19 $\%_{w/w}$, droplet spacing of 45 µm and UV surface treatment of 600s for growing VA-CNTs, the next study was conducted to determine the feasibility of using inkjet printing to deposit catalyst on other substrates for VA-CNT growth.

3.3.2.4 Printing on Other Substrates

All the growth so far has been carried out on silicon wafers coated with a buffer layer of 10 nm alumina deposited using an e-beam deposition system as this combination of catalyst and buffer layer is conventionally used to study the fundamentals of CNT growth. However, many applications require growth or transfer of these structures on other materials especially as the insulating buffer layer can sometimes create a barrier between the conductive substrate. Therefore, experiments were conducted to understand if VA-CNTs could be grown by directly depositing catalyst on a silicon substrate without the presence of a buffer layer.

SEM micrographs in Figure 46 show that lines of VA-CNTs can be grown without the presence of a buffer layer on UV treated silicon wafers by printing ink concentration 2.19 $\%_{w/w}$ at a droplet spacing of 45 µm. As the ink concentration, UV treatment and droplet

spacing were kept constant for all substrates, the forests can be compared by calculating the densities of the forests grown. The VA-CNT forest density was calculated by measuring the wafer chips before and after CVD growth. It can be seen from the data presented in Figure 46 that the highest forest density (1.11 g/cm^3) is achieved on the 10ASW substrates. When printing on an uncoated silicon wafer, larger spreading of the catalyst is observed on the catalyst with the width of the printed catalyst layer calculated to be greater than that on the 10ASW substrate. This signifies that the iron oxide nanoparticles are spreading more resulting in a loss of packing of the catalyst. Even though the height of the forest grown is larger, the forest density is lower (0.23 g/cm^3). This result verifies the importance of the buffer layer in achieving the right packing of the nucleated catalyst in order to grow a dense VA-CNT forest.

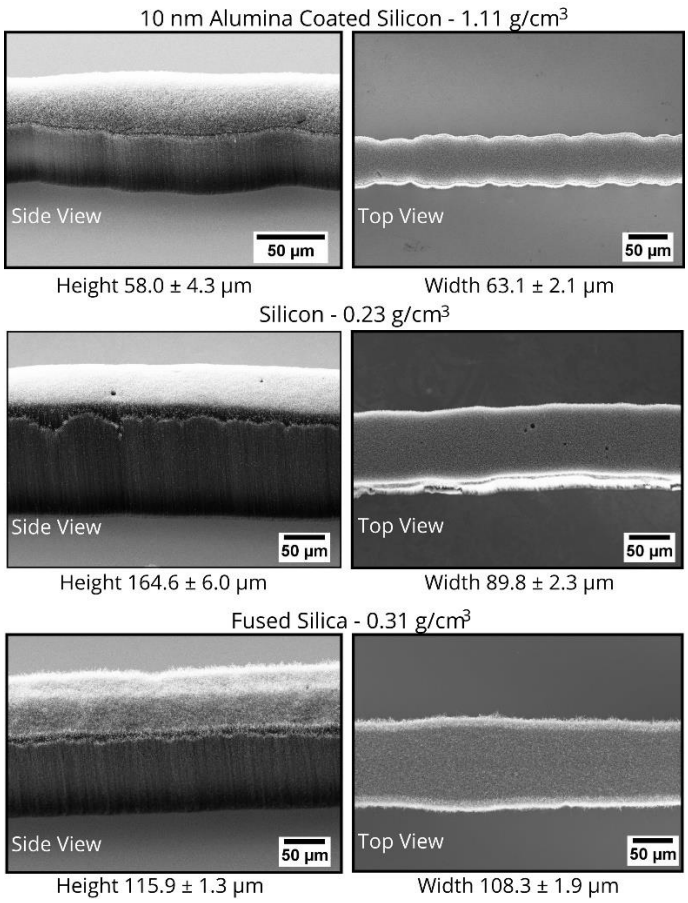

Figure 46: *SEM micrographs of the top* ***(right)*** *and side* ***(left)*** *view of VA-CNTs grown from ink concentration 2.19 %$_{w/w}$ printed on UV treated* ***(top)*** *10 nm alumina coated silicon wafers,* ***(middle)*** *silicon wafers and* ***(bottom)*** *fused silica chips. All errors have been calculated as a 95% CI.*

Some applications require VA-CNTs grown on non-conductive substrates and connected with electrodes to limit the conductive path to the VA-CNTs such as electrochemical sensors as discussed in Chapter 1. Fused silica is a low cost transparent substrate that can be used for this purpose. It can be seen in Figure 46 that using the same ink concentration, UV treatment and droplet spacing settings, lines of VA-CNTs can be grown on fused silica substrates. The CNT forest density was calculated to be 0.31 g/cm^3, which is greater than that of the VA-CNTs grown on untreated silicon wafer substrates, but lower than that grown on 10ASW substrates.

The results so far demonstrate a complex interplay between ink particle density, surface tension, droplet spacing and substrate wettability required to achieve homogeneous catalyst lines and even growth of VA-CNTs. As found in Chapter 2, CNT alignment is dependent on the growth rate, where adjoining CNTs with similar growth rates adhere together and those with dissimilar growth rates bend or buckle. Although SEM micrographs have been a useful tool to analyse the VA-CNT forests, it is important to study the effect of varying ink concentration droplet spacing and surface wettability on the formation of catalyst nano-islands during the annealing step of the CVD Growth.

3.3.3 Printing Effects on Catalyst Nano-island Formation

From the literature reviewed in Chapter 2, varying catalyst thickness results in irregular size distribution of the catalyst nano-islands formed during annealing. Depending on the size and packing of the nano-islands formed, varying growths have been observed such as amorphous flakes, sparse/tangled CNT carpets and CNT forests[143]. In order to understand the varying CNT growth trends observed in section 3.3.2, this section

investigates in detail the morphology of the catalyst lines printed and how it impacts the catalyst nano-island formation during annealing, and thus VA-CNT growth.

3.3.3.1 Analysing Catalyst Layer Thickness

Catalyst layer thickness can be measured using a few different techniques. The thickness, and hence volume of a printed catalyst film can be measured by analysing its cross-section. Milling with a focused ion beam (FIB) is one technique to cross-section a printed film. Ink concentrations 1.45 – 14.59 $\%_{w/w}$ were printed on untreated 10ASW substrates and upon drying a cross section of the printed catalyst was milled with a FIB. Figure 47 shows SEM micrographs of the cross-section of the coffee ring of a line printed with ink concentration 14.59$\%_{w/w}$. As observed in the SEM micrograph shown in Figure 47.b, it is difficult to distinguish between the layers with imaging becoming increasingly difficult as magnetite concentration is reduced. SEM micrographs of the FIB milled cross sections of ink concentrations 1.45 – 10.93 $\%_{w/w}$ are shown in Figure C 7.

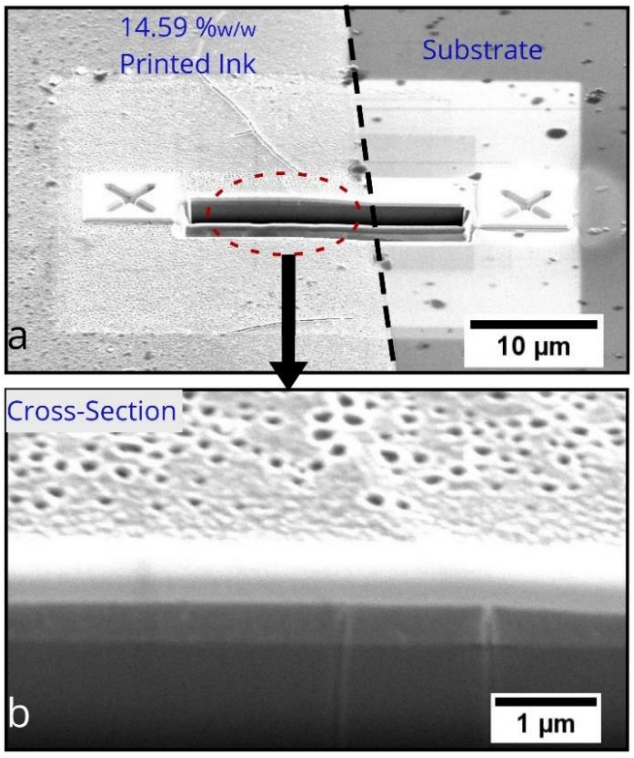

Figure 47: *SEM micrographs of* ***a)*** *the location of the FIB cross section at the edge of the line printed with an ink concentration 14.59 $\%_{w/w}$ and of* ***b)*** *a close up of the coffee ring.*

Other profiling methods were utilised to try and reveal additional details about the thickness of the printed lines. In the last section it was observed that printing on UV treated substrates increases the spread of the ink and a reduction in the size of the coffee ring. Therefore, the size of the coffee rings can be studied and the volume correlated to the overall thickness of the printed catalyst. By measuring the width of the coffee rings via optical microscopy and the height via AFM, the overall volume of the coffee ring for a given ink concentration, substrate wettability and droplet spacing can be calculated for a printed film length of 1 µm. AFM analysis was used to analyse the height of the coffee rings formed for ink concentrations 2.19 $\%_{w/w}$ and 6.57 $\%_{w/w}$ printed on untreated and UV treated 10ASW substrates at three droplet spacings representing S_O (5 µm), S_{OD} (45 µm) and S_{ID} (60 µm).

AFM imaging was conducted on the samples before and after annealing to understand how the printed catalyst film changes during CVD growth. Detailed results of the AFM analysis can be found in Figure C 8 and were analysed using Gwyddion. Height profile analysis on the AFM micrographs taken before annealing revealed a reduction in the coffee ring effect when printing on UV treated substrates in comparison to untreated. These results are shown in Figure 48.a, b and c. It can be seen in Figure 48.a.i that as droplet spacing increases for a given ink concentration, the height of the coffee ring reduces, whereas as ink concentration is increased the height of the coffee ring increases. Such is the effect of increasing the wettability of the substrate that the coffee ring heights of the two concentrations post UV treatment are relatively similar and uniform across the 5 µm to 60 µm droplet range. It can be further deduced from the graphs in Figure 48.a.ii and the AFM micrographs shown in Figure 48.b.i and ii that a dramatic thickness variation in the coffee ring occurs as a result of calcination during the annealing process. AFM is a specialist technique that though gives precise measurements, is difficult to be carried out on all samples. AFM imaging before and after annealing of 6.57 $\%_{w/w}$ printed on untreated

10ASW substrates at a droplet spacing of 5 µm could not be obtained as the height variation proved beyond the resolution of the AFM. Therefore, white light interferometry can be used as a complimentary technique to AFM owing to its fast and non-contact measurement approach to analyse coffee ring heights of the printed catalyst before annealing.

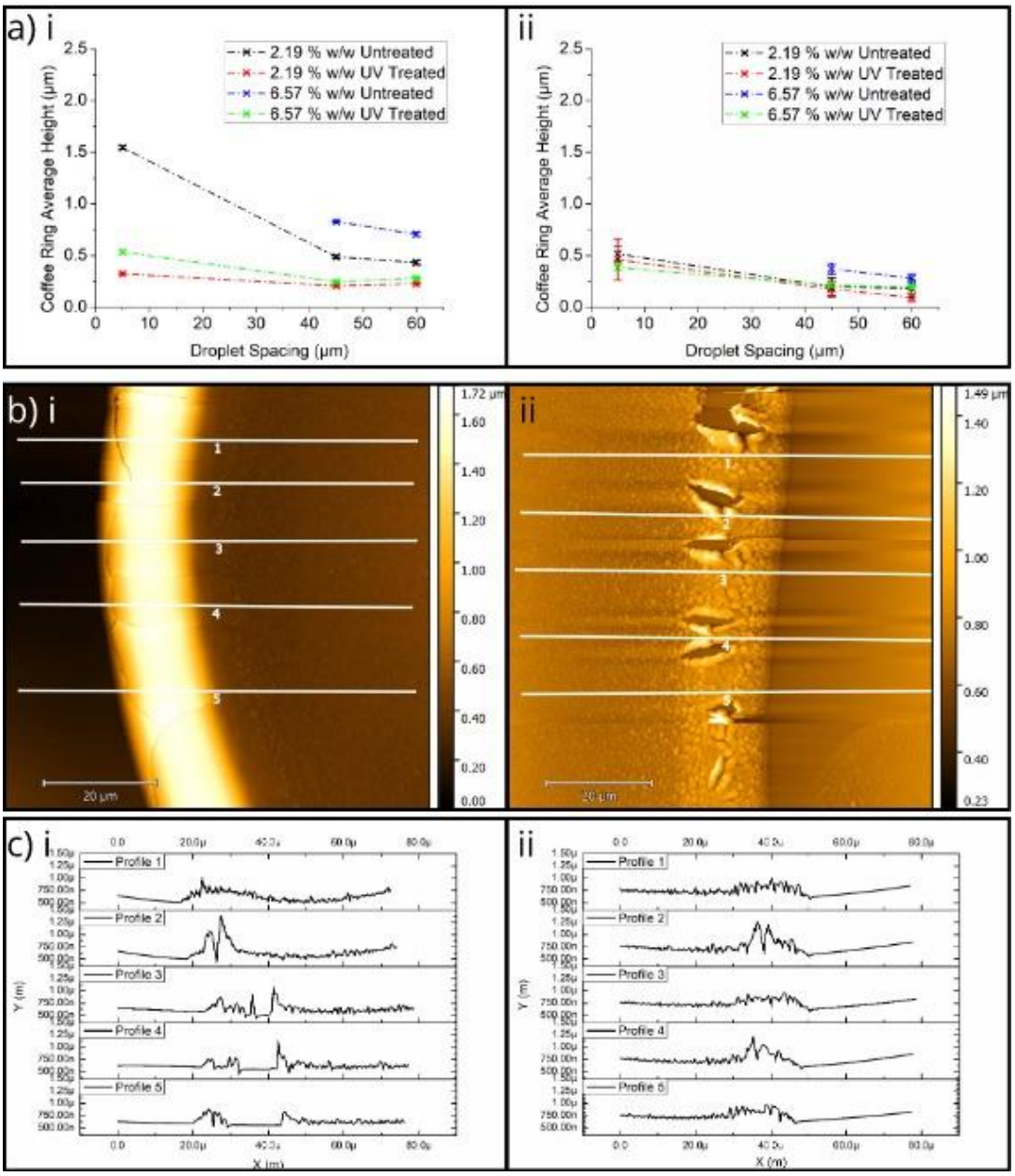

Figure 48: a) *Graphical representation of coffee ring average height (µm) vs droplet spacing (µm) for ink concentrations 2.19 $\%_{w/w}$ and 6.57 $\%_{w/w}$ printed on untreated and UV treated substrates* ***i)*** *before (a relative standard error of < ± 5 % estimated for the average heights calculated) and* ***ii)*** *after annealing (a relative standard error of < ± 15 % estimated for the average heights calculated).* ***b)*** *Representative AFM micrographs and* ***c)*** *graphical representation of height profiles analysed for ink concentration 2.19 $\%_{w/w}$ printed at a droplet spacing of 5 µm on UV treated substrates* ***i)*** *before and* ***ii)*** *after annealing.*

All the interferometer micrographs obtained for 2.19 $\%_{w/w}$ and 6.57 $\%_{w/w}$ can be found in Figure C 9. The height profile analysis methodology is shown in Figure 49.a and b. All images were analysed using Gwyddion. The measurements revealed as shown in Figure 49.c, that the interferometry results follow a similar pattern to those from AFM where the height of the coffee ring reduces as droplet spacing is increased, and increases when ink concentration is increased. Hence, white light interferometry can be used as a complimentary technique to AFM for analysing the coffee ring height of printed catalyst. However, for more precise measurements AFM is still more suitable. Graphs comparing height measurements from AFM and interferometer micrographs can be found in Figure C 10 and height measurement values can be found in Table C 5 .

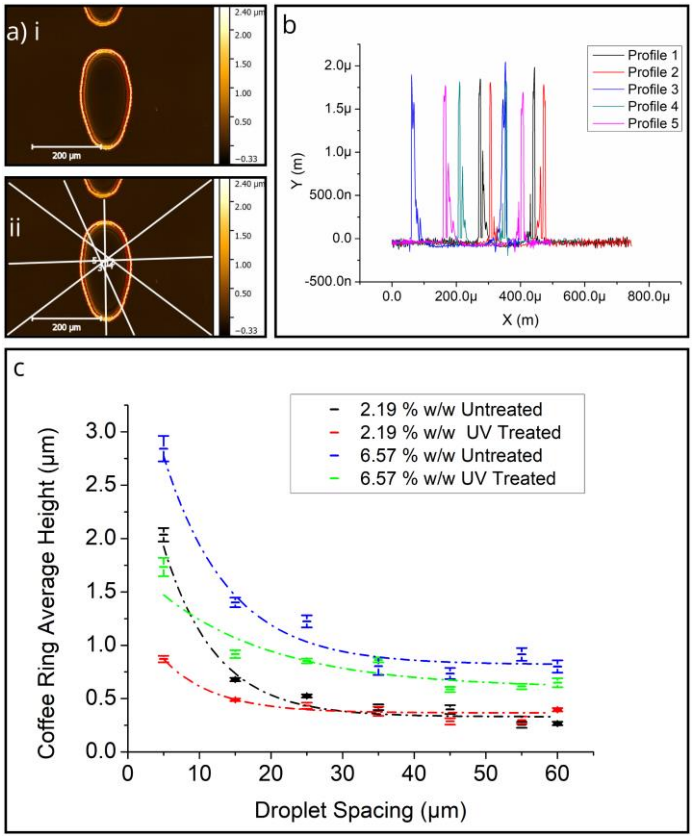

Figure 49: a) *Representative interferometer micrographs of* ***i)*** *ink concentration 2.19 $\%_{w/w}$ printed on untreated 10 nm alumina coated silicon substrates and* ***ii)*** *the profile locations.* ***b)*** *Graphical representation of the height profiles analysed.* ***c)*** *Graphical representation of coffee ring average height (µm) vs droplet spacing (µm) for ink concentrations 2.19 $\%_{w/w}$ and 6.57 $\%_{w/w}$ printed on untreated and UV treated substrates before annealing. A relative standard error of < ± 12 % estimated for the average heights calculated.*

The width of the coffee ring was measured via optical microscopy, detailed images for which can be found in Figure C 11, Figure C 12, Figure C 13 and Figure C 14 and the tables of calculations can be found in Table C 6. All optical micrographs were analysed using ImageJ. Representative optical micrographs and the line profiles of 2.19 $\%_{w/w}$ printed at a droplet spacing of 5µm on untreated and UV treated 10ASW substrates can be seen in Figure 50.a and b. Line profiles measuring the width were possible on account of the colour variation across the printed film. The width profile measurements revealed a similar trend as that observed for height where, as droplet spacing is increased, the width of the coffee ring decreases and as ink concentration increased the width of the coffee ring increases.

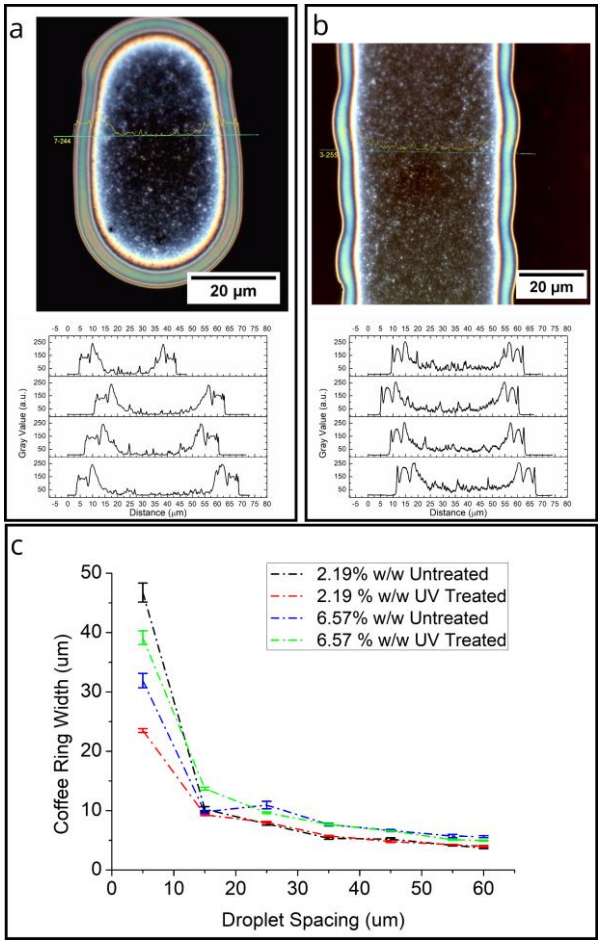

Figure 50: *Representative optical micrographs and width profiles analysed for ink concentration 2.19 $\%_{w/w}$ printed at a droplet spacing of 5 µm on* ***a)*** *untreated and* ***b)*** *UV treated 10 nm alumina coated silicon substrates.* ***c)*** *Graphical representation of coffee ring average height (µm) vs droplet spacing (µm) for ink concentrations 2.19 $\%_{w/w}$ and 6.57 $\%_{w/w}$ printed on untreated and UV treated substrates. The standard errors have been shown in the graph. A relative standard error of < ± 6 % estimated for the average widths calculated.*

The results are shown in Figure 51 and reveal that for both 2.19 %w/w and 6.57 %w/w printed on untreated and UV treated 10ASW substrates, the volume of the coffee ring reduces as ink droplet spacing is increased. However, the largest variation in coffee ring volume is for the lower droplet spacings. The coffee ring volume values converge as droplet spacing is increased beyond 45µm for both ink concentrations and substrate wettability. The volume calculations can be found in Table C 7.

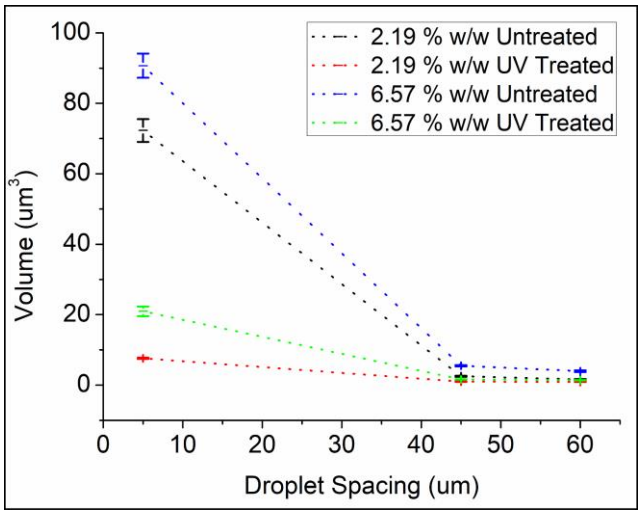

Figure 51: *Graphical representation of volume (µm³) vs Droplet Spacing (µm) for ink concentrations 2.19 %$_{w/w}$ and 6.57 %$_{w/w}$ printed on Untreated and UV treated 10 nm alumina coated silicon wafers. The standard errors have been shown in the graph. . A relative standard error of < ± 8 % estimated for the average widths calculated.*

It can be established from the results that CNT alignment is highly dependent on the concentration of nanoparticles in the printed lines. In order to further determine how the thickness of the catalyst layer influences catalytic evolution into nano-islands during the CVD annealing process for CNT growth, particle size analysis is required in the central region of the printed catalyst.

3.3.3.2 Particle Size Measurement of Annealed Catalyst Nano-islands

Prior to annealing, the surfactant encapsulating the nanoparticles inhibits detailed imaging, but annealing initiates the evaporation of the surfactant and the formation of catalytic nano-islands. The catalyst nano-islands can be analysed with either SEM or AFM imaging. AFM

analysis was conducted on annealed samples of ink concentrations 2.19 $\%_{w/w}$ and 6.57 $\%_{w/w}$ printed on UV treated 10ASW substrates at droplet spacings 5 µm, 45 µm and 60 µm. AFM micrographs of the catalyst nano-islands formed in the centre of the printed lines show distortion and stretching as shown in Figure C 15. Although AFM was suitable for measuring the coffee ring heights, owing to cracking and low adherence of the delicate printed catalyst to the substrate post annealing, similar to that earlier observed in Chapter 2. Therefore, SEM was used to analyse the annealed films.

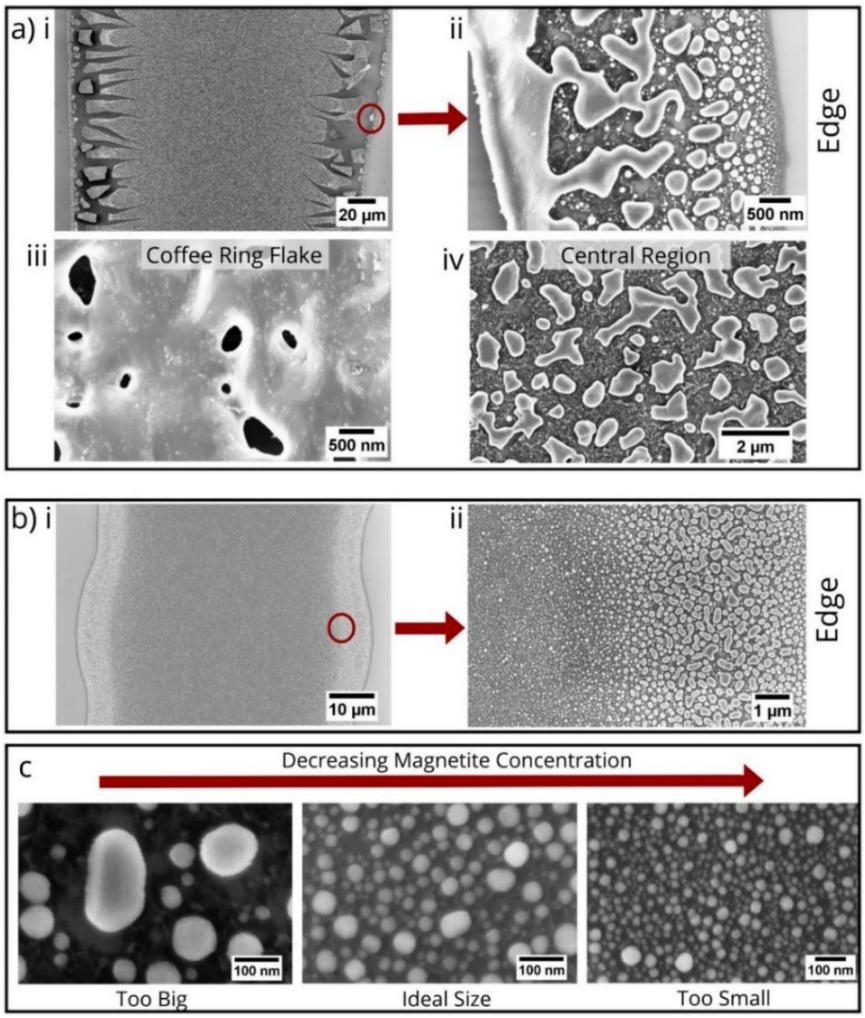

Figure 52: *a) SEM micrographs of ink concentration 6.56 $\%_{w/w}$ printed on a UV treated 10 nm alumina coated sample at a droplet spacing of 5 µm showing i) the overall printed line, ii) edge of the printed line, iii) film formation at the coffee ring and iv) catalyst island nucleation in the central region. B) SEM micrographs of ink concentration 2.19 $\%_{w/w}$ printed on a UV treated 10 nm alumina coated sample at a droplet spacing of 45 µm showing i) an overall view of the printed line and ii) the particle variation from edge to centre. c) SEM micrographs of catalyst nano-island nucleation in the central region of the printed line as magnetite concentration is increased.*

Detailed SEM micrographs can be found in Figure C 16, Figure C 17 and Figure C 18. For both ink concentrations upon subjection to hydrogen at high temperatures, the thick edges of the lines printed at a droplet spacing of 5 µm begin to crack as shown in Figure 52 a.i. Varying sizes of catalyst nano-islands can be seen at the edge of the printed line in Figure 52.a.ii on account of the curved coffee ring. As the coffee ring height increases, the size of the nano-islands also increases. It was also noted, as shown in Figure 52 a.iii, that when the catalyst film is too thick (as in the coffee ring for ink concentration 6.57 $\%_{w/w}$ printed at droplet spacing 5 µm) a melted sheet of catalyst is formed in the thickest regions of the coffee ring. As the catalyst layer gets thinner towards the central region of the printed line, nano-islands begin to form as shown in Figure 52 a.iv. For all the samples analysed, it was revealed that the catalyst film nucleated into larger particles on the edge of the printed line on account of the coffee ring effect in comparison to the central region of the printed line (Figure 52 b.i and ii). It is shown in Figure 52.c that as magnetite concentration is decreased the particle size of the catalyst nano-islands decreases and the packing increases.

The density of the nano-islands in a given region is crucial to VA-CNT growth as the individual CNTs need to be close to each other in order for them to support one another through Van der Waal forces and align into a forest. UV treatment minimises, but does not diminish the coffee-ring effect completely. Therefore, larger catalytic nano-islands are observed post annealing on the coffee ring than in the centre of the printed line. Hence, SEM micrographs are captured in the central region of the printed line as the uneven nature of the catalytic layer near the edges is not representative of the general particle distribution.

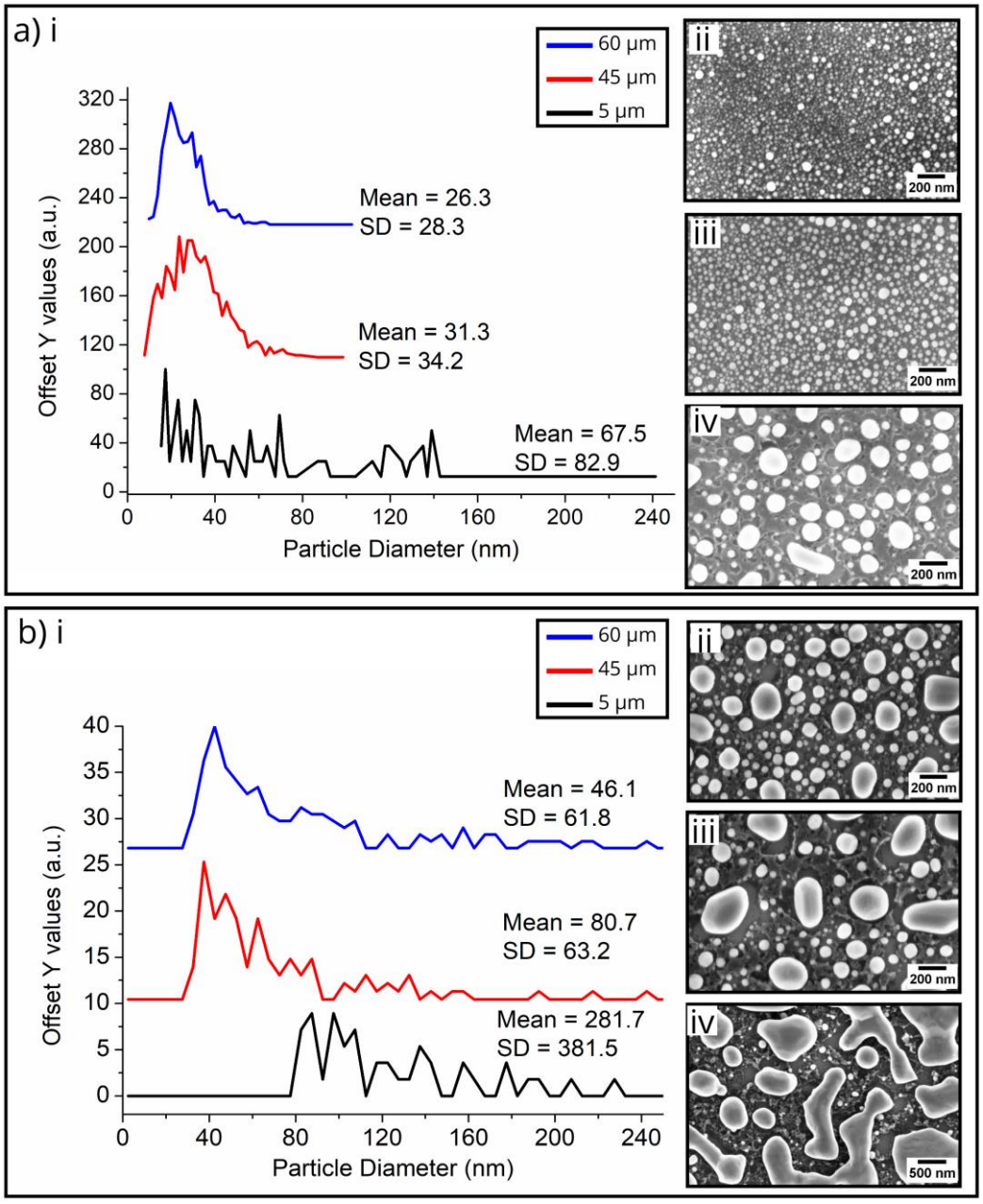

Figure 53: *Graphical representation* ***(i)*** *and SEM micrographs of particle size distribution post CVD annealing, for ink concentrations* ***a)*** *2.18 %$_{w/w}$ and* ***b)*** *6.65 %$_{w/w}$ deposited on UV-treated 10nm Al2O3 coated silicon substrates at droplet spacing 5 µm* ***(ii)****, 45 µm* ***(iii)*** *and 60 µm* ***(iv)****.*

Particle size analysis was conducted on the SEM micrographs using ImageJ to determine the particle size distribution for all samples. The histograms for each analysis can be found in Figure C 19. Particle size analysis reveals the significance of catalyst layer thickness on the morphology of the nano-islands formed during annealing. As particle density and layer thickness are increased, the average nano-island particle diameter increases with a broadening of the particle distribution as shown in Figure 53 a. and b. The average particle

size range across the 3 representative droplet spacings was calculated between 25 nm and 70 nm for 2.19 $\%_{w/w}$ and 45 nm to 300 nm for 6.57 $\%_{w/w.}$ This concludes that an increase in concentration and decrease in droplet spacing results in an increased size of the nucleated nano-islands. However, owing to oxidation of the catalyst upon removal of samples from the oxygen-free annealing environment, the calculated particle diameters are in fact larger than those existing during CNT growth. The mean particle diameter required to grow lines of free standing VA-CNTs was determined to be 31.3 nm, with a standard deviation of 34.2 nm, for 2.19 $\%_{w/w}$ printed at a droplet spacing of 45 µm on UV-treated 10ASW substrates. Previously, in-situ analysis using atomic-scale environmental transmission electron microscopy (ETEM) has been used to show the initial de-wetting of evaporated thin film catalyst into isolated particles, with a broadening of particle diameter distributions up until 5 minutes of annealing, after which a narrowing of the distribution is observed evidencing surface diffusion.[159], [251] Hence, in-situ ETEM analysis can also be used in the future to analyse the evolution of inkjet printed iron oxide nanoparticle films during annealing.

3.4 Conclusion

The results in this chapter present new knowledge in the field of scalable manufacture of VA-CNTs by inkjet printing iron oxide nanoparticles as catalyst. The results evidence that by selectively controlling jetting parameters and substrate conditions, layers of iron oxide nanoparticles can be deposited such that VA-CNTs can be grown. These results are ground breaking for the development of a scalable manufacturing platform for fabricating VA-CNT based devices. The need for lithographic steps is eliminated and CNTs can be grown with two steps; inkjet printing and CVD growth. Key findings from this chapter are highlighted below and presented in Figure 54.

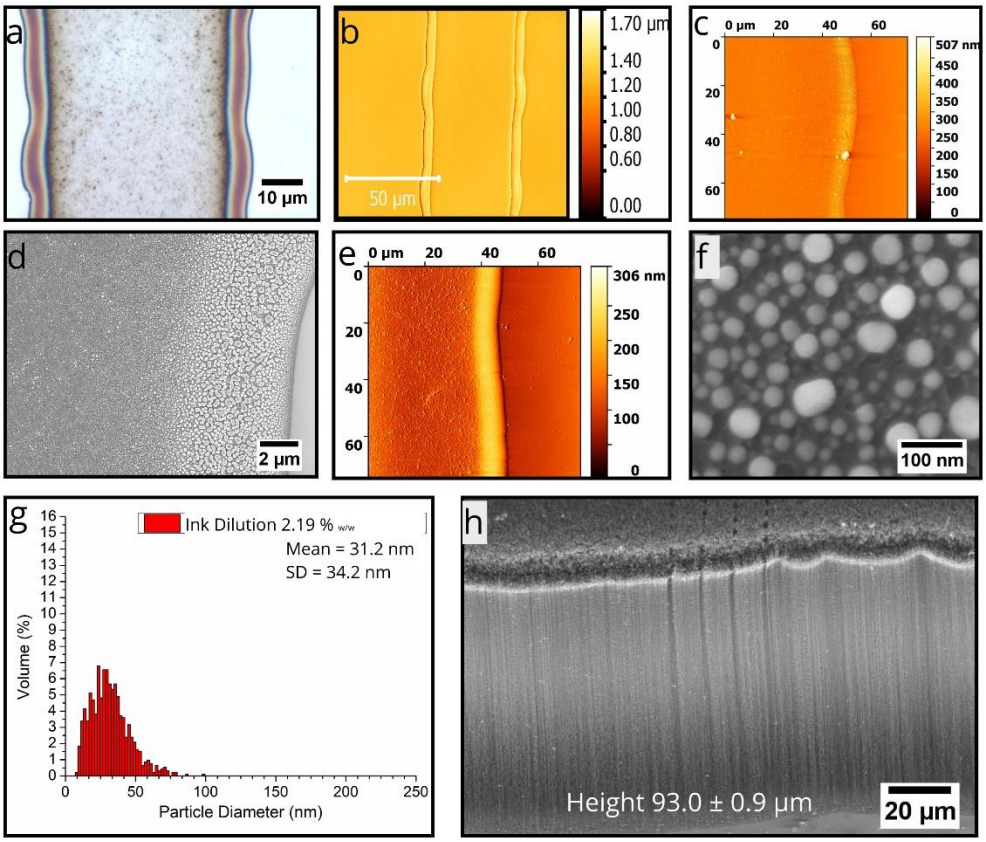

Figure 54: *Results summary for VA-CNTs grown from ink concentration 2.18 $\%_{w/w}$ printed on UV treated 10 alumina coated silicon substrates at a droplet spacing of 45 µm.* ***a)*** *Optical micrograph of as printed ink,* ***b)*** *interferometer micrograph of as printed ink* ***c)*** *AFM micrograph of as printed ink,* ***d)*** *SEM micrograph of ink edge after annealing,* ***e)*** *AFM micrograph of printed ink after annealing,* ***f)*** *SEM micrograph of nano-island nucleation in central region of printed ink post annealing,* ***g)*** *graphical representation of particle size distribution and* ***h)*** *SEM micrograph of VA-CNTs grown with the forest height stated. The error is reported as a 95% CI.*

- The dimensional analysis demonstrated that the ink is printable using a Dimatix printhead of nozzle orifice 21.5 µm, but with probable satellite droplets. However, it was determined via HIS that the jetting behaviour of the ink is unstable when printed with a larger nozzle orifice.
- UV treatment was used to increase the wettability of the substrate and achieve uniform lines of catalyst (Figure 54.a) with minimised coffee rings. A combination of white light interferometry, AFM and optical microscopy were used to analyse the coffee ring. (Figure 54.b and c).

- Upon annealing larger nano-islands were observed at the edge of the printed line than in the centre, on account of the coffee ring (Figure 54.d). However, as the overall volume of the coffee ring was minimised upon annealing ((Figure 54.e), and the nano-islands reduced the overall VA-CNT growth was not hindered.
- The overall size of the nano-islands formed in the central region of the catalyst layer were found to have a mean diameter of 31.3 ± 34.2 nm (Figure 54.f and g).
- VA-CNTs of height 93.0 ± 0.9 µmm were observed when printing ink concentration 2.19 $\%_{w/w}$ on UV treated 10 ASW substrates at a droplet spacing of 45 µm (Figure 54.h).

The results present a new approach for depositing catalyst for VA-CNT growth and open opportunities for developing devices on new substrates with unique VA-CNT structures. However, to optimise the printing process at industrial scale detailed HSI characterisation should be conducted on the Dimatix cartridge, but was beyond the scope of this research. Although AFM gave the highest resolution of images, white light interferometry was found to be an effective technique for print verification, especially at an industrial scale where fast inspection is required. Though the standard deviation for the particle analysis conducted is high, the particles are packed tightly allowing alignment of CNTs grown from smaller nano-islands. Increasing the catalyst thickness resulted in an increase in annealed nano-island size. The resulting forest height was found to degrade when either increasing or decreasing droplet spacing. This finding was verified through existing models and literature analysed found at the time of writing. Such a detailed particle analysis on VA-CNT growth from inkjet printed nanoparticles as catalyst has never been conducted before. A novel combination of SEM, optical microscopy and AFM was employed to analyse the coffee ring effect on the printed catalyst. These findings add new knowledge base for

accurate modelling of the deposition process in the future and confirm that VA-CNTs can be grown from a range of catalyst materials and thicknesses.

The chapter establishes a thorough investigation into the effects of varying printing parameters, substrate interactions and ink concentration. However, it is necessary to optimise these conditions on an industrial scale printhead. Therefore, this chapter as described earlier in Chapter 1 only fulfils the feasibility stage of the development phase. Additional analysis using *in situ* EELS, XRD, XPS, SIMS or ETEM technologies could be incorporated into the manufacture assembly line as a verification tool set. However, these developments are beyond the scope of this research. After specifying the assistive CVD technique and determining the feasibility of using inkjet printing as an additive technique, the next phase of research will analyse the feasibility of using ultrafast laser patterning as a subtractive patterning technique.

Chapter 4

LASER PATTERNING – SUBTRACTIVE MANUFACTURE

Recent trends in research into the development of scalable micro/nano-patterning focus on bringing nanotechnology closer to market, by developing economically sustainable, industrially reliable, and scalable nano-devices [5]. CNTs can be grown by locally depositing catalyst on a substrate using a laser and a catalyst source target [30]. However, laser assisted deposition systems are quite complex requiring in some cases high vacuum or gas environments, multiple masking steps, and are usually carried out at high temperatures, and thus not suitable for scale-up [54]. Therefore, in the previous chapter we explored the feasibility of using inkjet printing for depositing catalyst as it can be operated at room temperature, is scalable, and compatible with deposition of multiple functional materials to create complex devices. However, some VA-CNT applications require very complex structures with small feature sizes. Therefore, subtractive techniques are required to achieve these structures. VA-CNTs can be patterned using two strategies: direct patterning of the catalyst / substrate or direct patterning of the VA-CNT forest [85]. Techniques such as photolithography and e-beam lithography have been studied extensively for the direct patterning of catalyst, and laser irradiation for the direct patterning of VA-CNT arrays [121]. Laser irradiation of VA-CNTs can damage the structures of the surrounding CNTs and is difficult to scale-up due to the requirement of complex ventilation systems, as the effect of CNT inhalation is still not fully understood [253], [254] Consequently, laser patterning of catalyst films before growth is more suitable, especially on account of a consistently increasing interest from industries in developing laser ablation

techniques as a micro and nano manufacturing process [51]. Therefore, after the successful growth of VA-CNTs using inkjet printing as an additive technique, the research in this chapter examines the feasibility of using laser ablation as a subtractive technique for post deposition patterning of catalyst to achieve sub-micron scale VA-CNT structures [1], [2].

One example of an industrial combination of inkjet printing and laser processing is found in the M-SOLV MSV200 series machine described by Brunton and Crozier (2018) for the production of large area electronics [125]. The system uses three Fujifilm Dimatix Starfire printheads, a 355nm UV laser pulse galvanometer and scanner, allowing trimming of features down to 15 μm, and a UV lamp for curing [125]. The use of a precise multilayer selective ablation scheme known as SPLA-DAT has also been reported as a tool combining inkjet printing and laser patterning as a hybrid fabrication tool for patterning multiple materials for large-area printed application [128]. As this route already shows industrial promise, a similar approach is discussed in this chapter for patterning of catalyst for VA-CNT growth. The quality, rate and mechanism of ablation is dependent on the laser pulse width, repetition rate, wavelength, irradiance and fluence [255]–[257]. Femtosecond laser treatment of thin film iron catalyst during the CVD process has been researched and shown to improve CNT growth [254], [258]. However, the effects of femtosecond laser treatment in manufacturing are rarely studied at a more fundamental level, and this is true also for iron oxide nanoparticle films acting as a catalyst for VA-CNT growth. Therefore, this chapter explores the feasibility of scalable femtosecond laser patterning of magnetite catalyst for the growth of VA-CNT structures. The chapter has three main objectives:

- To study the heat affect zone (HAZ) for the ultrafast laser by benchmarking the effects of varying laser fluence and the distance between laser paths (pitch) on e-beam deposited catalyst

- To determine the constant and variable parameters to be studied when patterning inkjet printed catalyst from observations when patterning e-beam deposited catalyst.
- To investigate the effect of varying selected laser parameters on inkjet printed catalyst.
- To quantify the effects of laser patterning on the catalyst by studying the catalyst nano-islands formed post annealing and subsequent CNT forest growth.

4.1 Theoretical Section

Laser milling is now being used to pattern an array of materials such as metals, plastics, ceramics and glass [259]. Laser ablation can be used for chemical and physical modification of surfaces, but the laser plasma surface interactions responsible for these modifications are complex and not fully understood [260]. The laser ablation regime is dependent on the laser parameters selected such as; pulse duration, fluence, wavelength, repetition rate [8], [255] During laser processing, a sequence of pulses with a determined pulse length and repetition rate are delivered to a workpiece, allowing energy to be delivered in short time intervals [261]. The energy density in a given area (also known as fluence), can be controlled by focusing the laser beam on a spot [261]. The material and laser interaction in this spot can be defined by three different regimes, femtosecond, picosecond and nanosecond [262].

Ultrashort or femtosecond lasers have been most actively studied in recent years as they provide flexible, simple and precise laser ablation thresholds, at reduced laser energy densities on multiple substrates [257], [263]. Vorobyev and Guo (2013) review some of the latest developments in femtosecond laser nano/micro structuring applications, and illustrate the ablation mechanism as shown in Figure 55 [264]. Thermal effects are minimised with ultrashort and femtosecond lasers as the pulse duration is much shorter than the time

required for energy to be transferred into the substrate as heat [19], [265] This reduction in thermal diffusion into the surrounding material allows for lower ablation thresholds, reduction in molten material and negligible heat affected zones, giving more reproducible ablation in comparison to nanosecond lasers [266]. The ablation process is a direct solid-to-vapour transition with fluence controlled in the range 10^3 - 10^6 J/cm^3 [8], [261].

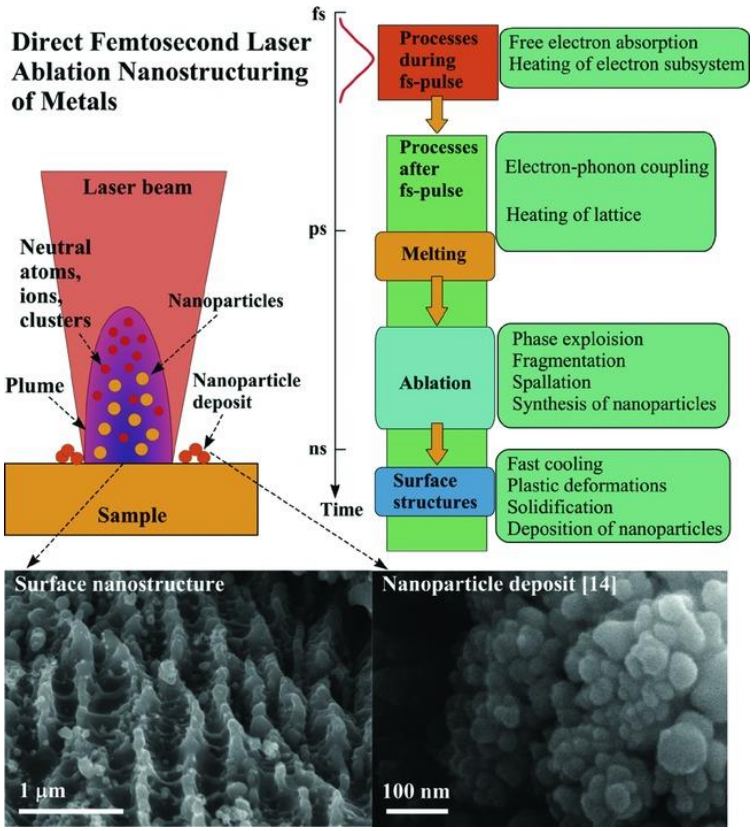

Figure 55*: Femtosecond laser ablation nano-structuring of metals as illustrated by Vorobyev and Guo (2013)* [264].

Pereira *et al.* (2004) demonstrated that when patterning low carbon steel surfaces with a femtosecond laser, an increase in fluence results in an increase in thermal impact to the surface, such that nanoclusters are formed around the ablated region due to backward deposition [260]. Lee *et al.* (2008) and Zhu *et al.* (2012) also reported laser fluence to have a direct effect on the ablation rate and behaviour, evidenced by the formation of fine particles ejected as molten material around the laser spot at high fluence [255], [267]. The

size of the nanoparticles generated can be controlled by varying the laser fluence [260]. Semaltianos *et al.* (2008) reported that when patterning a silicon substrate with a femtosecond laser, nanoparticles are ejected [268]. The size of the nanoparticles ejected increases from 70 nm to 500 nm when increasing laser fluence between 0.25 J/cm^2 to 4.38 J/cm^2 [268]. However, with a further increase of fluence the size of the nanoparticles begins to reduce, eventually settling at 170 nm at a fluence of 8 J/cm^2 [268]. Figure 56 shows irradiation at varying fluence as presented by Lee *et al.* (2008). It can be seen in the image that as fluence is increased, material ejection and re-deposition also increases. Research by Matsumura *et al* (2005) defines the debris around the laser spot as having a *"cotton-like appearance"* [269].

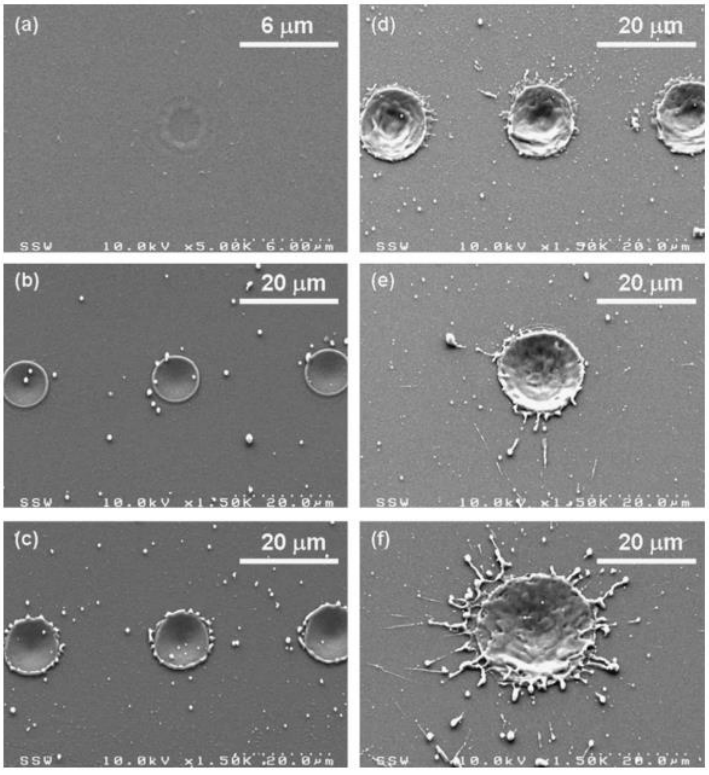

Figure 56*: SEM micrographs of ablation craters created by single shots of a 775 nm Ti: Sapphire, 150 fs laser operated at a repetition rate of 1 kHz at increasing laser fluence of* ***a)*** *0.63 J/cm², **b)** 3.3 J/cm², **c)** 12.5 J/cm², **d)** 25 J/cm², **e)** 125 J/cm² and **f)** 250 J/cm² on a silicon substrate* [267].

When thin films are irradiated by a Gaussian spacial intensity distribution, a ring pattern is generally observed known as spatial self-phase modulation [270]. Femtosecond lasers have

a Gaussian beam profile and are expected to produce cone like ablation profiles [255], [271]. The cone like shape of the Gaussian profile means that a single laser pulse has different regions of interaction with the substrate defined as modification, annealing and ablation [256]. This interaction defined by Bonse *et al.* (2002) can be seen in Figure 57. Varying morphological phenomenon are observed by Bonse *et al.* (2002) when varying laser fluence such as oxidation, amorphization, re-crystallisation, formation of bubbles and ablation [256], [271], [272]. On account of the circular Gaussian laser spot, any debris ablated during femtosecond laser ablation is deposited in circular patterns around the laser spot [268]. Femtosecond laser interactions with thin films are still not fully understood. However, Schrider (2017) in his doctoral thesis explores laser interactions with ultrathin metal films, including iron as catalyst for CNT growth [254]. His findings showed that femtosecond laser irradiation enhanced growth of CNTs in poor CVD growth conditions, indicating an increase in the area density of the active catalyst. However, this technique falls under laser-assisted CVD growth and does not analyse catalyst nano-island formation during growth. The use of femtosecond lasers as a catalyst patterning technique, before CVD growth, has not been widely explored. Rouleau *et al* (2014) demonstrated the use of femtosecond lasers for ablation of iron and molybdenum thin film bilayers, for the localised generation of nanoparticles of size 10 nm to 200 nm, for CNT growth [273]. The size and shape of these nanoparticles can be controlled by varying the laser ablation energy [268]. Gaussian beam profiles are expected to produce a bimodal particle size distribution of nanoparticles ejected [274].

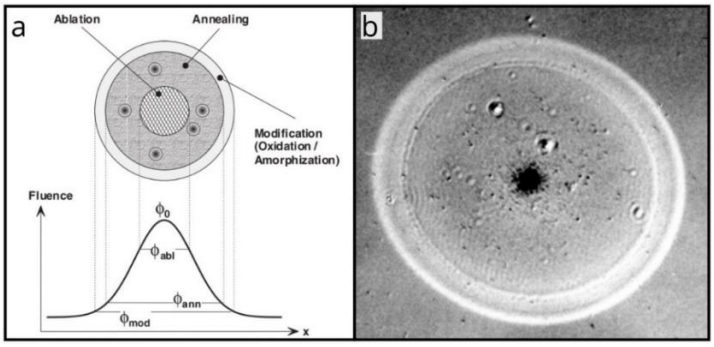

Figure 57: a) *Schematic showing physical processes during modification of silicon with femtosecond laser pulses and their threshold frequency.* ***b)*** *Optical micrograph of sample silicon surface irradiated with single pulse in air with an 800 nm, 130 fs laser at fluence 1.5 J/cm²* [256].

The literature presented evidence of the complex interactions between femtosecond Gaussian beams and the solid substrate on account of re-deposition and melting at higher fluence values. Femtosecond patterning of catalyst for VA-CNT growth has only been conducted during CVD growth as an assistive technique. Atmospheric femtosecond laser treatment of catalyst has successfully resulted in improved growth of CNT mats [254]. However, focused femtosecond patterning of iron oxide nanoparticles as a catalyst has not been explored. The effects of femtosecond patterning of catalyst on VA-CNT growth are also yet to be fully explored. Therefore, in the experiments to follow it is essential to determine whether femtosecond laser patterning of iron oxide nanoparticle films is feasible for growing patterning VA-CNTs. As fluence is the major parameter in determining nanoparticle redistribution, patterning will need to explore varying laser fluence, and the effects around the laser spot analysed via SEM and AFM. Laser patterning of PVD deposited iron films and inkjet printed iron oxide nanoparticle films will be conducted to understand how the two sources of catalyst respond to varying fluence values.

4.2 Experimental Methodology

This section describes the equipment and experimental procedures used. Silicon and fused silica wafers of diameter 100 mm and thickness 500 µm were procured from University

Wafers. All alumina was deposited using an e-beam deposition system, procedure as detailed in Chapter 2. Based on the findings in Chapter 3 an ink concentration of 2.19 $\%_{w/w}$ iron oxide nanoparticles was deposited on the wafers at droplet spacings between 5 µm – 60 µm. The CVD growth conditions are reported in Chapter 2. The catalyst was analysed using optical microscopy, AFM and SEM, details of which can be found in Chapter 2 and Chapter 3.

4.2.1 Laser Patterning

The Satsuma femtosecond laser by Amplitude Systems was used for the laser processing. The system consists of an ultrafast seed oscillator which generates ultrashort pulses at a frequency of a few MHz and a pulse picker used to select pulses that enter the amplification stage, which are then pumped by a diode system. The laser has a reported pulse width of 280 fs, a wavelength of 1030 nm and a maximum repetitive rate of 500 kHz. The gain medium for the amplification stage is an ytterbium-doped photonic crystal fibre. The repetition rate is reduced in integers to achieve lower frequency without having an effect on the energy pulse. The laser patterning protocol (start-up, alignment, validation procedures) was developed by Jason Ten, Industrial Photonics Group, Department of Engineering, at the University of Cambridge. The main parameters explored in laser patterning experiments include (Figure 58)

- **Pulse spacing:** the distance between consecutive laser spots when patterning a line across the substrate.
- **Path Pitch:** the distance between individual laser lines patterned.
- **Fluence:** amount of pulse energy delivered per unit area.

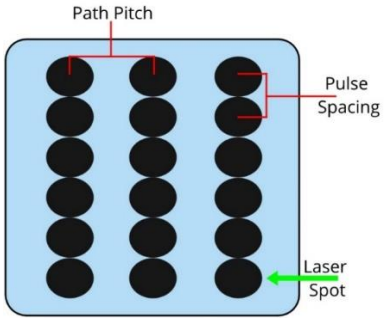

Figure 58: *Schematic illustrating laser path pitch and pulse spacing.*

4.2.1.1 Alignment, Focal Point and Power Readings

The laser set-up is split in two sections as shown in Figure 59 showing the laser optics set-up. The optics set-up consists of a beam expander to increase the beam diameter of the Satsuma laser in order to reduce the final focal spot. Laser alignment through the beam expander is achieved by mounting it on an adjustable horizontal and vertical stage. An attenuation wheel is also placed to control laser energy, alignment through which is adjusted using a tip/tilt mirror. A visual inspection is carried out with an IR card and an IR camera to ensure beam alignment and position. All the optics are cleaned with a hand-held camera air duster. The focal point of the laser is adjusted by switching on the laser and adjusting the Z stage and focusing the spot size on a glass slide. The focal point is found when the laser spot viewed in the camera is smallest. The Dino microscope is used for inspection instead of the camera as it has a higher resolution.

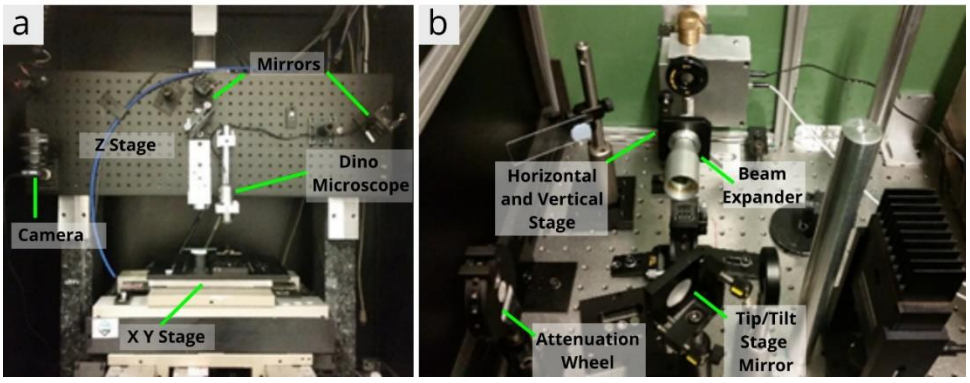

Figure 59: *Images Showing Satsuma Laser Optics*

The laser power for a set repetition rate can be varied using the modulation efficiency. The modulation efficiency is increased in integers to increase the power. The power readings were measured using a coherent fieldmaster thermal power meter for values between 30 mW - 2000 mW, and a S120C Thorlabs photodiode capable for values between 0.01 mW - 50 mW. Over the course of the research, servicing and other alterations to the Satsuma setup were expected to cause very minor changes to the transmitted power at each modulation efficiency. Therefore, power measurements were regularly taken and the fluence values calculated can be referred to in Table D 1. Spot size and power transmittance calculations for the satsuma ultrafast laser can be seen in Table 5. A minimum spot radius of 2.1 ± 0.1 µm was calculated.

Table 5: *Ultrafast laser Satsuma input parameters and calculated parameters.*

Input Parameters	**Satsuma**
Pulse Duration ***(fs)***	280
Wavelength ***(nm)***	1030
Pulse Repetition Rate ***(kHz)***	1
Raw Beam Radius ***(mm)***	2.2
Laser Beam Quality Factor M^2	1.1
Focal Length ***(mm)***	12.7
Calculated Parameters	
Minimum Spot Radius ***(µm)***	2.1
Area ***(cm²)***	1.36E-07
Transmission of Comar Lens	
Before Objective ***(mW)***	154
After Objective ***(mW)***	133
Transmission	86%

4.2.1.2 Stage Movement and Control

The substrates are mounted on a high precision linear air bearing XY stage by Aerotech with a maximum range of motion 200 x 200 mm. The stage can be driven at a maximum speed of 300 mm/s, with a resolution of 20 nm, and an overall accuracy of ±3 µm. The Z

stage is also provided by Aerotech with a maximum speed of 100 mm/s and accuracy ±5 µm. The stage is controlled by converting 2D drawings or 3D CAD into g-code. Inkscape was used for creating and converting 2D images into g-code. Although complicated patterns can be achieved using g-code generating software, for the results presented in this chapter, simple lines were patterned across the catalyst for simplicity and ease of processing.

4.3 Results and Discussion

As laser ablation has not been previously used to pattern inkjet printed nanoparticle films as catalyst for VA-CNT growth, this chapter investigates the effect of varying the amount of energy delivered during patterning, and its subsequent effect on catalyst redeposition and VA-CNT growth. The research questions have been answered by laser patterning **1)** e-beam deposited iron thin films and **2)** inkjet printed nanoparticles as catalyst on 10ASW substrates, and studying the effects via analysis of VA-CNT growth and catalyst nano-island agglomeration. As identified in the literature in section 4.1, the HAZ can cause changes in the catalyst surrounding a Gaussian beam spot at high fluence values. The satsuma ultrafast laser setup used is a customised system with a Gaussian laser beam profile, making it essential to investigate whether a HAZ exists, its impact on the catalyst and how it can be minimised. Therefore, when patterning e-beam deposited catalyst, two laser parameters were varied: ***fluence*** and ***pitch*** (defined in section 4.2). From the experiments a suitable pitch will be selected and kept constant for experiments on inkjet printed catalyst so that ablation effects can be studied in more detail. When patterning inkjet deposited catalyst source two parameters were varied: ***inkjet droplet spacing*** (defined in Chapter 3) and ***laser fluence*** (defined in section 4.2).

4.2.1 Laser Patterning of E-Beam Deposited Catalyst

This section presents the results from experiments on e-beam deposited catalyst. The experiments in this chapter were conducted in collaboration with Jason Ten, who helped train and provide guidance for the initial equipment set-up and laser patterning methodology.

4.2.1.1 Varying Laser Pitch

The first set of experiments focus on varying the pitch. Due to the Gaussian beam, there is expected to be a threshold pitch, beyond which the catalyst surrounding the laser spot is subjected to HAZ effects. The patterning parameters can be seen in Table 6. Sets of ten lines were patterned at varying pitch and constant fluence. The ablation threshold for the substrate was determined to be 0.39 J/cm^2. The Satsuma laser power is varied using the modulation efficiency, described in section 4.2.1, and was used to set a slightly higher fluence of 0.52 J/cm^2 than the ablation threshold.

Table 6: *Laser patterning parameters for experiments varying pitch*

Parameter	**Constant Parameters**	**Variable Parameters**
Pulse Repetition Rate ***(kHz)***	0.5	-
Processing Speed ***(mm/s)***	3	-
Pulse Spacing ***(µm)***	3	-
Fluence ***(J/cm²)***	0.52	-
Pitch ***(µm)***	-	2, 3, 4, 5, 6, 7, 10, 20

Optical micrographs of the sets patterned at a selection of pitch variations can be seen in Figure 60. As the laser spot size is measured to have a 3 µm diameter, at a pitch of 2 µm, the lines are seen to overlap with the first visible gap noticeable between the lines when patterning at a pitch of 4 µm. Upon CVD growth, SEM micrographs in Figure 61 show the effects of varying pitch on VA-CNT growth. As the laser spot diameter is approximately 3 µm, SEM analysis between laser paths post CVD growth reveals no VA-CNT forest growth

resulting from an overlap of laser paths at a pitch of 2 µm (Figure 61.a.i and ii). When patterning at a laser path pitch of 3 µm, SEM analysis in Figure 61.b.i and ii reveals a short carpet growth between the lines. As the spacing is increased further to 4 µm, VA- CNTs are achieved albeit of a shorter height than the surrounding forest as shown in Figure 61.c. As pitch is increased to 5 µm, sheets of VA-CNTs matching the height of the bulk forest are grown between the laser paths as shown in Figure 61.d. However, the VA-CNTs cannot support each other resulting in bending of the structures. With further increase in pitch to 6 µm and 7 µm, the bending of the forest is improved as shown in Figure 61.e and f.

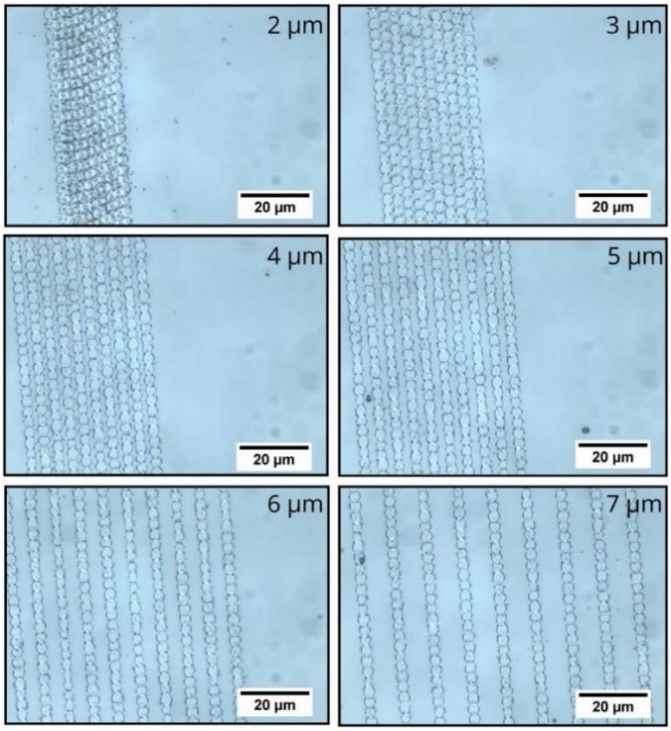

Figure 60: *Optical micrographs of lines laser patterned on e-beam deposited iron catalyst on 10ASW substrate at a fluence of 0.52/J/cm² and laser path pitch of 2 µm, 3 µm, 4 µm, 5 µm, 6 µm and 7 µm*

The results are indicative of a radial thermal effect around the focal spot, resulting in changes to the iron catalyst functionality. Although in femtosecond lasers the HAZ is reduced on account of short pulse durations minimising plasma build up, this is only true at lower fluence values. At higher fluence values debris surrounding laser ablated bulk iron and brass has been previously reported, owing to thermal effects and plasma backward deposition [266], [268], [275]. It has been postulated that the thermal effects are a result

of the femtosecond beam not having a Gaussian energy distribution at high fluence values, or by an inhomogeneous laser beam profile [18], [19]. Therefore, even though the laser processing is being carried out at the ablation threshold of the 1nm coated 10ASW substrate, the surrounding material can still undergo a rise in temperature due to the absorbed energy from the laser beam. This effect can be primarily described as an excessive annealing effect by the laser which is reduced by increasing the spacing between laser paths. As the gap between laser paths is increased, the thermal overlap of the laser spots is minimised, ensuring availability of catalyst for VA-CNT growth.

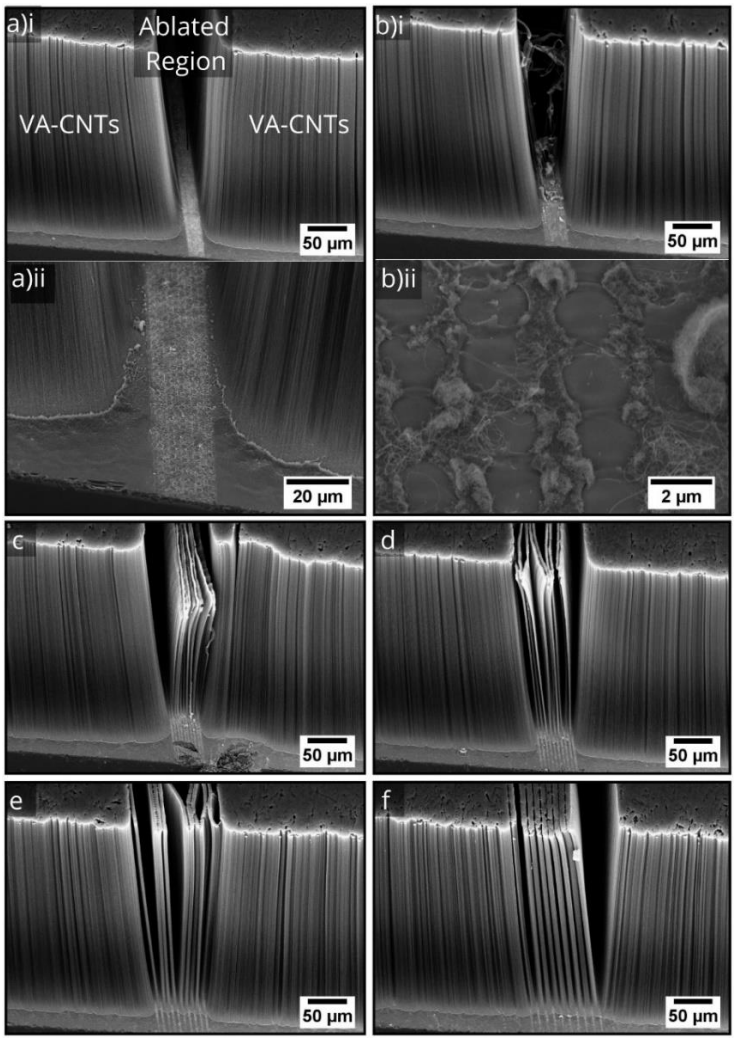

Figure 61: *SEM micrographs of VA-CNTs grown after patterning lines on e-beam deposited iron catalyst on a 10ASW substrate, at a fluence of 0.52/J/cm² and laser path pitch* ***a) i*** *2 µm,* ***b) i*** *3 µm,* ***c)*** *4 µm,* ***d)*** *5 µm,* ***e)*** *6 µm and* ***f)*** *7 µm with higher magnification images shown for laser path pitch* ***a) ii)*** *2 µm and* ***b) ii)*** *3 µm.*

4.2.1.2 Varying Laser Fluence

After investigating the effects of varying the distance between laser paths, the effects of laser fluence on catalyst functionality were studied. Laser fluence can be varied using either the attenuation wheel or the pulse modulation efficiency that is incremented in single units as a percentage. The graph in Figure 62.a shows that when modulation efficiency is increased with the attenuation wheel set at position number 2, the fluence increases. Whereas, the graph in Figure 62.b shows that when the attenuation wheel number is increased for a constant modulation efficiency of 30%, the fluence decreases. Therefore, modulation efficiency can be used for larger incremental changes in fluence whereas the attenuation wheel can be used for smaller increments.

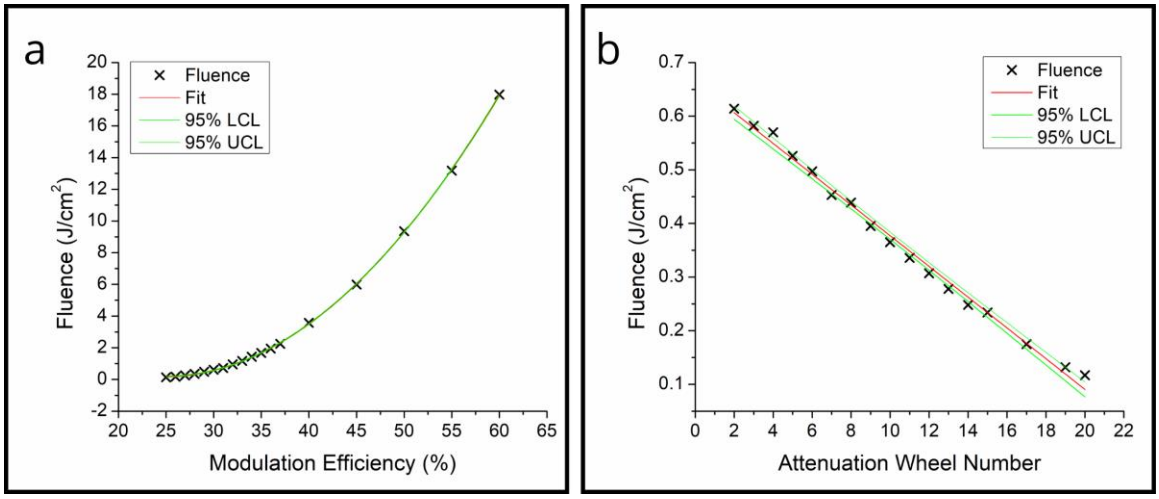

Figure 62: *Graphical representation of* ***a)*** *modulation efficiency (%) vs fluence (J/cm²) and* ***b)*** *attenuation wheel number vs fluence (J/cm²). The green lines represent a 95% CI of ± 0.05 J/cm² and ± 0.01 J/cm² respectively.*

- *Modulation Efficiency Varied, Attenuation Wheel Constant*

Modulation efficiency was first used to vary fluence between 0.52 and 3.43 J/cm^2 and the attenuation wheel was set at position number 2. The patterning parameters used can be seen in Table 7.

Table 7: *Laser patterning parameters for experiments varying laser fluence using modulation efficiency*

Parameter	**Constant Parameters**	**Variable Parameters**
Pulse Repetition Rate ***(kHz)***	1	-
Processing Speed ***(mm/s)***	3	-
Pulse Spacing ***(µm)***	3	-
Fluence ***(J/cm²)***	-	< 0.87 J/cm^2 Low Fluence (F_{low})
	-	0.87 J/cm^2 ≥ and ≤ 2.18 J/cm^2 Medium Fluence (F_{med})
	-	> 2.18 J/cm^2 High Fluence (F_{high})
Pitch ***(µm)***	10	-

Sets of ten lines were patterned at varying fluence and constant pitch. A pitch of 10 µm was selected to ensure enough gap between the laser spots was maintained, and effects of overlapping laser spots eliminated. A selection of optical micrographs in Figure 63 show that as fluence is increased, debris is observed surrounding the laser paths.

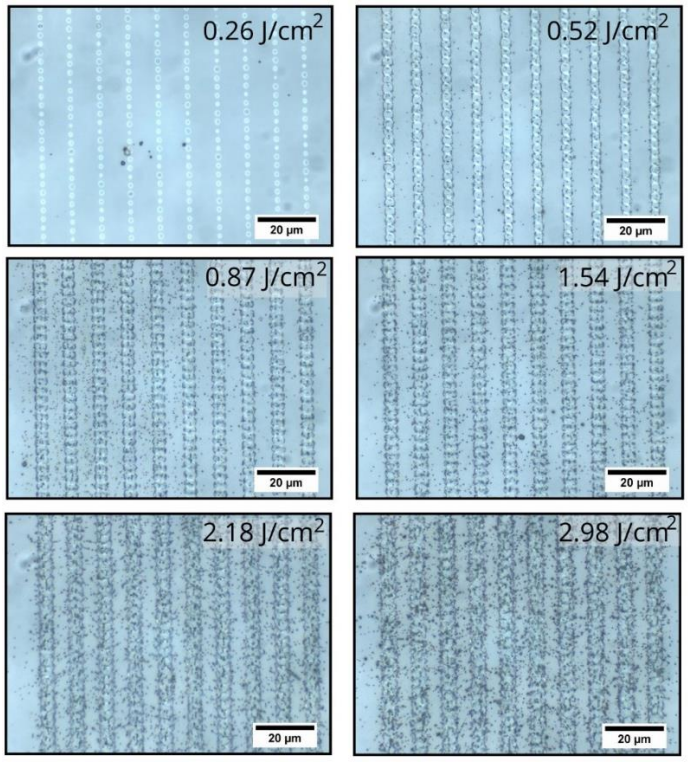

Figure 63: *Optical micrographs of lines laser patterned on e-beam deposited iron catalyst on 10ASW substrates at a constant pitch of 10 µm, attenuation wheel number 2 and varying fluence of 0.26 J/cm², 0.52 J/cm², 0.87 J/cm², 1.54 J/cm², 2.18 J/cm² and 2.98 J/cm².*

Samples patterned at fluence on the lower (1.28 J/cm^2) and higher (2.18 J/cm^2) boundary of F_{med} were selected and studied via SEM analysis. For lines patterned at the lower end of F_{med}, splitting and folding of the substrate surface is observed with sharp edges (Figure 64.a.i). However, as fluence is increased to the higher end of F_{med} (2.18 J/cm^2), the edges of the laser spot become less defined (Figure 64.a.ii). The rounded edges and reduced definition indicate melting as seen in Figure 64.a.ii. Globular particles around the laser spot indicate redeposition and melting of the substrate. The debris and redeposited material surrounding the laser patterned region appears minimised when the substrates are cleaned via sonication in IPA as shown in Figure 64.b.i and ii comparing before and after cleaning results. However, catalyst re-deposition is not the only factor affecting catalyst functionality. Melting in the laser spots indicates increased thermal effects that can affect the surrounding catalyst.

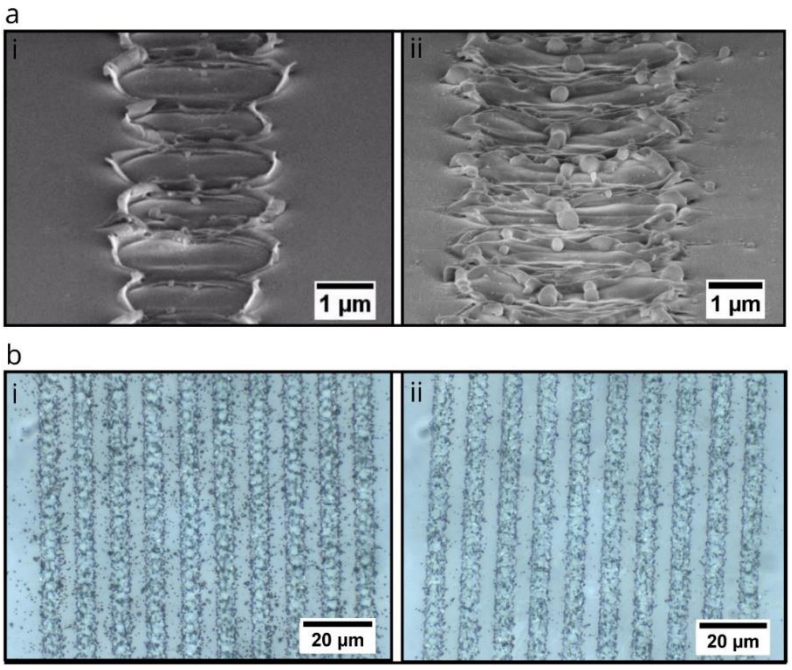

Figure 64: a) *SEM micrographs of laser spots when patterning e-beam deposited iron catalyst on a 10ASW substrate at a laser path pitch of 10 µm, attenuation wheel number 2 and fluence i) 1.27 J/cm^2 and ii) 2.18 J/cm^2.* ***b)*** *Optical micrographs of e-beam iron deposited 10ASW substrate* ***i)*** *before and* ***ii)*** *after cleaning when patterned at a fluence of 3.43 J/cm^2*

Upon CVD growth, SEM analysis revealed that an increase in laser fluence reduces alignment and height of the CNT forest, as shown in Figure 65. SEM micrographs of VA-CNT sheets with uniform height and alignment grown between lines patterned at F_{low} can be seen in Figure 65.a and b. However, as fluence is increased the height of the VA-CNTs grown between the laser paths decreases in comparison to the height of the surrounding bulk CNT forest grown on untreated catalyst seen in Figure 65.b. When patterning at $F_{med,}$ the SEM micrographs seen in Figure 65.c, d, e and f reveal that, although sporadic and dispersed, growth of non-uniform VA-CNTs can be observed in some sections of the patterned region. As a result, the fluence range is unsuitable for patterning VA-CNT structures. Increasing fluence within this range results in the reduction of any CNT growth with no growth observed when patterning at F_{high}.

Detailed SEM micrographs of the area between the laser paths for samples patterned at fluence on the lower (1.27 J/cm^2) and higher (2.18 J/cm^2) boundary of F_{med} can be seen in Figure 65.g and h. It is evident that for the lower boundary values, a CNT carpet can be observed between the laser paths (Figure 65.g). However, as fluence is increased towards the higher boundary, no carpet growth is visible apart from a few localised strands of CNTs between the laser paths (Figure 65.h). An increased number of spherical particles are observed between the laser paths shown in Figure 65.h and are probably redeposited particles not removed during cleaning. Re-deposition of catalyst can alter the particle density of the region, affecting CNT growth. However, before embarking on a detailed study into the effects of varying laser fluence on catalyst nano-island formation during annealing, a second set of experiments was conducted by varying the laser fluence with smaller increments using the attenuation wheel to determine a finer range of fluence values suitable for patterning VA-CNT structures.

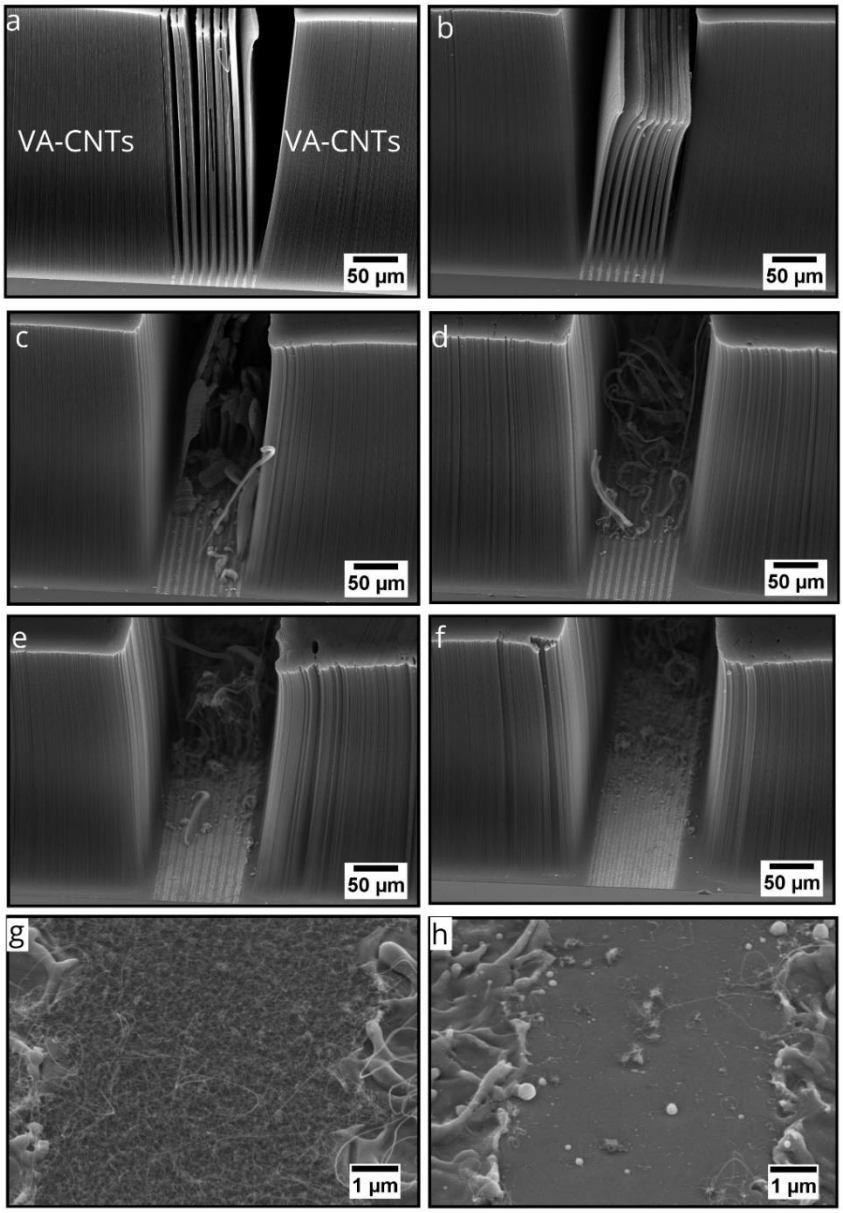

Figure 65: *SEM micrographs showing CVD Growth of laser patterned e-beam deposited 10ASW substrate at a laser path pitch of 10 µm, attenuation wheel number 2 and fluence of* ***a)*** *0.52 J/cm², **b)** 0.68 J/cm², **c)** 0.87 J/cm², **d)** 1.27 J/cm², **e)** 1.85 J/cm² and **f)** 2.18 J/cm² varied using modulation efficiency. Higher magnification SEM of region between laser paths for lines printed fluence **g)** 1.27 J/cm² and **h)** 2.18 J/cm².*

- *Attenuation Wheel Varied, Modulation Efficiency Constant*

From the growth results presented in Figure 65, laser patterning in fluence range F_{low} (<0.87 J/cm^2) is suitable for achieving uniform VA-CNT structures. A fluence of 0.87 J/cm^2 was set with a modulation efficiency of 30% and attenuation wheel position 2. Variations in F_{low} were investigated by varying the attenuation wheel positions between 2 and 13. The

patterning parameters can be seen in Table 8. Sets of ten lines were patterned at varying fluence and constant pitch

Table 8: *Laser patterning parameters for experiments varying laser fluence using the attenuation wheel*

Parameter	**Constant Parameters**	**Variable Parameters**
Pulse Repetition Rate ***(kHz)***	1	-
Processing Speed ***(mm/s)***	3	-
Pulse Spacing ***(µm)***	3	-
Fluence ***(J/cm²)***	-	0.87, 0.85, 0.79, 0.74, 0.70, 0.65, 0.61, 0.57, 0.52, 0.48, 0.45
Pitch ***(µm)***	10	-

SEM analysis upon CVD growth of the patterned samples shown in Figure 66 revealed that VA-CNT structures can be patterned within a fluence range of 0.48 – 0.65 J/cm^2 Figure 66.b.c.d). This result is consonant with the results presented in Figure 65. It can be seen in Figure 66.e, that increasing the fluence beyond 0.65 J/cm^2, results in an initial reduction of the VA-CNT height in comparison to the bulk of the forest grown, then sporadic unaligned CNT growth and eventually no growth at a fluence of 0.87 J/cm^2. The results presented are evident that VA-CNT structures can be patterned with an ultrafast laser fluence between 0.48 – 0.65 J/cm^2, when patterning e-beam deposited iron catalyst. However, detailed analysis is necessary to understand the effects of the laser spot on the catalyst by analysing the ablation mechanism. Therefore, patterning of the iron coated 10ASW wafers was conducted at fluence below this range to understand ablation effects.

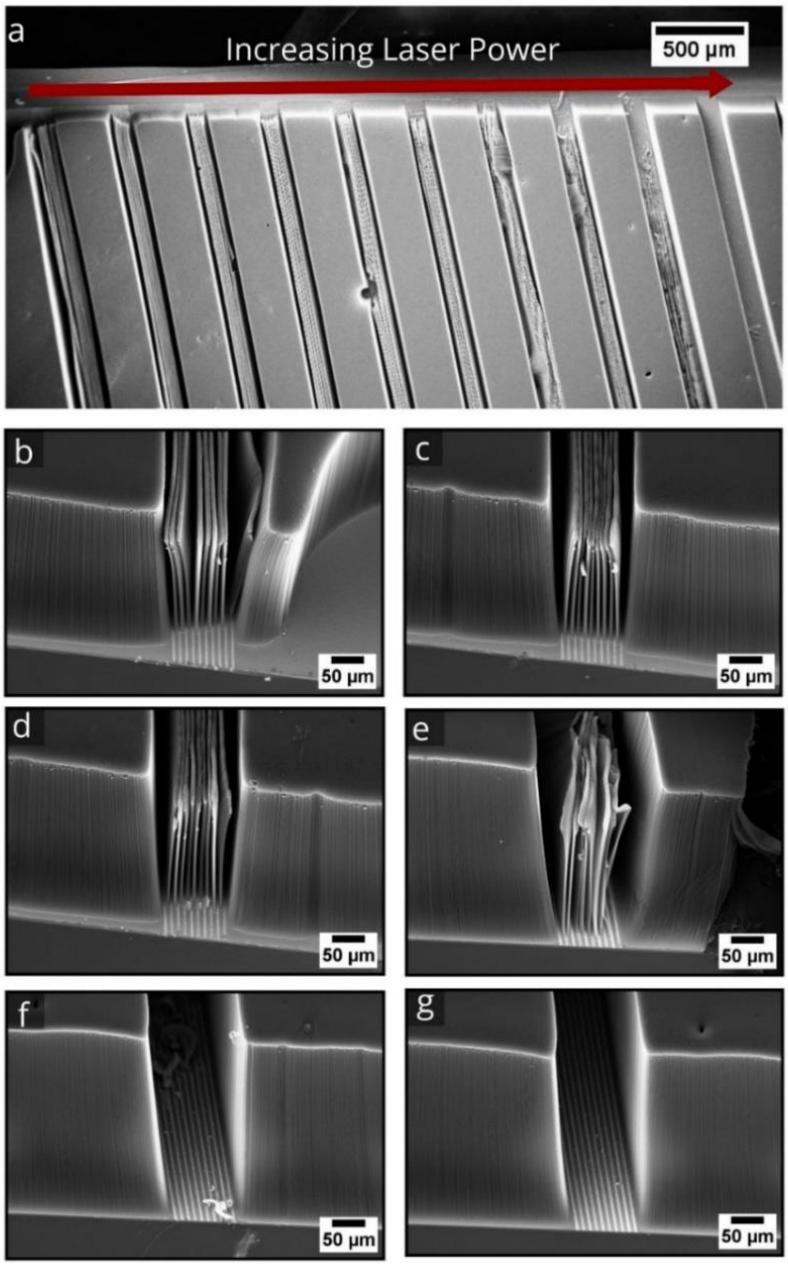

Figure 66: a) *SEM micrographs showing overall CVD Growth of laser patterned e-beam deposited 10ASW substrate at a laser path pitch of 10 µm and varying fluence using an attenuation wheel. Higher magnification SEM micrographs of CVD growth of patterned lines at a fluence of* ***b)*** *0.48 J/cm², **c)** 0.57 J/cm², **d)** 0.65 J/cm², **e)** 0.74 J/cm² **f)** 0.85 J/cm² and **g)** 0.87 J/cm².*

The laser patterning parameters can be seen in Table 9. Single pulse spots were patterned at varying fluence slightly below and above the ablation threshold by setting the modulation efficiency at 28 % and varying the attenuation wheel position between 13 and 19.

Table 9: *Laser patterning parameters for experiments varying laser fluence using attenuation wheel*

Parameter	**Constant Parameters**	**Variable Parameters**
Pulse Repetition Rate ***(kHz)***	1	-
Processing Speed ***(mm/s)***	3	-
Pulse Spacing ***(µm)***	3	-
Fluence ***(J/cm²)***	-	0.20, 0.23, 0.27, 0.30, 0.34, 0.37, 0.41, 0.45
Pitch ***(µm)***	10	

Representative optical micrographs of the patterned substrates can be seen in Figure 67 and the rest found in Figure D 1. It can be seen in Figure 67.a that when patterning at fluence significantly lower than the ablation threshold of 0.39 J/cm^2, no laser spots are visible. Although the first imprints of the laser spots are visible when patterning at fluence 0.27 J/cm^2, the laser spots are faint and dispersed. This indicates a variation in each laser pulse with the first uniform laser patterning optically visible when patterning at a fluence of 0.34 J/cm^2. The laser spot area also increases as the fluence is increased. Upon increasing beyond the ablation threshold, the optical micrographs of laser spots patterned at a fluence of 0.45 J/cm^2 show variations between the laser spots that are not distinguishable via optical microscopy, and so analysis via SEM is required.

SEM micrographs in Figure 68 show higher magnification images of the laser pulses patterned. The micrographs shown are evident of a Gaussian beam on account of the ring patterns visible around the laser spot in Figure 68.a. These patterns are typically observed when a thin non-linear substrate is illuminated by a Gaussian beam in a phenomenon known as spatial self-phase modulation, discussed earlier [270]. Although still not completely understood, these ring formations are generally thought to occur as a result of interference between the incident laser beam and surface scattered electromagnetic wave induced by the surface roughness of the substrate [271]. The modulation of the absorbed energy eventually results in selective ablation and formation of ripples around the laser spot. As fluence is

increased beyond the ablation threshold, splitting of the catalyst surface at the location of the laser pulse is observed on account of higher energy being delivered to the laser spot (Figure 68.a.iii and iv).

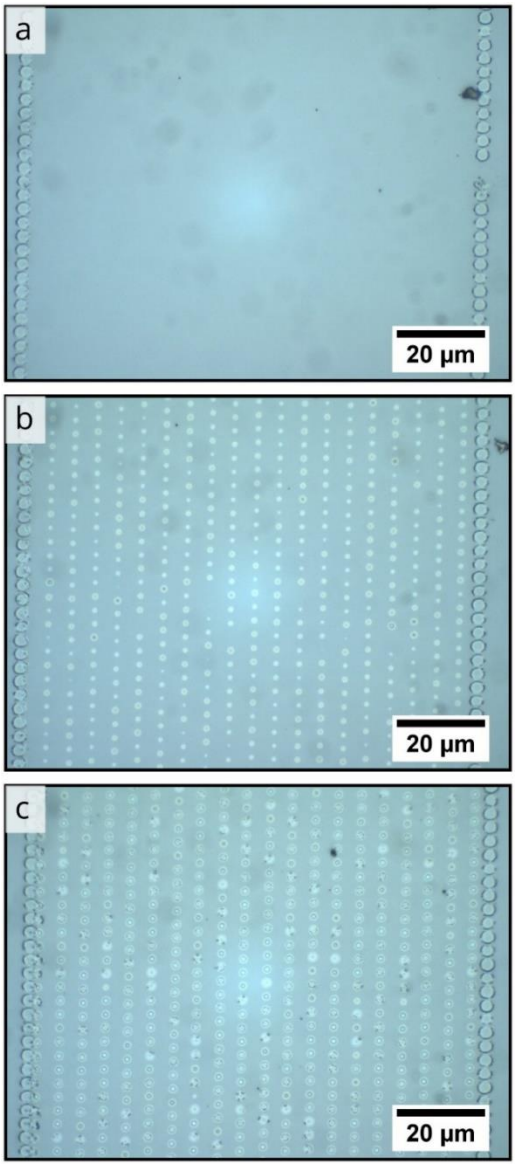

Figure 67: *Optical micrographs of 1 nm iron coated 10ASW substrates patterned at fluence* ***a)*** *0.23 J/cm², **b)** 0.34 J/cm² and **c)** 0.45 J/cm².*

The modification, annealing and ablation areas occurring in the laser spot on account of a higher energy being delivered are clearly visible in the crater of the laser spot patterned at fluence 0.37 J/cm^2, seen in Figure 68.b.i. As the laser intensity is increased, an increase in swelling under the surface of the laser target is observed in Figure 68.b.ii with eventual splitting of the surface visible in Figure 68.b.iii. This evidences that as fluence is increased,

a melt pool or plasma build up under the surface, attributed to a locally enhanced carrier density, causes saturation and overheating of the surface layer eventually leading to surface explosion. However, the non-ablation modifications for pulses patterned at higher laser fluence is not uniform where some laser spots show ablation and others show non-ablation modification as seen in Figure 68.a.iv. These differences in pulse effects can be explained by variation in substrate height and vibrations of the laser platform during processing.

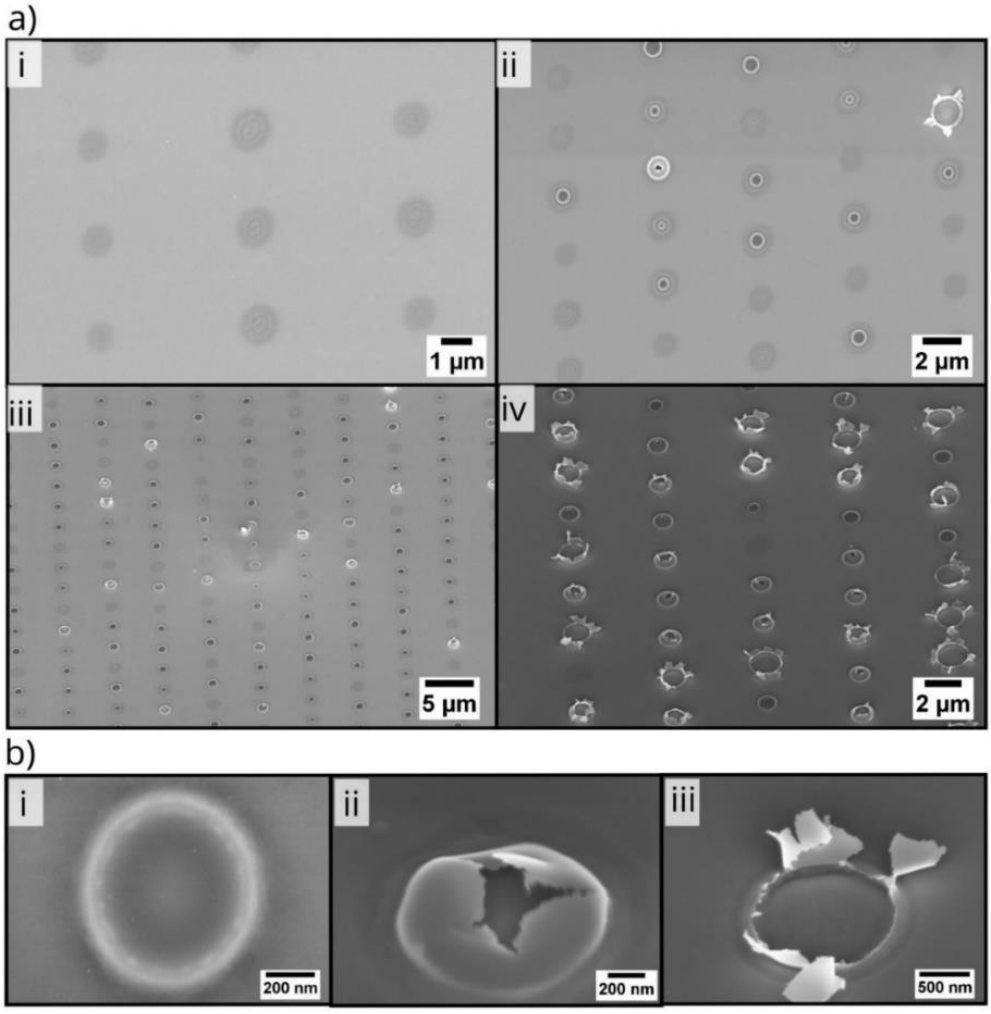

Figure 68: *a) SEM micrographs of pulses patterned at fluence* ***i)*** *0.34 J/cm², **ii)** 0.37 J/cm², **iii)** 0.41 J/cm² **iv)** 0.45 J/cm². SEM micrographs of the impact of the pulses patterned at increasing fluence of **i)** 0.37 J/cm², **ii)** 0.41 J/cm², **iii)** 0.45 J/cm² on the 1 nm iron coated 10ASW substrate.*

Upon subjection to CVD growth, no variation was observed between the heights of the VA-CNTs grown in the laser exposed area and the bulk CNT forest (Figure 69 and Figure D 2). However, when viewed from above, the effects of non-ablation modifications to the

catalyst can be observed in the micrographs shown in Figure 69 and Figure D 3. Spots on the surface of the VA-CNT are clearly visible indicating annealing changes to laser exposed surface. As the laser has an effective Gaussian beam profile, the presence of a HAZ is the most feasible explanation to describe the variation in VA-CNTs alignment and height between the laser paths, when patterning above the ablation threshold as shown earlier. It was discussed earlier in Chapter 2 that variation in catalyst nano-island size during the annealing phase of the CVD process can lead to different VA-CNT growth. Therefore, it is important to analyse laser affected catalyst post annealing and compare the size of the nano-islands formed when treated with varying laser fluence.

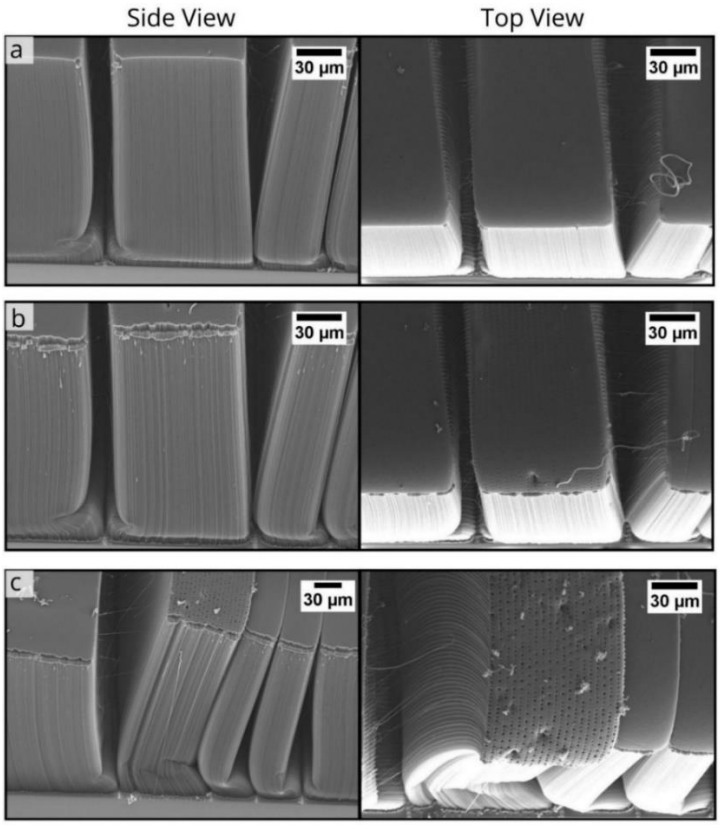

Figure 69: *SEM micrographs of VA-CNTs grown from 1 nm alumina coated 10ASW substrates laser patterned at fluence* ***a)*** *0.23 J/cm², **b)** 0.34 J/cm² and **c)** 0.45 J/cm².*

4.2.1.3 Analysis of Catalyst Nano-island Formation Post Annealing

Samples patterned at fluence values between 0.28 J/cm^2 and 3.43 J/cm^2 were annealed and the areas between the laser paths studied. Catalyst nano-island size cannot be studied via

SEM and a higher resolution technique is required such as AFM. Figure 70 shows a selection of AFM micrographs taken for samples patterned above the ablation threshold. Additional AFM graphs for this can be found in Figure D 4. It can be seen that as the fluence is increased the average height of the catalyst nano-islands between the laser paths also increases. An average particle height of 1.5 ± 0.1 nm was measured when no laser ablation was carried out, with a 12.4 ± 0.6 nm average height of post annealed nano-islands measured for the highest laser fluence of 3.43 J/cm^2

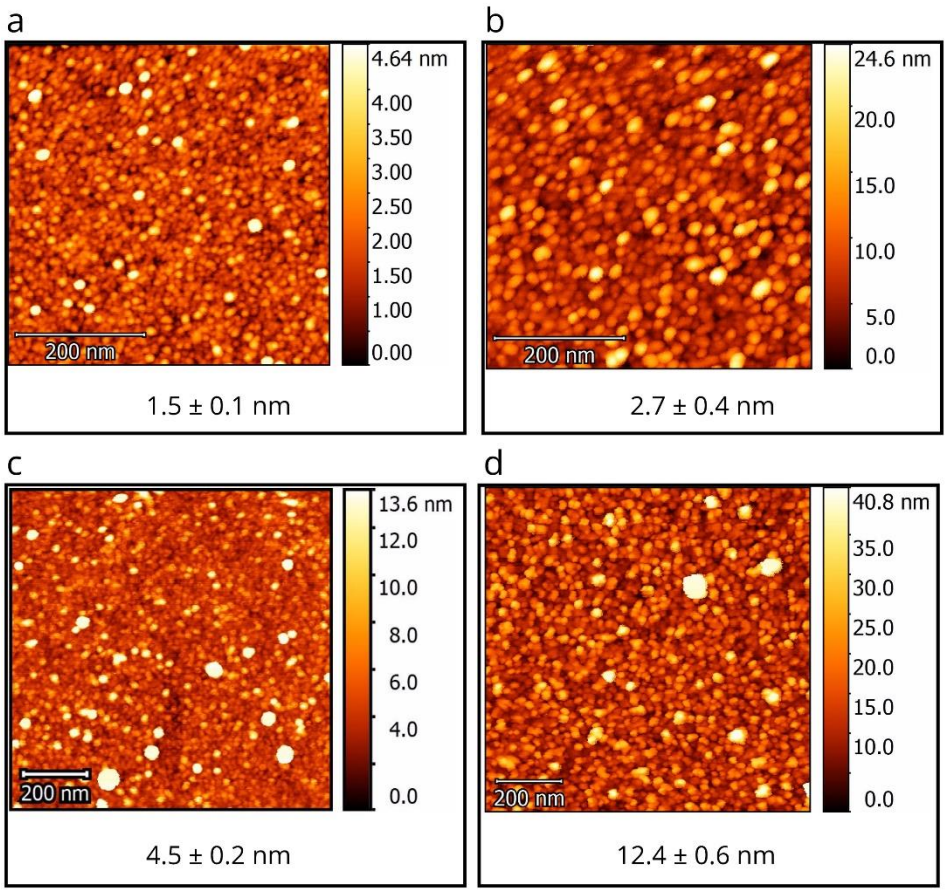

Figure 70: *AFM micrographs of annealed 1 nm iron coated 10ASW substrates a) without laser treatment and between laser paths patterned at fluence* ***b)*** *0.87 J/cm², **c)** 1.85 J/cm² and **d)** 3.43 J/cm². All errors represent the standard error calculated.*

The graph in Figure 71, shows that as fluence is increased, the average particle height of the nano-islands formed also increased. The degradation of forest height and alignment observed in the previous section when fluence is increased are a result of this increase in catalyst nano-island size. As the catalyst nano-island size is measured between laser paths

the AFM micrographs evidence changes to the catalyst. Redeposition and melting affects were observed around the laser spots in the optical micrographs previously shown. The larger nano-islands could be on account of the redeposited debris annealing into nano-islands of varying size, causing earlier growth termination, and a reduced forest height. As previously stated in Chapter 2, alignment is dependent on catalyst nano-island packing. The redeposited catalyst causes changes the catalyst layer morphology affecting nano-island formation during annealing. In addition to this, thermal effects of the Gaussian beam profile increase with a higher fluence, causing annealing of the catalyst surrounding the laser spot.

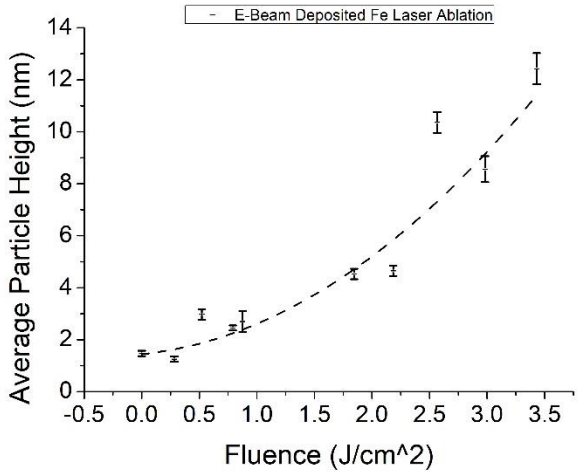

Figure 71: *Graphical representation of average particle height (nm) vs. laser fluence (J/cm²). The error bars indicate the standard error calculated.*

After understanding the effects of laser patterning on conventionally deposited catalyst, the findings can now be used to understand effects on laser patterned catalyst.

4.2.2 Laser Patterning of Inkjet Printed Catalyst

When patterning e-beam deposited catalyst it was found that the Gaussian beam profile of the ultrafast laser causes changes in the catalyst surrounding the laser spot as a result of catalyst redeposition and thermal effects. Therefore, in this section experiments are presented showing the effect of varying laser fluence on inkjet deposited nanoparticles. A

constant pitch of 10 µm will be maintained, as only fluence effects on the VA-CNT growth and catalyst nano-island formation are going to be studied for varying catalyst layer thickness.

4.2.2.1 Varying Laser Fluence and Droplet Spacing

Magnetite ink concentration 2.19 $\%_{w/w}$ (LIC) was printed on 600 s UV treated 10ASW at three droplet spacings 5µm, 45µm and 60µm. The films were laser patterned at varying fluence, using the modulation efficiency and the attenuation wheel set at position 2, at a constant pitch of 10 µm. Laser patterning parameters can be seen in Table 10

Table 10: *Laser patterning parameters for experiments varying laser fluence using modulation efficiency*

Parameter	**Constant Parameters**	**Variable Parameters**
Pulse Repetition Rate ***(kHz)***	1	-
Processing Speed ***(mm/s)***	3	-
Pulse Spacing ***(µm)***	3	-
Fluence ***(J/cm²)***	-	< 0.35 J/cm^2 Low Fluence (F_{low})
	-	0.35 J/cm^2 > and < 0.95 J/cm^2 Medium Fluences (F_{med})
	-	> 0.95 J/cm^2 High Fluence (F_{high})
Pitch ***(µm)***	10	-

A selection of optical micrographs of the printed ink patterned at representative fluence values 0.26 J/cm^2 (F_{low}), 0.73 J/cm^2 (F_{med}) and 1.68 J/cm^2 (F_{high}) can be seen in Figure 72 and show the increased definition of the patterned lines as fluence increases.

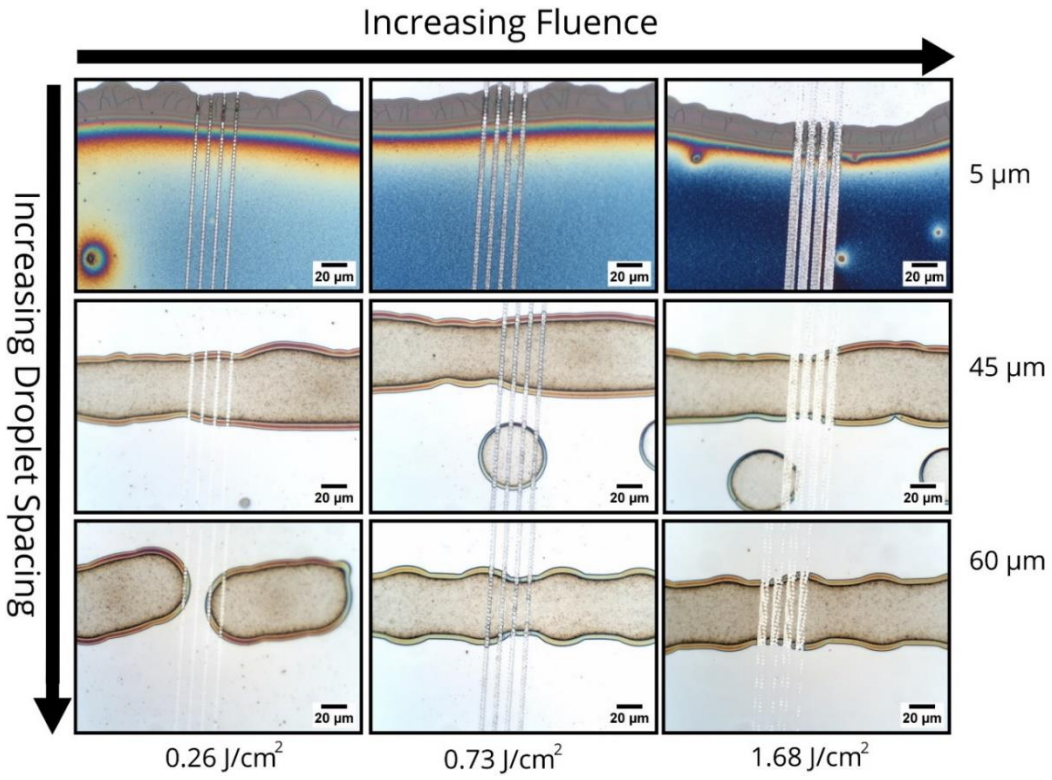

Figure 72: *Optical micrographs of inkjet printed magnetite ink concentration 2.19 %$_{w/w}$, on 10ASW substrates, laser patterned at fluence 0.26 J/cm², 0.73/Jcm² and 1.68J/cm².*

SEM micrographs of the patterned catalysts post CVD growth can be seen in Figure 73. Upon CVD growth, SEM micrographs of VA-CNTs grown between laser paths revealed that laser patterning of catalyst printed at droplet spacing 5 µm exhibited a unique behaviour, unlike previously observed for e-beam deposited catalyst. It can be seen in Figure 73, that when patterned at F_{high} range VA-CNTs with increased alignment and height were grown between the laser paths for catalyst deposited at a droplet spacing of 5 µm. On the other hand for catalyst printed at a droplet spacing of 45 µm, patterning at F_{high} range resulted in CNT forest height reduction and thinning at the base. The height degradation effects are even more accentuated for catalyst printed at droplet spacing 60 µm. When patterning ink printed at 5 µm droplet spacing at F_{med}, an improvement in the alignment and height of the CNTs grown was observed, but not as amplified as that observed when patterning at $F_{high.}$ For catalyst printed at 45 µm droplet spacing, patterning at F_{med} improved structural definition and reduced crust of the forest grown. The height of the

forest grown between the laser paths was concurrently maintained at the same height as that of the bulk forest. For catalyst printed at 60 µm droplet spacing, patterning at F_{med} improved the height of the forests grown between the laser paths in comparison to that observed when patterning at F_{high}. However, the overall height of the forest grown is observed to be shorter than that of the bulk forest. Patterning at F_{low} had no effect on ink printed at 5 µm droplet spacing. A ridged pattern, on account of the laser spots overlapping along the laser paths, was observed for VA-CNTs grown when patterning ink printed at 45 µm droplet spacing at F_{low}. For ink printed at 60 µm droplet spacing, the forest was patterned and sheets of VA-CNTs were observed between the laser paths.

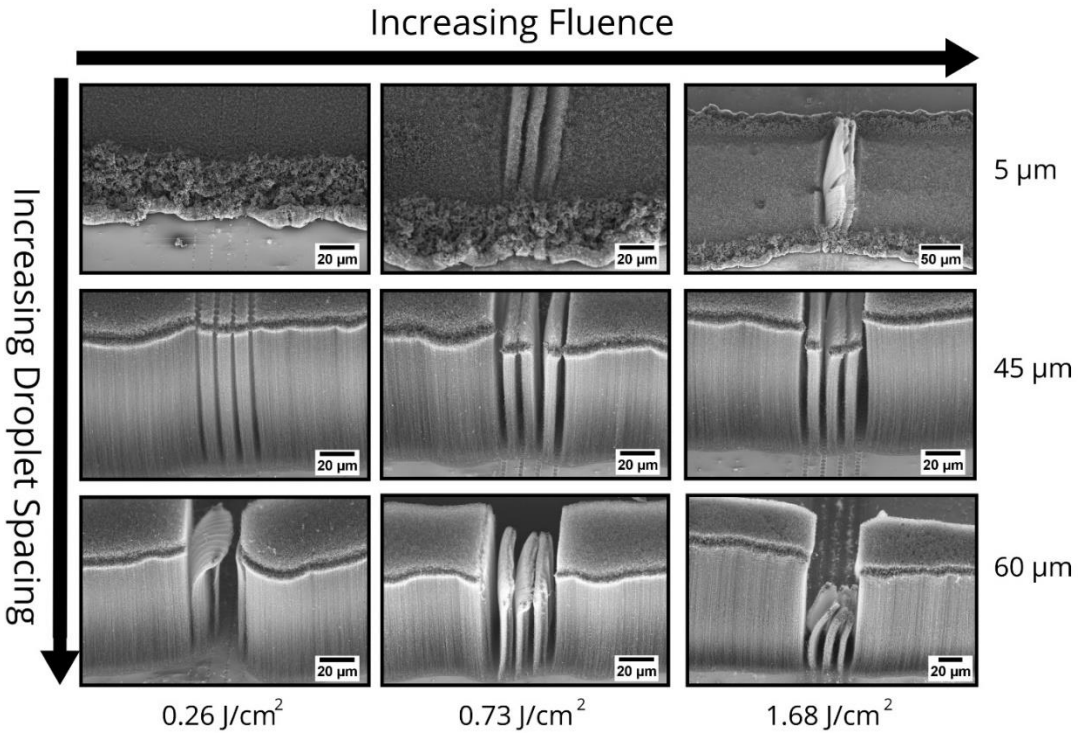

Figure 73: *SEM micrographs of VA-CNTs grown from inkjet printed magnetite ink concentration 2.19 %$_{w/w}$, on 10ASW substrates, laser patterned at fluence 0.26 J/cm², 0.73/Jcm² and 1.68J/cm².*

The results demonstrate that the effect of laser fluence is dependent on thickness of the catalyst layer. Patterning with high laser fluence values improves CNT height and alignment for thicker catalyst layers and degrades CNT height and alignment for thinner CNT layers. These effects can be explained by removal and redeposition of material around the laser spot having a thinning effect on the catalyst. As identified in Chapter 3, the printed

catalyst layers are thicker than e-beam deposited layer. However, the alignment and height degradation of the thinner printed catalyst layer is similar to that observed for e-beam deposited catalyst layer in section 4.2.1. Detailed analysis of the catalyst nano-islands formed during annealing is required to identify how the catalyst is changing for the thick and thin printed films resulting in contrary effects on VA-CNT growth, to test the hypothesis noted above.

4.2.2.2 Analysis of Catalyst Nano-Island Formation Post Annealing

VA-CNTs grown from LIC printed at 45 µm droplet spacing had the maximum forest height as identified in Chapter 3. VA-CNT forests from LIC printed at 5 µm droplet spacing gives a short forest and at 45 µm gives the highest forest (as identified earlier in Chapter 3). Therefore, samples with catalyst printed and patterned at these two droplet spacings have been selected for analysis via SEM. As discussed earlier un-sintered nanoparticle films have been reported to form disconnected tracks, allowing for thermal diffusion through the film and confinement of laser energy absorbed in the nanoparticles, causing agglomeration into larger particles upon melting, and thus affecting catalyst nucleation and particle size [22], [23]. Although there is a sufficient gap between the laser paths, effects on quality of VA-CNTs grown between the laser paths indicates a similar impact on nanoparticle films, as found for bulk material when patterning at higher femtosecond laser fluence. It can be seen in the SEM micrographs of annealed samples shown in Figure 74, that the debris surrounding the laser spots increases as fluence is increased.

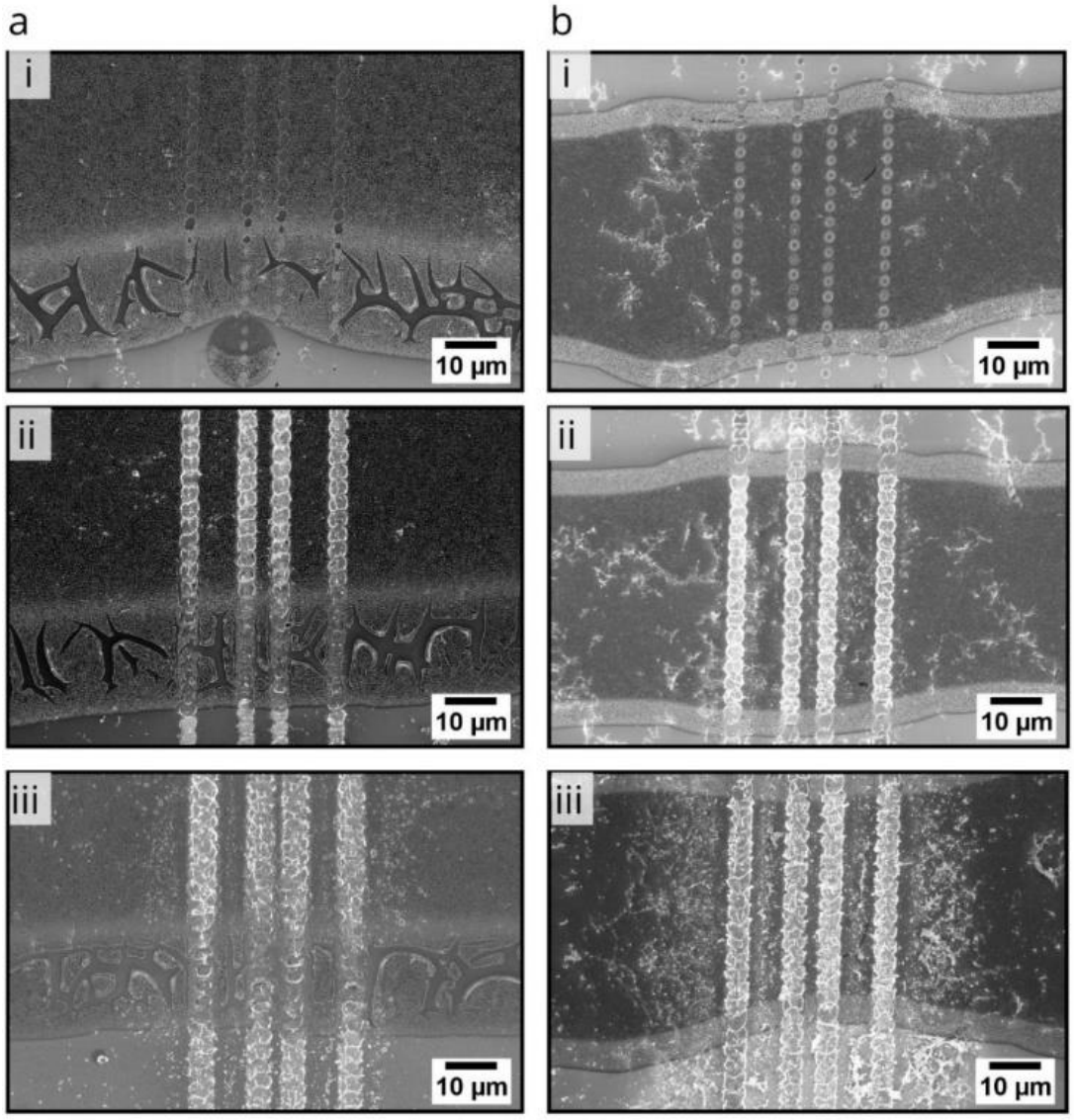

Figure 74: *SEM micrographs of annealed samples of inkjet printed magnetite ink concentration 2.19 $\%_{w/w}$, printed on 10ASW substrates at droplet spacings* ***a)*** *5 µm and* ***b)*** *45 µm and laser patterned at fluence* ***i)*** *0.26 J/cm², **ii)** 0.73/Jcm² and **iii)** 1.68J/cm².*

Magnified images of the laser spots can be seen in SEM micrographs shown in Figure 75. It can be seen in the micrographs that as fluence is increased, the size of the laser spot area also increases, with melting of the substrate observed. These results are similar to that observed when patterning PVD deposited catalyst film.

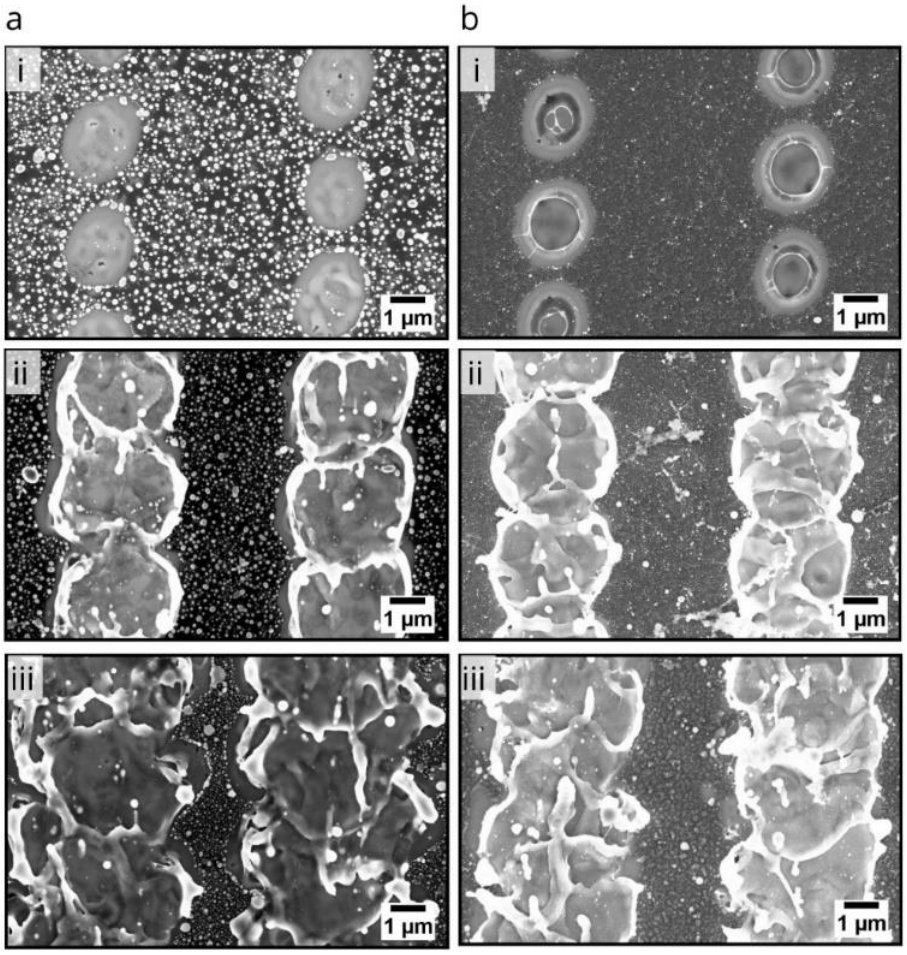

Figure 75: *SEM micrographs of laser spots when patterning inkjet printed magnetite ink concentration 2.19 $\%_{w/w}$, on 10ASW substrates at droplet spacings* ***a)*** *5 µm and* ***b)*** *45 µm, and patterning at fluence* ***i)*** *0.26 J/cm², **ii)** 0.73/Jcm² and **iii)** 1.68J/cm².*

As maximum variation in VA-CNT growth was observed when patterning at F_{high}, energy dispersive x-ray spectroscopy (EDX) was conducted between laser paths, comparing catalyst printed at 5 µm and 45 µm droplet spacing, before and after patterning at a fluence of 1.95 J/cm^2. EDX micrographs for catalyst printed at droplet spacing 5 µm, before and after laser patterning can be seen in Figure 76, showing a clear evidence of the weight percentage of catalyst reducing from 8.4 $\%_{w/w}$ before patterning to 6.8 $\%_{w/w}$ after patterning. This can be interpreted as the thinning of the catalyst mentioned earlier in section 4.2.2.1 resulting in improved VA-CNT growth.

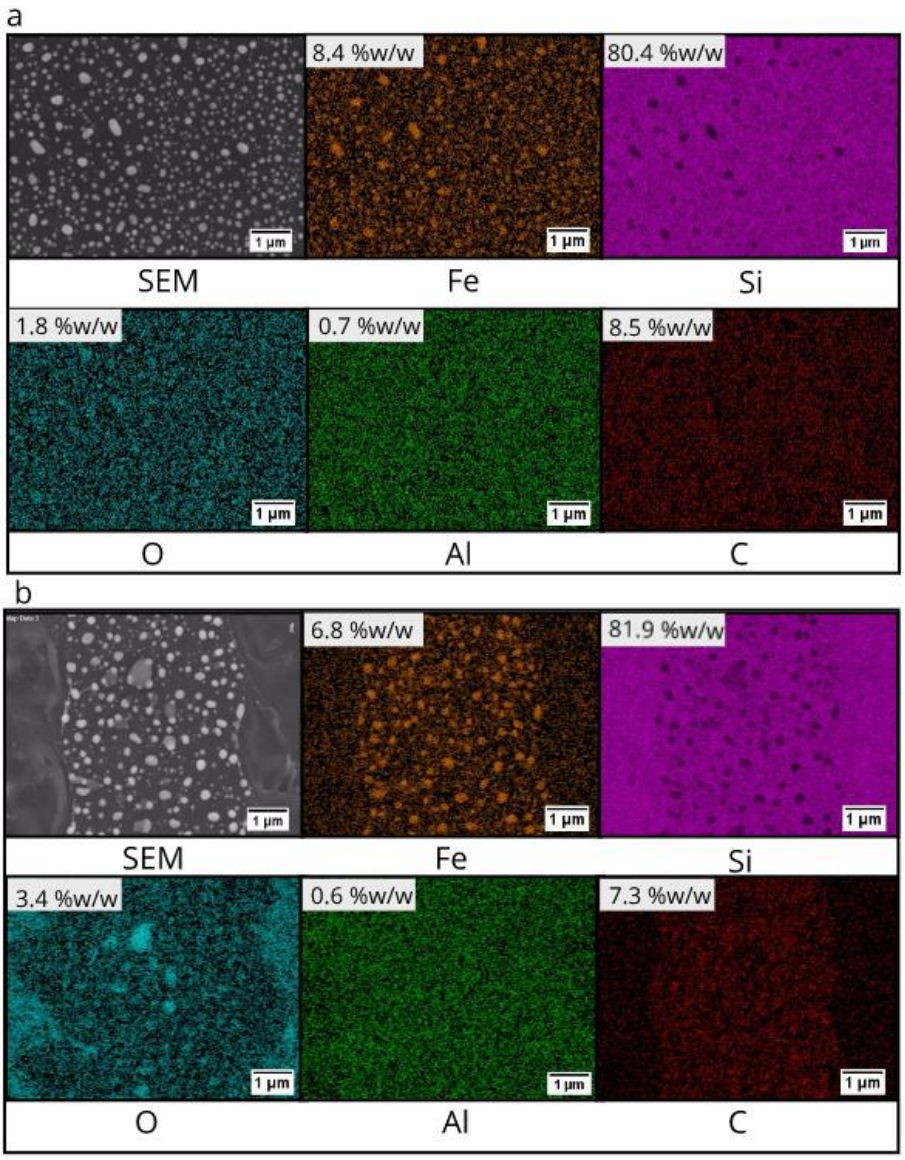

Figure 76: *EDX micrographs of annealed samples of magnetite ink concentration 2.19 $\%_{w/w}$ printed at droplet spacing 5 µm* ***a)*** *before and* ***b)*** *after laser patterning at fluence 1.95 J/cm².*

Figure 77 shows EDX micrographs of catalyst printed at droplet spacing 45 µm, before and after laser patterning. As the catalyst layer is thinner, obtaining EDX micrographs proved difficult as enough signal could not be generated for elements apart from oxygen. However, a minute reduction in iron levels post patterning was observed. The percentage iron detected reduced from 3.1 $\%_{w/w}$ before patterning to 2.4 $\%_{w/w}$ after patterning could suggest thinning of the catalyst layer. The variation in the percentage change of iron for EDX data

presented in both figures is very low, and so more sensitive analysis techniques are required to look at the catalyst redistribution in further detail.

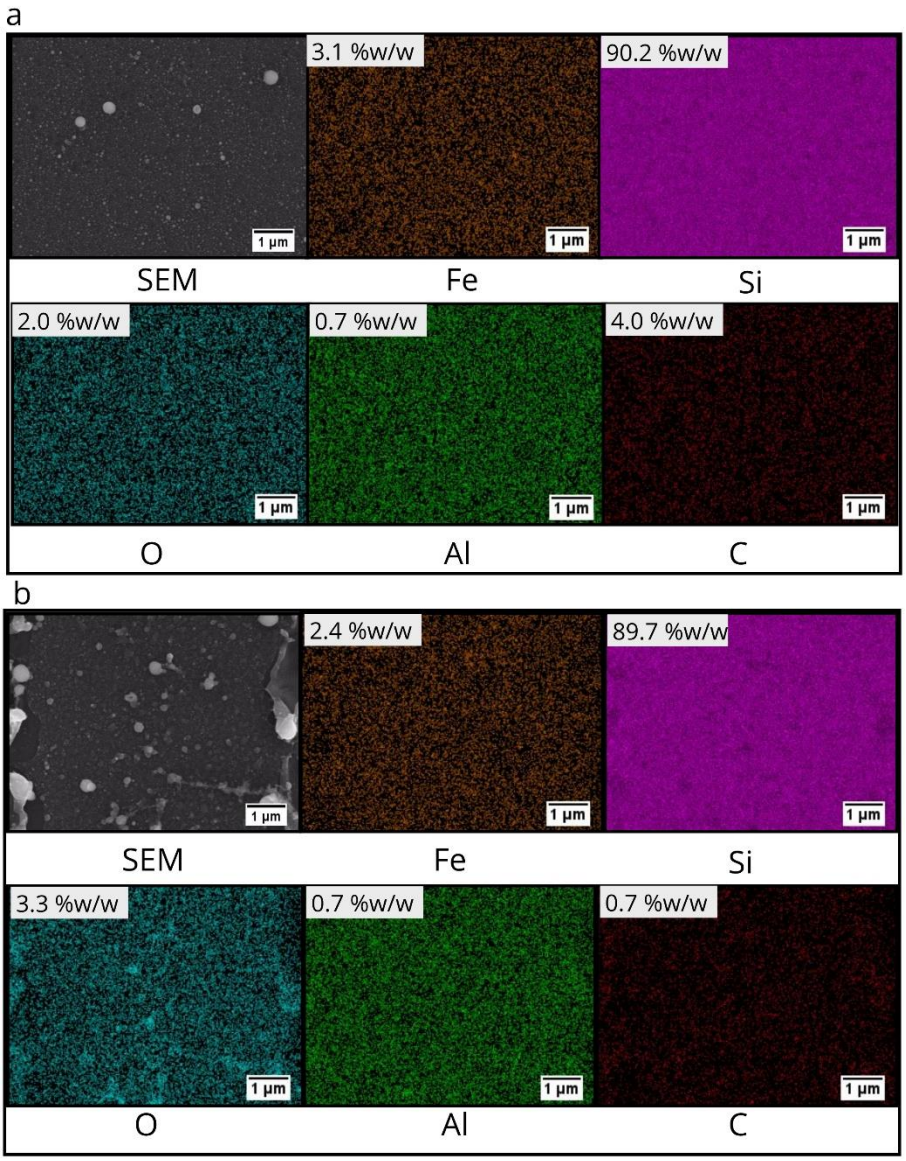

Figure 77: *EDX micrographs of annealed samples of magnetite ink concentration 2.19 $\%_{w/w}$ printed at droplet spacing 45 µm* ***a)*** *before and* ***b)*** *after laser patterning at fluence 1.95 J/cm²*

The SEM and EDX observations are evidence of laser annealing and re-deposition effects on the iron oxide nanoparticle post patterning, but are inconclusive in quantifying this change. Therefore, particle analysis of the catalyst nano-islands formed during annealing is required to compare the catalyst between the laser paths at varying fluence values. SEM analysis was used to determine average particle size owing to the drying and cracking of

the catalyst proving unsuitable for AFM (as previously found in Chapter 2 and Chapter 3.) Selected particle size distribution histograms and SEM micrographs for laser treated catalyst printed at a droplet spacing of 5 µm can be seen in Figure 78.

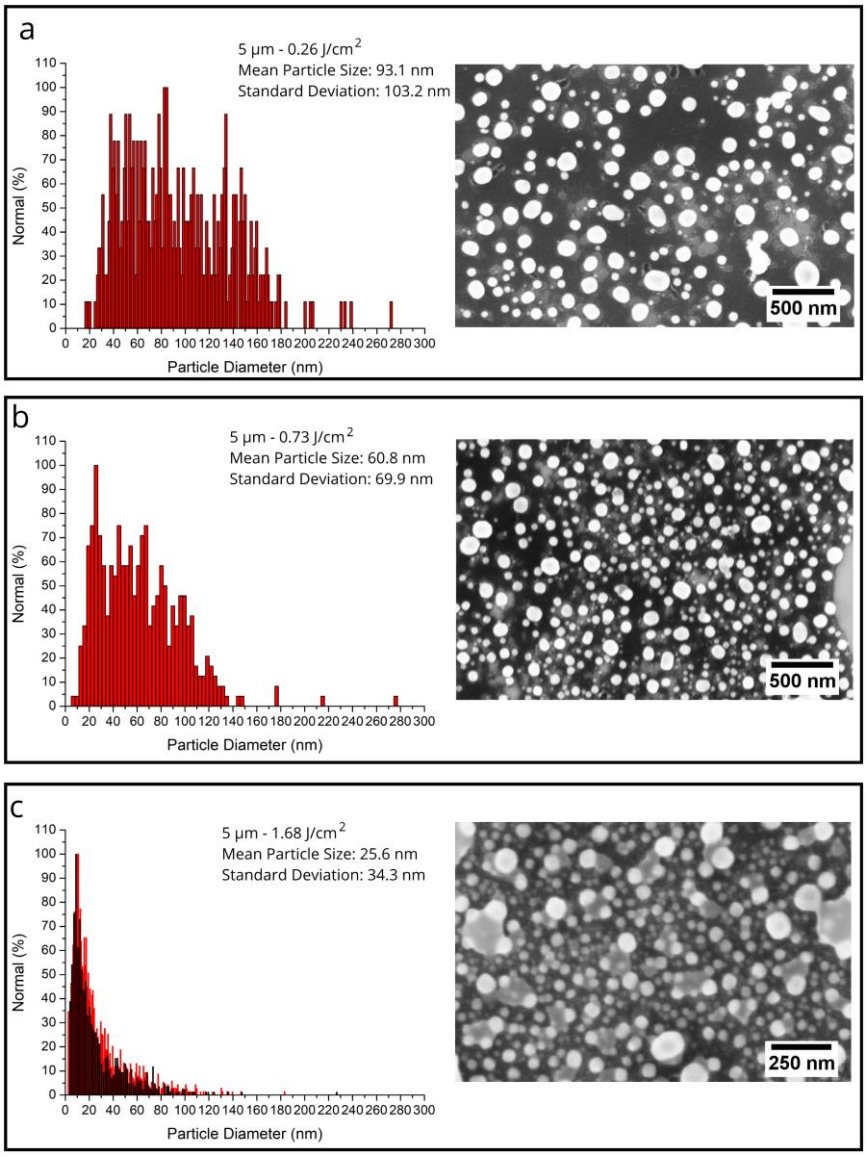

Figure 78: *Graphical distributions and post annealing SEM micrographs of ink concentration 2.19 %$_{w/w}$ printed at droplet spacing 5 µm, laser patterned at fluence* ***a)*** *0.26 J/cm², **b)** 0.73 J/cm² and **c)** 1.68 J/cm².*

The re-solidified molten material in the laser targeted area, and charged spherical and fibrous fragments, spread around the ablated region, are clearly visible in the SEM micrographs in Figure 78 when patterning at F_{high}. The histograms in Figure 78 show that

as patterning fluence is increased, the diameter of the annealed catalyst nano-islands is reduced and the particle packing, resulting in improved alignment and growth of VA-CNTs.

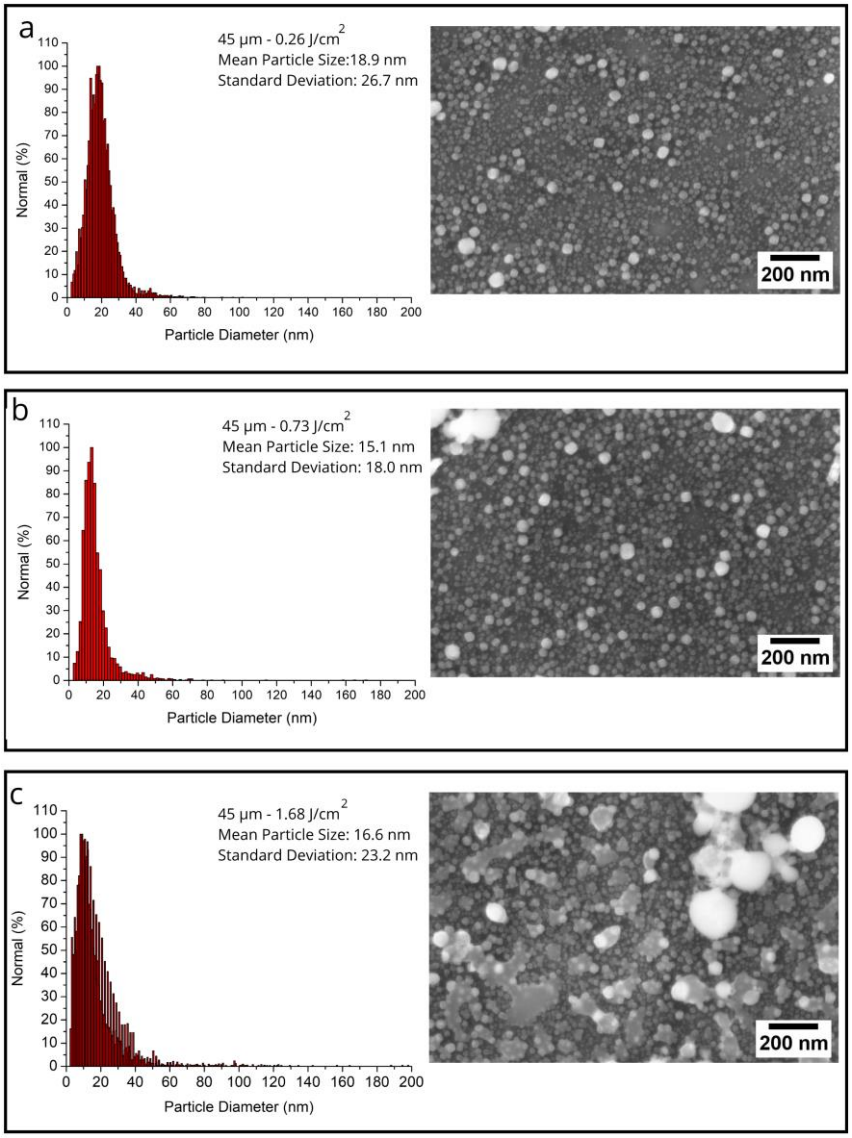

Figure 79: *Graphical distributions and post annealing SEM micrographs of ink concentration 2.19 %$_{w/w}$ printed at droplet spacing 45 µm, laser patterned at fluence* ***a)*** *0.26 J/cm², **b)** 0.73 J/cm² and **c)** 1.68 J/cm².*

Selected particle size distribution histograms and SEM micrographs for laser treated catalyst printed at a droplet spacing of 45 µm can be seen in Figure 79. The histograms shown in Figure 79 are evidence that as fluence is increased, the diameter of the catalyst nano-islands formed during annealing also increases. Detailed SEM micrographs and particle size distribution histograms for all the samples can be found in Figure D 5, Figure D 6, Figure D 7 and Figure D 8. The results indicate that increasing laser fluence

when patterning catalyst layers printed at a droplet spacing of 5 µm, a thinning effect is observed, resulting in a reduction in catalyst nano-island size formation during annealing, and thus improving CNT alignment and height. However, for a thinner catalyst film layers printed at a droplet spacing of 45 µm, an increase in fluence removes the catalyst resulting in degradation of VA-CNT height and alignment.

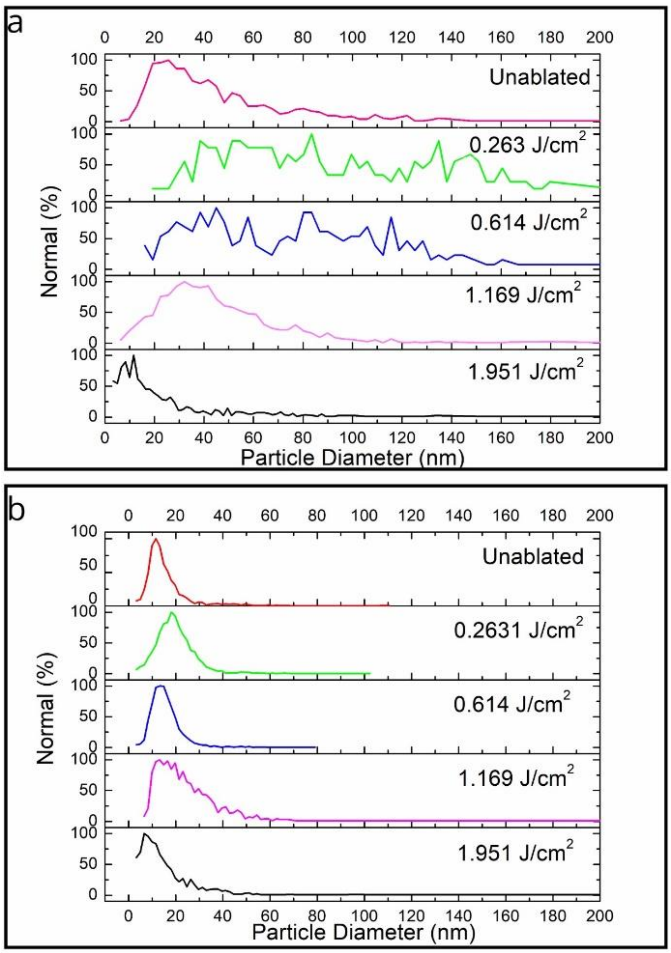

***Figure 80**: Post annealing graphical representation of particle size distribution for lase patterned 2.19 %$_{w/w}$ ink printed at droplet spacing **a)** 5 µm and **b)** 45 µm on 10ASW substrates.*

The nano-island diameter size distribution comparing the results from laser patterning both 5 µm and 45 µm droplet spacing can be seen in Figure 80. The diameter size distribution can be seen to broaden up until the middle of the F_{med} range (0.61 J/cm^2) for both droplet spacings. Beyond this, a narrowing of distribution and reduction in mean size of the nano-island diameter is observed. The post laser patterning average catalytic nano-island size for

e-beam deposited iron is 1.5 ± 0.1 nm, and for printed iron oxide nanoparticles is 15.1 ± 18.0 nm, giving an approximate size difference of 13 nm. This indicates that the catalyst nano-island size formed during annealing, although important, has a critical range rather than a critical size. However, this is dependent on the type of catalyst used. Therefore, a narrow particle size distribution and packing appear to be more critical factors for VA-CNT growth from printed catalyst. The average particle diameter of the annealed catalyst nano-islands, between the laser paths, for droplet spacing 5 µm was found to reduce from 93.1 ± 103.2 nm to 24.5 ± 34.9 nm, and for droplet spacing 45 µm was found to reduce from 18.0 ± 20.7 nm to 16.0 ± 23.0 nm with increasing laser fluence.

4.4 Conclusion

In this chapter we have demonstrated for the first time that by controlling the fluence of an ultrafast laser we can pattern iron oxide nanoparticle films of varying thickness such that VA-CNTs can be grown. The results presented in this chapter evidence that femtosecond lasers can be used at a controlled fluence to successfully pattern catalyst for CVD growth. Some of the key findings in this chapter are highlighted below:

- When patterning e-beam deposited catalyst, a minimum path distance of 5 µm is required when patterning with the satsuma laser. It was found that when patterning e-beam deposited catalyst, a fluence range between 0.48 J/cm^2 and 0.65 J/cm^2 should be used.
- The optimum parameters for growing patterned VA-CNT structures from magnetite ink are; by printing ink concentration 2.19 %$_{w/w}$, at a droplet spacing of 45 µm, on UV treated 10ASW substrates, and patterned at a fluence of 0.73 J/cm^2.
- For fluence values greater than the range recommended, thermal effects of the Gaussian beam became more prominent, resulting in damage to the surrounding

catalyst causing degradation of VA-CNT growth. SEM micrograph of single laser spots revealed the modification, annealing and ablation areas of the Gaussian beam profile.

- AFM analysis revealed that as the laser fluence was increased, the size of the nano-islands formed around the laser spot also increased, causing changes in CNT height and alignment.
- VA-CNTs were successfully grown from annealed e-beam catalyst nano-islands of size 1.5 ± 0.1 nm and from annealed printed iron oxide nano-islands of size 15.1 ± 18.0 nm, revealing that alignment of CNTs is not only dependent on the annealed catalyst nano-islands size, but also the distribution.

These findings shed new light on the process of growing aligned CNTs and can be used for further research on the CVD growth mechanism. When patterning inkjet printed nanoparticles it was found that for thicker catalyst layers increasing the fluence improved CNT alignment and height, whereas for thinner catalyst layers an increase in fluence resulted in degradation of the forest, as observed for e-beam deposited catalyst. These variations in growth are explained by redeposition effects observed during SEM and EDX analysis of the patterned films. Particle analysis of the catalyst surrounding the laser spots revealed that when patterning at high fluence values, the size of the nano-islands formed during annealing decreased for thick catalyst layers, and decreased for thin catalyst layers. Although the results demonstrate feasibility of patterning catalyst with an ultrafast laser, it is important to optimise these conditions on an industrial scale. With the specifications and feasibility of using the assistive CVD, additive inkjet printing and subtractive laser patterning determined, the next phase of research will focus on a conceptualisation study into the transition of this technology into industry and possible applications.

Chapter 5

INDUSTRIAL TRANSITION AND APPLICATION

Nanomaterials for the past two decades have generated a significant interest in the development of sensing devices, owing to their unique mechanical, structural and electrical properties. However, it is essential to develop novel nanotechnology and micro-technology interfaces for organising these materials into controlled surface architectures, that can be integrated into functional devices [278]. We have successfully demonstrated the feasibility of developing an integrated inkjet printing and laser ablation technology to pattern structures of VA-CNTs. Scale-up of this technology requires utilising industrial set-ups that are low cost and can pattern wider areas at high speeds.

M-Solv Ltd. have already developed a configurable inkjet-laser hybrid system, MSV200 series machines, for scalable high-throughput manufacture of large area electronics [125]. The system can be configured with lasers and inkjet printers of choice. The Dimatix, piezo DOD inkjet technology can be integrated in many systems industrially, and has been incorporated by M-Solv in their inkjet and laser hybrid MSV200 series machine [107], [125]. The Scan Mask Imaging (SMI) Solid State Laser has been developed by David Myles at M-Solv. Multiple layers of material can be patterned using the system by raster scanning binary masks that are imaged onto a substrate [279]. The SMI system can be integrated with a Dimatix inkjet printer for the deposition and patterning of VA-CNT growth. The ability to produce VA-CNT structures using already existing industrial tools is a major advantage in establishing a platform tool for developing and testing an array of nanomaterial device architectures.

Research into the development of nanomaterial base gas sensors has increased as a result of an increase in pollutant and greenhouse gases such as: CO_2, CH_4, CO, SO_2, NO_x and NH_3 [280]. CNTs are currently being research for applications in chemical, gas, mechanical, humidity, environmental and biological sensors [83], [93], [281]. However, they have low selectivity, and thus are required to be decorated or functionalised with other nanomaterials to increase selectivity. Metal oxides have been identified as a route for novel gas sensing especially when combined with CNTs [282], [283]. This combination of CNTs and metal oxides is particularly of interest for gas sensing, where metal oxides perform well at high temperature sensing and CNTs perform well at even low temperatures [280]. CNTs can naturally detect high energy absorption gasses like NO_2, and so testing the gas sensing capabilities of inkjet printed catalyst grown VA-CNTs serves as an ideal first application test [284]. Once feasibility of gas sensing applications has been determined, other more complex platform technologies requiring complex detecting mechanisms such as functionalisation of CNTs can be explored.

After successfully combining inkjet printing (additive), laser patterning (subtractive) and CVD (assistive) techniques as a hybrid tool for the aligned growth of VA-CNTs, this chapter now focuses on conceptualising translation of this technique into an industrial process and develop sensing devices. Therefore, the chapter has four main objectives.

- Determining the effects of using the SMI system developed by M-Solv to pattern catalyst for VA-CNT growth.
- Demonstrate a trial gas sensing chip with inkjet printed catalyst grown VA-CNTs.
- Study the effect of coating VA-CNTs with a metal oxide on sensing capability.

However, before commencing the experiments, literature has to be reviewed to develop a knowledge base for SMI system and CNT based gas sensors. This literature analysis has been presented in the next section.

5.1 Theoretical Section

For the study of industrial translation of technologies, literature analysing the current trends in scalable laser patterning processes and VA-CNT application is presented in two sections.

5.1.1 Application of Industrial Patterning Systems

Brunton and Crozier (2018) have identified that by combining inkjet and laser patterning as a hybrid technology, multiple sensors can be made on the same assembly line with minimal changes to the line operation [125]. Therefore, on many occasions inkjet printing and laser patterning have been integrated as a hybrid technology. Inkjet printed nanoparticle films can be ablated with pulsed nanosecond (Nd:YAG) lasers, for low temperature fabrication of electrical components as demonstrated by Ko *et al.* (2005) [126]. Suzuki *et al.* (2013) have demonstrated a hybrid inkjet and excimer laser patterning technique for processing organic thin film transistor (TFT) arrays [285]. M-Solv Ltd. have developed a laser and inkjet hybrid system for processing thin film photovoltaics. The system uses Fujifilm Dimatix Starfire printheads and a 355 nm UV laser galvanometer scanner to achieve feature resolutions of 15 µm, with the option of installing a UV curing lamp [125]. The literature analysed is evidence that new scalable inkjet printing and laser patterning hybrid systems will soon be available for processing a wide range of devices. However, even though Dimatix printheads are being incorporated into industrial systems, the use of femtosecond lasers for patterning films at an industrial scale has not been reported.

Solid state lasers are low cost, but have processing times dependent on pattern complexity, whereas excimer lasers, although offering high throughput, are expensive to operate [279]. Milne and Myles (2015) at M-Solv Ltd. have developed a *"Scanned Mask Imaging (SMI)"* system, where a UV multi-mode solid state laser and scanner are used to illuminate a photo-mask, and the image of the mask de-magnified and projected on a substrate [286]. A schematic of the optical system used for the SMI is shown in Figure 81. SMI patterning can be carried out at a low cost to achieve feature resolution down to a few micrometres. The system also has a flat top beam shape instead of a Gaussian beam, thus reducing the appearance of diffraction fringes at the edge of the ablated features, and improving uniformity of fluence across the beam profile [279]. Therefore, it is important to explore the feasibility of using such a system for patterning catalyst for VA-CNT growth.

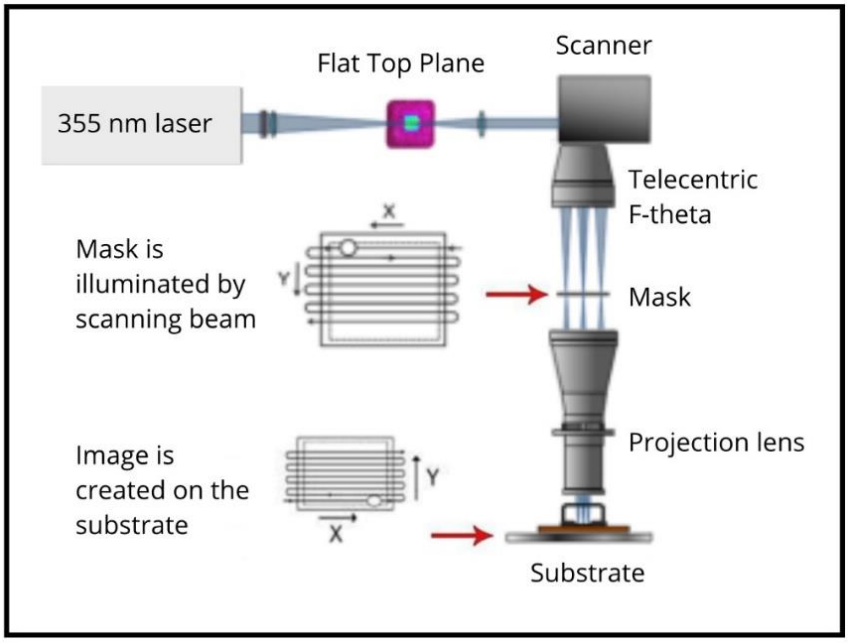

Figure 81: *SMI Optical system schematic provided by M-Solv Ltd.* [287]

5.1.2 Sensing Applications

At the same time as testing technology transfer to an industrial set-up, it is essential to develop a first test application for the VA-CNT device being fabricated [288]. The test application will serve as a design for manufacture knowledge base, findings from which can be used to develop further sensing platforms and devices. Although CNTs are inert, their electrical properties are highly sensitive to chemical doping, and thus CNTs have been developed for a range of analytical applications such as gas sensing, biosensing and voltammetry as reviewed by Trojanowicz (2006) [289]. Traditionally metal oxides and polymers have been developed for sensing applications as they are highly reactive with many target gases and are low [88], [280]. However, CNTs are now being explored as a suitable material for gas sensing applications, as they have a large single atom surface area with many absorption points, giving a route for miniaturisation and improved sensitivity [290]. Fam *et al.* (2011) identifies that CNTs in the recent years have been intensely studied for applications in bio and chemical sensing, but the commercialisation of these applications has been hindered by lack of repeatable synthesis techniques [291]. With a repeatable and industrially scalable fabrication methodology, CNTs can serve as a platform technology for the development of multiple environmental sensors. Kauffman and Star (2008) have reviewed a large number of research focused towards developing CNTs for the selective detection of CO, CO_2, NO, NO_2, NH_3, CH_4, H_2, O_2, SO_2, H_2S [290].

CNTs can exist as either metallic or semiconducting depending on their diameter and chirality, but for gas sensing semiconducting CNTs are required [280]. When gases are absorbed by CNTs, the gaseous molecules either donate or withdraw electrons from the CNT causing changes in electrical properties [292]. This indicates that reproducible synthesis and fabrication techniques are required to maintain CNT properties across the

device batch [291]. Huang *et al.* (2005) have identified that to produce highly sensitive gas sensors it is important to use well aligned CNTs. Therefore CNTs should be directly grown on the sensor substrate being used [293]. CNTs are highly reactive to NO_2 and NH_3 on account of their large absorption energy [292]. NO_2 is an oxidising gas and takes electrons from the CNTs causing a drop in resistance, whereas NH_3 is a reducing gas and denotes an electron to the CNTs resulting in an increase in resistan[280], [294]. Ueda *et al.* (2008) demonstrated the use of VA-CNTs for NOx detection and Lin *et al.* (2015) have reported the development of a room temperature flexible CNT sensor for detecting CO_2, where the reducing gas causes an increase in device [281], [295], for unmodified CNT gas sensors the desorption time required for the gas being detected can be slow, and thus require heat [89], [284], [296], [297]

Septiani and Yuliarto (2016) have identified that metal oxide modification of the CNTs can provide an accelerated electron path to and from the CNTs and polymer modification can increase the charge carrier density in CNTs, and thus device sensitivity [280]. CNTs are p-type semiconductors and modifications with other materials creates a PN-junction to increase device selectivity [298]. Decorating CNTs with gold nanoparticles has been shown to improve sensor sensitivity for detecting NO_2 and CO as demonstrated by Zanolli (2011) [282]. Mudimela *et al.* (2014) have also developed a gold decorated CNT sensor for detecting NO_2 [299]. Lee *et al.* (2013) have developed a transparent and flexible, gold decorated CNT sensor for detecting NH_3, except with slow recovery times [300]. Tulliani *et al.* (2011) have demonstrated a room temperature NH_3 sensor with recovery times based on zinc oxide and palladium doped carboxyl functionalised CNTs, and fluorinated or nitrogenous functionalised graphite and VA-CNTs [301]. Zinc and Iron metal oxides are also highly suitable for gas applications and exhibit n-type semiconductivity, and thus are suitable materials for coating CNTs to create PN junctions [298]. A recent review by Long

et al. (2015) highlights the potential of using iron oxide materials for next generation gas sensors for detection and identification of toxic gases in air ambience [302]. Iron oxide nanoparticles have also been demonstrated as a suitable material for humidity [303], [304]. Lee *et al*. (2015) demonstrated the use of iron oxide nanoparticle decorated CNTs for humidity sensing [305].

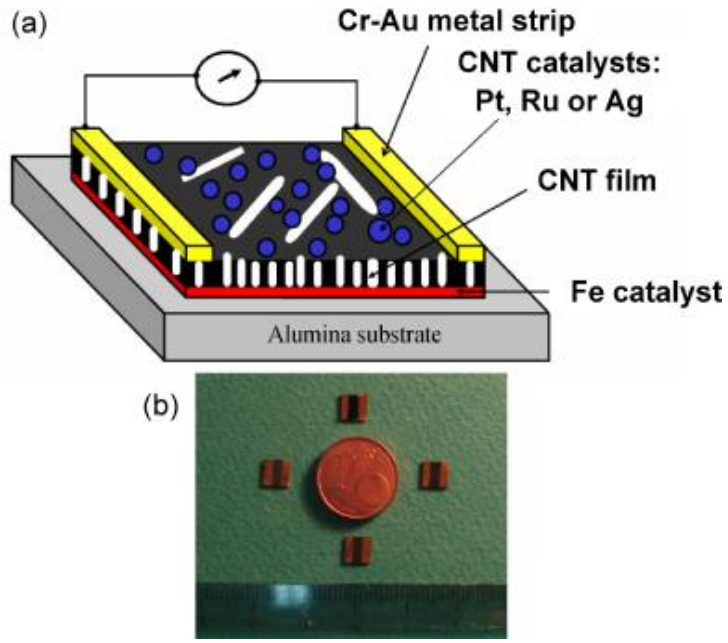

Figure 82: a) *Schematic of the two electrode VA-CNT chemical resistor.* ***b)*** *Image of the four individual (unmodified, and Pt, Ru and Ag coated) individual VA-CNT chemical resistors developed by Penza et al. (2010)* [306].

The literature demonstrates that multiple materials can be used to alter the CNT selectivity allowing potential for development of CNT sensor arrays for either multiple gas sensing applications or for the detection of low quantities of a select gases in a mixture. The CNTs can either be chemically functionalised or physically coated with the nanoparticles or polymers selected [88]. Functionalisation of CNTs is a complex procedure and can be conducted as a chemical or dry gas-phase procedure [307]. Penza *et al.* (2010) have developed a VA-CNT gas sensor array composed of four sensing elements with unmodified CNTs, and platinum, ruthenium and silver sputtered CNTs, that can successfully discriminate NO_2 in a gas mixture consisting of other common landfill gases, such as CO_2,

H_2, CH_4 and NH_3 [89]. A schematic of the sensor and an image of the individual arrays can be seen in Figure 82.

The literature reviewed evidences the importance of developing CNT applications and fabrication techniques in parallel. Therefore, for the conceptualisation phase of development it is important to conduct initial fabrication tests on industrially compatible alternative patterning platforms, such as the M-Solv developed SMI system. As VA-CNTs can be used for gas sensing applications with minimal modification, VA-CNTs grown form inkjet printed catalyst will be tested as a sensor for detecting humidity, NO_2, NH_3 and CO_2 as a preliminary application. The experiments will determine whether an industrial laser patterning system is compatible for patterning catalyst for VA-CNT growth, the potential scope for commercial applications, and the next steps required.

5.2 Experimental Methodology

This section describes the equipment and experimental procedures used. The substrate details, catalyst deposition and characterisation technique details can be found in Chapter 2 and 3. The molybdenum electrodes were deposited using a shadow mask and the LEV – Lesker PVD 75 system.

5.2.1 Scan Mask Imaging

A 10ASW substrate with 1 nm iron deposited via e-beam was prepared. The Scan mask imaging system used is a frequency tripled (355 nm), Q-switched multi-mode, diode pumped solid state (DPSS) YAG laser. The laser has a maximum pulse repetition rate of approximately 10 kHz, with low average powers of < 100 W, and low pulse energies in the mill joule regime.

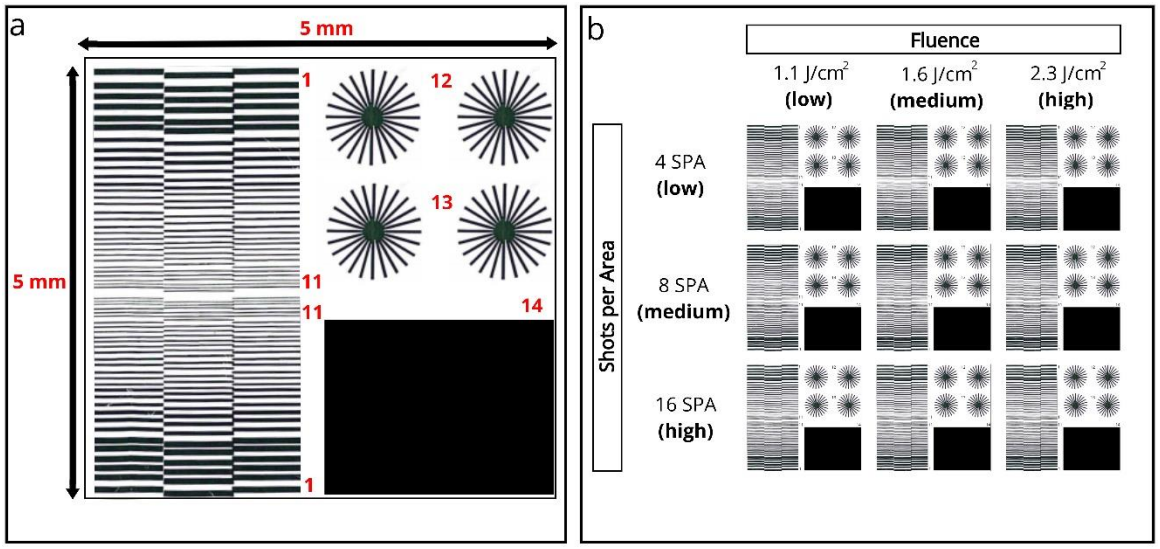

Figure 83: *Schematic of* ***a)*** *test design for SMI patterning of 1 nm iron catalyst coated 10ASW and* ***b)*** *pattern array and laser parameters.*

Figure 83.a shows the resolution test design patterned with the SMI system. Details of the dimensions of the features patterned can be found in Table E 1. The scanning was carried out at a repetition rate of 5 kHz on a full 100 mm diameter 1 nm iron coated 10ASW substrate. The design was patterned in a 3 x 3 array for varying laser fluence and shots per area (SPA) as shown in Figure 83.b. The laser scanning was carried out at fluence values 1.1 J/cm^2 ***(low)***, 1.6 J/cm^2 ***(medium)*** and 2.3 J/cm^2 ***(high)***, and 4 ***(low)***, 8 ***(medium)*** and 16 ***(high)*** shots per area. The shots delivered per area are controlled by varying the mark speed and pitch of the raster scanned laser lines. The wafer was divided into nine chips before CVD growth. The CVD growth conditions can be found in Chapter 2.

5.2.2 Gas Sensing

Gas sensing chips were made by e-beam deposition of 40 nm molybdenum electrodes on fused silica wafers. The chips were UV treated for 10 minutes, and lines of 2.19 $\%_{w/w}$ magnetite suspension inkjet printed across the electrodes at a droplet spacing of 45 µm, and VA-CNTs grown. All printing, surface wettability and substrate cleaning methodologies can be found in Chapter 3 and the CVD growth recipe in Chapter 2. The Kenosistic Gas

Sensor Testing System developed with the help of IMQ- Istituto Italiano Del Marchio Di qualita was used for all sensing experiments. The main features of the system include [308]:

- Sensors constantly monitoring pressure, temperature, relative humidity and flow speed.
- Thermally regulated chamber.
- Microprocessors controlling valves, calculating gas flows and gas mixtures at desired concentration, humidity and temperature.
- Three mass flow controllers: two controlling dry and wet air and one controlling the gas with a valve system to distribute gas mixture flow.
- Mass spectrometer to monitor actual gas concentration.
- Software PPt430 allowing constant monitoring of cell contents and gas concentration.

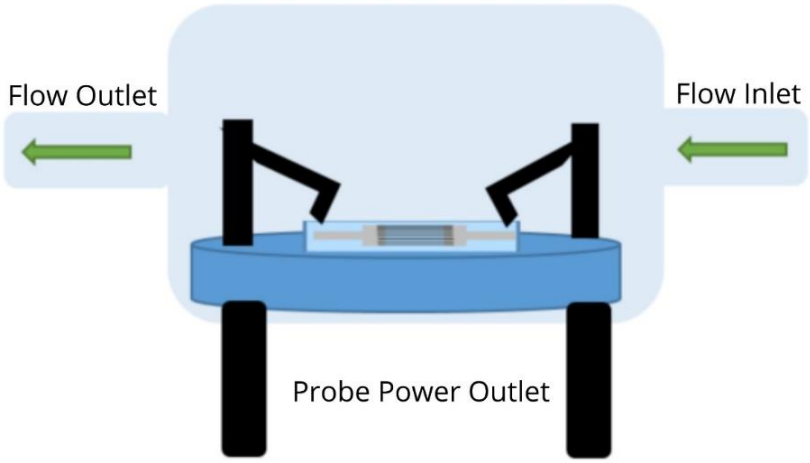

Figure 84: *Sensing platform schematic*

Although the gas testing system has 4 probes, only 2 probe testing were used. A schematic of the set-up has been seen in Figure 84. Tests were conducted to detect resistance changes in the VA-CNT chip, by varying the concentration of humidity and three gases: NO_2, NH_3 and CO_2. The recipes for the tests can be found in Table E 2, Table E 3 and Table E 4. All

gas experiments were conducted in room temperature. Between each gas experiment a heating cycle was run at a 100 ° C for 1 hour to ensure all the trapped gas within the VA-CNT structures was released.

5.3 Results and Discussion

The experiments presented in this section were conducted to explore two scale-up concepts: ***1)*** the feasibility of using the M-Solv SMI set-up for patterning catalyst for VA-CNT growth and ***2)*** the applicability of inkjet printed catalyst grown VA-CNTs in gas sensing devices. Therefore, the results in this chapters have been presented in two. In the first section, 10ASW substrates e-beam deposited with 1 a nm iron layer are patterned using a scan mask imaging system at varying laser fluence and number of shots per area. The features patterned were studied using optical microscopy, SEM and Raman spectra. The second section demonstrates the feasibility of growing VA-CNTs from inkjet printed catalyst on a fused silica substrates for gas sensing. The gas sensing experiments were conducted for varying concentrations of humidity, NO_2, CO_2 and NH_3.

5.3.1 Scan Mask Imaging

10ASW substrates e-beam coated with 1 nm iron films were patterned with the SMI laser at varying fluence and shots per area as detailed earlier in Figure 83.a. The patterned substrates were analysed under the optical microscope, and a selection of features analysed and presented in this section in a three by three grid giving results for all nine combinations of SPA and fluence. We first analysed feature 14, optical micrographs of which can be seen in Figure 85.

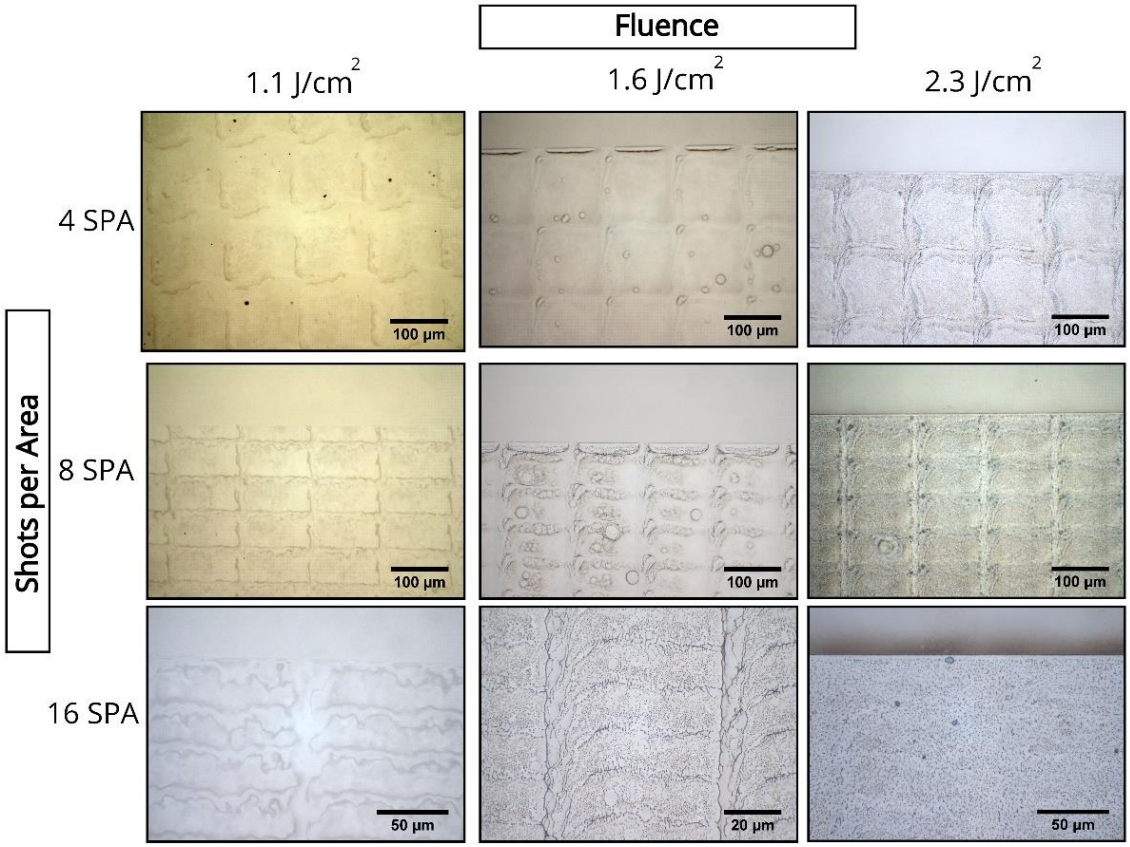

Figure 85: *Optical micrographs of pattern 14 scanned on 1 nm iron coated 10ASW substrate at varying fluence and shots per area.*

A faint outline of the top hat profile of the laser beam is clearly visible in the micrograph shown for low SPA and low fluence. The outline of the square profile becomes more visible as the fluence is increased at the low SPA setting. The definition of the top hat square becomes prominent when increasing the fluence values, while maintaining 4 SPA. However, on the other hand when fluence is kept constant and the SPA increased, the laser spots are harder to differentiate with probable melting observed in the wave like structures visible at high SPA and low to medium fluence. The laser spots are indistinguishable when patterning at high SPA and high fluence. To analyse the effect of varying SPA and fluence on the catalyst film, the substrates were subjected to CVD growth.

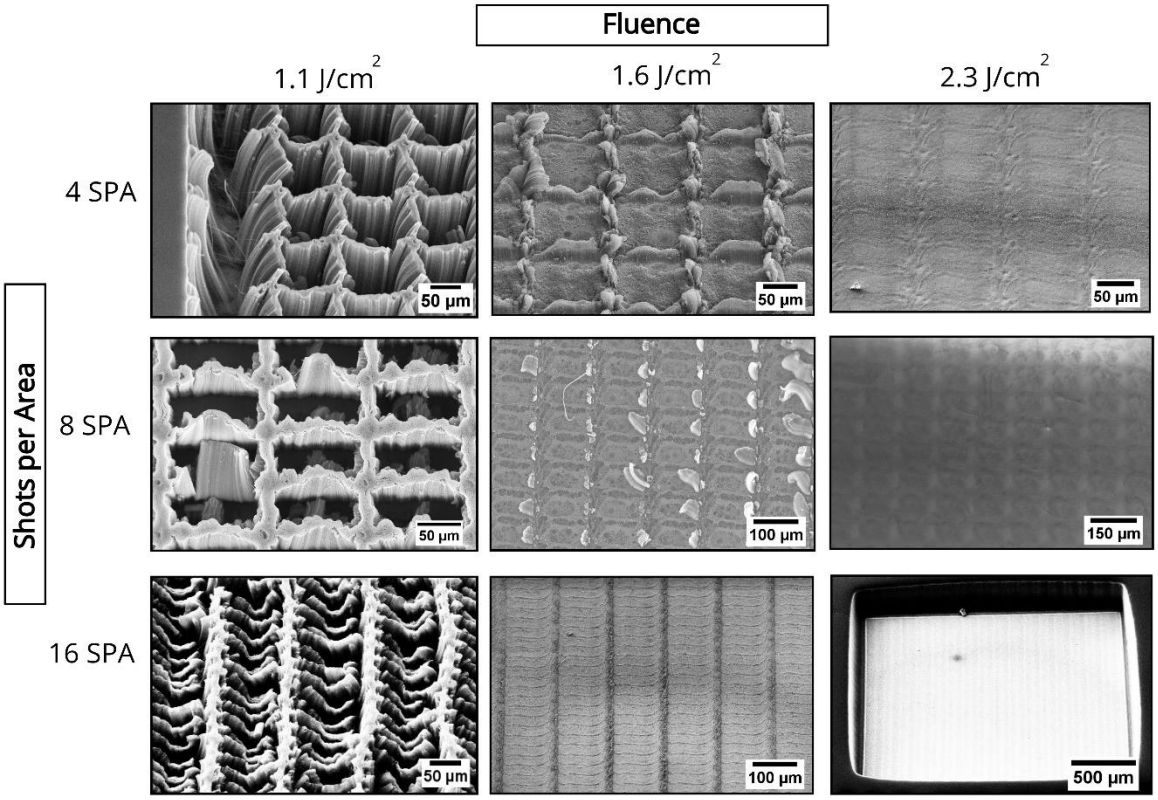

Figure 86: *SEM micrographs of pattern 14 scanned on 1 nm iron coated 10ASW substrate at varying fluence and shots per area.*

SEM micrographs showing post CVD growth results can be seen in Figure 86. It can be seen that no growth was observed when scanning with a high fluence at all three SPA settings. However, when scanning at a low fluence growth is observed for all SPA settings, with the structural integrity of the square wells and height of the forest degrading with increasing SPA. When patterning at a medium fluence no growth was observed at high SPA. However, as the shots per area are reduced, partial growth can be seen around the laser spots. High VA-CNTs walls can be seen around the laser spots, the definition of which reduces as the shots per area are increased. All growth results reflect the ablation patterns observed in the optical micrographs taken prior to growth as seen in Figure 85. The complete removal of catalyst was only observed when scanning at a high fluence setting for all SPA, or at a medium fluence and high SPA setting.

Table 11: *Results summary for feature 14 patterned with the SMI system on PVD deposited iron catalyst with green highlighting settings giving the desired outcome and grey highlighting the settings with undesirable results.*

Feature 14

	Fluence		
Shots per Area	**Low, Low** • Top hat profile visible before CVD growth • VA-CNT cells grown, but of shorter height than bulk forest	**Low, Medium** • Top hat profile visible before CVD growth • Short CNT outlines	**Low, High** • Top hat profile visible before CVD growth • No VA-CNT growth
	Medium, Low • Top hat profile overlap before CVD growth • VA-CNT cells grown with inhomogeneous wall height and bending	**Medium, Medium** • Top hat profile overlap before CVD growth • Partial CNT growth around edges.	**Medium, High** • Top hat profile overlap before CVD growth • No VA-CNT Growth
	High, Low • Top hat profile indistinguishable and melting visible before CVD growth • VA-CNTs grown with bending and insufficient structural integrity	**High, Medium** • Top hat profile indistinguishable and melting visible before CVD growth • No VA-CNT growth	**High, High** • No outline of the laser spot visible before CVD growth. • No VA-CNT growth

Table 11 shows a summary of the results for feature 14. Feature 14 was patterned to completely remove the catalyst which can be achieved with 4 combinations of fluence and SPA settings as highlighted in the summary table. However, as melting was observed with increasing SPA and fluence values, it is important to analyse finer features to determine the adequate settings for patterning catalyst with the SMI system.

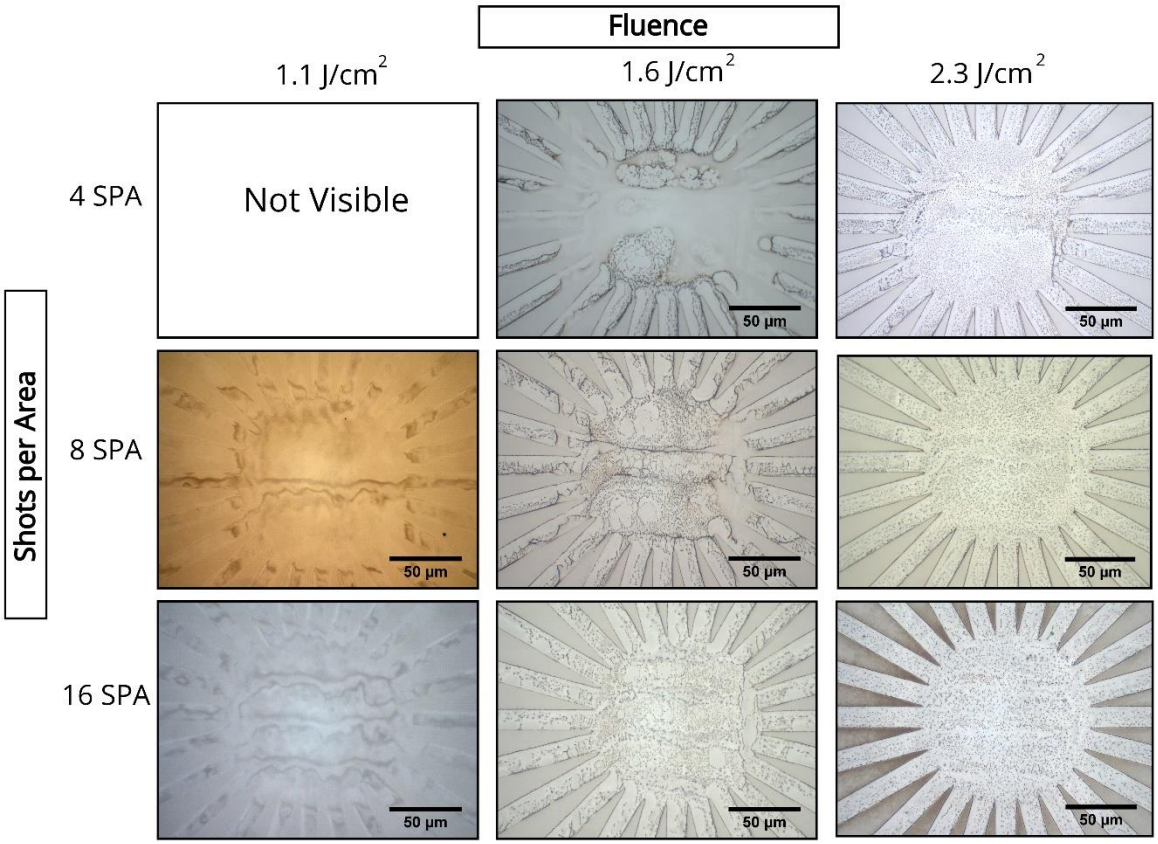

Figure 87: *Optical micrographs of pattern 12 scanned on 1 nm iron coated 10ASW substrate at varying fluence and shots per area.*

Features 12 and 13 are a suitable pattern to understand the effects of varying fluence and SPA. The lines extending out of the central circle give a variation in the width of the VA-CNT forest to be grown. The tip like features in between the cleared laser paths can be used to determine the HAZ of the laser paths. Figure 87 shows optical micrographs of feature 12 patterned at varying fluence and SPA settings. The patterned feature is not visible when scanning at a low fluence and low SPA settings. As the SPA are increased, while maintaining a low fluence, the star feature becomes more visible, but with the edges of the

feature still not distinguishable. The patterned feature only becomes more visible when the fluence is increased for all SPA settings. When patterning at a medium fluence uneven sections of patterned feature are visible for low and medium SPA, and an even outline of the feature can be seen at high SPA. When patterning at a high fluence the features are visible for all SPA. However, darkening of the substrate indicating HAZ around the patterned feature can be seen when scanning at a high fluence and high SPA setting. With such variation in patterning observed via optical microscopy, the samples were subjected to CVD growth to understand scanning effects on VA-CNTs.

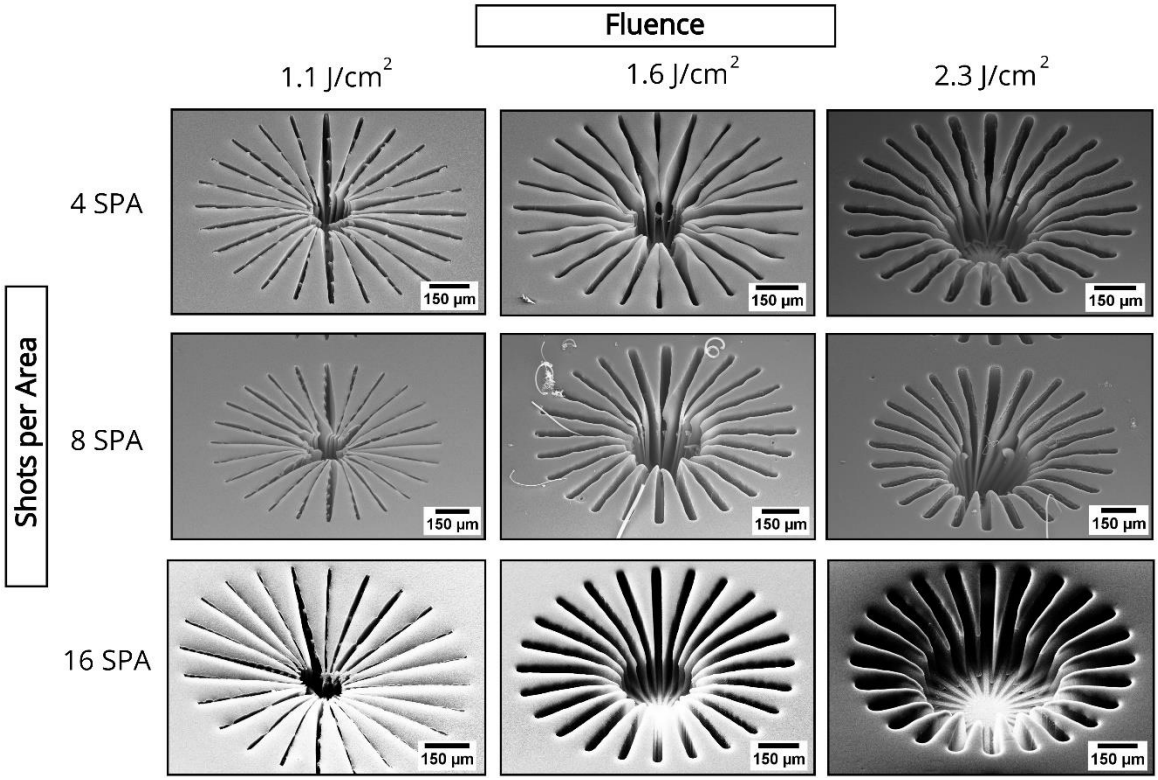

Figure 88: *SEM micrographs of pattern 12 scanned on 1 nm iron coated 10ASW substrate at varying fluence and shots per area.*

CVD Growth results for feature 12 can be seen in Figure 88**.** The SEM micrographs reveal that when scanning at a low fluence setting the patterned VA-CNTs are not clearly defined for all SPA settings. As the fluence is increased to medium the feature definition improves for low and medium SPA settings. However, maximum feature resolution is observed when

patterning at a medium fluence and high SPA setting. Increasing to high fluence results in a decrease in feature definition for all SPA settings.

Table 12: *Results summary for feature 12 patterned with the SMI system on PVD deposited iron catalyst with green highlighting settings giving the desired outcome and grey highlighting the settings with undesirable results.*

Feature 12

	Fluence		
Shots per Area	**Low, Low** • Feature not visible before CVD growth • Partially patterned VA-CNTs	**Low, Medium** • Uneven sections of patterned feature visible before CVD growth • Uneven outlines of patterned VA-CNTs	**Low, High** • Feature fully visible before CVD growth • Uneven outlines and bending of patterned VA-CNTS
	Medium, Low • Faint outline of feature visible before CVD growth • Partially patterned VA-CNTs	**Medium, Medium** • Uneven sections of patterned feature visible before CVD growth • Uneven outlines of patterned VA-CNT	**Medium, High** • Feature fully visible before CVD growth • Uneven outlines and bending of VA-CNTs with degradation of forest in the centre of feature
	High, Low • Faint outline of feature visible with possible melting before CVD growth • Partially patterned VA-CNTs	**High, Medium** • Feature fully visible before CVD growth • VA-CNTs grown with even height and maximum coverage in unpatterned regions	**High, High** • Feature and HAZ visible before CVD growth • VA-CNTs not fully grown. Degradation of forest in centre of feature

A results summary for feature 12 can be found in Table 12. From the table it is evident that even though the best patterning result was achieved at medium SPA and high fluence, visual inspection alone is not sufficient to determine the influence of SMI scanning on VA-CNT growth. Therefore, more quantitative analysis is required to determine which fluence settings and number of shots per area are suitable for patterning VA-CNTS with maximum feature definition and minimum HAZ.

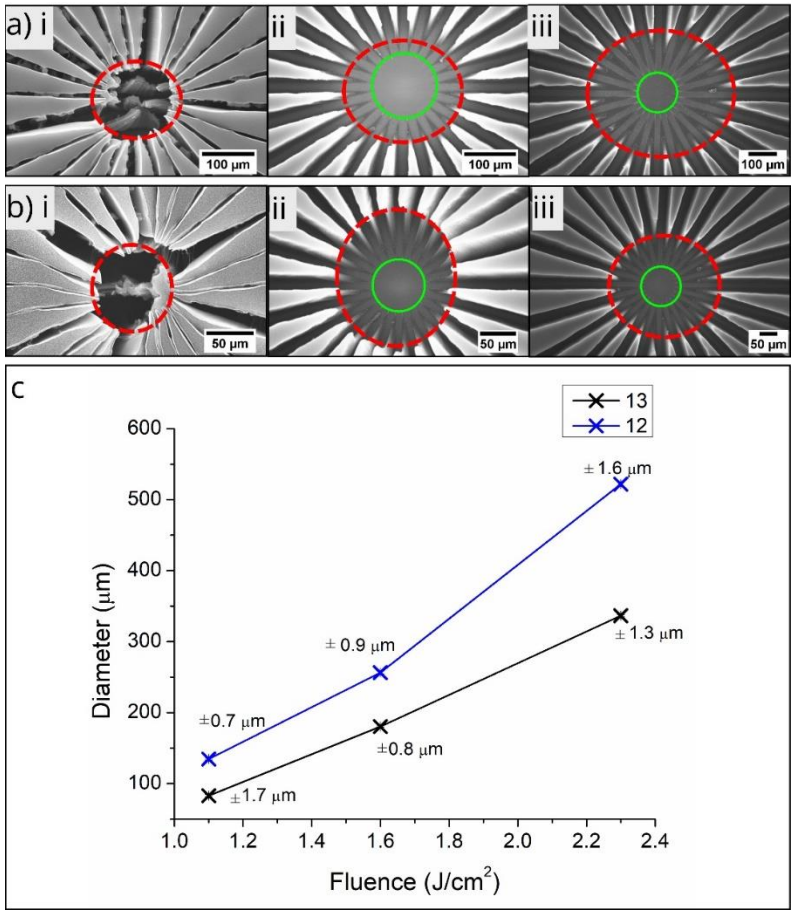

Figure 89: *SEM micrographs showing top view of VA-CNTs grown for features* ***a)*** *12 and* ***b)*** *13 when patterning at fluence* ***i)*** *1.1 J/cm², **ii)** 1.6 J/cm² and **iii)** 2.3 J/cm² with 16 SPA.* ***c)*** *Graphical representation of post CVD growth diameter (µm) of features and 12 and 13 vs fluence (J/cm²) when patterning at 16 SPA. The errors reported have been calculated as a 95% CI.*

Degradation of VA-CNT forest and height was observed in the SEM micrographs shown in Figure 88 as the laser fluence is increased. This is particularly visible when looking at the central region of the feature where the start lines converge and no growth is expected. However, it is observed that as the SPA and fluence values are increased, VA-CNT growth

occurs further away from this central region. This indicates a HAZ occurring around the laser path causing changes to the catalyst such that no growth occurs when the laser paths are too close together. This can be seen in Figure 89.a and b, where top view SEM micrographs of feature 12 and 13 are shown for features patterned at low, medium and high fluence with high SPA. The green circle represents the actual patterning area for feature 12 and 13, and the red circle shows the point where VA-CNTs grow at the same rate as the bulk forest. The diameter of the inner patterned circle for feature 12 was measured to be approximately 120 µm, and that of feature 13 measured to be approximately 65 µm, before CNT growth. However, from the SEM micrographs shown in Figure 89.a and b, it is evident that as fluence is increased the HAZ increases and results in VA-CNTs growing further away from the inner circle on account of the laser paths converging towards the centre of the patterned feature. This increase in diameter has been measured and presented in the graph in Figure 89.c.

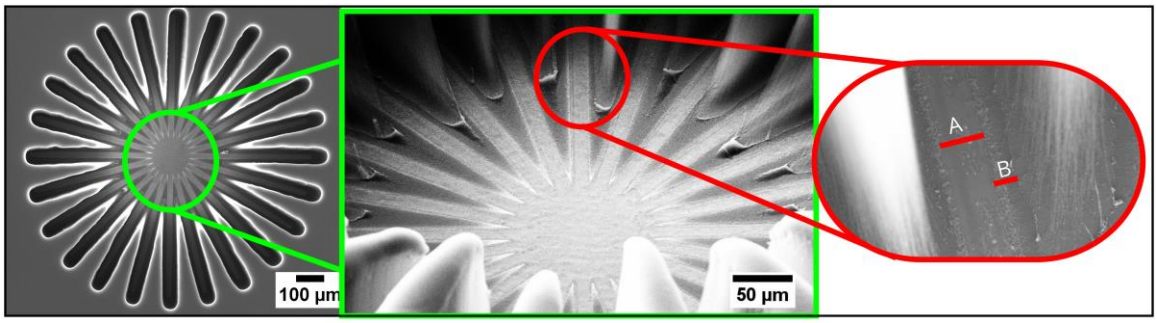

Figure 90: *SEM micrographs of VA-CNTS grown for feature 13 patterned at a fluence of 2.6 J/cm² and with 16 SPA. The graphs show the HAZ effects of the laser on the catalyst surrounding the laser path and the measurements taken.*

The HAZ can also be calculated by directly measuring the width of the visible laser path (A) and the distance at which VA-CNTs grow (B), as shown in Figure 90. The measurements have only been taken for features 12 and 13 patterned at low and medium fluence with high SPA, as the paths are not visible when patterning at other settings. The measurements taken are presented in Table 13.

Table 13: *Tabulated data of the A – the minimum laser path width and B – the distance at which VA-CNTs grow from the laser path. Errors have been calculated to a 95% CI.*

	12		**13**	
Fluence (J/cm²)	**A (µm)**	**B (µm)**	**A (µm)**	**B (µm)**
1.6	11 ± 1.9	2.8 ± 0.3	7.9 ± 0.7	1.9 ± 0.2
2.3	30.1 ± 4.1	7.0 ± 0.7	17.5 ± 1.6	4.2 ± 0.4

It can be seen from the results presented that as fluence is increased, the VA-CNT growth occurs further away from the laser path, evidencing HAZ effects of the laser on the surrounding catalyst. The width of the laser path also increases as fluence increases, on account of laser HAZ effects. The measurements prove that scanning at a medium fluence and high SPA setting allows for patterning of the catalyst such that well defined VA-CNT structures can be achieved with minimal HAZ.

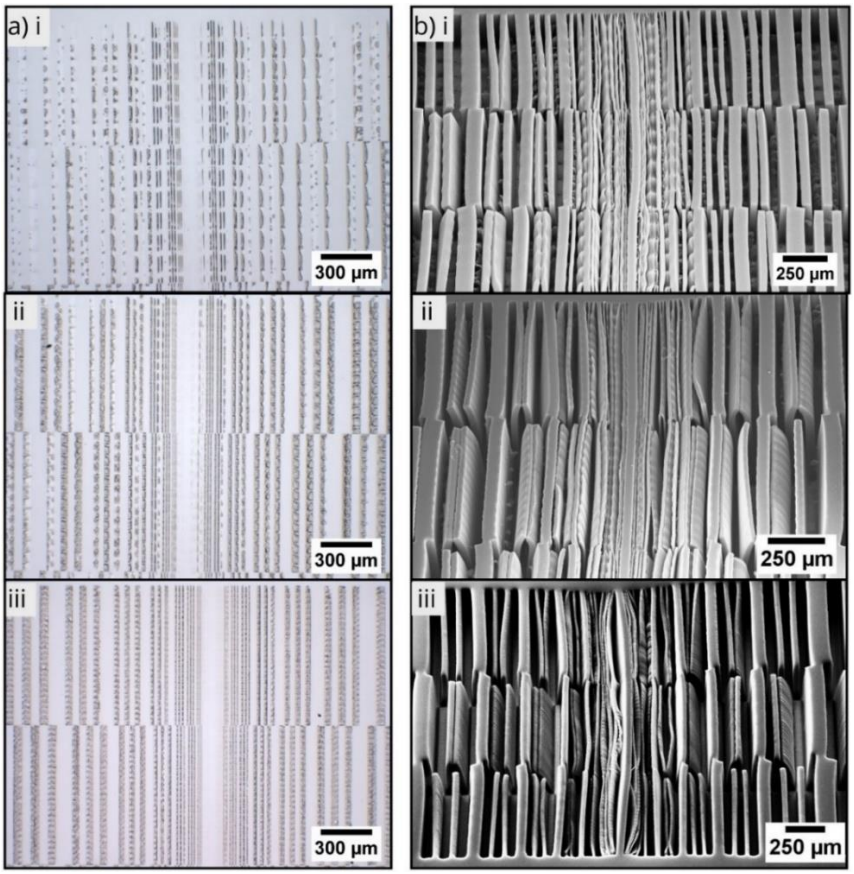

Figure 91: a) *Optical and* ***b)*** *SEM micrographs of lines patterned for features 1 and 11 at fluence 1.6 J/cm² at* ***i)*** *4,* ***ii)*** *8 and* ***iii)*** *16 shots per area.*

Optical and SEM micrographs in Figure 91 show VA-CNTs patterned for features 1 – 11 when scanning at a medium fluence with low, medium and high SPA. It can be seen from the results that by maintaining a medium fluence and varying the SPA, VA-CNT walls with varying thicknesses can be achieved. Even though visually a range of structures can be grown by controlling the SPA and fluence settings, it is important to understand how the patterning affects CNT quality.

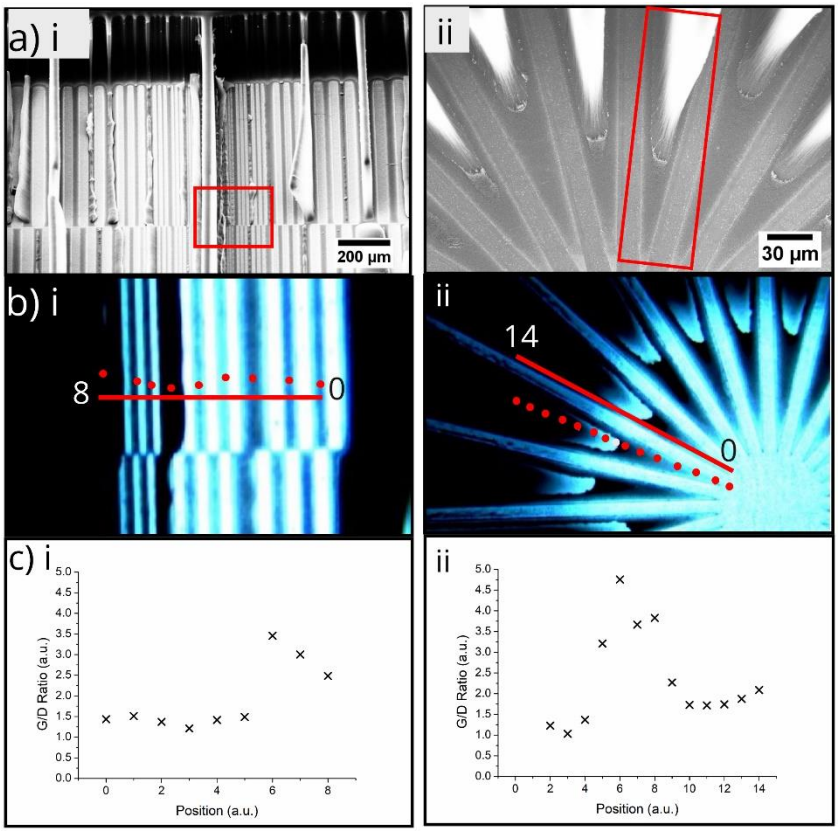

Figure 92: a) *SEM micrographs showing area for Raman analysis,* ***b)*** *optical images showing location of Raman spectra and* ***c)*** *graphical representation of G/D ratios calculated at the position, for features* ***i)*** *11 and* ***ii)*** *patterned at fluence 2.3 J/cm² with 16 SPA. A standard error of < ± 10% was estimated for all ratios calculated.*

Raman analysis was conducted on features 11 and 12 patterned at high fluence and SPA settings, as they give a range of CNT alignment and structures when visually observed via SEM, as shown in Figure 92.a.i and ii. Raman analysis in the marked areas determines whether the quality of the growth structure can be quantified. The locations of the Raman spot analysis can be seen in Figure 92.b.i and ii. It is evident from the G/D ratios calculated

(Figure 92.c.i and ii) that the quality of VA-CNTs can be mapped using Raman spectrometry. It can be seen in the graph shown in Figure 92.c.i, that for feature 12 the quality of the VA-CNTs is greater when analysing between points 5-8. The increase in VA-CNT quality, evidenced by the large G/D ratio is on account of the VA-CNTs growing at an angle, and thus giving a greater signal in the region shown in Figure 92.a.i. When analysing the region marked in Figure 92.b.ii for feature 11, it can be seen that some of the structures are more in focus than the other. This indicates a height variation in the structures grown. Raman spectroscopy is highly dependent on the focus of the laser, so for positions 6-8 a greater G/D ratio is calculated as the structures are more in focus than the structures at position 0-5.

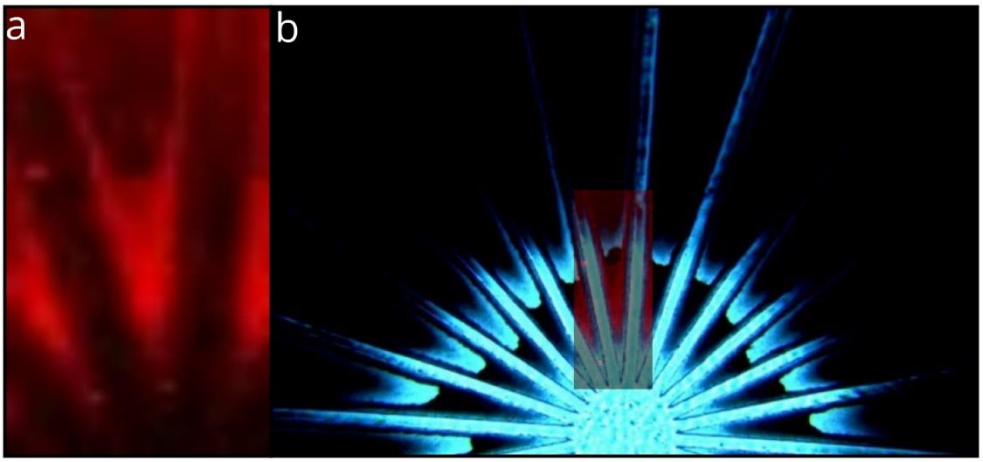

Figure 93: *Optical images showing* ***a)*** *G/D ratio map and* ***b)*** *superimposed G/D ratio map on the selected VA-CNT growth region.*

Raman analysis can also be carried out by constructing a G/D map of a selected VA-CNT growth region as shown in Figure 93. The bright red regions indicate a greater G/D ratio in comparison to the darker regions. The brighter tips shown are on account of the tilted VA-CNTs grown. The results shown in this section clearly indicate that the scan mask imaging set-up can be successfully used to pattern VA-CNTs. The system can be developed in sync with an industrial inkjet printhead to deposit and pattern select areas of catalyst. Raman analysis of VA-CNTs was successful in identifying varying regions of growth. However,

the results might vary for inkjet printed catalyst. Therefore, patterning of inkjet deposited catalyst is required.

The results presented in this section demonstrate the use of a novel and industrially scalable laser patterning technique to pattern catalyst for VA-CNT growth that has not been conducted before. The applicability of an industrial patterning system to create unique VA-CNT structures creates opportunity for developing arrange of different applications. However, before the technique can be optimised with inkjet printed catalyst, it is important to test VA-CNTs grown from inkjet printed catalyst on a preliminary device from where the electrical properties of the VA-CNTs can be confirmed and directions for future devices determined.

5.3.2 Gas Sensing

With the feasibility and specifications of a scalable additive and subtractive technique for depositing and patterning catalyst for VA-CNT growth defined, the next phase requires determining the applicability of VA-CNTs grown from inkjet printed catalyst in sensing applications. So far, all VA-CNTs from inkjet printed catalyst have been grown on a single material. As electrodes connect various materials in a sensor, it is important to determine whether VA-CNTs can be grown across the base material and electrode interface. Molybdenum electrodes were deposited on fused silica chips using e-beam lithography as shown in Figure 94.a.i. Lines of magnetite ink (concentration 2.19 $\%_{w/w}$) were printed across the two electrodes as shown in Figure 94.a.ii. The ink was successfully printed across the molybdenum electrode and fused silica substrate as shown in the optical micrograph in Figure 94.b without any breaking at the interface on account of increased surface wettability from UV treatment. Upon CVD growth, a degradation of VA-CNT height was observed at the interface of the electrode and fused silica substrate, whereas VA-CNT

growth on the fused silica was consistent. This could be on account of diffusion in the molybdenum layer or an increase in catalyst layer thickness, due to the change in wettability.

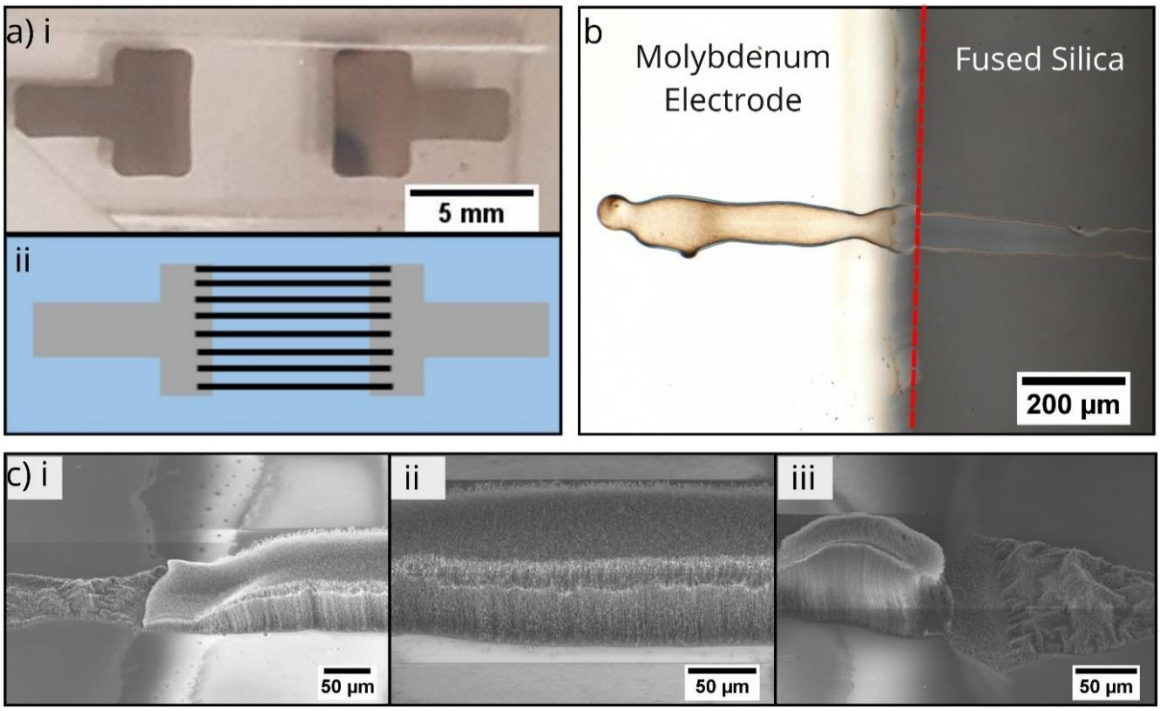

Figure 94: a) i) *Optical micrograph of the 2 electrode fused silica chip and* ***ii)*** *schematic drawing showing the catalyst printed across the electrodes.* ***b)*** *Optical micrograph of magnetite ink concentration 2.19 % $_{w/w}$ printed across the fused silica and molybdenum electrode interface,* ***c)*** *SEM micrographs of VA-CNTS grown across* ***i)*** *the interface of electrode 1 and fused silica substrate,* ***ii)*** *the fused silica substrate and* ***iii)*** *the interface of electrode 2 and fused silica substrate.*

Two gas sensing chips were made. The first gas sensing chip was tested for varying concentrations of humidity, NO2, and NH3. Recipes for the gas sensing experiments can be found in Table E 2 and Table E 3. Results for the gas experiments are shown in the micrographs in Figure 95. It can be seen in Figure 95.a that an initial increase in water vapour flow rate causes the resistance of gas sensor 1 to drop, but no further drops in resistance are visible for further increase in humidity. The initial drop of resistance could be on account of the VA-CNTs adjusting to the sudden flow of gas in the test chamber. A similar result was observed for varying ammonia flow rate, except an initial increase in resistance was observed instead of a decrease seen in the humidity experiments. It can be seen in Figure 95.a and b that the starting resistance of the sensors is different. One of the

lines of the VA-CNTs grown was damaged when removing the chip from the test chamber, resulting in a change in the initial device resistance. When testing the gas sensor with varying concentration of nitrogen dioxide, steps of resistance change were observed at each flow rate introduced evidencing a clear response of the VA-CNTs to change in nitrogen dioxide concentration. However, the sensors does not fully recover between each step and at the end of each test cycle.

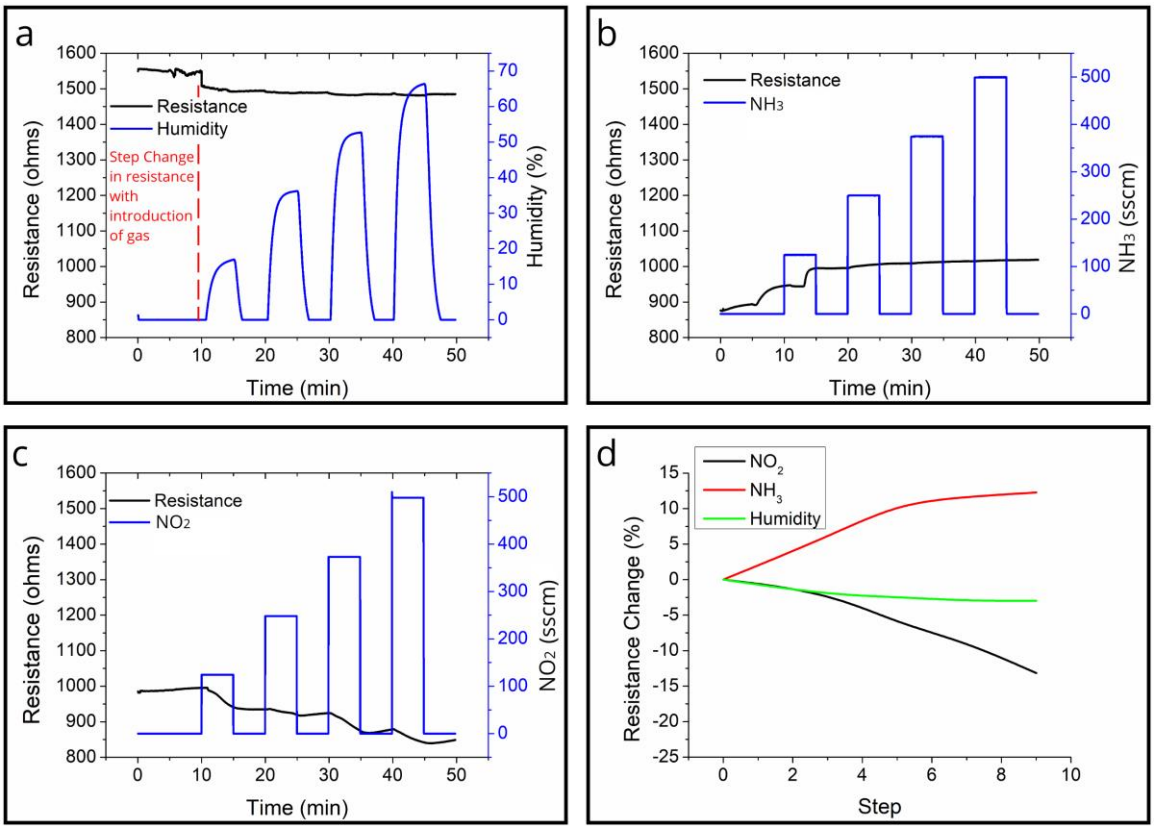

Figure 95: *Graphical Representation of Resistance Change (ohms) vs Gas concentration (%) or flow rate (sccm) for gas sensor 1 when varying a) humidity b) NH_3 and c) NO_2.*

All tests were conducted without any treatment of the VA-CNTs. The effect of gas concentration from the results appear to be irreversible as the original resistance is not achieved during the evacuation period. One of the plausible explanations for this is that as the VA-CNTs have not been densified, the gas becomes entrapped in the forest and the chamber is not being evacuated for long enough for the trapped gas to be released from the CNT structures. Increasing the evacuation time and heating the sample between each test

cycle can help release the trapped gas. Another explanation is that the CNTs are defective and their structure is altered by the gases introduced. Coating and functionalisation of the CNTs with another material can help prevent this, giving more selective sensors.

A second chip was used to test the effects of coating VA-CNTs with iron oxide nanoparticles on gas sensing. Iron oxide has been shown to successfully detect humidity changes, so the effects of coating iron oxide nanoparticles on VA-CNT for gas sensing were studied. The test was conducted in three stages. The first test was conducted on an as grown uncoated chip labelled gas sensor 2. The second test was conducted on the chip by inkjet printing three layers of magnetite ink concentration 14.59 $\%_{w/w}$ and labelled as gas sensor 3. The third test was conducted on the chip by inkjet printing another three layers, equalling in total six layers of magnetite ink suspension 14.59 $\%_{w/w}$ on the VA-CNTs and labelled as gas sensor 4.

The individual graphs of the gas sensing tests for gas sensor 2, 3 and 4 can be found in Figure E 1, 2 and 3. Sensitivity of the sensor to carbon dioxide was also tested. Figure 96 shows graphs comparing percentage resistance change at varying concentrations of humidity, nitrogen dioxide, ammonia and carbon dioxide for gas sensor 2, 3 and 4. It can be seen in Figure 96.a that no visible resistance change occurs when varying humidity and carbon dioxide for uncoated VA-CNTs. A minute increase in resistance can be seen when the concentration of ammonia is increased. Varying the concentration of nitrogen dioxide causes the maximum resistance change in the sensor with the sensor resistance decreasing. When coated with three layers of magnetite nanoparticles, no resistance change was observed when varying carbon dioxide and ammonia as seen in Figure 96.b. However, an increase in resistance was observed when varying humidity. Maximum resistance change occurred when varying the concentration of nitrogen dioxide. Similar trends were observed

when coating the VA-CNTs with six layers of magnetite as seen in Figure 96.c. However, the resistance to varying nitrogen dioxide is less than that observed for three layers of coating.

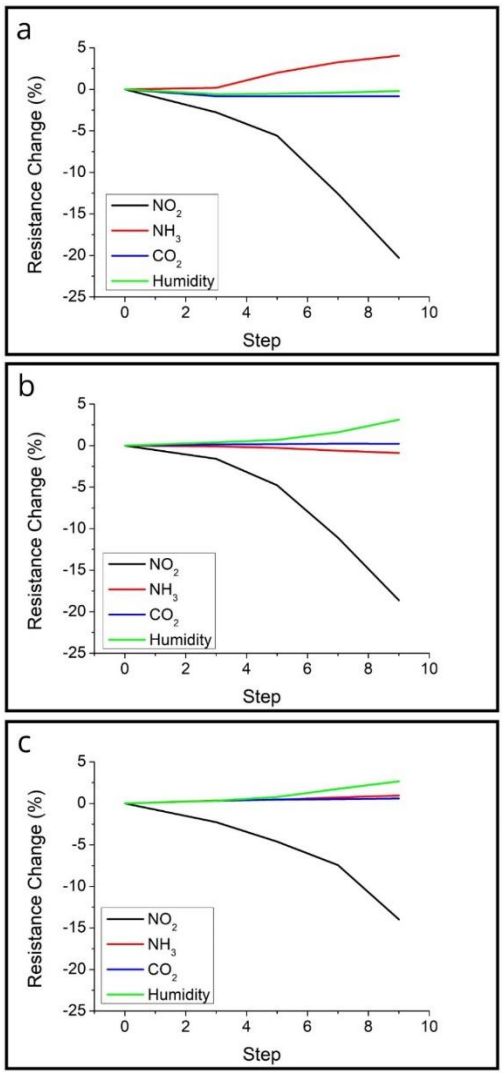

Figure 96: *Graphical representation of percentage resistance change (%) vs gas recipe step for* ***a)*** *uncoated,* ***b)*** *3 layer Fe_3O_4 coated and* ***c)*** *6 layer Fe_3O_4 coated gas sensors.*

The results described above indicate that coating the VA-CNTs with magnetite nanoparticles increases the sensor's response to humidity, but dampens it to ammonia. Graphs comparing the responses of sensors 2, 3 and 4 can be seen in Figure 97. Figure 97.a. shows that upon coating the VA-CNTs the response to humidity increases, whereas in Figure 97.b it can be seen that the sensor's response to ammonia decreases. No significant response change is observed for carbon dioxide and nitrogen (Figure 97.c and d). The

results show that the VA-CNT gas sensors can be made more selective by coating or functionalising them with other materials such as metal oxides. However, the gas sensor did not fully recover between each test cycle. Heat and evacuation cycles were run to ensure all gases trapped were released before each run. Densification of VA-CNTS can prevent entrapment of gases, albeit the surface area of the forest is reduced. Further detailed testing is required to determine what chemical and structural changes can be made to the VA-CNTs grown to develop a reusable and selective gas sensor.

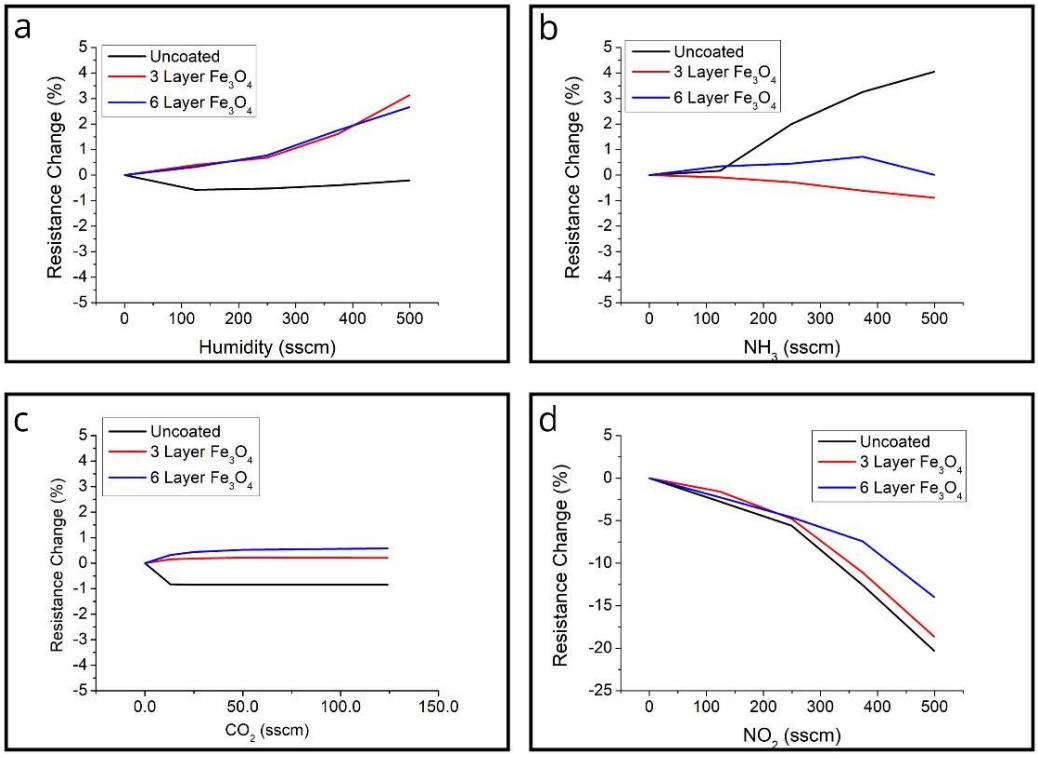

Figure 97: *Graphical representation of percentage resistance percentage change (%) vs gas flow rate (sccm) for comparing gas sensors 2, 3 and 4 when varying concentration of* ***a)*** *humidity,* ***b)*** *NH3,* ***c)*** *CO2 and* ***d)*** *NO2.*

Therefore, it can be concluded that VA-CNTs grown from inkjet printed catalyst are suitable for incorporation in sensors. The inherent sensitivity of the CNTs to nitrogen dioxide make it a suitable candidate for development of NOx sensors. The CNTs can also be coated with biological materials for electrochemical biosensor applications. Integration of the printing and the SMI patterning technique can allow for a host of materials to be deposited and patterned, hence enabling future development of lab-on-a-chip systems.

5.4 Conclusions

The results presented in this chapter encompass the initial stages of the conceptualisation phase, where an industrial laser patterning techniques was explored for patterning iron catalyst for VA-CNT growth, and the suitability of VA-CNTs grown from inkjet printed catalyst tested for gas sensing applications. The SMI system used is a completely novel set-up designed by M-Solve Ltd. and has never been used for the processing of nanomaterials. The raster scan laser patterning methodology proved suitable for patterning catalyst for VA-CNT growth. Although the SMI system is not a digital technique, the top hat beam profile achieves greater feature resolution than the satsuma Gaussian beam. The fluence and SPA settings can be changed to achieve a range of VA-CNT structures. However, the masks can be configured to have multiple sensor array designs.

Gas sensing experiments revealed that VA-CNTs grown from inkjet printed catalyst can be used for sensing NO_2 and NH_3 gases, with an increase in resistance observed when increasing NH_3 concentration and decrease in resistance observed when increasing NO_2 concentration. No response to CO_2 was observed. When layers of magnetite nanoparticles were printed on the VA-CNTs, the CNTs were modified such that no more detection of NH_3 was achieved. However, an increase in resistance was observed in response to increasing humidity. This trend was expected as iron oxide nanoparticles have been reported in literature to respond to humidity changes. The sensor had to be heated under vacuum to release absorbed gases indicating poor recovery. Therefore, the VA-CNTs require either plasma treatment, densification, or coating and functionalisation of other materials to reduce recovery time. The greatest response of the VA-CNTs was to NO_2, indicating scope for NOx sensor development.

The SMI and gas sensing results are a pathway for scalable future development of nanomaterial based sensors. The SMI technique gives a new direction for patterning large scale chips for VA-CNT growth. The gas sensing experiments on the other hand set up a base for developing other biosensing devices. This manufacturing methodology is particularly advantageous for developing lab-on-a-chip systems as multiple materials can be patterned at the same time. Nonetheless, many biosensing applications require functionalisation of the CNTs. Therefore, techniques such as spray systems and functionalisation methodologies need to be developed for coating the sensors with suitable materials. As functionalisation of the CNTs is dependent on the sensing application, these applications have to be developed in parallel to the scale-up, and is outside the scope of the project. The next chapter summaries the findings of this thesis. The chapter also discusses the steps required to further develop this new hybrid inkjet deposition of catalyst and laser patterning methodology for fabricating VA-CNT devices.

Chapter 6

RESEARCH OUTCOMES

At the beginning of this thesis, a gap was identified in the scalable manufacture of VA-CNTs for applications in industry. In this research a hybrid additive and subtractive direct-write digital fabrication platform has been developed to deposit and pattern catalyst for VA-CNT Growth. Inkjet printing has been explored as the additive technology for depositing magnetite nanoparticles as catalyst and laser ablation has been studied as a patterning technique to grow VA-CNTs structures using chemical vapour deposition as an assistive growth procedure. In order to design scalable VA-CNT device fabrication strategies, it was determined that a combination of research methodologies is required to address VA-CNT manufacturing challenges. Therefore Pugh's six stages of design were combined with the U.S DoD's defined TRLs and MRLs, to develop a research framework that allows for minimal risk technology transfer. The research frame was divided into six phases: feasibility, specification, conceptualisation embodiment, detail design and release. It was determined that lab based research for nanotechnology scale-up can only develop fabrication techniques and devices till the conceptualisation phase. The research conducted in each phase are highlighted below.

- Feasibility Phase: CVD growth conditions and characterisation techniques optimised and catalyst ink formulations made.
- Specification Phase: Additive inkjet printing technique and subtractive laser patterning technique defined and verified for VA-CNT growth using magnetite nanoparticles.

- Conceptualisation Phase: Development of a test sensor and incorporation of industrial technologies in the manufacturing process chain.

A knowledge base of the nanomaterials (CNTs and magnetite nanoparticles), inkjet printing, laser patterning and CVD techniques was built by analysing existing literature to understand the questions required to be answered at each development stage. The scientific findings for each phase have been summarised and future research goals identified in the sections below.

6.1 Summary of Findings

This section summarises findings from each phase of development.

6.1.1 Feasibility Phase

In the feasibility phase of development, the non-variable operating conditions for the assistive CVD growth technique were established. The growth conditions were first optimised for PVD deposited iron thin films as catalyst. It was found that for repeatable growth of VA-CNTs, it is necessary to condition the quartz tube in which samples are grown. Raman spectroscopy was used to verify growth of CNTs. The PVD deposited catalyst samples were then grown in the presence of the magnetite ink and early catalyst activity termination was observed. Upon comparison of the annealed PVD deposited catalyst and magnetite nanoparticle films, it was observed that the magnetite ink films formed larger catalyst nano-islands during annealing than those formed with PVD deposited iron films. Therefore, when transitioning from metal thin films to nanoparticles films as catalyst it is critical to control the thickness of the films to ensure the correct range of catalyst nano-island size is achieved for VA-CNT growth. The magnetite ink was diluted into 7 formulations. Surface tension measurements indicated the presence of a surfactant,

but the exact nature of the surfactant is unknown. The size of the magnetite nanoparticles was verified by TEM and XRD to be 9.3 ± 0.6 nm. Characterisation of the magnetite nanoparticle ink was conducted to not only verify supplier specifications, but also determine its behaviour during inkjet printing.

6.1.2 Specification Phase

In the specification phase of development two technologies were explored inkjet printing and ultrafast laser patterning.

6.1.2.1 Inkjet Printing – Additive Technology

It was determined that by controlling the inkjet parameters and substrate conditions, layers of iron oxide nanoparticles can be deposited. A maximum height of 93.0 ± 0.9 µm was observed via SEM for VA-CNTs grown when printing ink concentration 2.19 $\%_{w/w}$ on UV treated and 10 nm alumina coated silicon substrates at a 45 µm droplet spacing. Although successfully printed with the 20 µm Dimatix print nozzles, it was difficult to print the ink using nozzles of larger sizes as instabilities were observed via HIS, on account of the high water content of the ink. Therefore, in order to scale-up the inkjet printing technique for depositing iron nanoparticles as catalyst, it is important to optimise the technique on industrial printheads. FIB, AFM and optical microscopy were used to analyse the volume of the ink deposited and post annealing analysis using SEM identified the size of the active catalyst nano-islands formed to be of a mean diameter of 31.3 ± 34.2 nm. Although the standard deviation is high, the particle packing is such that it allows alignment of CNTs grown from smaller nano-islands.

6.1.2.2 Laser Patterning – Subtractive Technology

When laser patterning e-beam deposited catalyst with the satsuma it was determined that a minimum path distance of 5 µm was required to ensure VA-CNTs were grown with height and alignment consistent with that of the bulk forest. The effects on the catalyst surrounding the laser spot were observed to undergo modification, annealing and ablation as fluence was increased. This behaviour is indicative of a Gaussian beam profile of the laser. It was found that as patterning fluence was increased, the size of the nano-islands formed during annealing also increased, causing VA-CNT height and alignment to decrease. It was determined that a fluence range of 0.48 J/cm^2 and 0.64 J/cm^2 should be used when patterning e-beam deposited catalyst with the satsuma femtosecond laser. For inkjet printed catalysts it was found that for thicker catalyst layer, increasing the fluence improved VA-CNT height and alignment, whereas for thinner catalyst layers it resulted in degradation of forest height and alignment. As fluence is increased redeposition of catalyst as observed during SEM and EDX analysis causes variation in nano-island size formed during CVD annealing and the VA-CNTs grown. It was found that when growing VA-CNTs from inkjet printed catalyst, a magnetite ink concentration of 2.19 %$_{w/w}$ should be printed on UV treated 10ASW substrates and patterned using the satsuma ultrafast laser at a fluence of 0.73 J/cm^2. The post annealing catalyst nano-island size of the e-beam deposited catalyst was calculated to be 1.5 ± 0.1 nm, whereas that of inkjet printed catalyst was calculated to be 15.01 ± 17.9 nm for growing VA-CNTs. This indicates that the size of the catalyst nano-islands formed during annealing, although important, has a critical range rather than a critical size. The inkjet printing system can also be configured for growth on multiple substrates such as fused silica.

The results of the specification phase indicate that inkjet printing and laser ablation can be used to deposit magnetite nanoparticles as catalyst for VA-CNT growth. It was found that the range of the catalyst nano-islands formed is key for achieving alignment of CNTs. With the feasibility of techniques and specification of conditions proven for VA-CNT growth using a hybrid inkjet, laser ablation and CVD system, the transition of these scientific findings was tested on industrial systems and conceptual applications.

6.1.2 Conceptualisation Phase

TRLs, MRLs and Pugh's six stages of design were analysed to determine that the conceptualisation phase should be conducted half in the lab and half at industrial scale to allow the smooth transition of concepts to the detailed phase. An industrial Scan Mask Imaging system by M-Solv Ltd. was tested for patterning e-beam deposited catalyst. The laser with a top hat profile achieved greater feature resolution than the Satsuma Gaussian beam. M-Solv have already developed a configurable inkjet and laser hybrid system for photovoltaic applications. Their lasers and printheads can be combined according to specifications, making the SMI system ideal for applications in multiple sensor array designs.

VA-CNTs were grown from inkjet deposited catalyst on fused silica samples for gas sensing applications. The device was tested for detection of NH_3, NO_2, CO_2 and humidity. The highest resistance change was observed when varying NO_2 concentration for uncoated VA-CNTs. However, coating the VA-CNTs by printing magnetite nanoparticles improved their detection of humidity and reduced detection of NH_3. No signal change was observed when varying CO_2. The gas sensing experiments show potential for the VA-CNTs to be used for sensing applications. Many VA-CNT applications have been developed before at research level. However, the main challenge of utilising VA-CNTs at industrial scale is

their fabrication and growth. Therefore, before applications can be developed the VA-CNT production has to be developed at industrial scale.

6.2 Future Work

Fabrication limitations have previously hindered exploitation of VA-CNTs. The research conducted in this thesis successfully presents the scope for non-contact, digital fabrication of VA-CNTs. The research presents a new inkjet and laser manufacturing system for deposition and patterning of iron oxide nanoparticles as catalyst for VA-CNT growth. The proof and development of technology has been conducted up until the conceptualisation phase. However, as previously highlighted, it is important to further investigate this fabrication methodology at industrial scale, but is outside the scope of this thesis. It is also essential to identify techniques, models and experimentation that can be improved or added to the process chain.

6.2.1 CVD Growth – Assistive Technology

The CVD system used in this thesis is a custom built set-up that can only process two 1 cm x 1 cm chips at a time. For large scale production an industrial CVD system is required that can give repeatable VA-CNT growth over multiple samples and growth cycles. Preparing samples for XRD or EDX analysis proved difficult as the substrates had to be removed from the CVD set-up for analysis upon which air exposure resulted in changes in the catalyst surface. Therefore, in order to better understand the CVD growth mechanism of inkjet printed and laser patterned iron oxide nanoparticles for VA-CNT growth, *in situ* analysis is necessary. The CVD system in the NanoManufacturing group has been based on the set up in Prof. John Hart's Mechanosynthesis group, at University of Michigan. Hence, a collaboration should be initiated to analyse catalyst evolution with the GI-SAXS.

This detailed understanding of the growth mechanism will allow further development to improve VA-CNT growth rates.

6.2.2 Inkjet Printing – Additive Technology

Inkjet printing although successful with the 21.5 μm nozzle diameter Dimatix printer proved difficult when printing with a larger Microfab nozzle of 80 μm on account of instabilities during droplet formation. When scaling up to an industrial printer it is important to use a similar nozzle size and jetting conditions. In order to ensure minimal variations during scale-up a model can be developed that will take into consideration not just the print conditions, such as those defined by Beard *et al.* (2013), but also the flow conditions of the ink during droplet formation and impact [48]. This model can then be used for simulations and other detailed studies to further optimise printing.

It was determined in Chapter 3 that inkjet printing while suitable for depositing localised catalyst is not suitable for large area deposition. Hence, other digital techniques such as spray systems can be explored for large area deposition of catalyst [309], [310]. When depositing nanoparticle inks, achieving thickness uniformity within a nanometre range is difficult over several micrometres or millimetres [15]. Other techniques can be employed to deposit material over these length scales. Carbon nanotubes have been grown from catalyst deposited using a range of different techniques such as spin coating, laser printing, blade casting and roll-to- roll printing [143], [180], [311], [312] However, none of the techniques fully provide the non-contact and digital advantages of inkjet printing. Therefore, other techniques can be explored for large area deposition of catalyst such as the microfluidic spray nozzle developed by Kartanas *et al.* (2017) as part of a label free biosensing MEMs device [313]. The spray system can also be used to deposit other materials, such as coatings for CNTs.

6.2.3 Laser Patterning – Subtractive Technology

Although ultrafast ablation was used to successfully pattern VA-CNTs, the processing times are slow and thermal effects around the laser spot were observed. Therefore, the SMI system, with a top hat profile was tested and proved more suitable for large scale processing. The SMI experiments were only conducted on PVD deposited iron catalyst and need to be optimised for inkjet printing catalyst. Detailed particle analysis is required to be conducted for an in-depth understanding of how the scanning beam affects the catalyst functionality. However, these experiments have to be conducted with consultation of M-Solv Ltd.

6.2.4 Sensor Development

Hybrid inkjet and laser patterning technique gives scope for combining a range of materials to develop complex arrays for biosensing applications and scope for developing lab-on-a-chip systems. With a scalable manufacturing methodology defined, the findings from this research give an array of opportunities to researchers in the future for developing applications that exploit the sensing capability of VA-CNTS. As the gas sensors tested proved suitable for detecting NO_2, the devices can be optimised for NOx detection. However, functionalisation or coating of the VA-CNTs with additional nanomaterials and polymers is required to make the sensors more selective and to improve recovery times. CNT have also been used for electrochemical biosensing [38], [314]. Therefore, applications for biosensors should also be explored with functionalisation of VA-CNTS with biological materials tested i.e. glucose oxidase. The application and fabrication technology have to be developed in parallel to ensure that any additional functionalisation or coating steps can be incorporated into the assembly line. A flow chart outlining guidelines for achieving this has been shown in 98. The guidelines show a basic process flow for developing a biological or gas sensor. With the feasibility of using a hybrid inkjet printing and laser patterning technique for growing VA-CNTs already determined, the flow

chart represents the phases of development of a VA-CNT based biological or gas sensor starting at the specification phase and ending at the detailed design phase. The guidelines presented are applicable to the development of any biosensor or gas sensor, and thus require the addition of detailed steps specific to the application being developed.

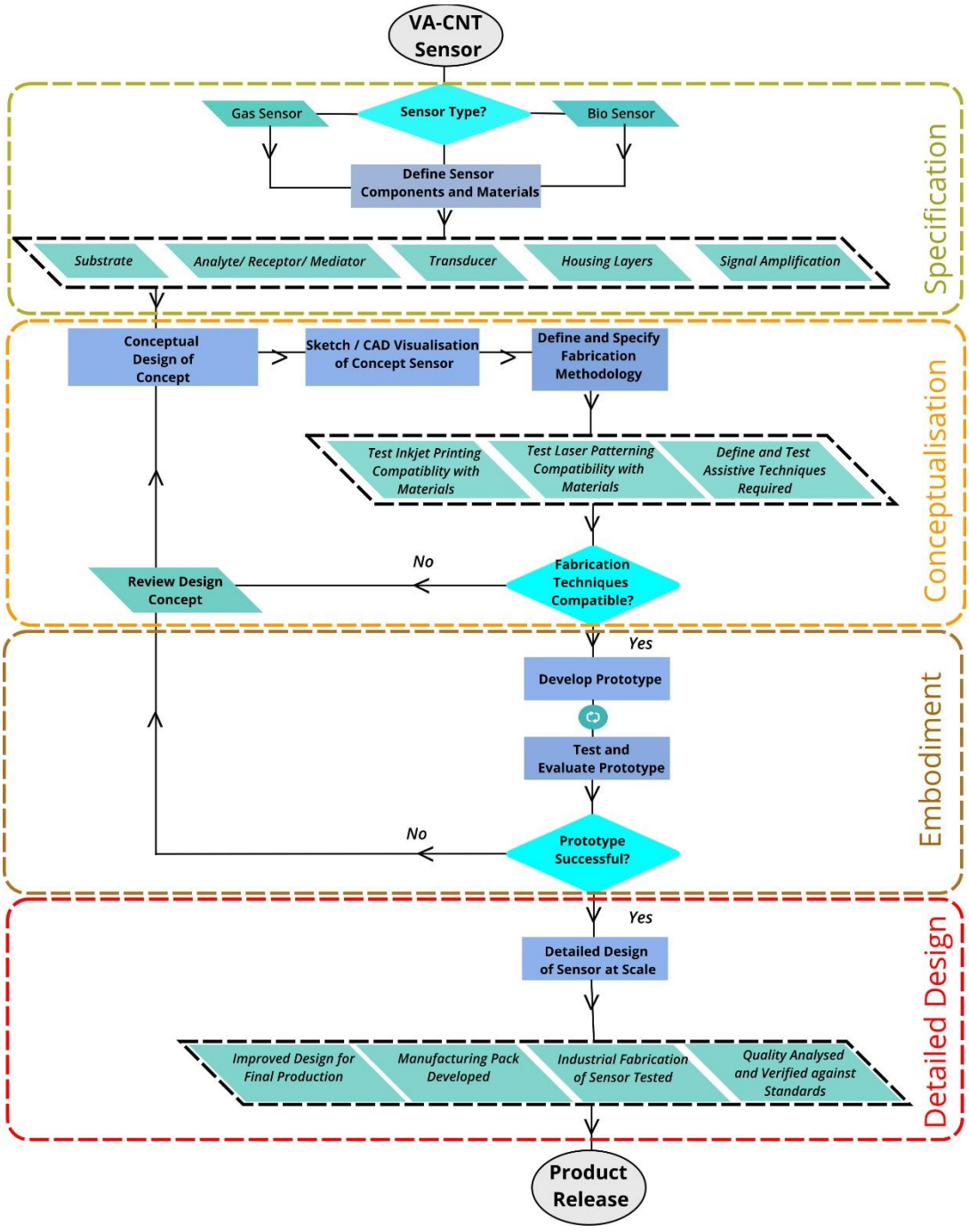

98: *Flowchart for developing sensor.*

References

[1] M. Reibold, P. Paufler, A. A. Levin, W. Kochmann, N. Pätzke, and D. C. Meyer, "Materials: Carbon Nanotubes in an Ancient Damascus Sabre," *Nature*, vol. 444, no. 7117, p. 286, Nov. 2006.

[2] R. W. Whatmore, "Nanotechnology:Big Prospects for Small Engineering," *Ingenia*, vol. 9, pp. 28–34, 2001.

[3] K. K. B. Hon, L. Li, and I. M. Hutchings, "Direct Writing Technology—Advances and Developments," *CIRP Ann. - Manuf. Technol.*, vol. 57, pp. 601–620, 2008.

[4] M. C. Roco, "International Strategy for Nanotechnology Research and Development," *J. Nanoparticle Res.*, vol. 3, pp. 353–360, 2001.

[5] K. Du, I. Wathuthanthri, and C.-H. Choi, "The Rise of Scalable Micro/Nanopatterning," *Micromachines*, vol. 8, no. 9, p. 275, Sep. 2017.

[6] M. C. Roco, C. A. Mirkin, and M. C. Hersam, "Nanotechnology Research Directions for Societal Needs in 2020: Summary of International Study," *J. Nanoparticle Res.*, vol. 13, no. 3, pp. 897–919, 2011.

[7] S. Lenhert, P. Sun, Y. Wang, H. Fuchs, and C. A. Mirkin, "Massively Parallel Dip-Pen Nanolithography of Heterogeneous Supported Phospholipid Multilayer Patterns," *Small*, vol. 3, no. 1, pp. 71–75, Jan. 2007.

[8] E. B. Brousseau, S. S. Dimov, and D. T. Pham, "Some Recent Advances in Multi-Material Micro-and Nano-Manufacturing," *Int. J. Adv. Manuf. Technol.*, vol. 47, no. 1–4, pp. 161–180, 2010.

[9] S. Dimov, E. Brousseau, R. Minev, and S. Bigot, "Micro-and nano-Manufacturing: Challenges and Opportunities," *Proc. Inst. Mech. Eng. Part C J. Mech. Eng. Sci.*, vol. 226, no. 1, pp. 3–15, 2011.

[10] R. Ameloot, "Digital Fabrication in Catalytic Technology," in *Nanotechnology in Catalysis*, Weinheim, Germany: Wiley-VCH Verlag GmbH & Co. KGaA, 2017, pp. 359–382.

[11] J. A. Lewis and G. M. Gratson, "Direct Writing in Three Dimensions," *Mater. Today*, vol. 7, pp. 32–39, 2004.

[12] C. Thiele and R. Das, "Carbon Nanotubes and Graphene for Electronics Applications 2010-2020," 2010.

[13] "Nanoscience and Nanotechnologies: Opportunities and Uncertainties," *R. Soc. R. Acad. Eng.*, p. 127, 2004.

[14] O. Heinz, M. Aghajani, A. R. Greenberg, and Y. Ding, "Surface-Patterning of Polymeric Membranes: Fabrication and Performance," *Curr. Opin. Chem. Eng.*, vol. 20, pp. 1–12, Jun. 2018.

[15] A. Matavž and B. Malič, "Inkjet Printing of Functional Oxide Nanostructures From

Solution-Based Inks," *J. Sol-Gel Sci. Technol.*, pp. 1–21, Jun. 2018.

[16] P. Gao, A. Hunter, M. J. Summe, and W. A. Phillip, "A Method for the Efficient Fabrication of Multifunctional Mosaic Membranes by Inkjet Printing," *ACS Appl. Mater. Interfaces*, vol. 8, no. 30, pp. 19772–19779, Aug. 2016.

[17] A. Piqué and D. B. Chrisey, *Direct-Write Technologies for Rapid Prototyping Applications: Sensors, Electronics and Integrated Power Sources*. Academic Press, 2002.

[18] S. Wang, Y. Yu, H. Liu, K. T. P. Lim, B. M. Srinivasan, Y. W. Zhang, and J. K. W. Yang, "Sub-10-nm Suspended Nano-Web Formation by Direct Laser Writing," *Nano Futur.*, May 2018.

[19] D. T. Pham, S. S. Dimov, P. V Petkov, and S. P. Petkov, "Laser Milling," *Proc. Inst. Mech. Eng. Part B J. Eng. Manuf.*, vol. 216, no. 5, pp. 657–667, 2002.

[20] I. Gibson, D. W. Rosen, and B. Stucker, *Additive Manufacturing Technologies : Rapid Prototyping to Direct Digital Manufacturing*. Springer, 2010.

[21] M. J. Pitkethly, "Nanomaterials – The Driving Force," *Mater. Today*, vol. 7, no. 12, pp. 20–29, Dec. 2004.

[22] C. Jianrong, M. Yuqing, H. Nongyue, W. Xiaohua, and L. Sijiao, "Nanotechnology and Biosensors," *Biotechnol. Adv.*, vol. 22, no. 7, pp. 505–518, 2004.

[23] M. F. L. De Volder, S. H. Tawfick, R. H. Baughman, and A. J. Hart, "Carbon Nanotubes: Present and Future Commercial Applications," *Science (80-.).*, vol. 339, no. 6119, pp. 535–539.

[24] K. Banerjee, H. Li, and N. Srivastava, "Current Status and Future Perspectives of Carbon Nanotube Interconnects," *8th IEEE Conf. Nanotechnol.*, pp. 432–436, 2008.

[25] S.-J. Han, J. Tang, B. Kumar, A. Falk, D. Farmer, G. Tulevski, K. Jenkins, A. Afzali, S. Oida, J. Ott, J. Hannon, and W. Haensch, "High - Speed Logic Integrated Circuits with Solution-Processed Self-Assembled Carbon Nanotubes," *Nat. Nanotechnol.*, vol. 12, pp. 861–865, Jul. 2017.

[26] C. P. Bergmann and M. J. de. Andrade, *Nanostructured Materials for Engineering Applications*. Springer, 2011.

[27] A. Javey and J. Kong, *Carbon Nanotube Electronics*. Springer Science and Business Media, 2009.

[28] L. Vaisman, H. D. Wagner, and G. Marom, "The Role of Surfactants in Dispersion of Carbon Nanotubes," *Adv. Col*, vol. 128, pp. 37–46, 2007.

[29] P.-C. Ma, N. A. Siddiqui, G. Marom, and J.-K. Kim, "Dispersion and Functionalization of Carbon Nanotubes for Polymer-Based Nanocomposites: A Review," *Compos. Part A*, vol. 41, pp. 1345–1367, 2010.

[30] X. Z. Ding, L. Huang, X. T. Zeng, S. P. Lau, B. K. Tay, W. Y. Cheung, and S. P. Wong, "Catalytic Chemical Vapor Deposition of Vertically Aligned Carbon Nanotubes on Iron Nanoislands formed from Fe+- Implanted SiO2 Films," *Carbon N. Y.*, vol. 42, no. 14, pp. 3030–3033, 2004.

[31] Z. Ren, Y. Lan, and Y. Wang, “Aligned Carbon Nanotubes: Physics, Concepts, Fabrication and Devices,” *NanoScience and Technology*. Springer Science and Business Media, 2013.

[32] C.-M. Seah, S.-P. Chai, and A. R. Mohamed, “Synthesis of Aligned Carbon Nanotubes,” *Carbon N. Y.*, vol. 49, no. 14, pp. 4613–4635, 2011.

[33] S. Sakurai, H. Nishino, D. N. Futaba, S. Yasuda, T. Yamada, A. Maigne, Y. Matsuo, E. Nakamura, M. Yumura, and K. Hata, “Role of Subsurface Diffusion and Ostwald Ripening in Catalyst Formation for Single-Walled Carbon Nanotube Forest Growth,” *J. Am. Chem. Soc.*, vol. 134, no. 4, pp. 2148–2153, 2012.

[34] J.-P. Tessonnier and D. S. Su, “Recent progress on The growth Mechanism of Carbon Nanotubes: A Review.,” *ChemSusChem*, vol. 4, no. 7, pp. 824–847, 2011.

[35] A. R. Harutyunyan, G. Chen, T. M. Paronyan, E. M. Pigos, O. A. Kuznetsov, K. Hewaparakrama, S. M. Kim, D. Zakharov, E. A. Stach, and G. U. Sumanasekera, “Preferential Growth of Single-Walled Carbon Nanotubes with Metallic Conductivity,” *Science (80-.).*, vol. 326, no. 5949, pp. 116–120, 2009.

[36] A. A. Puretzky, D. B. Geohegan, S. Jesse, I. N. Ivanov, and G. Eres, “In Situ Measurements and Modeling of Carbon Nanotube Array Growth Kinetics During Chemical Vapor Deposition,” *Appl. Phys. A*, vol. 81, no. 2, pp. 223–240, Jul. 2005.

[37] A. Börjesson and K. Bolton, “First Principles Studies of the Effect of Ostwald Ripening on Carbon Nanotube Chirality Distributions,” *ACS Nano*, vol. 5, no. 2, pp. 771–779, 2011.

[38] J. Wang, “Carbon-Nanotube Based Electrochemical Biosensors: A review,” *Electroanalysis*, vol. 17, no. 1, pp. 7–14, 2005.

[39] Y. Yoon, G. S. Lee, K. Yoo, and J. B. Lee, “Fabrication of a Microneedle/CNT Hierarchical Micro/Nano Surface Electrochemical Sensor and Its In-Vitro Glucose Sensing Characterization,” *Sensors*, vol. 13, no. 12, pp. 16672–16681, 2013.

[40] R. H. Baughman, A. a Zakhidov, and W. a de Heer, “Carbon Nanotubes - The Route Toward Applications,” *Science (80-.).*, vol. 297, pp. 787–92, 2002.

[41] D. N. Futaba, K. Hata, T. Yamada, T. Hiraoka, Y. Hayamizu, Y. Kakudate, O. Tanaike, H. Hatori, M. Yumura, and S. Iijima, “Shape-Engineerable and Highly Densely Packed Single-Walled Carbon NAnotubes and their Applications as Super-Capacitor Electrodes,” *Nat. Mater.*, vol. 5, no. 12, pp. 987–994, 2006.

[42] G. Barbillon, F. Hamouda, and B. Bartenlian, “Large Surface Nanostructuring by Lithographic Techniques for Bioplasmonic Applications,” in *Manufacturing Nanostructures*, W. Ahmed and N. Ali, Eds. One Central Press (OCP), 2014, pp. 245–260.

[43] A. Roch, T. Roch, E. R. Talens, B. Kaiser, A. Lasagni, E. Beyer, O. Jost, G. Cuniberti, and A. Leson, “Selective laser treatment and laser patterning of metallic and semiconducting nanotubes in single walled carbon nanotube films,” *Diam. Relat. Mater.*, vol. 45, pp. 70–75, 2014.

[44] K. Kwok and W. K. S. Chiu, “Growth of Carbon Nanotubes by Open-Air Laser-Induced Chemical Vapor Deposition,” *Carbon N. Y.*, vol. 43, no. 2, pp. 437–446, 2005.

[45] L. L. Lebel, B. Aissa, M. A. El Khakani, and D. Therriault, “Ultraviolet-Assisted Direct-Write Fabrication of Carbon Nanotube/Polymer Nanocomposite Microcoils,” *Adv. Mater.*, vol. 22, no. 5, pp. 592–596, Feb. 2010.

[46] M. Mansoor, I. Kinloch, and B. Derby, “Inkjet Printing of Catalyst-Inks on Si Wafers and the Subsequent Synthesis of Carbon Nanotubes by Chemical Vapour Deposition,” *Key Eng. Mater.*, vol. 442, pp. 7–14, 2010.

[47] C. Chatzikomis, S. W. Pattinson, K. K. K. Koziol, and I. M. Hutchings, “Patterning of Carbon Nanotube Structure by Inkjet Printing of Catalyst,” *J. Mater. Sci.*, vol. 47, no. 15, pp. 5760–5765, 2012.

[48] J. D. Beard, J. Stringer, O. R. Ghita, and P. J. Smith, “High Yield Growth of Patterned Vertically Aligned Carbon Nanotubes Using Inkjet-Printed Catalyst,” *Appl. Mater. Interfaces*, vol. 5, pp. 9785–9790, 2013.

[49] P. Li, N. Lei, D. A. Sheadel, J. Xu, and W. Xue, “Integration of Nanosensors into a Sealed Microchannel in a Hybrid Lab-on-a-chip Device,” *Sensors Actuators B Chem.*, vol. 166, pp. 870–877, 2012.

[50] E. B. Brousseau, R. Barton, S. Dimov, and S. Bigot, “Technology Maturity Assessment of Micro and Nano Manufacturing Processes,” *Proc. M*, vol. 4, pp. 23–25, 2009.

[51] P. C. Vella, S. S. Dimov, R. Minev, and E. B. Brousseau, “Technology Maturity Assessment of Micro and Nano Manufacturing Processes and Process Chains,” *Proc. Inst. Mech. Eng. Part B J. Eng. Manuf.*, vol. 0954405416, p. 22, 2016.

[52] J. Smith, “An Alternative to Technology Readiness Levels for Non-Developmental Item (NDI) Software,” *Syst. Sci. 2005. HICSS’05. Proc. 38th Annu. Hawaii Int. Conf. IEEE*, p. 315a–315a, 2005.

[53] K. Cooper and Khershed, “Scalable Nanomanufacturing—A Review,” *Micromachines*, vol. 8, no. 1, p. 20, Jan. 2017.

[54] S. Desai, P. De, and F. Gomes, “Design for Nano/Micro Manufacturing: A Holistic Approach Towards Achieving Manufacturing Excellence.”

[55] H. Chen, A. Roy, J.-B. Baek, L. Zhu, J. Qu, and L. Dai, “Controlled Growth and Modification of Vertically-Aligned Carbon Nanotubes for Multifunctional Applications,” *Mater. Sci. Eng. R*, vol. 70, pp. 63–91, 2010.

[56] E. Van Hooijdonk, C. Bittencourt, R. Snyders, and J.-F. Colomer, “Beilstein Journal of Nanotechnology,” *Beilstein J. Nanotechnol.*, vol. 4, no. 1, pp. 129–152, Feb. 2013.

[57] W.-S. Chu, C.-S. Kim, H.-T. Lee, J.-O. Choi, J.-I. Park, J.-H. Song, K.-H. Jang, and S.-H. Ahn, “Hybrid Manufacturing in Micro/Nano Scale: A Review,” *Int. J. Precis. Eng. Manuf. Technol.*, vol. 1, no. 1, pp. 75–92, 2014.

[58] G. Kumari, “Role of Nanotechnology for Crop Protection in Horticultural Crops.” p. 64, 2015.

[59] B. Godin, “The Linear Model of Innovation The Historical Construction of an Analytical Framework,” *Sci. Technol. Hum. Values*, vol. 31, no. 6, pp. 639–667, 2006.

[60] M. D. Mehta, “Nanoscience and Nanotechnology: Assessing the Nature of Innovation in These Fields What Is Nanotechnology?,” *Bull. Sci. Technol. Soc.*, vol. 22, pp. 269–273, 2002.

[61] J. L. Woolley and R. M. Rottner, “Innovation Policy and Nanotechnology Entrepreneurship,” *Entrep. Theory Pract.*, vol. 32, no. 5, pp. 791–811, Sep. 2008.

[62] J. Schoen, T. Mason, W. Kline, and R. Bunch, “The Innovation Cycle: A New Model and Case Study for the Invention to Innovation Process,” *Eng. Manag. J.*, vol. 17, no. 3, p. 10, 2005.

[63] J. D. Linton and S. T. Walsh, “A Theory of Innovation for Process-Based Innovations Such As Nanotechnology,” *Technol. Forecast. Soc. Change*, vol. 75, no. 5, pp. 583–594, Jun. 2008.

[64] N. Islam and K. Miyazaki, “Nanotechnology Innovation System: Understanding Hidden Dynamics of Nanoscience Fusion Trajectories,” *Technol. Forecast. Soc. Change*, vol. 76, no. 1, pp. 128–140, Jan. 2009.

[65] G. Boothroyd, “Product Design for Manufacture and Assembly,” *Comput. Aided Des.*, vol. 26, p. 17, 1994.

[66] T.-C. Kuo, S. H. Huang, and H.-C. Zhang, “Design for Manufacture and Design for ‘X’: Concepts, Applications, and Perspectives,” *Comput. Ind. Eng.*, vol. 41, pp. 241–260, 2001.

[67] K. M. Adams, “Design Methodologies,” in *Non-Functional Requirements in Systems Analysis and Design*, Springer, 2015.

[68] R. . Finke, T. . Ward, and S. . Smith, “Creative cognition: Theory, research, and applications,” *Comput. Math. with Appl.*, pp. 238–247, 1996.

[69] S. Pugh, “Engineering Design—Unscrambling the Research Issues Engineering Design-Unscrambling the Research Issues,” *J. Eng. Des.*, vol. 1, no. 1, pp. 65–72, 1990.

[70] S. Pugh, “Design Activity Models: Worldwide Emergence and Convergence,” *Des. Stud.*, vol. 7, no. 3, pp. 167–173, 1986.

[71] S. Pugh, *Total design : integrated methods for successful product engineering*. Addison-Wesley Pub. Co, 1991.

[72] Assistant Secretary of Defense for Research and Engineering, “Technology Readiness Assessment Guidance,” 2011.

[73] H. Chen, A. Roy, J.-B. B. Baek, L. Zhu, J. Qu, and L. Dai, “Controlled growth and modification of vertically-aligned carbon nanotubes for multifunctional applications,” *Mater. Sci. Eng. R Reports*, vol. 70, no. 3–6, pp. 63–91, 2010.

[74] Y. Lan, Y. Wang, and Z. F. Ren, “Physics and applications of aligned carbon nanotubes,” *Adv. Phys.*, vol. 60, no. 4, pp. 553–678, 2011.

[75] L. X. Kang, D. Li, Z. Z. Yong, X. H. Zhang, and Q. Li, “Growth of Aligned Carbon Nanotubes and Their Applications,” in *Industrial Applications of Carbon Nanotubes*, Elsevier, 2017, pp. 381–403.

[76] N. . Lee, D. . Chung, I. . Han, J. . Kang, Y. . Choi, H. . Kim, S. . Park, Y. . Jin, W. .

Yi, M. . Yun, J. . Jung, C. . Lee, J. . You, S. . Jo, C. . Lee, and J. . Kim, "Application of Carbon Nanotubes to Field Emission Displays," *Diam. Relat. Mater.*, vol. 10, pp. 265–270, 2001.

[77] R. Amade, E. Jover, B. Caglar, T. Mutlu, and E. Bertran, "Optimization of MnO2/Vertically Aligned Carbon Nanotube Composite for Supercapacitor Application," *J. Power Sources*, vol. 196, no. 13, pp. 5779–5783, Jul. 2011.

[78] S. Kumar, R. Rani, N. Dilbaghi, K. Tankeshwar, and K.-H. Kim, "Carbon Nanotubes: A Novel Material for Multifaceted Applications in Human Healthcare," *Chem. Soc. Rev.*, vol. 46, no. 1, pp. 158–196, Jan. 2017.

[79] J. Kim, J. Elsnab, C. Gehrke, J. Li, and B. K. Gale, "Microfluidic Integrated Multi-Walled Carbon Nanotube (MWCNT) Sensor for Electrochemical Nucleic Acid Concentration Measurement," *Sensors Actuators B Chem.*, vol. 185, pp. 370–376, 2013.

[80] T. H. S. Dhahi, U. D. A. Bin Hashim, N. M. Ahmed, and A. Mat Taib, "A Review on the Electrochemical Sensors and Biosensors Composed of Nanowires as Sensing Material," *J. Optoelectron. Adv. Mater.*, vol. 12, no. 9, pp. 1857–1862, 2010.

[81] T. Chen, L. Wei, Z. Zhou, D. Shi, J. Wang, J. Zhao, Y. Yu, Y. Wang, and Y. Zhang, "Highly Enhanced Gas SEnsing in Single-Walled Carbon Nanotube-Based Thin-Film Transistor Sensors by Ultraviolet Light Irradiation," *Nanoscale Res. Lett.*, vol. 7, no. 1, p. 644, Nov. 2012.

[82] C. Yang, M. E. Denno, P. Pyakurel, and B. J. Venton, "Recent Trends in Carbon Nanomaterial-Based Electrochemical Sensors for Biomolecules: A Review," *Anal. Chim. Acta*, vol. 887, pp. 17–37, Aug. 2015.

[83] C. Gao, Z. Guo, J.-H. Liu, and X.-J. Huang, "The New Age of Carbon Nanotubes: An Updated Review of Functionalized Carbon Nanotubes in Electrochemical Sensors," *Nanoscale*, vol. 4, pp. 1948–1963, 2012.

[84] V. D. Punetha, S. Rana, H. J. Yoo, A. Chaurasia, J. T. McLeskey, M. S. Ramasamy, N. G. Sahoo, and J. W. Cho, "Functionalization of Carbon Nanomaterials for Advanced Polymer Nanocomposites: A Comparison Study Between CNT and Graphene," *Prog. Polym. Sci.*, vol. 67, pp. 1–47, Apr. 2017.

[85] E. Van Hooijdonk, C. Bittencourt, R. Snyders, and J.-F. Colomer, "Functionalization of Vertically Aligned Carbon Nanotubes," *Beilstein J. Nanotechnol*, vol. 4, pp. 129–152, 2013.

[86] W. Feng and P. Ji, "Enzymes Immobilized on carbon Nanotubes," *Biotechnol. Adv.*, vol. 29, no. 6, pp. 889–895, 2011.

[87] M. Yang, S. Sun, Y. Kostov, and A. Rasooly, "Lab-On-A-Chip for Carbon Nanotubes Based Immunoassay Detection of Staphylcoccal Enterotoxin B (SEM)," *Lab Chip*, vol. 10, no. 8, pp. 1011–1017, 2010.

[88] Y. Wang and J. T. W. Yeow, "A Review of Carbon-Nanotube Based Gas Sensors," *J. Sensors*, vol. 2009, p. 24, 2009.

[89] M. Penza, R. Rossi, M. Alvisi, and E. Serra, "Metal-Modified and Vertically Aligned Carbon Nanotube Sensor Arrays for Landfill Gas Monitoring

Applications," *Nanotechnology*, vol. 21, no. 105501, p. 14, 2010.

[90] C. Wei, L. Dai, A. Roy, and T. B. Tolle, "Multifunctional Chemical Vapor Sensors of Aligned Carbon Nanotube and Polymer Composites," *JACS*, vol. 128, pp. 1412–1413, 2006.

[91] N. Yang, X. Chen, T. Ren, P. Zhang, and D. Yang, "Carbon Nanotube Based Sensors," *Sensors Actuators B Chem.*, vol. 207, pp. 690–715, 2015.

[92] F. Lamberti, M. Giomo, and N. Elvassore, "Electrochemical biosensing with carbon nanotubes," *Carbon Nanotub. Appl. InTech*, pp. 278–298, 2011.

[93] K. Balasubramanian and M. Burghard, "Biosensors Based on Carbon Nanotubes," *Anal. Bioanal. Chem.*, vol. 385, no. 3, pp. 452–468, 2006.

[94] J. Li and N. Wu, *Biosensors based on nanomaterials and nanodevices*. CRC Press, 2013.

[95] Z. G. Zhu, L. Garcia-gancedo, C. Chen, X. R. Zhu, H. Q. Xie, A. J. Flewitt, and W. I. Milne, "Enzyme-free Glucose BiosensorBased on Low Density CNT Forest Grown Directly on a Si / SiO 2 Substrate," *Sensors Actuators B Chem.*, vol. 178, pp. 586–592, 2013.

[96] Z. Zhu, L. Garcia-Gancedo, A. J. Flewitt, H. Xie, F. Moussy, and W. I. Milne, "A Critical Review of Glucose Biosensors Based on Carbon Nanomaterials: Carbon Nanotubes and Graphene," *Sensors*, vol. 12, no. 5, pp. 5996–6022, 2012.

[97] T. C. Gokoglan, S. Soylemez, M. Kesik, I. B. Dogru, O. Turel, R. Yuksel, H. E. Unalan, and L. Toppare, "A Novel Approach for the Fabrication of a FLexible Glucose Biosensor: The Combination of Vertically Aligned CNTs and a Conjugated Polymer," *Food Chem.*, vol. 220, pp. 299–305, Apr. 2017.

[98] Y. Lin, F. Lu, Y. Tu, and Z. Ren, "Glucose Biosensors Based on Carbon Nanotube Nanoelectrode Ensembles," *Nano Lett.*, vol. 4, no. 2, pp. 191–195, Feb. 2004.

[99] S. Roy, H. Vedala, and W. Choi, "Vertically Aligned Carbon Nanotube Probes for Monitoring Blood Cholestrol," *Nanotechnology*, vol. 17, pp. S14–S18, 2006.

[100] M. Abdolahad, M. Taghinejad, H. Taghinejad, M. Janmaleki, and S. Mohajerzadeh, "A Vertically Aligned Carbon Nanotube-Based Impedance Sensing Biosensor for Rapid and High Sensitive Detection of Cancer Cells," *Lab Chip*, vol. 12, no. 6, pp. 1183–1190, 2012.

[101] G. A. Rivas, M. D. Rubianes, M. C. Rodríguez, N. F. Ferreyra, G. L. Luque, M. L. Pedano, S. A. Miscoria, and C. Parrado, "Carbon Nanotubes for Electrochemical Biosensing," *Talanta*, vol. 74, no. 3, pp. 291–307, 2007.

[102] C.-L. Choong, W. I. Milne, and K. B. K. Teo, "Review: Carbon Nanotube for Microfluidic Lab-On-A-Chip Application," *Int. J. Mater. Form.*, vol. 1, no. 2, pp. 117–125, 2008.

[103] A. Ghasemi, H. Amiri, H. Zare, M. Masroor, A. Hasanzadeh, A. Beyzavi, A. R. Aref, M. Karimi, and M. R. Hamblin, "Carbon Nanotubes in Microfluidic Lab-On-A-Chip Technology: Current Trends and Future Perspectives," *Microfluid. Nanofluidics*, vol. 21, no. 9, p. 151, Sep. 2017.

[104] Y. Zhouping, H. Yongan, B. Ningbin, W. Xiaomei, X. Youlun, Z. Yin, Y. Huang, N. Bu, X. Wang, and Y. Xiong, “Inkjet Printing for Flexible Electronics: Materials, Processes and Equipments,” *Chinese Sci. Bull.*, no. 30, pp. 3383–3407, Oct. 2010.

[105] A. D. Dias, D. M. Kingsley, and D. T. Corr, “Recent Advances in Bioprinting and Applications for Biosensing,” *Biosensors*, vol. 4, no. 2, pp. 111–136, Apr. 2014.

[106] H. Saito and H. Nakajo, “Metal Nanoparticle Conductive Inks for Industrial Inkjet Printing Applications,” in *Handbook of Industrial Inkjet Printing: A full system approach*, 2017, pp. 215–224.

[107] C. Griggs and J. Sumerel, “Opportunities for Inkjet Printing and Industrial Application,” 2010.

[108] A. Shimoni, S. Azoubel, and S. Magdassi, “Inkjet Printing of Flexible High-Performance Carbon Nanotube Transparent Conductive Films by ‘Coffee Ring Effect,’” *Nanoscale*, vol. 6, no. 19, pp. 11084–11089, Jun. 2014.

[109] K. Kordás, T. Mustonen, G. Tóth, H. Jantunen, M. Lajunen, C. Soldano, S. Talapatra, S. Kar, R. Vajtai, and P. M. Ajayan, “Inkjet Printing of Electrically Conductive Patterns of Carbon Nanotubes,” *Small*, vol. 2, no. 8–9, pp. 1021–1025, Aug. 2006.

[110] A. Denneulin, J. Bras, F. Carcone, C. Neuman, and A. Blayo, “Impact of ink formulation on carbon nanotube network organization within inkjet printed conductive films,” *Carbon N. Y.*, vol. 49, no. 8, pp. 2603–2614, Jul. 2011.

[111] R. Tortorich and J.-W. Choi, “Inkjet Printing of Carbon Nanotubes,” *Nanomaterials*, vol. 3, no. 3, pp. 453–468, Jul. 2013.

[112] M. Felisberto, L. Sacco, I. Mondragon, G. H. Rubiolo, R. J. Candal, and S. Goyanes, “The Growth of Carbon Nanotubes on Large Areas of Silicon Substrate Using Commercial Iron Oxide Nanoparticles as a Catalyst,” *Mater. Lett.*, vol. 64, no. 20, pp. 2188–2190, Oct. 2010.

[113] S. Lim, “Inkjet Printability of Electronic Materials Important to the Manufacture of Fully Printed OTFTs,” Western Michigan University, 2012.

[114] E. A. Roth, T. Xu, M. Das, C. Gregory, J. J. Hickman, and T. Boland, “Inkjet printing for high-throughput cell patterning,” *Biomaterials*, vol. 25, no. 17, pp. 3707–3715, Aug. 2004.

[115] M. A. Mulla, H. N. Yow, H. Zhang, O. J. Cayre, and S. Biggs, “Colloid Particles in Ink Formulations,” in *Fundamentals of Inkjet Printing*, Weinheim, Germany: Wiley-VCH Verlag GmbH & Co. KGaA, 2015, pp. 141–168.

[116] J. Young Kim, K. Cho, S. Ryu, S. Youn Kim, and B. Mook Weon, “Crack formation and prevention in colloidal drops,” *Nat. Publ. Gr.*, vol. 5, no. 13166, p. 9, 2015.

[117] W. Gao, Y. Zhang, D. Ramanujan, K. Ramani, Y. Chen, C. B. Williams, C. C. L. Wang, Y. C. Shin, S. Zhang, P. D. Zavattieri, and W. Gao, “The status, challenges, and future of additive manufacturing in engineering,” *Comput. Des.*, vol. 69, pp. 65–89, 2015.

[118] K. Blake Perez and C. B. Williams, “Combining Additive Manufacturing and

Direct Write for Integrated Electronics – A Review," in *The International SOoid Freeform Fabrication Symposium*, 2013, pp. 962–972.

[119] E. Stratakis, A. Ranella, and C. Fotakis, "Biomimetic micro/nanostructured functional surfaces for microfluidic and tissue engineering applications," *Biomicrofluidics*, vol. 5, no. 1, Mar. 2011.

[120] C. G. Khan Malek, "Laser processing for bio-microfluidics applications (part II)," *Anal. Bioanal. Chem.*, vol. 385, no. 8, pp. 1362–1369, Aug. 2006.

[121] K. Y. Lim, C. H. Sow, J. Lin, F. C. Cheong, Z. X. Shen, J. T. L. Thong, K. C. Chin, and A. T. S. Wee, "Laser Pruning of Carbon Nanotubes as a Route to Static and Movable Structures," *Adv. Mater.*, vol. 15, no. 4, pp. 300–303, Feb. 2003.

[122] W.-S. Su, C.-M. Lin, and T.-H. Chen, "Large area patterned arrays of aligned carbon nanotubes via laser trimming Patterning and growth of carbon nanotubes on a highly structured 3D substrate surface," *Nanotechnology*, vol. 14, pp. 433–437, 2003.

[123] N. Grobert, M. Terrones, S. Trasobares, K. Kordatos, H. Terrones, J. Olivares, J. P. Zhang, P. Redlich, W. K. Hsu, C. L. Reeves, D. J. Wallis, Y. Q. Zhu, J. P. Hare, A. J. Pidduck, H. W. Kroto, and D. R. M. Walton, "A novel route to aligned nanotubes and nanofibres using laser-patterned catalytic substrates," *Appl. Phys. A Mater. Sci. Process.*, vol. 70, no. 2, pp. 175–183, Feb. 2000.

[124] M. Terrones, N. Grobert, J. Olivares, J. P. Zhang, H. Terrones, K. Kordatos, W. K. Hsu, J. P. Hare, P. D. Townsend, K. Prassides, A. K. Cheetham, H. W. Kroto, and D. R. M. Walton, "Controlled production of aligned-nanotube bundles," *Nature*, vol. 388, no. 6637, pp. 52–55, Jul. 1997.

[125] A. Brunton and M. Crozier, "Inkjet and Laser Hybrid Processing: An Enabling Technology for Reliable Production of Fine Interconnects in Large-Area Electronics," in *Handbook of Industrial Inkjet Printing: A full system approach*, 2017, pp. 635–648.

[126] S. H. Ko, J. Chung, Y. Choi, D. J. Hwang, C. P. Grigoropoulos, and D. Poulikakos, "Substractive Laser Processing of Low Temperature Inkjet Printed Micro Electric Components of Functional Nano-Ink for Flexible Electronics," *Proc. IMECE2005*, no. June 2015, pp. 1–5, 2005.

[127] S. H. Ko, H. Pan, C. P. Grigoropoulos, C. K. Luscombe, J. M. J. Frechet, and D. Poulikakos, "All-inkjet-printed flexible electronics fabrication on a polymer substrate by low-temperature high-resolution selective laser sintering of metal nanoparticles," *Nanotechnology*, vol. 18, no. 34, p. 345202, Aug. 2007.

[128] S. H. Ko, H. Pan, · Costas, P. Grigoropoulos, J. M. J. Fréchet, C. K. Luscombe, D. Poulikakos, S. H. Ko, H. Pan, C. P. Grigoropoulos, J. M. J. Fréchet, C. K. Luscombe, and D. Poulikakos, "Lithography-free high-resolution organic transistor arrays on polymer substrate by low energy selective laser ablation of inkjet-printed nanoparticle film," *Appl Phys A*, vol. 92, pp. 579–587, 2008.

[129] C. B. Jacobs, M. J. Peairs, and B. J. Venton, "Review: Carbon nanotube based electrochemical sensors for biomolecules," *Anal. Chim. Acta*, vol. 662, no. 2, pp. 105–127, Mar. 2010.

[130] M. L. Terranova, V. Sessa, and M. Rossi, “The World of Carbon Nanotubes: An Overview of CVD Growth Methodologies,” *Chem. Vap. Depos.*, vol. 12, no. 6, pp. 315–325, Jun. 2006.

[131] K. Koziol, B. O. Boskovic, and N. Yahya, “Synthesis of Carbon Nanostructures by CVD Method,” Springer, Berlin, Heidelberg, 2010, pp. 23–49.

[132] M. Feng, H. Han, J. Zhang, H. Tachikawa, H. Han, J. Zhang, and H. Tachikawa, “Electrochemical Sensors Based on Carbon Nanotubes,” in *Electrochemical Sensors, Biosensors and their Biomedical Applications*, Elsevier, 2008, p. 459–VIII.

[133] M. Rümmeli, A. Bachmatiuk, F. Börrnert, F. Schäffel, I. Ibrahim, K. Cendrowski, G. Simha-Martynkova, D. Plachá, E. Borowiak-Palen, G. Cuniberti, and B. Büchner, “Synthesis of Carbon Nanotubes with and without catalyst Particles,” *Nanoscale Res. Lett.*, vol. 6, no. 1, p. 303, Apr. 2011.

[134] M. S. Dresselhaus, G. Dresselhaus, P. Avouris, and LINK (Online service), *Carbon nanotubes : synthesis, structure, properties, and applications*. Springer-Verlag, 2001.

[135] M. Kumar and Y. Ando, “Chemical Vapor Deposition of Carbon Nanotubes: A Review on Growth Mechanism and Mass Production,” *J. Nanosci. Nanotechnol.*, vol. 10, no. 6, pp. 3739–3758, 2010.

[136] M. Kumar, “Carbon Nanotube Synthesis and Growth Mechanism,” in *Carbon Nanotubes - Synthesis, Characterization, Applications*, S. Yellampalli, Ed. InTech, 2011.

[137] Y. Yao, L. K. . Falk, R. E. Morjan, N. O.A., and E. E. . Campbell, “Nucleation and Aligned Growth of Multi-Wall Carbon Nanotube Films During Thermal CVD,” *Carbon N. Y.*, vol. 45, no. 10, pp. 2065–2071, 2007.

[138] M. Rahmanian and M. H. Zandi, “Carbon Nanotubes Grown by CO2 Laser-Induced Chemical Vapor Deposition on Quartz,” *Int. J. Electrochem. Sci*, vol. 7, pp. 6904–6909, 2012.

[139] R. Alexandrescu, A. Crunteanu, R. . Morjan, I. Morjan, F. Rohmund, L. K. . Falk, G. Ledoux, and F. Huisken, “Synthesis of Carbon Nanotubes by CO2-Laser-Assisted Chemical Vapour Deposition,” *Infrared Phys. Technol.*, vol. 44, no. 1, pp. 43–50, Feb. 2003.

[140] Y. Y. Wei, G. Eres, V. I. Merkulov, and D. H. Lowndes, “Effect of Catalyst Film Thickness on Carbon Nanotube Growth by Selective Area Chemical Vapor Deposition,” *Appl. Phys. Lett.*, vol. 78, no. 10, pp. 1394–1396, 2001.

[141] R. T. K. Baker, P. S. Harris, R. B. Thomas, and R. J. Waite, “Formation of Filamentous Carbon From Iron, Cobalt and Chromium Catalyzed Decomposition of Acetylene,” *J. Catal.*, vol. 30, no. 1, pp. 86–95, Jul. 1973.

[142] R. S. Wagner and W. C. Ellis, “Vapor-Liquid-Solid Mechanism of Single Crystal Growth,” *Appl. Phys. Lett.*, vol. 4, no. 5, pp. 80–90, 1964.

[143] E. S. Polsen, M. Bedewy, and A. J. Hart, “Decoupled Control of Carbon Nanotube Forest Density and Diameter by Continuous-Feed Convective Assembly of Catalyst Particles,” *Small*, vol. 9, no. 15, pp. 2564–2575, Aug. 2013.

[144] L. M. Hoyos-Palacio, A. G. Garcia, J. F. Perez-Robles, J. Gonzalez, and H. V. Martinez Tejada, "Catalytic effect of Fe, Ni, Co and Mo on the CNTs Production," *IOP Conf. Ser. Mater. Sci. Eng.*, vol. 59, no. 1, p. 012005, 2014.

[145] M. Shuaib, M. Saheed, N. M. Mohamed, and Z. A. Burhanudin, "Effect of Different Catalyst Deposition Technique on Aligned Multiwalled Carbon Nanotubes Grown by Thermal Chemical Vapor Deposition," *J. Nanomater.*, vol. 43, p. 11, Apr. 2014.

[146] D. Roy and K. Ram, "Magnetite Nanoparticles by Organic-Phase Synthetic Route for Carbon Nanotube Growth," *Synth. Met.*, vol. 159, pp. 343–346, 2009.

[147] Y. An, Y. Liu, X. Yuan, and H. Tan, "Growth of Carbon Nanotubes on Iron Oxide Nanoparticles Catalyst Derived from Iron Storage Protein-Ferritin by CVD Method," *Int. J. Mod. Phys. B*, vol. 23, no. 6 & 7, pp. 1529–1534, 2009.

[148] S. Fan, M. G. Chapline, N. R. Franklin, T. W. Tombler, A. M. Cassell, and H. Dai, "Self-Oriented Regular Arrays of Carbon Nanotubes and Their Field Emission Properties," *Science (80-.).*, vol. 283, no. 5401, pp. 512–514, Jan. 1999.

[149] S. Amelinckx, X. B. Zhang, D. Bernaerts, X. F. Zhang, V. Ivanov, and J. B. Nagy, "A Formation Mechanism for Catalytically Grown Helix-Shaped Graphite Nanotubes," *Science (80-.).*, vol. 265, no. 5172, pp. 635–639, Jul. 1994.

[150] M. Hiramatsu, T. Deguchi, H. Nagao, and M. Hori, "Aligned Growth of Single-Walled and Double-Walled Carbon Nanotube Films by Control of Catalyst Preparation," *Jpn. J. Appl. Phys.*, vol. 46, no. 4L, p. L303, 2007.

[151] Michael J. Bronikowski, "CVD Growth of Carbon Nanotube Bundle Arrays," *Carbon N. Y.*, vol. 44, no. 13, pp. 2822–2832, 2006.

[152] P. B. Amama, C. L. Pint, M. K. Seung, L. McJilton, K. G. Eyink, E. A. Stach, R. H. Hauge, and B. Maruyama, "Influence of Alumina Type on the Evolution and Activity of Alumina- Supported Fe Catalysts in Single-Walled Carbon Nanotube Carpet Growth," *ACS Nano*, vol. 4, no. 2, pp. 895–904, 2010.

[153] K. Moulton, N. B. Morrill, A. M. Konneker, B. D. Jensen, R. R. Vanfleet, D. D. Allred, and R. C. Davis, "Effect of Iron Catalyst Thickness on Vertically Aligned Carbon Nanotube Forest Straightness for CNT-MEMS," *J. Micromechanics Microengineering*, vol. 22, no. 5, p. 9, May 2012.

[154] T. Yamada, T. Namai, K. Hata, D. N. Futaba, K. Mizuno, J. Fan, M. Yudasaka, M. Yumura, and S. Iijima, "Size-Selective Growth of Double-Walled Carbon Nanotube Forests from Engineered Iron Catalysts," *Nat. Nanotechnol.*, vol. 1, pp. 131–136, 2006.

[155] S. Hofmann, R. Blume, C. T. Wirth, M. Cantoro, R. Sharma, C. Ducati, M. Hävecker, S. Zafeiratos, P. Schnoerch, A. Oestereich, D. Teschner, M. Albrecht, A. Knop-Gericke, R. Schlögl, and J. Robertson, "State of Transition Metal Catalysts During Carbon Nanotube Growth," *J. Phys. Chem. C*, vol. 113, no. 5, pp. 1648–1656, 2009.

[156] G. Zhong, T. Iwasaki, J. Robertson, and H. Kawarada, "Growth Kinetics of 0.5 cm Vertically Aligned Single - Walled Carbon Nanotubes," *J. Phys. Chem. B*, vol. 111, no. 8, pp. 1907–1910, 2007.

[157] M. Chhowalla, K. B. K. Teo, C. Ducati, N. L. Rupesinghe, G. A. J. Amaratunga, A. C. Ferrari, D. Roy, J. Robertson, and W. I. Milne, "Growth Process Conditions of Vertically Aligned Carbon Nanotubes Using Plasma Enhanced Chemical Vapor Deposition," *J. Appl. Phys.*, vol. 90, no. 10, pp. 5308–5317, 2001.

[158] S. Hofmann, G. Csányi, A. C. Ferrari, M. C. Payne, and J. Robertson, "Surface Diffusion: The Low Activation Energy Path for Nanotube Growth," *Phys. Rev. Lett.*, vol. 95, no. 3, p. 036101, Jul. 2005.

[159] S. Min Kim, C. L. Pint, P. B. Amama, D. N. Zakharov, R. H. Hauge, B. Maruyama, and E. A. Stach, "Evolution in Catalyst Morphology Leads to Carbon Nanotube Growth Termination," *J. Phys. Chem. Lett*, vol. 1, pp. 918–922, 2010.

[160] H. Sato, Y. Hori, K. Hata, K. Seko, H. Nakahara, and Y. Saito, "Effect of Catalyst Oxidation on the Growth of Carbon Nanotubes by Thermal Chemical Vapor Deposition," *J. Appl. Phys.*, vol. 100, no. 10, p. 104321, Nov. 2006.

[161] P. M. Parthangal, R. E. Cavicchi, and M. R. Zachariah, "A Generic Process of Growing Aligned Carbon Nanotube Arrays on Metals and Metal Alloys," *Nanotechnology*, vol. 18, no. 18, p. 185605, 2007.

[162] C. Journet, M. Picher, and V. Jourdain, "Carbon Nanotube Synthesis: From Large-Scale Production to Atom-by-Atom Growth," *Nanotechnology*, vol. 23, no. 14, p. 142001, Apr. 2012.

[163] Y. Wang, Z. Luo, B. Li, P. S. Ho, Z. Yao, L. Shi, E. N. Bryan, and R. J. Nemanich, "Comparison Study of Catalyst Nanoparticle Formation and Carbon Nanotube Growth: Support Effect," *J. Appl. Phys.*, vol. 101, no. 12, p. 124310, 2007.

[164] M. Bedewy, "Data-Driven Understanding of Collective Carbon Nanotube Growth by In Situ Characterization and Nanoscale Metrology," *J. Mater. Res.*, vol. 32, no. 1, pp. 153–165, Jan. 2017.

[165] P. T. A. Reilly and W. B. Whitten, "The Role of Free Radical Condensates in the Production of Carbon Nanotubes During the Hydrocarbon CVD Process," *Carbon N. Y.*, vol. 44, no. 9, pp. 1653–1660, 2006.

[166] S. Sakurai, M. Inaguma, D. N. Futaba, M. Yumura, and K. Hata, "Diameter and Density Control of Single-Walled Carbon Nanotube Forests by Modulating Ostwald Ripening through Decoupling the Catalyst Formation and Growth Processes," *Small*, vol. 9, no. 21, pp. 3584–3592, Nov. 2013.

[167] M. Bedewy, E. R. Meshot, M. J. Reinker, and A. J. Hart, "Population Growth Dynamics of Carbon Nanotubes," *ACS Nano*, vol. 5, no. 11, pp. 8974–8989, 2011.

[168] M. Bedewy, ⊥ B Viswanath, E. R. Meshot, D. N. Zakharov, E. A. Stach, A. J. Hart, B. Viswanath, E. R. Meshot, D. N. Zakharov, E. A. Stach, and A. J. Hart, "Measurement of the Dewetting, Nucleation, and Deactivation Kinetics of Carbon Nanotube Population Growth by Environmental Transmission Electron Microscopy," *Chem. Mater.*, vol. 28, no. 11, pp. 3804–3813, Jun. 2016.

[169] E. R. Meshot, E. Verploegen, M. Bedewy, S. Tawfick, A. R. Woll, K. S. Green, M. Hromalik, L. J. Koerner, H. T. Philipp, M. W. Tate, S. M. Gruner, and A. J. Hart, "High-Speed in Situ X-ray Scattering of Carbon Nanotube Film Nucleation and Self-Organization," 2012.

[170] M. Bedewy, E. R. Meshot, and A. J. Hart, “Diameter-dependent kinetics of activation and deactivation in carbon nanotube population growth,” *Carbon N. Y.*, vol. 50, pp. 5106–5116, 2012.

[171] H. T. Ng, B. Chen, J. E. Koehne, A. M. Cassell, J. Li, J. Han, and M. Meyyappan, “Growth of Carbon Nanotubes: A Combinatorial Method To Study the Effects of Catalysts and Underlayers,” *J. Phys. Chem. B*, vol. 107, no. 33, pp. 8484–8489, 2003.

[172] C. T. Wirth, B. C. Bayer, A. D. Gamalski, S. Esconjauregui, R. S. Weatherup, C. Ducati, C. Baehtz, J. Robertson, and S. Hofmann, “The Phase of Iron Catalyst Nanoparticles during Carbon Nanotube Growth,” *Chem. Mater.*, vol. 24, no. 24, pp. 4633–4640, 2012.

[173] M. J. Behr, E. A. Gaulding, K. A. Mkhoyan, and E. S. Aydil, “Effect of Hydrogen on catalyst Nanoparticles in Carbon Nanotube Growth,” *J. Appl. Phys.*, vol. 108, no. 5, p. 053303, 2010.

[174] Y. Li, W. Kim, Y. Zhang, M. Rolandi, D. Wang, and H. Dai, “Growth of Single-Walled Carbon Nanotues from Discreate Catalytic Nanoparticles of Various Sizes,” *J. Phys. Chem. B*, vol. 105, no. 46, pp. 11424–31, 2001.

[175] “Classes of Magnetic Materials,” *University of Minnesota*. [Online]. Available: http://www.irm.umn.edu/hg2m/hg2m_b/hg2m_b.html. [Accessed: 01-Feb-2018].

[176] M. I. Dar and S. A. Shivashankar, “Single Crystalline Magnetite, Maghemite, and Hematite Nanoparticles with Rich Coercivity,” *RSC Adv.*, vol. 4, no. 8, pp. 4105–4113, 2014.

[177] W. Zhao, B. Basnet, S. Kim, and I. J. Kim, “Synthesis of Vertically Aligned Carbon Nanotubes on Silicalite-1 Monolayer-Supported Substrate,” *J. Nanomater.*, vol. 2014, pp. 1–5, Feb. 2014.

[178] T. T. Cao, V. C. Nguyen, T. T. T. Ngo, T. L. Le, T. L. Nguyen, E. D. Obraztsova, and M. Phan, Ngoc, “Effects of Ferrite Catalyst Concentration and Water Vapor on Growth of Vertically Aligned Carbon Nanotube,” *Adv. Nat. Sci. Nanosci. Nanotechnol.*, vol. 5, no. 4, p. 45009, 2014.

[179] C.-H. Chang, H. J. In, S. Takahashi, M. Deterre, H. J. Choi, K. W. Gotrik, and G. Barbastathis, “Assembling Nanoparticle Catalysts with Nanospheres for Periodic Carbon Nanotube Structure Growth,” *Nanotechnology*, vol. 22, no. 3, p. 035301, Jan. 2010.

[180] E. S. Polsen, A. G. Stevens, and A. J. Hart, “Laser Printing of Nanoparticle Toner Enables Digital Control of Micropatterned Carbon Nanotube Growth,” *ACS Appl. Mater. Interfaces*, vol. 5, no. 9, pp. 3656–3662, 2013.

[181] N. T. Alvarez, F. Li, C. L. Pint, J. T. Mayo, E. Z. Fisher, J. M. Tour, V. L. Colvin, and R. H. Hauge, “Uniform Large Diameter Carbon Nanotubes in Vertical Arrays from Premade Near-Monodisperse Nanoparticles,” *Chem. Mater.*, vol. 23, no. 15, pp. 3466–3475, Aug. 2011.

[182] S. Laurent, D. Forge, M. Port, A. Roch, C. Robic, L. Vander Elst, and R. N. Muller, “Magnetic Iron Oxide Nanoparticles: Synthesis, Stabilization, Vectorization, Physicochemical Characterizations, and Biological Applications

Sophie," *Chem. Rev.*, vol. 108, no. 6, pp. 2064–2110, 2008.

[183] C. Scherer and A. M. Figueiredo Neto, "Ferrofluids: Properties and Applications," *Brazilian J. Phys.*, vol. 35, no. 3A, pp. 718–727, 2005.

[184] Ö. B. Adıgüzel and K. Atalık, "Magnetic field effects on Newtonian and non-Newtonian ferrofluid flow past a circular cylinder," *Appl. Math. Model.*, vol. 42, pp. 161–174, Feb. 2017.

[185] T. A. Franklin, "Ferrofluid Flow Phenomena," MIT, 2003.

[186] L. Jodin, A.-C. Dupuis, E. Rouvière, and P. Reiss, "Influence of the Catalyst Type on the Growth of Carbon Nanotubes via Methane Chemical Vapor Deposition," *J. Phys. Chem. B*, vol. 110, no. 14, pp. 7328–7333, 2006.

[187] H. . El Ghandoor, H. M. Zidan, M. M. Khalil, and M. I. . Ismail, "Synthesis and Some Physical Properties of Magnetite (Fe3O4) Nanoparticles," *Int. J. Electrochem. Sci*, vol. 7, no. 6, pp. 5734–5745, 2012.

[188] S. Thomas, R. Thomas, A. K. Zachariah, and R. K. Mishra, *Thermal and Rheological Measurment Techniques for Nanomaterials Characterization Volume 3*. Elsevier, 2017.

[189] J. Lim, S. P. Yeap, H. X. Che, and S. C. Low, "Characterization of Magnetic Nanoparticle by Dynamic Light Scattering," *Nanoscale Res. Lett.*, vol. 8, no. 1, p. 381, Sep. 2013.

[190] Q. Yi, D. Li, B. Lin, A. M. Pavlov, D. Luo, Q. Gong, B. Song, H. Ai, and G. B. Sukhorukov, "Magnetic Resonance Imaging for Monitoring of Magnetic Polyelectrolyte Capsule In Vivo Delivery," *Bionanoscience*, vol. 4, no. 1, pp. 59–70, Mar. 2014.

[191] J. Hodkiewicz, "Characterizing Carbon Materials with Raman Spectroscopy," *Thermo Fish. Sci. Appl. Note 51901*, p. 5, 2010.

[192] "Carbon Nanotube | Purity Evaluation by G/D Ratio : SHIMADZU (Shimadzu Corporation)," *Shimadzu*, 2018. [Online]. Available: https://www.shimadzu.com/an/industry/ceramicsmetalsmining/cnt_0102010.htm. [Accessed: 25-Jan-2018].

[193] P. N. Nirmalraj, P. E. Lyons, S. De, J. N. Coleman, and J. J. Boland, "Electrical Connectivity in Single-Walled Carbon Nanotube Networks," *Nano Lett.*, vol. 9, no. 11, pp. 3890–3895, 2009.

[194] "Silicon Wafers." [Online]. Available: https://order.universitywafer.com/default.aspx?cat=Silicon. [Accessed: 26-Jun-2018].

[195] "Tap300-G AFM Probe - BudgetSensors." [Online]. Available: https://www.budgetsensors.com/tapping-mode-afm-probe-tap300. [Accessed: 26-Jun-2018].

[196] K. A. Bertness, "Dimensional Measurement of Nanostructures with Scanning Electron Microscopy," *NIST Spec. Publ.*, vol. 250, no. 96, p. 22, 2017.

[197] H. El Ghandoor, H. M. Zidan, M. M. H. Khalil, and M. I. M. Ismail, "Synthesis

and Some Physical Properties of Magnetite (Fe 3 O 4) Nanoparticles," *Int. J. Electrochem. Sci*, vol. 7, pp. 5734–5745, 2012.

[198] D. E. Tsentalovich, R. J. Headrick, F. Mirri, J. Hao, N. Behabtu, C. C. Young, and M. Pasquali, "Influence of Carbon Nanotube Characteristics on Macroscopic Fiber Properties," *Appl. Mater. Interfaces*, vol. 9, pp. 36189–36198, 2017.

[199] A. Eatemadi, H. Daraee, H. Karimkhanloo, M. Kouhi, N. Zarghami, A. Akbarzadeh, M. Abasi, Y. Hanifehpour, and S. W. Joo, "Carbon nanotubes: properties, synthesis, purification, and medical applications.," *Nanoscale Res. Lett.*, vol. 9, no. 1, p. 393, 2014.

[200] S. Takagi and Y. Matsumoto, "Surfactant Effects on Bubble Motion and Bubbly Flows Keywords," *Annu. Rev. Fluid Mech.*, vol. 43, pp. 615–636, 2011.

[201] W. J. Milliken, H. A. Stone, and L. G. Leal, "The Effect of Surfactant on the Transient Motion of Newtonian Drops," *Phys. Fluids A Fluid Dyn.*, vol. 5, no. 1, pp. 69–79, 1993.

[202] "Introduction to IR Spectra." [Online]. Available: https://webspectra.chem.ucla.edu/irintro.html. [Accessed: 14-Jun-2018].

[203] W.-T. Jian, E. Ac, P. R. K. Ai, M. T. Th, and J. W. Kim2, "TEM and XRD determination of crystallite size and lattice strain as a function of illite crystallinity in pelitic rocks," *J. Metamorph. Geol*, vol. 15, pp. 267–281, 1997.

[204] H. Borchert, E. V Shevchenko, A. Robert, I. Mekis, A. Kornowski, G. Grü, and H. Weller, "Determination of Nanocrystal Sizes: A Comparison of TEM, SAXS, and XRD Studies of Highly Monodisperse CoPt3 Particles," *Langmuir*, vol. 21, pp. 1931–1936, 2004.

[205] I. M. Hutchings, G. D. Martin, and S. D. Hoath, "Introductory Remarks," in *Fundamentals of Inkjet Printing*, Weinheim, Germany: Wiley-VCH Verlag GmbH & Co. KGaA, 2015, pp. 1–12.

[206] J. Dong, J. Liu, G. Kang, J. Xie, and Y. Wang, "Pushing the resolution of photolithography down to 15nm by surface plasmon interference," *Sci. Rep.*, vol. 4, no. 1, p. 5618, May 2015.

[207] J. A. Lim, W. H. Lee, H. S. Lee, J. H. Lee, Y. D. Park, and K. Cho, "Self-Organization of Ink-jet-Printed Triisopropylsilylethynyl Pentacene via Evaporation-Induced Flows in a Drying Droplet," *Adv. Funct. Mater.*, vol. 18, no. 2, pp. 229–234, Jan. 2008.

[208] J. Perelaer, P. Kröber, J. T. Delaney, and U. S. Schubert, "Fabrication of Two and Three-Dimensional Structures by Using Inkjet Printing," in *NIP25 and Digital Fabrication*, 2009.

[209] M. Singh, H. M. Haverinen, P. Dhagat, and G. E. Jabbour, "Inkjet Printing-Process and Its Applications," *Adv. Mater.*, vol. 22, no. 6, pp. 673–685, Feb. 2010.

[210] "Compendium of Chemical Hazards: Toluene Public Health Questions."

[211] R. Daly, "Surface Characterization," in *Fundamentals of Inkjet Printing*, Weinheim, Germany: Wiley-VCH Verlag GmbH & Co. KGaA, 2015, pp. 365–396.

[212] D. Jang, D. Kim, and J. Moon, “Influence of Fluid Physical Properties on Ink-Jet Printability,” *Langmuir*, vol. 25, no. 5, pp. 2629–2635, 2009.

[213] B. He, S. Yang, Z. Qin, B. Wen, and C. Zhang, “The Roles of Wettability and Surface Tension in Droplet Formation During Inkjet Printing,” *Sci. Reports2*, vol. 7, no. 1, p. 11841, 2017.

[214] L. Yang and C. D. Bain, “Liquid Jet Instability and Dynamic Surface Tension Effect on Breakup,” in *NIP and Digital Fabrication Conference*, 2009, vol. 1, pp. 79–82.

[215] J. Eastoe and J. . Dalton, “Dynamic Surface Tension and Adsorption Mechanisms of Surfactants at the Air–Water Interface,” *Adv. Colloid Interface Sci.*, vol. 85, no. 2–3, pp. 103–144, Mar. 2000.

[216] J. Perelaer, P. J. Smith, E. Van Den Bosch, S. S. C. Van Grootel, P. H. J. M. Ketelaars, and U. S. Schubert, “The Spreading of Inkjet-Printed Droplets with Varying Polymer Molar Mass on a Dry Solid Substrate,” *Macromol. Chem. Phys.*, vol. 210, pp. 495–502, 2009.

[217] D. Pesach and A. Marmur, “Marangoni effects in the spreading of liquid mixtures on a solid,” *Langmuir*, vol. 3, no. 4, pp. 519–524, Jul. 1987.

[218] R. Rioboo, C. Tropea, and M. Marengo, “Outcomes From a Drop Impact on Solid Surfaces,” *At. Sprays*, vol. 11, no. 2, p. 12, 2001.

[219] R. Rioboo, M. Marengo, and C. Tropea, “Time evolution of liquid drop impact onto solid, dry surfaces,” *Exp. Fluids*, vol. 33, pp. 112–124, 2002.

[220] S. Jung, H. J. Hwang, and S. H. Hong, “Drops on Substrates,” in *Fundamentals of Inkjet Printing*, Weinheim, Germany: Wiley-VCH Verlag GmbH & Co. KGaA, 2015, pp. 199–218.

[221] S. Jung, “Fluid characterisation and drop impact in inkjet printing for organic semiconductor devices,” University of Cambridge, 2011.

[222] Y. Son and C. Kim, “Spreading of inkjet droplet of non-Newtonian fluid on solid surface with controlled contact angle at low Weber and Reynolds numbers,” *J. Non-Newtonian Fluid Mech*, vol. 162, pp. 78–87, 2009.

[223] A. Khoufech and M. Benali, “Influence of liquid formulation and impact conditions on the wetting of hydrophobic surfaces by aqueous polymeric solutions,” *Chem. Eng. Res. Des.*, vol. 110, pp. 233–244, Jun. 2016.

[224] H.-Y. Kim and J.-H. Chun, “The recoiling of liquid droplets upon collision with solid surfaces,” *Phys. Fluids*, vol. 13, no. 3, pp. 643–659, Mar. 2001.

[225] W. Zhou, D. A. Loney, A. G. Fedorov, F. Levent Degertekin, and D. W. Rosen, “Droplet Impingement Dynamics in Ink-jet Deposition,” *Virtual Phys. Prototyp.*, vol. 7, no. 1, pp. 49–64, 2012.

[226] S. Schiaffino and A. A. Sonin, “Molten droplet deposition and solidification at low Weber numbers,” *Cit. Phys. Fluids*, vol. 9, 1997.

[227] G. H. Mckinley and M. Renardy, “Wolfgang von Ohnesorge,” *Phys. Fluids*, vol. 23, no. 12, 2011.

[228] B. Derby, “Inkjet Printing of Functional and Structural Materials: Fluid Property Requirements, Feature Stability, and Resolution,” *Annu. Rev. Mater. Res.*, vol. 40, no. 1, pp. 395–414, Jun. 2010.

[229] N. Reis, C. Ainsley, and B. Derby, “Ink-jet delivery of particle suspensions by piezoelectric droplet ejectors,” *J. Appl. Phys.*, vol. 97, no. 9, p. 094903, May 2005.

[230] M. S. . Schulkes, “The Contraction of liquid filaments,” *J. Fluid Mech*, vol. 309, pp. 277–300, 1996.

[231] P. K. Notz and O. A. Basaran, “Dynamics and breakup of a contracting liquid filament,” *J. Fluid Mech*, vol. 512, pp. 223–256, 2004.

[232] A. A. Castrejón-Pita, J. R. Castrejón-Pita, and I. M. Hutchings, “Breakup of Liquid Filaments,” *Phys. Rev. Lett.*, vol. 108, no. 7, 2012.

[233] C. Chen, L. Wang, and G. Jiang, “The Superiority of Silver Nanoellipsoids Synthesized Via A New Approach in Suppressing the Coffee-Ring Effect During Drying and Film Formation Processes,” *Nanotechnology*, vol. 25, p. 7, 2014.

[234] Z. Zhang, X. Zhang, Z. Xin, M. Deng, Y. Wen, and Y. Song, “Controlled Inkjetting of a Conductive Pattern of Silver Nanoparticles Based on the Coffee-Ring Effect,” *Adv. Mater.*, vol. 25, no. 46, pp. 6714–6718, Dec. 2013.

[235] J. A. Lim, W. H. Lee, H. S. Lee, J. H. Lee, Y. D. Park, and K. Cho, “Self-Organization of Ink-jet-Printed Triisopropylsilylethynyl Pentacene via Evaporation-Induced Flows in a Drying Droplet,” *Adv. Funct. Mater.*, vol. 18, no. 2, pp. 229–234, Jan. 2008.

[236] E. Talbot, C. Bain, R. De Dier, W. Sempels, and J. Vermant, “Droplets Drying on Surfaces,” in *Fundamentals of Inkjet Printing*, Weinheim, Germany: Wiley-VCH Verlag GmbH & Co. KGaA, 2015, pp. 251–280.

[237] D. Soltman, V. Subramanian, D. S. And, and V. Subramanian, “Inkjet-Printed Line Morphologies and Temperature Control of the Coffee Ring Effect,” *Langmuir*, vol. 24, no. 5, pp. 2224–2231, 2008.

[238] S. J. Jo, C. S. Kim, J. B. Kim, J. Kim, M. J. Lee, H. S. Hwang, H. K. Baik, and Y. S. Kim, “Surface property controllable multilayered gate dielectric for low voltage organic thin film transistors,” *Appl. Phys. Lett.*, vol. 93, no. 8, p. 083504, Aug. 2008.

[239] K. Efimenko, W. E. Wallace, and J. Genzer, “Surface Modification of Sylgard-184 Poly(dimethyl siloxane) Networks by Ultraviolet and Ultraviolet/Ozone Treatment,” *J. Colloid Interface Sci.*, vol. 254, no. 2, pp. 306–315, Oct. 2002.

[240] C. Ton-That, D. O. H. Teare, P. A. Campbell, and R. H. Bradley, “Surface characterisation of ultraviolet-ozone treated PET using atomic force microscopy and X-ray photoelectron spectroscopy,” *Surf. Sci.*, vol. 433–435, pp. 278–282, Aug. 1999.

[241] Three bond Technical News, “Ultraviolet-Ozone Surface Treatment,” 1987.

[242] J. Stringer and B. Derby, “Formation and Stability of Lines Produced by Inkjet Printing,” *Langmuir*, vol. 26, no. 12, pp. 10365–10372, 2010.

[243] W.-K. Hsiao and E. S. Betton, “Coalescence and Line Formation,” in *Fundamentals of Inkjet Printing*, Weinheim, Germany: Wiley-VCH Verlag GmbH & Co. KGaA, 2015, pp. 219–250.

[244] W.-K. Hsiao, G. D. Martin, and I. M. Hutchings, “Printing Stable Liquid Tracks on a Surface with Finite Receding Contact Angle,” *Langmuir*, vol. 30, no. 41, pp. 12447–12455, 2014.

[245] D. Soltman, B. Smith, H. Kang, S. J. S. Morris, and V. Subramanian, “Methodology for Inkjet Printing of Partially Wetting Films Dan,” *Langmuir*, vol. 26, no. 19, pp. 15686–15693, 2010.

[246] Fujifilm, “FUJIFILM Dimatix Materials Printer User Manual,” 2010.

[247] W. Zhou, D. A. Loney, A. G. Fedorov, F. Levent Degertekin, and D. W. Rosen, “Droplet impingement dynamics in ink-jet deposition,” *Virtual Phys. Prototyp.*, vol. 7, no. 10, pp. 49–64, 2012.

[248] K. Gotoh, A. Yasukawa, and Y. Kobayashi, “Wettability characteristics of poly(ethylene terephthalate) films treated by atmospheric pressure plasma and ultraviolet excimer light,” *Polym. J.*, vol. 43, pp. 545–551, 2011.

[249] J. Yang, S. Esconjauregui, R. Xie, H. Sugime, T. Makaryan, L. D ’arsie, D. L. Gonzalez Arellano, S. Bhardwaj, C. Cepek, and J. Robertson, “Effect of Oxygen Plasma Alumina Treatment on Growth of Carbon Nanotube Forests,” *J. Phys. Chem. C*, vol. 118, no. 32, pp. 18683–18692, 2014.

[250] P. Gokhale, D. Mitra, E. Sowade, K. Y. Mitra, H. L. Gomes, E. Ramon, A. Al-Hamry, O. Kanoun, and R. R. Baumann, “Controlling the crack formation in inkjet-printed silver nanoparticle thin-films for high resolution patterning using intense pulsed light treatment,” *Nanotechnology*, vol. 28, no. 49, p. 495301, Dec. 2017.

[251] S. Hofmann, R. Sharma, C. Ducati, G. Du, C. Mattevi, C. Cepek, M. Cantoro, S. Pisana, A. Parvez, F. Cervantes-Sodi, A. C. Ferrari, R. Dunin-Borkowski, S. Lizzit, L. Petaccia, A. Goldoni, and J. Robertson, “In situ Observations of Catalyst Dynamics during Surface-Bound Carbon Nanotube Nucleation,” *Nano Lett.*, vol. 7, no. 3, pp. 602–608, 2007.

[252] M. F. L. De Volder, S. J. Park, S. H. Tawfick, and D. O. Vidaud, “Fabrication and electrical integration of robust carbon nanotube micropillars by self-directed elastocapillary densification,” *J. Micromechanics Microengineering2*, vol. 21, no. 4, p. 045033, 2011.

[253] G. Oberdörster, V. Castranova, B. Asgharian, and P. Sayre, “Inhalation Exposure to Carbon Nanotubes (CNT) and Carbon Nanofibers (CNF): Methodology and Dosimetry,” *J. Toxicol. Environ. Heal. Part B*, vol. 18, no. 3–4, pp. 121–212, May 2015.

[254] K. J. Schrider, “Femtosecond Laser Interaction with Ultrathin Metal Films : Modifying Structure , Composition , and Morphology by,” University of Michigan, 2017.

[255] X. Zhu, A. Y. Naumov, D. M. Villeneuve, P. B. Corkum, S. Sebban, G. Grillon, P. Balcou, E. Förster, J. P. Geindre, P. Audebert, J. C. Gauthier, and D. Hulin,

"Influence of laser parameters and material properties on micro drilling with femtosecond laser pulses," *Appl. Phys. A Mater. Sci. Process.*, vol. 69, no. 7, pp. S367–S371, Dec. 2012.

[256] J. Bonse, S. Baudach, J. Krüger, W. Kautek, and M. Lenzner, "Femtosecond laser ablation of silicon–modification thresholds and morphology," *Appl. Phys. A Mater. Sci. Process.*, vol. 74, no. 1, pp. 19–25, 2002.

[257] T. Y. Choi and C. P. Grigoropoulos, "Plasma and ablation dynamics in ultrafast laser processing of crystalline silicon," *J. Appl. Phys.*, vol. 92, no. 9, pp. 4918–4925, Nov. 2002.

[258] H. Reinhardt, C. Hellmann, P. Nürnberger, S. Kachel, and N. Hampp, "Free Form Growth of Carbon Nanotube Microarchitectures on Stainless Steel Controlled via Laser-Stimulated Catalyst Formation," *Adv. Mater. Interfaces*, vol. 4, no. 16, p. 1700508, Aug. 2017.

[259] D. T. Pham, S. S. Dimov, C. Ji, P. V Petkov, and T. Dobrev, "Laser milling as a rapid micromanufacturing process," *Proc. Inst. Mech. Eng. Part B*, vol. 218, no. 1, pp. 1–7, 2004.

[260] A. Pereira, A. Cros, P. Delaporte, S. Georgiou, A. Manousaki, W. Marine, and M. Sentis, "Surface nanostructuring of metals by laser irradiation: effects of pulse duration, wavelength and gas atmosphere," *Appl. Phys. A*, vol. 79, no. 4–6, pp. 1433–1437, Sep. 2004.

[261] P. V Petkov, S. S. Dimov, R. M. Minev, and D. T. Pham, "Laser milling: pulse duration effects on surface integrity," *J. Phys. Chem. C*, vol. 118, no. 32, pp. 18683–18692, 2014.

[262] B. N. Chicbkov, C. Momma, S. Nolte, F. Yon Alvensleben, and A. Tiinnermann, "Femtosecond, Picosecond and Nanosecond Laser Ablation of Solids," *Appl. Phys. A*, vol. 63, pp. 109–115, 1996.

[263] K. Ahmmed, C. Grambow, and A.-M. Kietzig, "Fabrication of Micro/Nano Structures on Metals by Femtosecond Laser Micromachining," *Micromachines*, vol. 5, no. 4, pp. 1219–1253, Nov. 2014.

[264] A. Y. Vorobyev and C. Guo, "Direct femtosecond laser surface nano/microstructuring and its applications," *Laser Photon. Rev.*, vol. 7, no. 3, pp. 385–407, May 2013.

[265] M. S. Amer, M. A. El-Ashry, L. R. Dosser, K. E. Hix, J. F. Maguire, and B. Irwin, "Femtosecond versus nanosecond laser machining: comparison of induced stresses and structural changes in silicon wafers," *Appl. Surf. Sci.*, vol. 242, no. 1–2, pp. 162–167, Mar. 2005.

[266] M. E. Shaheen and B. J. Fryer, "Femtosecond laser ablation of brass: A study of surface morphology and ablation rate," *Laser Part. Beams*, vol. 30, pp. 473–479, 2012.

[267] S. Lee, D. Yang, and S. Nikumb, "Femtosecond laser micromilling of Si wafers," *Appl. Surf. Sci.*, vol. 254, pp. 2996–3005, 2008.

[268] N. G. Semaltianos, W. Perrie, V. Vishnyakov, R. Murray, C. J. Williams, S. P. Edwardson, G. Dearden, P. French, M. Sharp, S. Logothetidis, and K. G. Watkins,

"Nanoparticle formation by the debris produced by femtosecond laser ablation of silicon in ambient air," *Mater. Lett.*, vol. 62, pp. 2165–2170, 2008.

[269] T. Matsumura, A. Kazama, and T. Yagi, "Generation of debris in the femtosecond laser machining of a silicon substrate," *Appl. Phys. A*, vol. 81, no. 7, pp. 1393–1398, Nov. 2005.

[270] E. . Garcia Ramirez, M. . Arroyo Carrasco, M. . Otero, S. Chavez Cerda, and M. D. Iturbe Castillo, "Farfield Intensity Distributions Due to Spatial Self Phase Modulation of a Gaussian Beam by a Thin Nonlocal Nonlinear Media," *Opt. Express*, vol. 18, no. 21, pp. 22067–22079, 2010.

[271] J. J. Nivas, S. He, A. Rubano, A. Vecchione, D. Paparo, L. Marrucci, R. Bruzzese, and S. Amoruso, "Direct Femtosecond Laser Surface Structuring with Optical Vortex Beams Generated by a q-plate," *Sci. Rep.*, vol. 5, p. 17929, 2015.

[272] Y. Han and S. Qu, "The ripples and nanoparticles on silicon irradiated by femtosecond laser," *Chem. Phys. Lett.*, vol. 495, no. 4–6, pp. 241–244, Aug. 2010.

[273] C. M. Rouleau, M. Tian, A. A. Puretzky, M. Mahjouri-Samani, G. Duscher, and D. B. Geohegan, "Catalytic nanoparticles for carbon nanotube growth synthesized by through thin film femtosecond laser ablation," in *Synthesis and Photonics of Nanoscale Materials*, 2014, vol. 8969, p. 896907.

[274] S. Barcikowski, V. I. Mazhukin, A. Mené Ndez-Manjo´n, M. Manjo´n, S. Barcikowski, G. A. Shafeev, V. I. Mazhukin, and A. B. N. Chichkov, "Influence of beam intensity profile on the aerodynamic particle size distributions generated by femtosecond laser ablation," *Laser Part. Beams*, vol. 28, pp. 45–52, 2010.

[275] M. E. Shaheen, J. E. Gagnon, and B. J. Fryer, "Laser ablation of iron: A comparison between femtosecond and picosecond laser pulses," *J. Appl. Phys.*, vol. 114, no. 8, p. 083110, Aug. 2013.

[276] S. H. Ko, Y. Choi, D. J. Hwang, C. P. Grigoropoulos, J. Chung, and D. Poulikakos, "Nanosecond laser ablation of gold nanoparticle films," *Appl. Phys. Lett.*, vol. 89, no. 14, p. 141126, Oct. 2006.

[277] J. Chung, S. Han, D. Lee, S. Ahn, C. P. Grigoropoulos, J. Moon, and S. H. Ko, "Nanosecond laser ablation of silver nanoparticle film," *Opt. Eng.*, vol. 52, no. 2, p. 024302, Feb. 2013.

[278] J. Wang, "Nanomaterial-based electrochemical biosensors," *Analyst*, vol. 130, no. 4, p. 421, 2005.

[279] D. T. E. Myles, M. Ziyenge, J. D. Shephard, and D. C. Milne, "Scanned Mask Imaging Solid State Laser Tool for Cost Effective Flip Chip – Chip Scale Package Manufacture," *JLMN-Journal of Laser Micro/Nanoengineering*, vol. 10, no. 1, 2015.

[280] N. L. W. Septiani and B. Yuliarto, "Review—The Development of Gas Sensor Based on Carbon Nanotubes," *J. Electrochem. Soc.*, vol. 163, no. 3, pp. B97–B106, 2016.

[281] Z. Lin, S. Young, and S. Chang, "CO2 Gas Sensors Based on Carbon Nanotube Thin Films Using a Simple Transfer Method on Flexible Substrate," *IEEE Sensors J.*, vol. 15, no. 12, pp. 7017–7020, 2015.

[282] Z. Zanolli, R. Leghrib, A. Felten, J.-J. Pireaux, E. Llobet, and J.-C. Charlier, “Gas Sensing with Au-Decorated Carbon Nanotubes,” *ACS Nano*, vol. 5, no. 6, pp. 4592–4599, 2011.

[283] A. Biswas, I. S. Bayer, A. S. Biris, T. Wang, E. Dervishi, and F. Faupel, “Advances in top–down and bottom–up surface nanofabrication: Techniques, applications & future prospects,” *Adv. Colloid Interface Sci.*, vol. 170, no. 1–2, pp. 2–27, Jan. 2012.

[284] I. Sayago, H. Santos, M. C. Horrillo, M. Aleixandre, M. J. Fernández, E. Terrado, I. Tacchini, R. Aroz, W. K. Maser, A. M. Benito, M. T. Martínez, J. Gutiérrez, and E. Muñoz, “Carbon nanotube networks as gas sensors for NO2 detection,” *Talanta*, vol. 77, no. 2, pp. 758–764, Dec. 2008.

[285] K. Suzuki, K. Tsuji, A. Onodera, T. Shibuya, T. Tano, and H. Miura, “High-resolution Patterning Technologies using Ink-jet Printing and Laser Processing for Organic TFT Array,” in *NIP and Digital Fabrication Conference*, 2013, vol. 2013, pp. 489–493.

[286] D. Milne and D. Myles, “Scanned Mask Imaging: The economical approach to high resolution micro-machining using UV solid state lasers,” in *Laser in Manufacturing Conference*, 2015.

[287] M.-S. Ltd., “MSV-302C Advanced IC Package Manufacturing Tool Product Datasheet,” Kidlington, 2015.

[288] I. Ferrer, J. Rios, and J. Ciurana, “An approach to integrate manufacturing process information in part design phases,” *J. Mater. Process. Technol.*, vol. 209, no. 4, pp. 2085–2091, Feb. 2009.

[289] M. Trojanowicz, “Analytical applications of carbon nanotubes: a review,” *TrAC - Trends Anal. Chem.*, vol. 25, no. 5, pp. 480–489, 2006.

[290] D. R. Kauffman, A. Star, A. Star, and D. R. Kauffman, “Carbon Nanotube Gas and Vapor Sensors,” *Angew. Chem. Int. Ed*, vol. 47, pp. 6550–6570, 2008.

[291] D. W. H. Fam, A. Palaniappan, A. I. Y. Tok, B. Liedberg, and S. M. Moochhala, “A review on technological aspects influencing commercialization of carbon nanotube sensors,” *Sensors Actuators B Chem.*, vol. 157, no. 1, pp. 1–7, Sep. 2011.

[292] J. Zhao, A. Buldum, J. Han, and J. P. Lu, “Gas molecule adsorption in carbon nanotubes and nanotube bundles,” *Nanotechnology*, vol. 13, no. 2, pp. 195–200, Apr. 2002.

[293] C. S. Huang, B. R. Huang, Y. H. Jang, M. S. Tsai, and C. Y. Yeh, “Three-terminal CNTs gas sensor for N2 detection,” *Diam. Relat. Mater.*, vol. 14, no. 11–12, pp. 1872–1875, Nov. 2005.

[294] I. V. Zaporotskova, N. P. Boroznina, Y. N. Parkhomenko, and L. V. Kozhitov, “Carbon nanotubes: Sensor properties. A review,” *Mod. Electron. Mater.*, vol. 2, no. 4, pp. 95–105, Dec. 2016.

[295] T. Ueda, M. M. H. Bhuiyan, H. Norimatsu, S. Katsuki, T. Ikegami, and F. Mitsugi, “Development of carbon nanotube-based gas sensors for NOx gas detection working at low temperature,” *Phys. E Low-dimensional Syst. Nanostructures*, vol. 40, no. 7, pp. 2272–2277, May 2008.

[296] H.-Q. Nguyen and J.-S. Huh, “Behavior of single-walled carbon nanotube-based gas sensors at various temperatures of treatment and operation,” *Sensors Actuators B Chem.*, vol. 117, no. 2, pp. 426–430, Oct. 2006.

[297] X. Zhang, X. Wu, B. Yang, and H. Xiao, “Enhancement of Gas Sensing Characteristics of Multiwalled Carbon Nanotubes by CF 4 Plasma Treatment for SF 6 Decomposition Component Detection,” *J. Nanomater.*, vol. 171545, pp. 1–9, 2015.

[298] H.-J. Kim and J.-H. Lee, “Highly sensitive and selective gas sensors using p-type oxide semiconductors: Overview,” *Sensors Actuators B Chem.*, vol. 192, pp. 607–627, Mar. 2014.

[299] P. R. Mudimela, M. Scardamaglia, O. González-León, N. Reckinger, R. Snyders, E. Llobet, C. Bittencourt, and J.-F. Colomer, “Gas sensing with gold-decorated vertically aligned carbon nanotubes,” *Beilstein J. Nanotechnol.*, vol. 5, no. 1, pp. 910–918, Jun. 2014.

[300] K. Lee, V. Scardaci, H.-Y. Kim, T. Hallam, H. Nolan, B. E. Bolf, G. S. Maltbie, J. E. Abbott, and G. S. Duesberg, “Highly sensitive, transparent, and flexible gas sensors based on gold nanoparticle decorated carbon nanotubes,” *Sensors Actuators B. Chem.*, vol. 188, pp. 571–575, 2013.

[301] J. M. Tulliani, A. Cavalieri, S. Musso, E. Sardella, and F. Geobaldo, “Room temperature ammonia sensors based on zinc oxide and functionalized graphite and multi-walled carbon nanotubes,” *Sensors Actuators, B Chem.*, vol. 152, no. 2, pp. 144–154, 2011.

[302] N. V. Long, T. Teranishi, Y. Yang, C. M. Thi, Y. Cao, and M. Nagomi, “Iron Oxide Nanoparticles for Next Generation Gas Sensors Fe 3 O 4 , α-Fe 2 O 3 , Metal nanoparticles,” *Int. J. Metall. Mater. Eng.*, vol. 119, p. 18, 2015.

[303] S. Taccola, F. Greco, A. Zucca, C. Innocenti, C. de Julián Fernández, G. Campo, C. Sangregorio, B. Mazzolai, and V. Mattoli, “Characterization of Free-Standing PEDOT:PSS/Iron Oxide Nanoparticle Composite Thin Films and Application As Conformable Humidity Sensors,” *ACS Appl. Mater. Interfaces*, vol. 5, no. 13, pp. 6324–6332, Jul. 2013.

[304] U. V. Patil, C. S. Rout, and D. J. Late, “Impedimetric humidity sensor based on α-Fe $_2$ O $_3$ nanoparticles,” *Adv. Device Mater.*, vol. 1, no. 3, pp. 88–92, Jul. 2015.

[305] J. Lee, S. Mulmi, V. Thangadurai, and S. S. Park, “Magnetically Aligned Iron Oxide/Gold Nanoparticle-Decorated Carbon Nanotube Hybrid Structure as a Humidity Sensor,” *Appl. Mater. Interfaces*, vol. 7, pp. 15506–15513, 2015.

[306] M. Penza, R. Rossi, M. Alvisi, M. A. Signore, G. Cassano, R. Pentassuglia, D. Suriano, V. Pfister, and E. Serra, “Metal-Functionalized and Vertically-Aligned Multiwalled Carbon Nanotube Layers for Low Temperature Gas Sensing Applications,” Springer, Dordrecht, 2010, pp. 185–191.

[307] J. R. Johansson, N. Bosaeus, N. Kann, B. Åkerman, B. Nordén, and W. Khalid, “Covalent functionalization of carbon nanotube forests grown in situ on a metal-silicon chip,” *Proc. SPIE 8344, Nanosensors, Biosensors, Info-Tech Sensors Syst.*, vol. 8344, pp. 834411–834412, 2012.

[308] “Gas Sensor Testing System.” [Online]. Available: http://www.kenosistec.com/en/product_card.php?id=9. [Accessed: 24-May-2018].

[309] K. X. Steirer, J. J. Berry, M. O. Reese, M. F. A. M. Van Hest, A. Miedaner, M. W. Liberatore, R. T. Collins, and D. S. Ginley, “Ultrasonically sprayed and inkjet printed thin film electrodes for organic solar cells,” *Thin Solid Films*, vol. 517, pp. 2781–2786, 2009.

[310] V. Scardaci, R. Coull, P. E. Lyons, D. Rickard, and J. N. Coleman, “Spray Deposition of Highly Transparent, Low-Resistance Networks of Silver Nanowires over Large Areas,” *Small*, vol. 7, no. 18, pp. 2621–2628, Sep. 2011.

[311] S. P. Patole, H.-I. Kim, J.-H. Jung, A. S. Patole, H.-J. Kim, I.-T. Han, V. N. Bhoraskar, and J.-B. Yoo, “The synthesis of vertically-aligned carbon nanotubes on an aluminum foil laminated on stainless steel,” *Carbon N. Y.*, vol. 49, no. 11, pp. 3522–3528, Sep. 2011.

[312] G. S. Choi, Y. S. Cho, K. H. Son, and D. J. Kim, “Mass production of carbon nanotubes using spin-coating of nanoparticles,” *Microelectron. Eng.*, vol. 66, no. 1–4, pp. 77–82, Apr. 2003.

[313] T. Kartanas, V. Ostanin, P. K. Challa, R. Daly, J. Charmet, and T. P. J. Knowles, “Enhanced Quality Factor Label-free Biosensing with Micro- Cantilevers Integrated into Microfluidic Systems,” *Anal. Chem.*, vol. 89, pp. 11929–11936, 2017.

[314] M. Trojanowicz, “Analytical applications of carbon nanotubes: a review,” *TrAC Trends Anal. Chem.*, vol. 25, no. 5, pp. 480–489, May 2006.

[315] United States DOD, “Technology Readiness Levels in the Department of Defense,” no. April, pp. 1–8, 2011.

Appendices

Appendix A

Table A 1: *Technology Readiness Levels adapted from U.S Department of Defence (2011)* [72] [315].

Phase	*TRL*	*Description*
Concept development	1	Scientific research translated to apply R&D with basic principles observed and reported. Publish research identify the principles that underline this technology
	2	Technology concept and application formulated and practical inventions underway. Detailed analytical studies and analysis conducted
	3	Active research and development with analytical studying and laboratory experiments for proof of concept. Elements of the technology separately studied.
Prototype	4	Component validation in laboratory environment. The basic technology is integrated to establish what the product could look like
	5	The technological components are validated in a simulated environment with supporting material that can be tested in a high fidelity laboratory
Verification	6	The technology system and subsystems are demonstrated with a prototype in a relevant environment
	7	Technology systems are prototyped and tested in an operational environment
Production and Release	8	The final technology system is developed and qualified with relevant tests and demonstrations
	9	The final application of the technology is released and proven successful through operational mission conditions

Table A 2: *Manufacturing Readiness Levels adapted from U.S Department of Defence (2011)* [72] [315].

	MRL	*Description*
Materials Solutions Analysis	1	Basic manufacturing implications identified using scientific principles that may have manufacturing implications.
	2	Manufacturing concepts identified. Invention begins with the manufacturing science or concept described in application context. The identification of material and process approaches are limited to paper studies and analysis.
	3	Manufacturing proof of concept developed with analytical and laboratory experiments to validate paper studies. But are not yet integrated or representative. Materials and processes characterised but further evaluation required.
	4	Capability to produce technology in laboratory with required investments such as manufacturing technology development identified. Processes to ensure manufacturability, reproducibility and quality are in place and sufficient to produce technology demonstrators.
Technology Development	5	Capability to produce prototype components in a production relevant environment. The risk management plan constructed and the manufacturing strategy refined. Prototype materials, tooling, test equipment and personnel skills have been demonstrated but majority of manufacturing processes and procedures still in development
	6	Capability to produce a prototype or subsystem in a production relevant environment. Initial manufacturing approach developed and majority of manufacturing process have been defined and characterised.
Engineering and Manufacturing Development	7	Capability to produce systems, subsystems and components in a production representative environment with detail design underway. The material specifications are approved and ready for deployment on the pilot line.
	8	Pilot line demonstrated for low production rate. The detailed system design is essentially complete and sufficiently stable to enter low rate production. Manufacturing and quality processes and procedures proven in pilot line environment.
Production and Deployment	9	Major design features proven in test and evaluation with full rate production demonstrated. Materials and manufacturing processes established and read to meet planned rate production
	10	Full rate production demonstration and lean production practices in place with engineering and design changes limited to quality and cost improvements only.

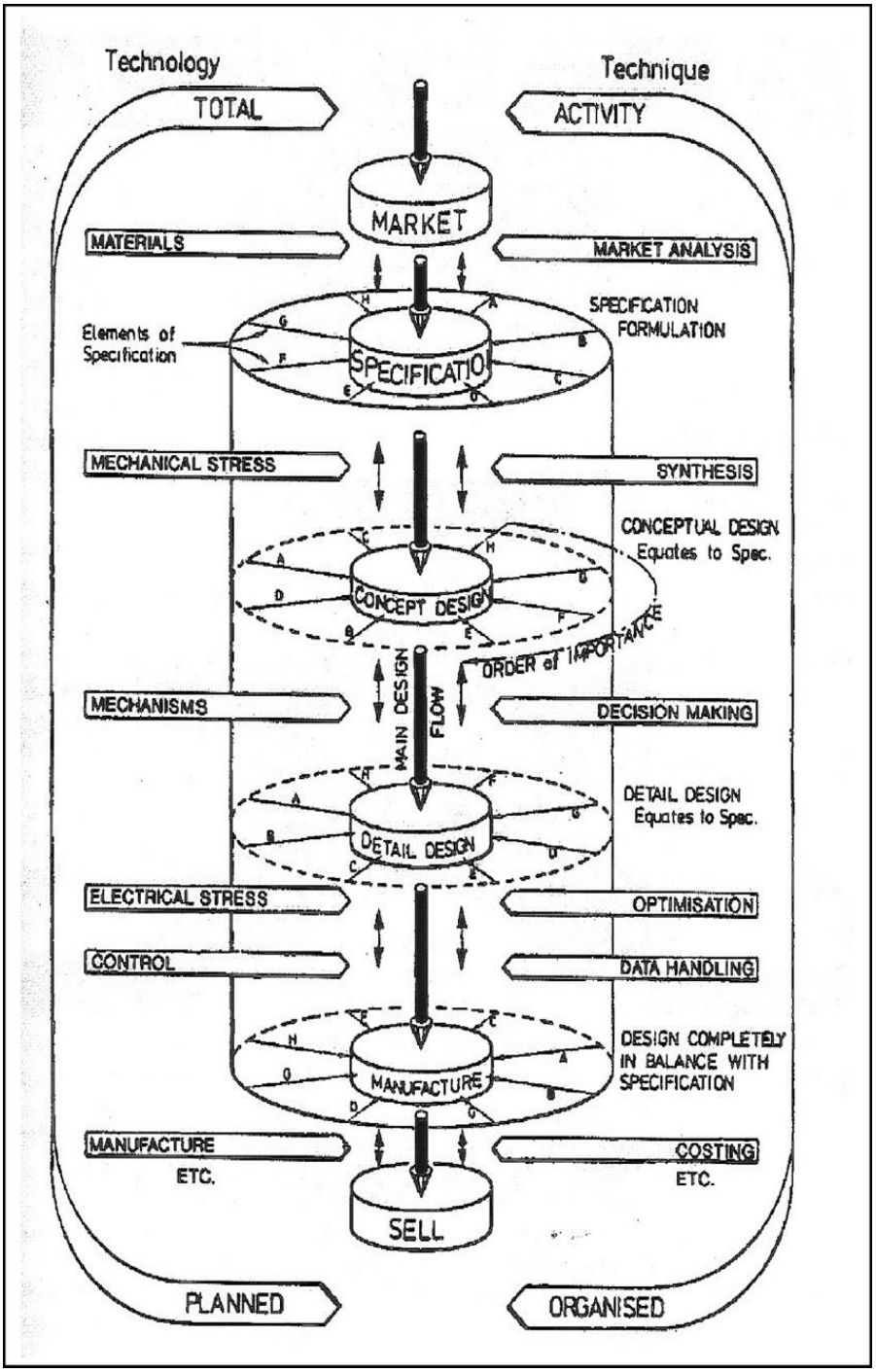

Figure A 1: *Total Design Methodology* [69] .

Appendix B

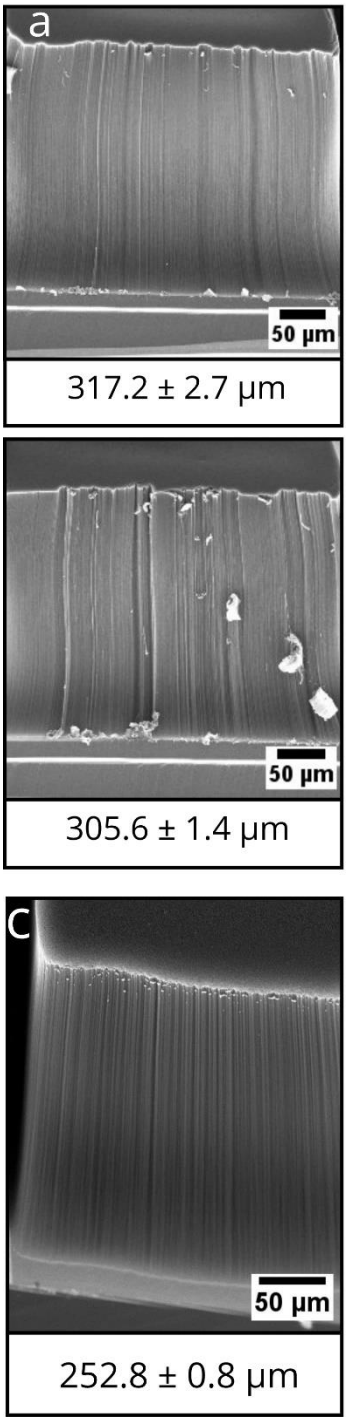

Figure B 1: *SEM micrographs showing VA-CNTs on samples* ***a)*** *1,* ***b)*** *2 and* ***c)*** *3, with VA-CNT heights listed as calculated from the SEM micrographs with a 45° tilt angle corrections. All errors have been calculated to a 95% CI.*

Table B 1: *Magnetite Weight Concentration in MSGW10 as procured.*

MSGW10			
Supplier Specifications	Density of MSGW10 Suspension	1180	kg/ml
	Magnetite (Fe3O4)	2.8-3.5%	% volume
	Water Soluble Dispersant	2.0-4.0	% volume
	DI Water	92.5-95.5	% volume
	Food Grade Fragrance	0.05	% volume
Magnetite Density Calculation	Description	Value	Units
	Density of Iron III Oxide	5740	kg/m^3
	Volume of magnetite in 1ml MSGW10 Suspension	0.03	ml
		3 E-08	m^3
	Mass of Magnetite in 1ml	1.72E-04	kg
	Density of Magnetite in MSGW10 Suspension	**172.20**	**mg/ml**

Table B 2: *Calculations for ink dilutions.*

Solution	Calculations	MSGW10	D.I. Water	Total
5%	Mass (mg)	262.26	4982.95	5245.21
	Volume (ml)	0.22	4.98	5.21
	Mass of magnetite (mg)	38.27		
	Density of Solution (mg/ml)	**1007.69**		
	w/w of Magnetite	**0.73**		
10%	Mass (mg)	450.00	4049.89	4499.89
	Volume (ml)	0.38	4.05	4.43
	Mass of magnetite (mg)	65.67		
	Density (mg/ml)	**1015.49**		
	w/w of Magnetite	**1.46**		
15%	Mass (mg)	5441.60	30856.00	36297.60
	Volume (ml)	4.61	30.86	35.47
	Mass of magnetite (mg)	794.10		
	Density (mg/ml)	**1023.40**		
	w/w of Magnetite	**2.19**		
30%	Mass (mg)	1534.50	3526.80	5061.30
	Volume (ml)	1.30	3.53	4.83
	Mass of magnetite (mg)	223.93		
	Density (mg/ml)	**1048.49**		
	w/w of Magnetite	**4.42**		
45%	Mass (mg)	15015.40	18338.80	33354.20
	Volume (ml)	12.72	18.34	31.06
	Mass of magnetite (mg)	2191.23		
	Density (mg/ml)	**1073.74**		
	w/w of Magnetite	**6.57**		
60%	Mass (mg)	3801.40	2564.90	6366.30
	Volume (ml)	3.22	2.56	5.79
	Mass of magnetite (mg)	554.75		
	Density (mg/ml)	**1100.21**		
	w/w of Magnetite	**8.71**		
75%	Mass (mg)	7223.90	2421.40	9645.30
	Volume (ml)	6.12	2.42	8.54
	Mass of magnetite (mg)	1054.20		
	Density (mg/ml)	**1128.98**		
	w/w of Magnetite	**10.93**		
100%	Mass (mg)	10000.00	0.00	10000.00
	Volume (ml)	8.47	0.00	8.47
	Mass of magnetite (mg)	1459.32		
	Density (mg/ml)	**1180.00**		
	w/w of Magnetite	**14.59**		

Appendix C

Table C 1: Calculations for ink printing velocity, Ohnesorge number, Weber number and Reynolds number.

Nozzle Diameter (m)	Strobe delay (s)
2.15E-05	**3.00E-05**

Ink Concentration (% w/w)	Viscosity (cP)	Viscosity (kg/ms)	Distance Travelled (um)	Velocity (m/s)	Density (kg/m^3)	Surface Tension (mN/m)	Surface Tension (kg/s^2)	Z (1/Ohnesorge Number)	Ohnesorge Number	Weber number	Reynolds number
2.19	1.10	1.10E-03	2.30E+02	7.71	1027.00	69.35	6.94E-02	**35.57**	**2.81E-02**	**15.77**	**141.29**
			2.29E+02								
			2.36E+02								
			2.31E+02								
6.567	1.20	1.20E-03	1.75E+02	5.91	1081.00	61.46	6.15E-02	**31.49**	**3.18E-02**	**18.74**	**136.32**
			1.58E+02								
			1.99E+02								
			1.77E+02								
14.59	1.80	1.80E-03	2.28E+02	7.49	1180.00	50.65	5.07E-02	**19.91**	**5.02E-02**	**24.82**	**99.21**
			2.18E+02								
			2.28E+02								
			2.25E+02	**Average 7.04**							

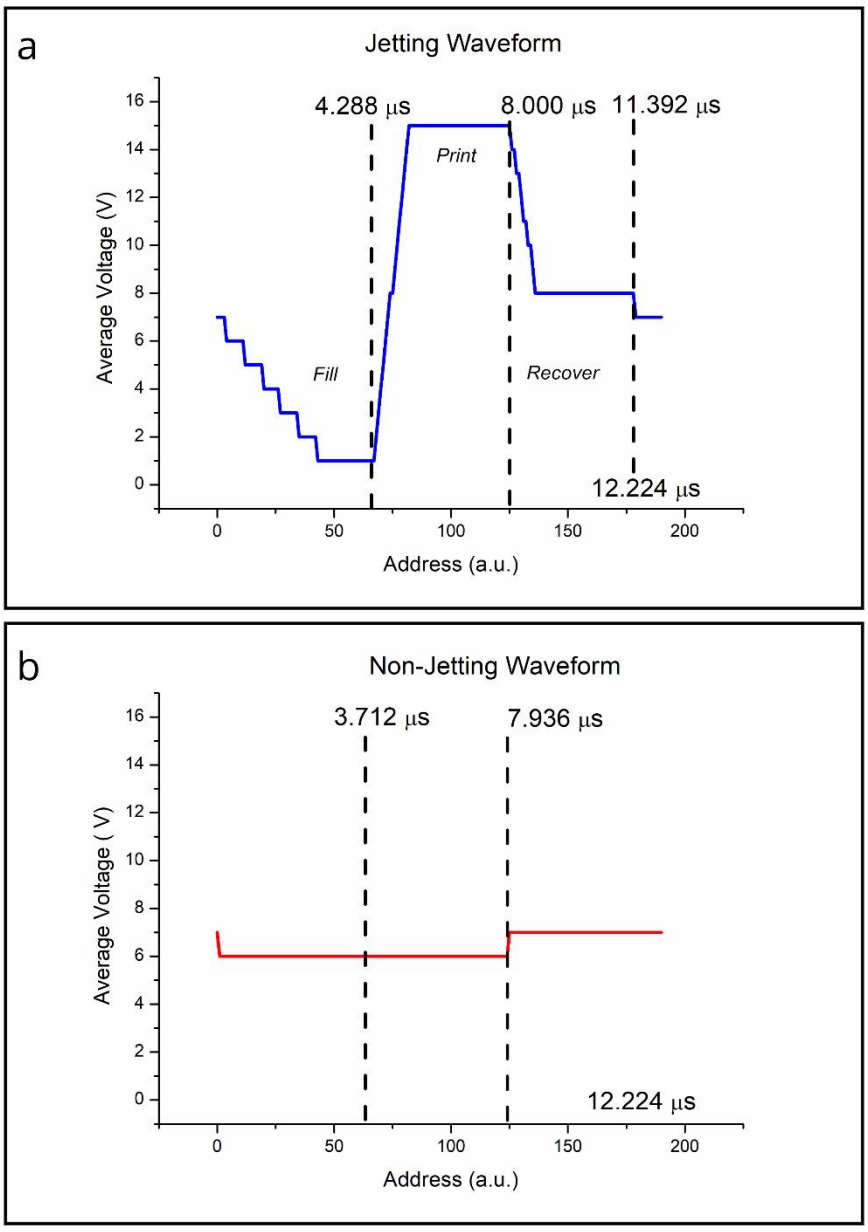

Figure C 1: *Waveform for printing all ink concentrations.*

Table C 2: *Calculations according to the Soltman et al. (2010) model for Radius of the Resultant Bead (R_1) and the Maximum Contact Radius to which a newly deposited droplet can spread (R_{imp}), for varying droplet spacings (*Δx) [245].

Droplet Spacing Δx	**R_1**	**R_{imp}**
5	4.22	0.78
10	2.99	7.01
15	2.44	12.56
20	2.11	17.89
25	1.89	23.11
30	1.72	28.28
35	1.60	33.40
40	1.49	38.51
45	1.41	43.59
50	1.34	48.66
55	1.27	53.73
60	1.22	58.78
65	1.17	63.83

Table C 3: *Calculations for average volume per droplet.*

		Units	***2.19 %$_{w/w}$***	***6.57 %$_{w/w}$***	***14.59 %$_{w/w}$***
1	Weight of Slide	**(g)**	1.24E-01	1.28E-01	1.23E-01
	Weight of Slide + Droplets	**(g)**	1.30E-01	1.34E-01	1.31E-01
	Weight of Droplets	**(g)**	5.40E-03	6.40E-03	8.17E-03
2	Weight of Slide	**(g)**	1.25E-01	1.30E-01	1.23E-01
	Weight of Slide + Droplets	**(g)**	1.32E-01	1.35E-01	1.31E-01
	Weight of Droplets	**(g)**	7.10E-03	5.60E-03	8.35E-03
3	Weight of Slide	**(g)**	1.21E-01	1.25E-01	1.24E-01
	Weight of Slide + Droplets	**(g)**	1.27E-01	1.29E-01	1.32E-01
	Weight of Droplets	**(g)**	6.20E-03	4.50E-03	8.15E-03
Calculations	*Average Weight of Droplets*	*(g)*	*6.23E-03*	*5.50E-03*	*8.22E-03*
	Volume	*(pL)*	*6.09E+06*	*5.12E+06*	*6.97E+06*
	Volume per Droplet	*(pL)*	*8.12E+00*	*6.83E+00*	*9.29E+00*
	Average Volume per Droplet	***(pL)***	***8.08E+00***		
Inkjet Printing Parameters	**3 nozzles 50 seconds 5kHz 750K Drops**				
Density of 2.19 %$_{w/w}$ (kg/m3)	1023.403792				
Density of 6.57 %$_{w/w}$ (kg/m3)	1073.735055				
Density of 14.59 %$_{w/w}$ (kg/m3)	1180				

Table C 4: *Calculations for mass deposited per metre by varying droplet spacing and ink concentration.*

		Droplet Spacing (µm)												
		5	**10**	**15**	**20**	**25**	**30**	**35**	**40**	**45**	**50**	**55**	**60**	**65**
No. of overlapping Droplets		*4.30E+00*	*2.15E+00*	*1.43E+00*	*1.08E+00*	*8.60E-01*	*7.17E-01*	*6.14E-01*	*5.38E-01*	*4.78E-01*	*4.30E-01*	*3.91E-01*	*3.58E-01*	*3.31E-01*
Total Volume (µm³)		*3.47E+04*	*1.74E+04*	*1.16E+04*	*8.69E+03*	*6.95E+03*	*5.79E+03*	*4.96E+03*	*4.34E+03*	*3.86E+03*	*3.47E+03*	*3.16E+03*	*2.90E+03*	*2.67E+03*
Ink Concentration ($\%_{w/w}$)	*Density kg/µm³*	**`Mass deposited in one metre (µg)**												
0.73	*1.01E-15*	3.50E-02	1.75E-02	1.17E-02	8.75E-03	7.00E-03	5.84E-03	5.00E-03	4.38E-03	3.89E-03	3.50E-03	3.18E-03	2.92E-03	2.69E-03
1.46	*1.02E-15*	3.53E-02	1.76E-02	1.18E-02	8.82E-03	7.06E-03	5.88E-03	5.04E-03	4.41E-03	3.92E-03	3.53E-03	3.21E-03	2.94E-03	2.71E-03
2.18	*1.02E-15*	3.56E-02	1.78E-02	1.19E-02	8.89E-03	7.11E-03	5.93E-03	5.08E-03	4.45E-03	3.95E-03	3.56E-03	3.23E-03	2.96E-03	2.74E-03
4.42	*1.05E-15*	3.64E-02	1.82E-02	1.21E-02	9.11E-03	7.29E-03	6.07E-03	5.20E-03	4.55E-03	4.05E-03	3.64E-03	3.31E-03	3.04E-03	2.80E-03
6.56	*1.07E-15*	3.73E-02	1.87E-02	1.24E-02	9.33E-03	7.46E-03	6.22E-03	5.33E-03	4.66E-03	4.15E-03	3.73E-03	3.39E-03	3.11E-03	2.87E-03
8.71	*1.10E-15*	3.82E-02	1.91E-02	1.27E-02	9.56E-03	7.65E-03	6.37E-03	5.46E-03	4.78E-03	4.25E-03	3.82E-03	3.48E-03	3.19E-03	2.94E-03
10.92	*1.13E-15*	3.92E-02	1.96E-02	1.31E-02	9.81E-03	7.85E-03	6.54E-03	5.60E-03	4.90E-03	4.36E-03	3.92E-03	3.57E-03	3.27E-03	3.02E-03
14.59	*1.18E-15*	4.10E-02	2.05E-02	1.37E-02	1.03E-02	8.20E-03	6.83E-03	5.86E-03	5.13E-03	4.56E-03	4.10E-03	3.73E-03	3.42E-03	3.15E-03

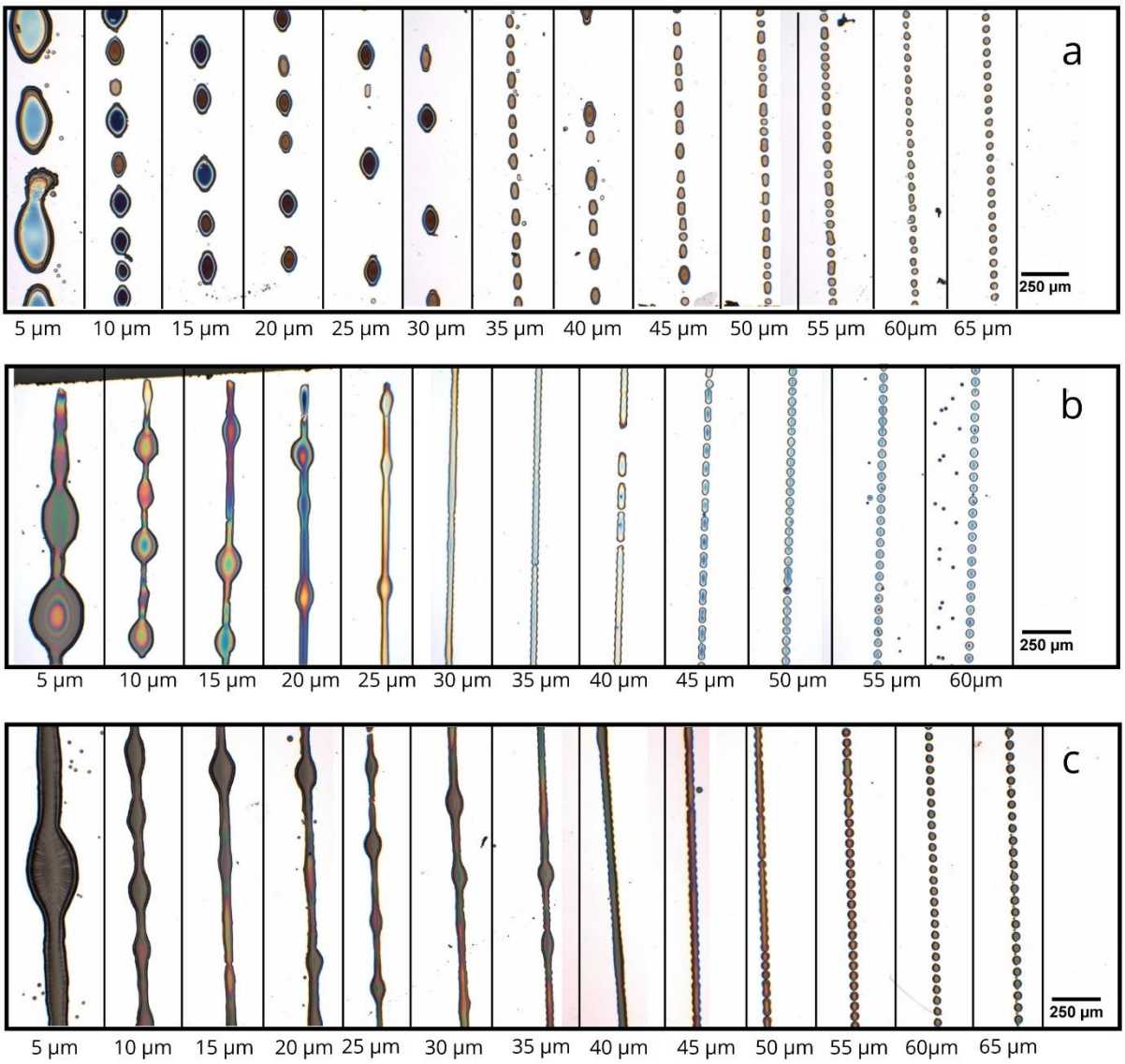

Figure C 2: *Optical micrographs showing ink concentrations* ***a)*** *2.19 %w/w,* ***b)*** *6.57 %w/w and* ***c)*** *14.59 %w/w printed at varying droplet spacings on untreated 10 nm alumina coated silicon wafers.*

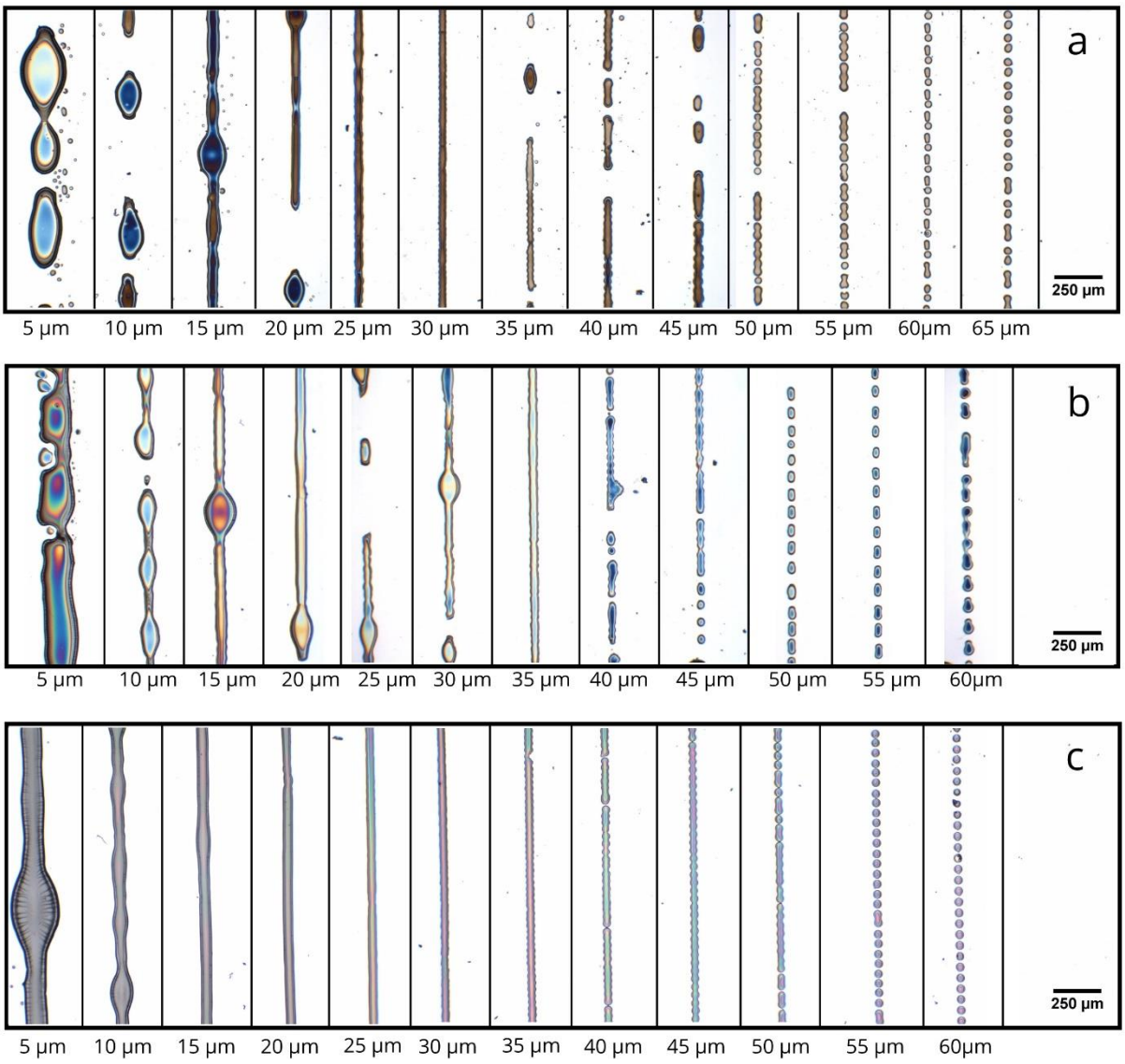

Figure C 3: *Optical micrographs showing ink concentrations* ***a)*** *2.19 %$_{w/w}$,* ***b)*** *6.57 %$_{w/w}$ and* ***c)*** *14.59 %$_{w/w}$ printed at varying droplet spacings on untreated 10 nm alumina coated silicon wafers plasma treated for 60 s.*

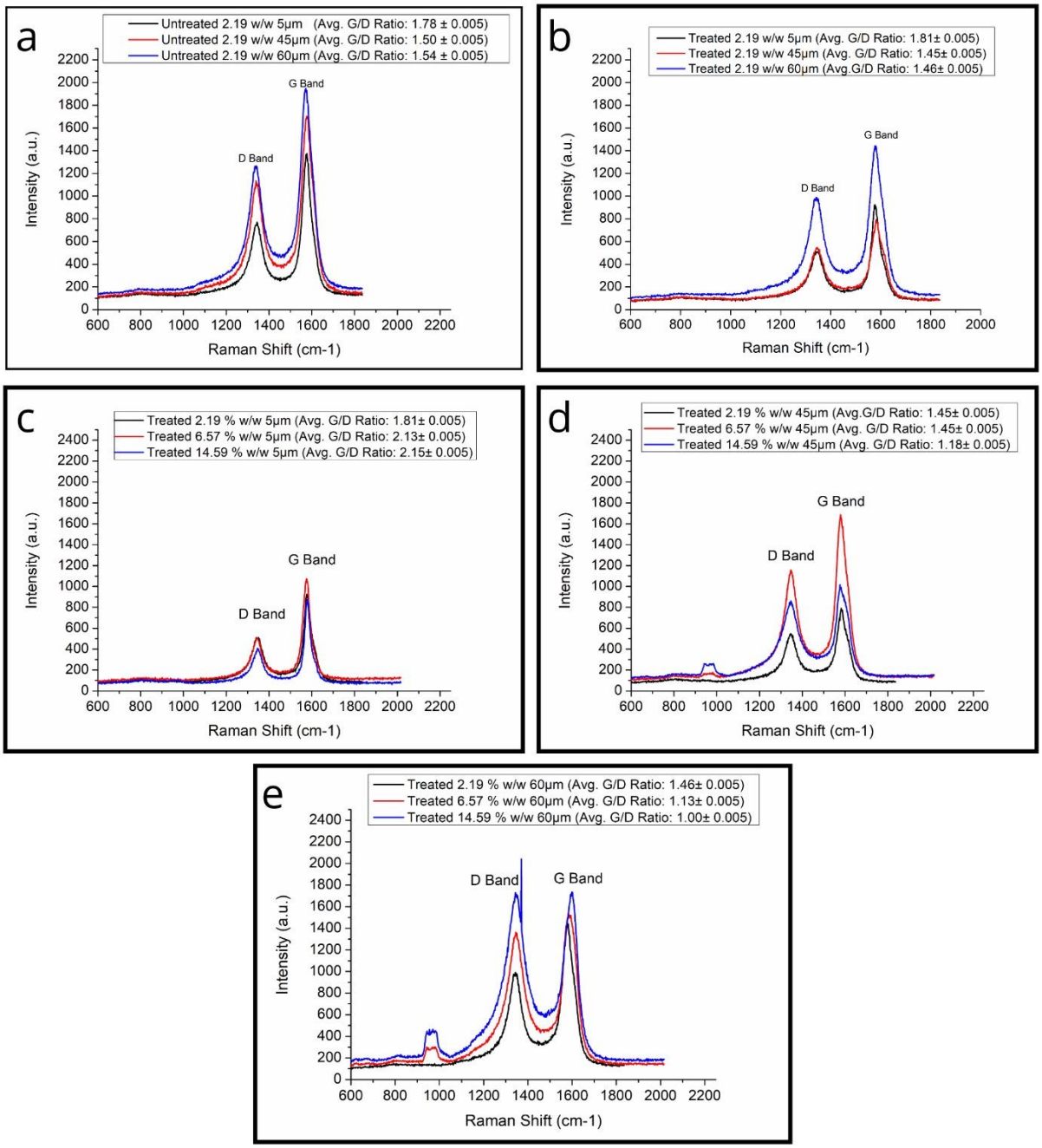

Figure C 4: *Graphical representation comparing Raman spectra of ink concentration 2.19 %w/w printed at droplet spacings 5 µm, 45 µm and 60 µm on* ***a)*** *Untreated and* ***b)*** *10 s plasma treated substrates and raman spectra of ink concentrations 2.19 %w/w, 6.56 %w/w and 14.*

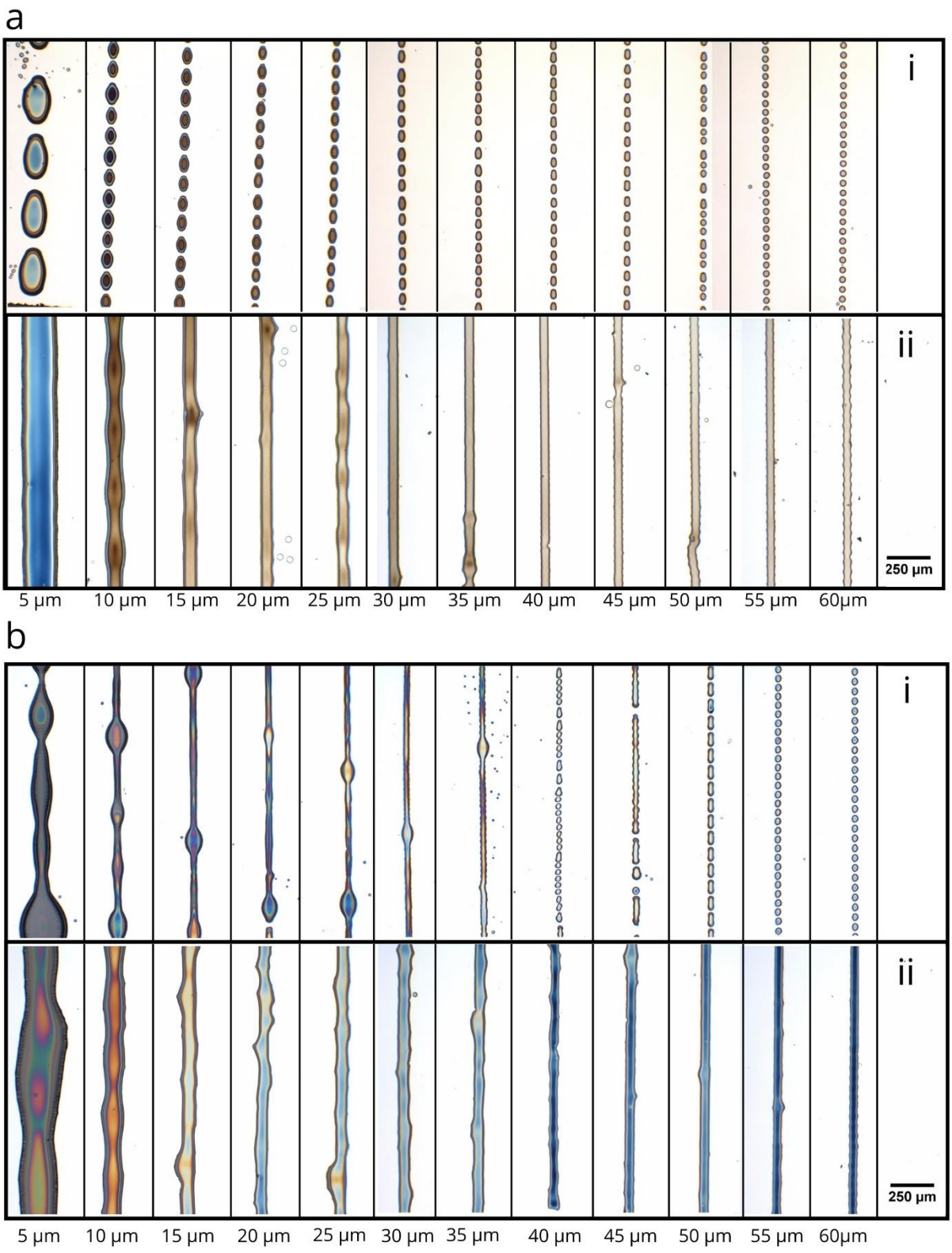

Figure C 5: *Optical micrographs showing ink concentrations* ***a)*** *2.19 $\%_{w/w}$ and* ***b)*** *6.57 $\%_{w/w}$ printed at varying droplet spacings on* ***i)*** *untreated and* ***ii)*** *60 s plasma treated 10 nm alumina coated silicon wafers.*

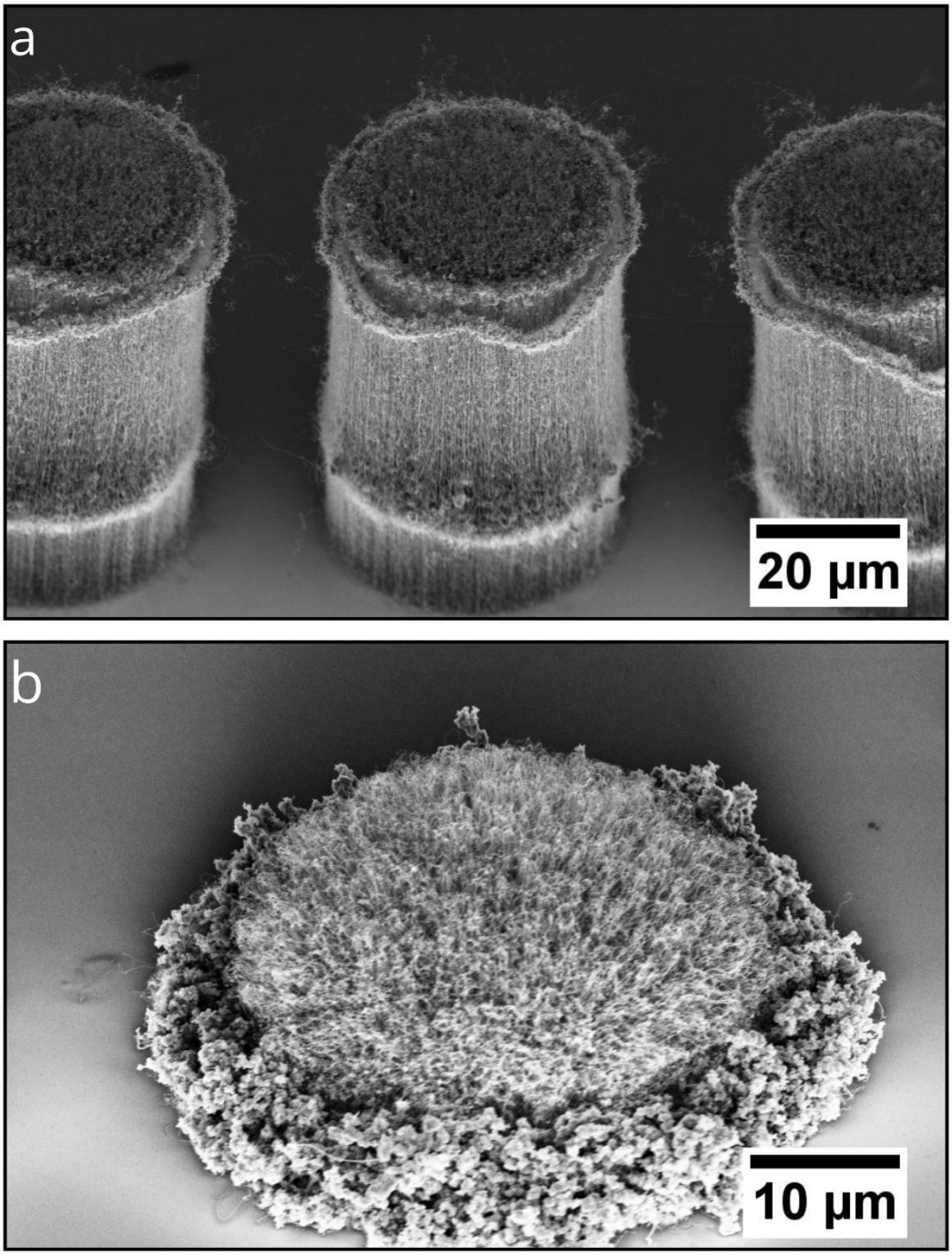

Figure C 6: *SEM Micrograph comparing CNTs grown from magnetite ink concentration 2.19 %w/w on untreated substrate* ***a)*** *sample 1 and* ***b)*** *sample 2 printed at 60 µm droplet spacing.*

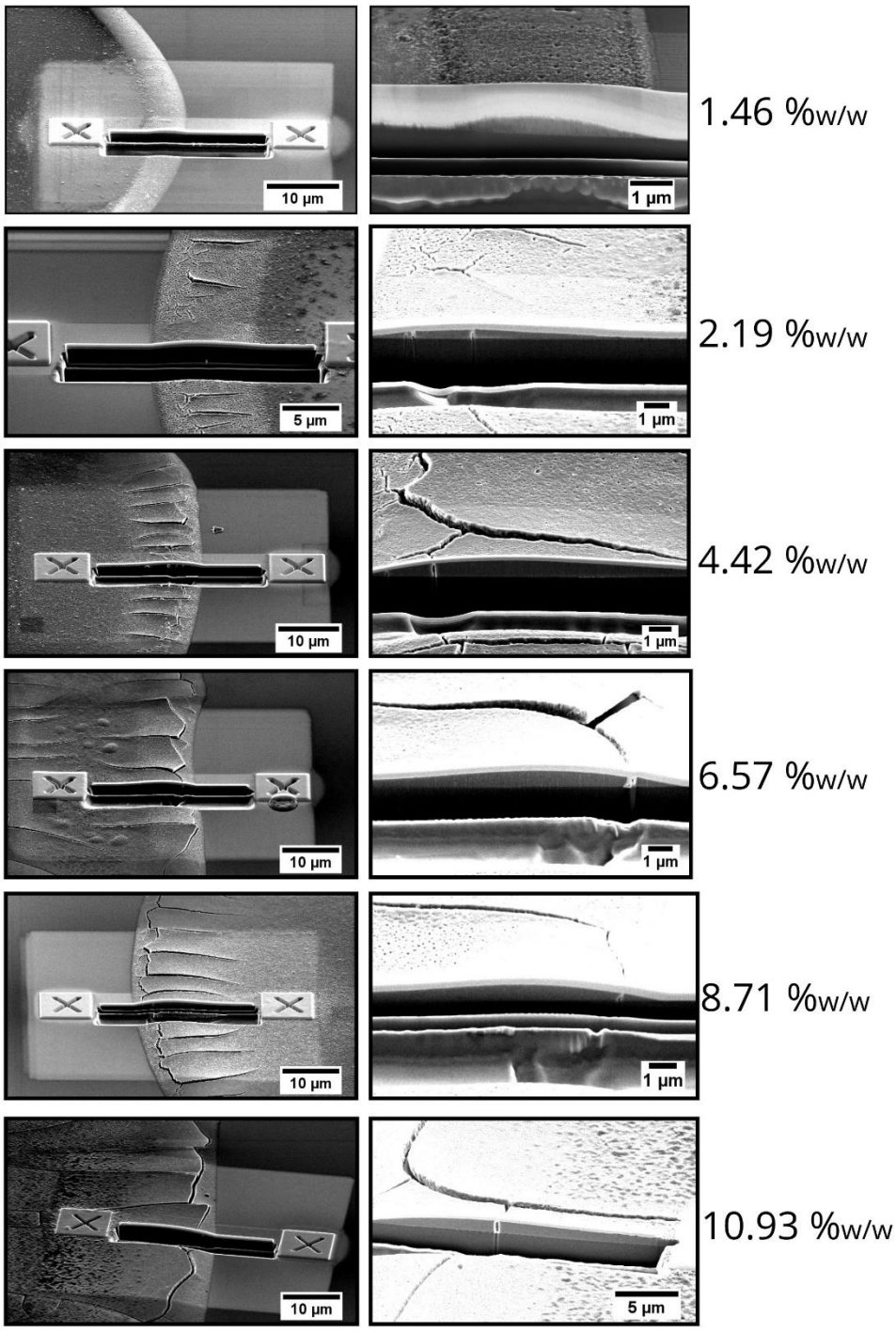

Figure C 7: *SEM micrographs of FIB milled cross section of ink concentrations 1.46 %w/w, 2.19 % w/w, 4.42 % w/w, 6.57 % w/w, 8.71 % w/w, and 10.93 % w/w printed on Untreated 10 nm alumina coated silicon wafers.*

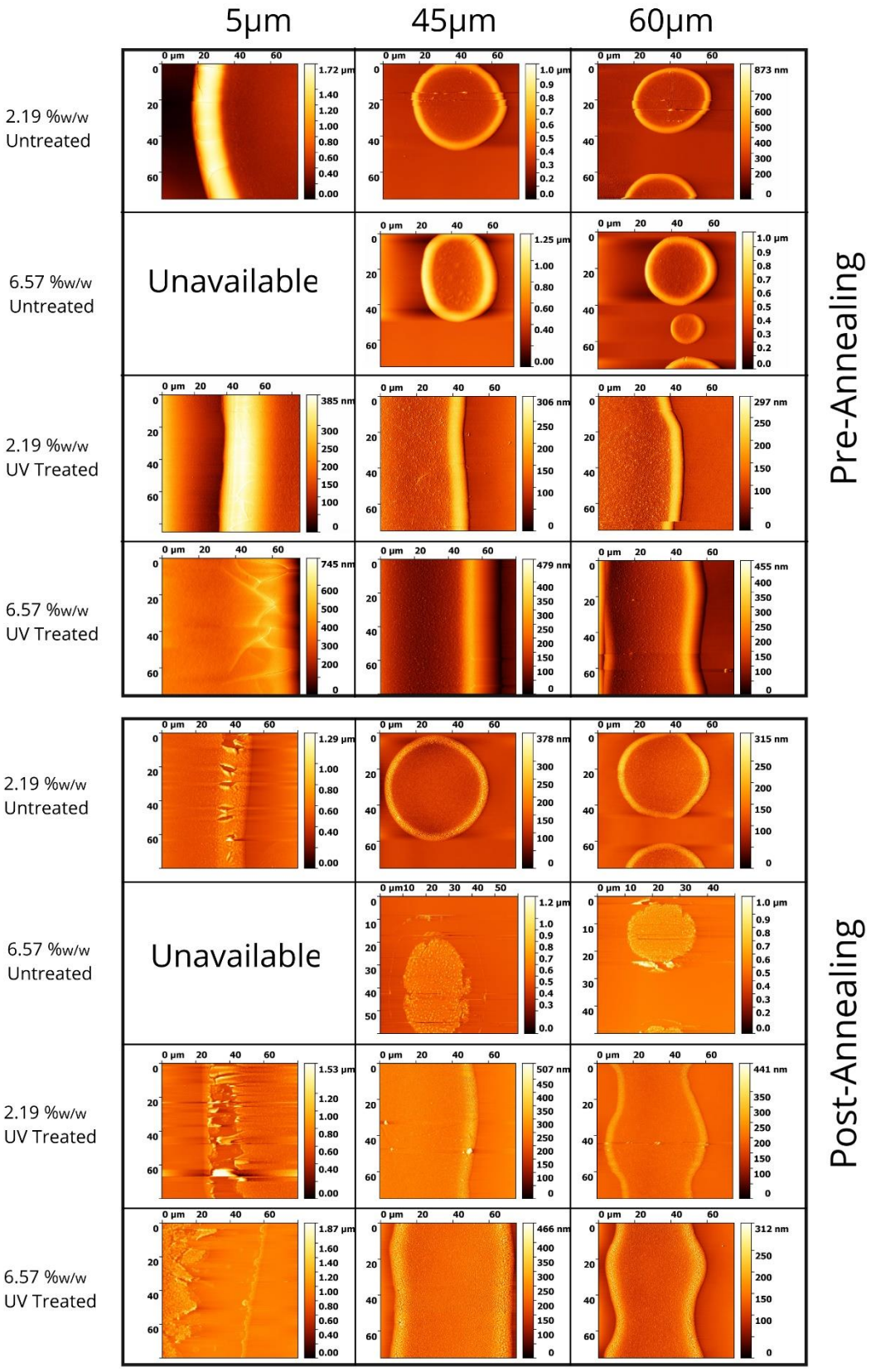

Figure C 8: *AFM micrographs of ink concentrations 2.19 % w/w, and 6.57 % w/w, printed on untreated and UV treated 10 nm alumina coated silicon substrates at droplet spacings 5 µm, 45 µm and 60 µm before and after annealing.*

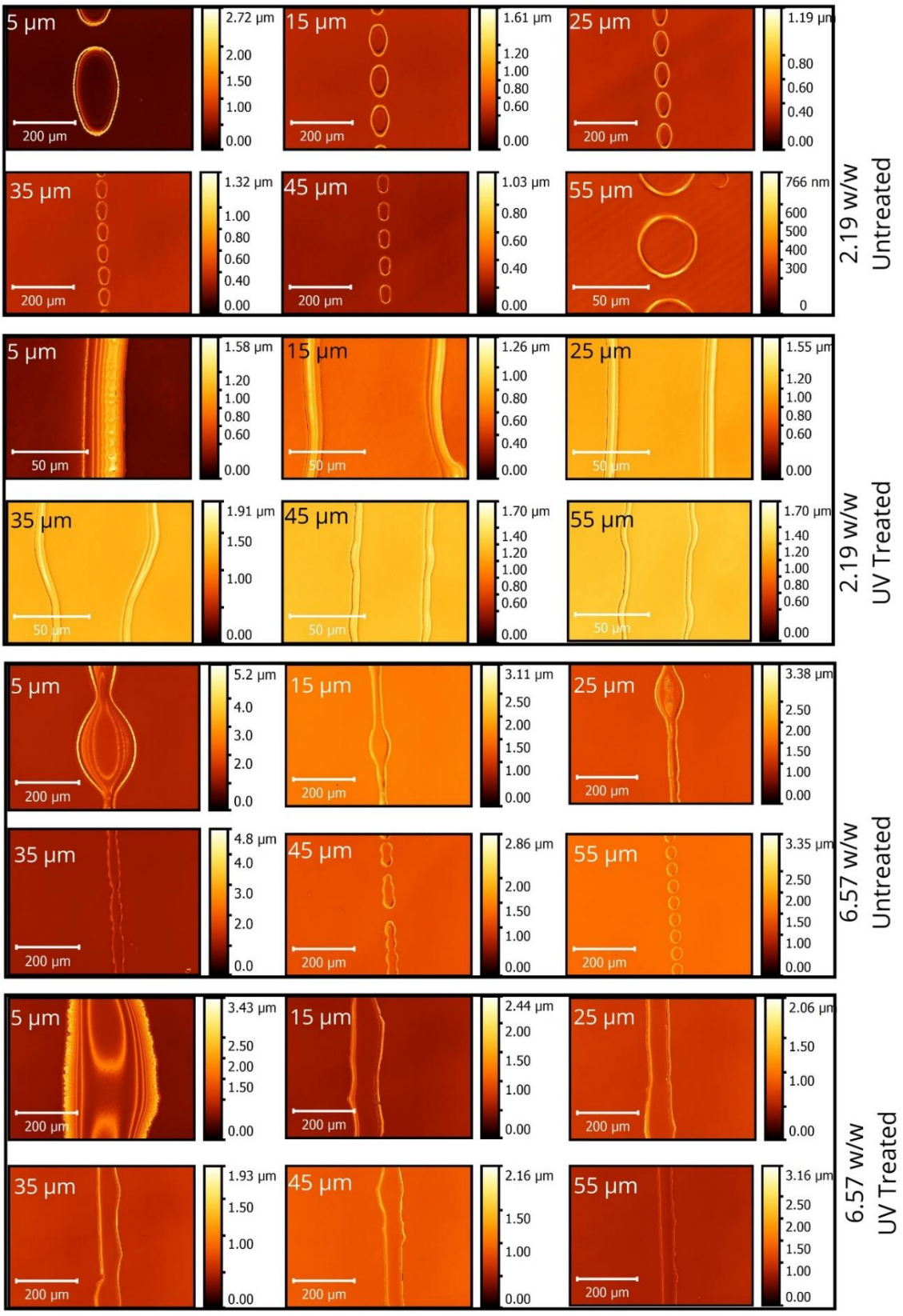

Figure C 9: *Interferometer micrographs of ink concentrations 2.19 % w/w, and 6.57 % w/w, printed at droplet spacings between 5 µm - 60 µm, at 10 µm intervals, on untreated and UV treated 10 nm alumina coated silicon substrates.*

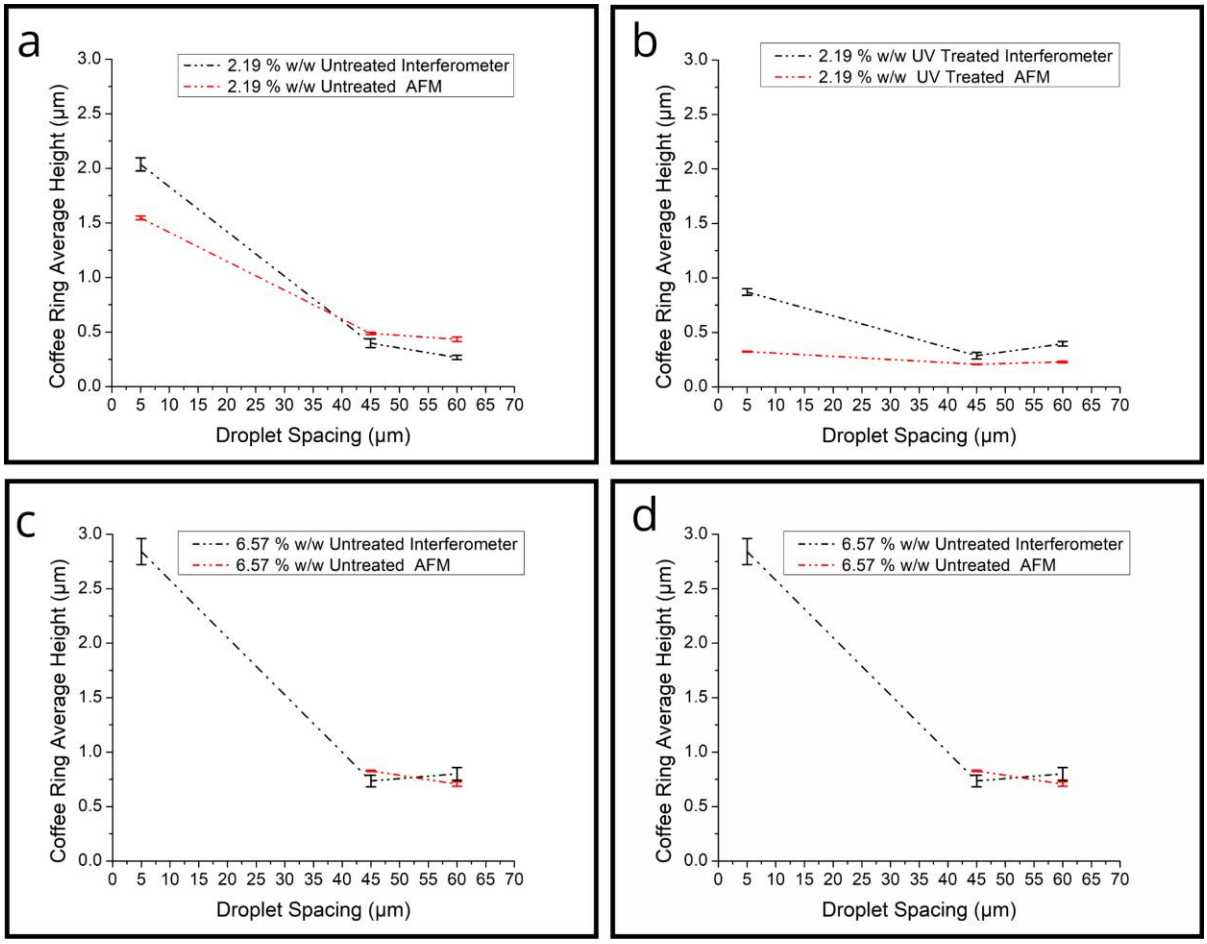

Figure C 10: *Graphical representation of coffee ring average height (µm) vs droplet spacing (µm) comparing data collected with interferometer and AFM for ink concentration 2.19 %$_{w/w}$ printed on* ***a)*** *untreated and* ***b)*** *UV treated substrates and for ink concentration 6.57%$_{w/w}$ on* ***c)*** *untreated and* ***d)*** *UV treated substrates at varying droplet spacings. The standard errors are shown in the graph.*

Table C 5: *Calculations for coffee ring height measurements via white light interferometry and AFM.*

Droplet Spacing (µm)	2.19 $\%_{w/w}$ Untreated	Standard Error (±)	2.19 $\%_{w/w}$ UV Treated	Standard Error (±)	6.57 $\%_{w/w}$ Untreated	Standard Error (±)	6.57 $\%_{w/w}$ UV Treated	Standard Error (±)
Pre Annealed Coffee Ring Height (µm) - Interferometer								
5	2.036059	0.062763	0.870206	0.029842	2.842102	0.119752	1.733468	0.085709
15	0.678758	0.016069	0.488824	0.011923	1.401705	0.044948	0.916651	0.036798
25	0.524402	0.015212	0.432405	0.029298	1.223857	0.056043	0.853178	0.022269
35	0.419039	0.026433	0.381602	0.042988	0.803308	0.081114	0.8626	0.022935
45	0.397306	0.040363	0.285986	0.029527	0.734783	0.052622	0.58546	0.025062
55	0.254178	0.028007	0.297544	0.034757	0.914214	0.059653	0.613987	0.025193
60	0.254178	0.016449	0.395335	0.015348	0.800796	0.058092	0.647943	0.041789
Pre Annealing Coffee Ring Height (µm) - AFM								
5	1.546257	0.016617	0.323888	0.004104			0.5357	0.018683
45	0.4872	0.010934	0.20721	0.002471	0.828035	0.00558	0.245967	0.002948
60	0.433597	0.020175	0.228254	0.006701	0.706764	0.021281	0.280351	0.003531
Post Annealing Coffee Ring Height (µm) - AFM								
5	0.517101	0.068773	0.460533	0.201387			0.384816	0.026626
45	0.196672	0.087205	0.175066	0.079765	0.372636	0.054184	0.213389	0.01129
60	0.181837	0.08201	0.094022	0.041047	0.280646	0.041134	0.195125	0.005563

Table C 6: *Calculations for coffee ring width measurements via optical microscopy.*

	Coffee Ring Width (µm)							
Droplet Spacing (µm)	2.18 $\%_{w/w}$ Untreated	Standard Error (±)	2.18 $\%_{w/w}$ UV Treated	Standard Error (±)	6.56 $\%_{w/w}$ Untreated	Standard Error (±)	6.56 $\%_{w/w}$ UV Treated	Standard Error (±)
5	46.74	1.60	23.50	0.32	31.90	1.21	39.13	1.16
15	10.25	0.43	9.29	0.14	9.78	0.23	13.69	0.25
25	7.76	0.21	8.02	0.14	10.94	0.64	9.63	0.14
35	5.34	0.18	5.74	0.09	7.65	0.24	7.68	0.13
45	5.19	0.21	4.79	0.16	6.65	0.17	6.58	0.05
55	4.15	0.10	4.26	0.07	5.72	0.29	5.10	0.08
60	3.71	0.12	3.99	0.14	5.61	0.17	4.94	0.09

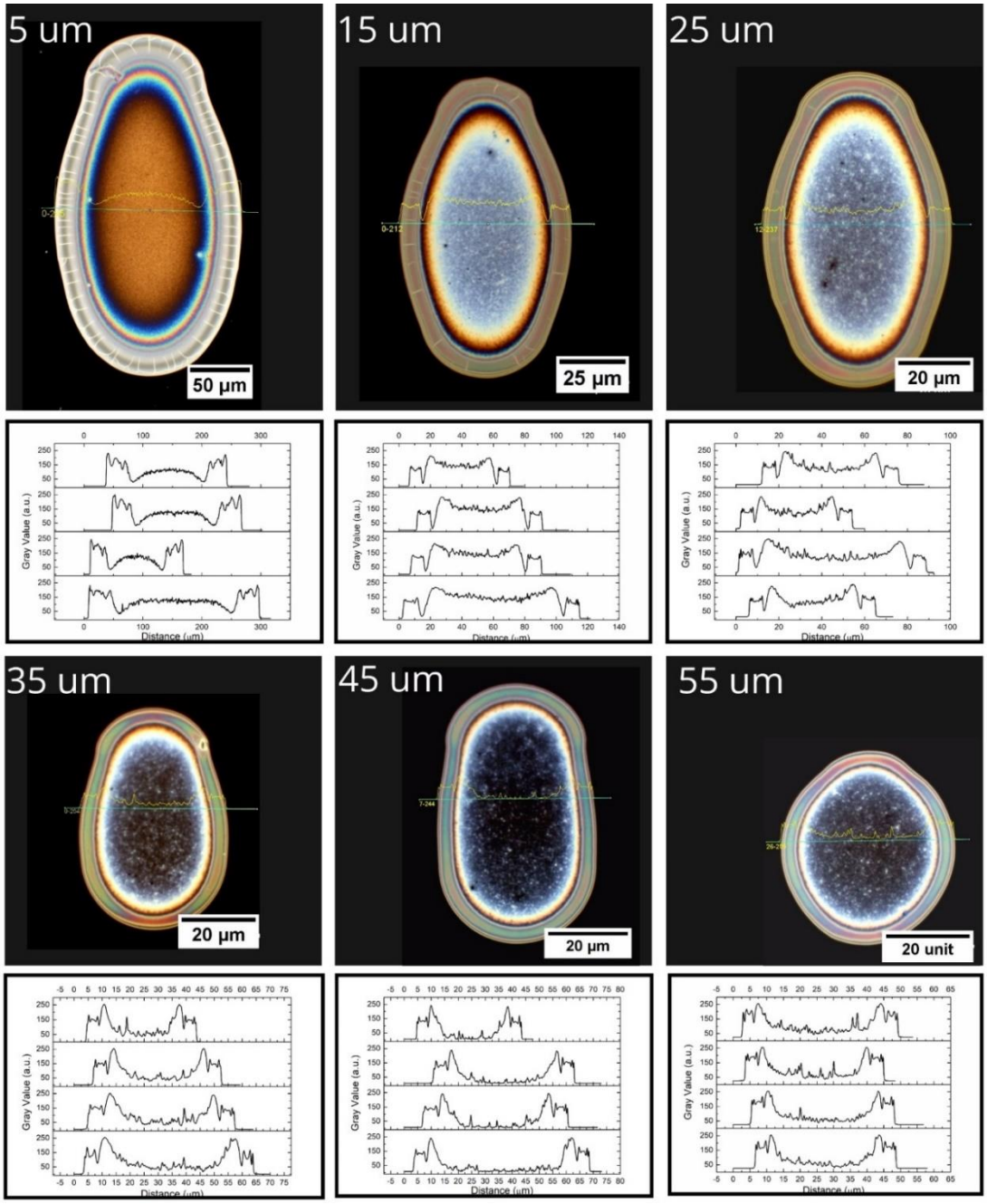

Figure C 11: *Optical micrographs and width profiles of ink concentration 2.19 % $_{w/w,}$ printed on untreated 10 nm alumina coated silicon wafer substrates.*

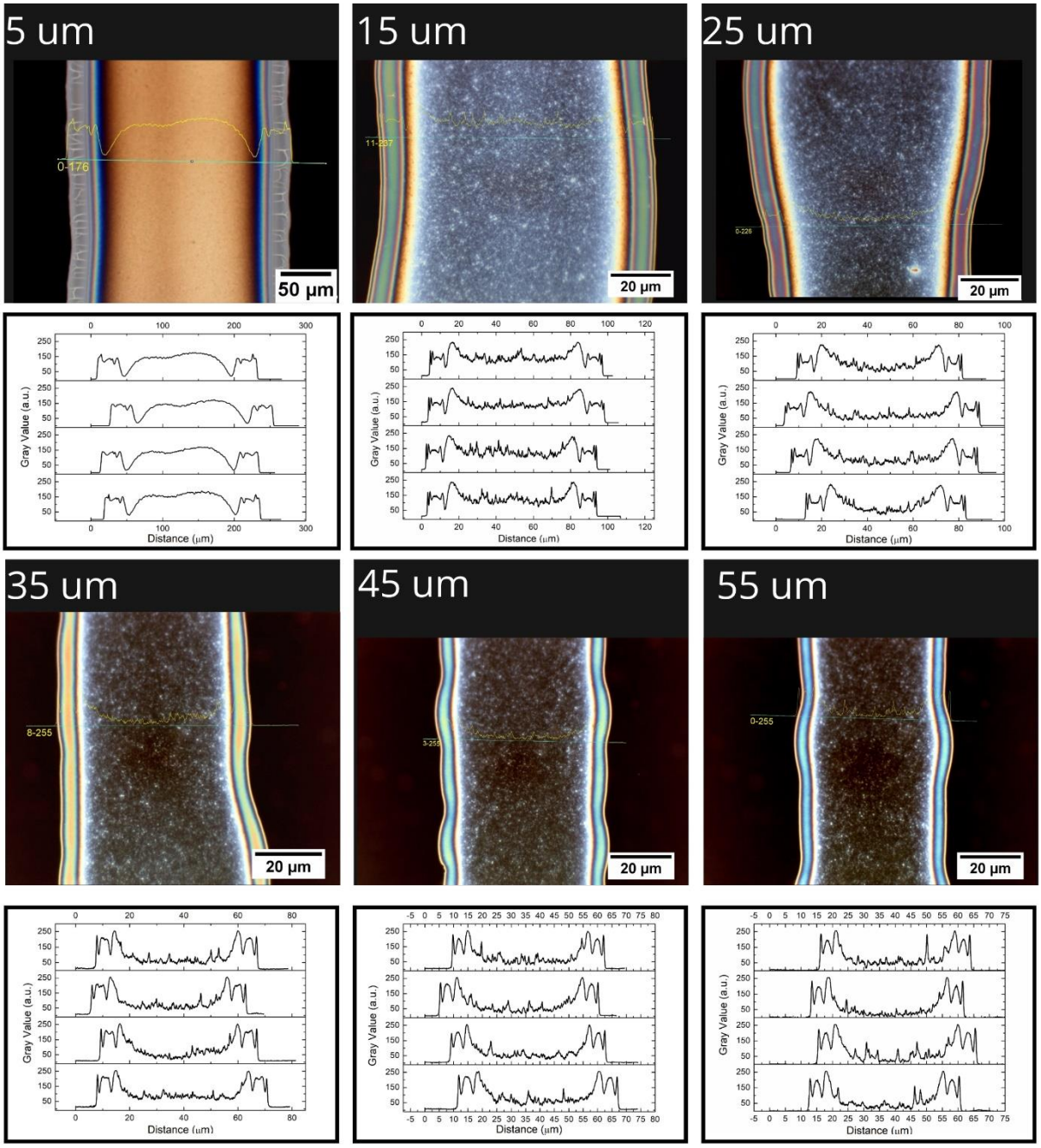

Figure C 12: *Optical micrographs and width profiles of ink concentration 2.19 % $_{w/w,}$ printed on UV treated 10 nm alumina coated silicon wafer substrates.*

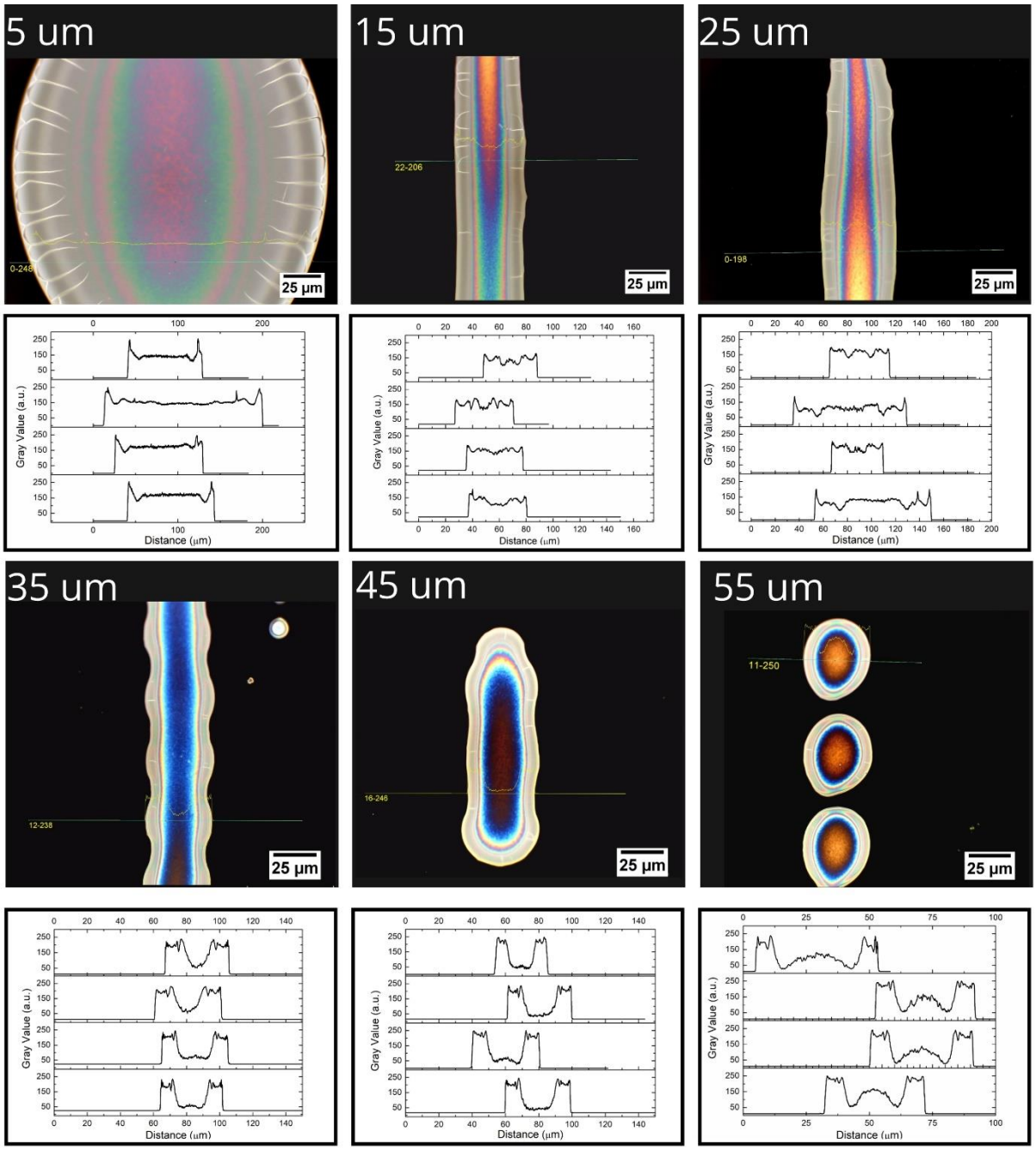

Figure C 13: *Optical micrographs and width profiles of ink concentration 6.57 % $_{w/w,}$ printed on untreated 10 nm alumina coated silicon wafer substrates.*

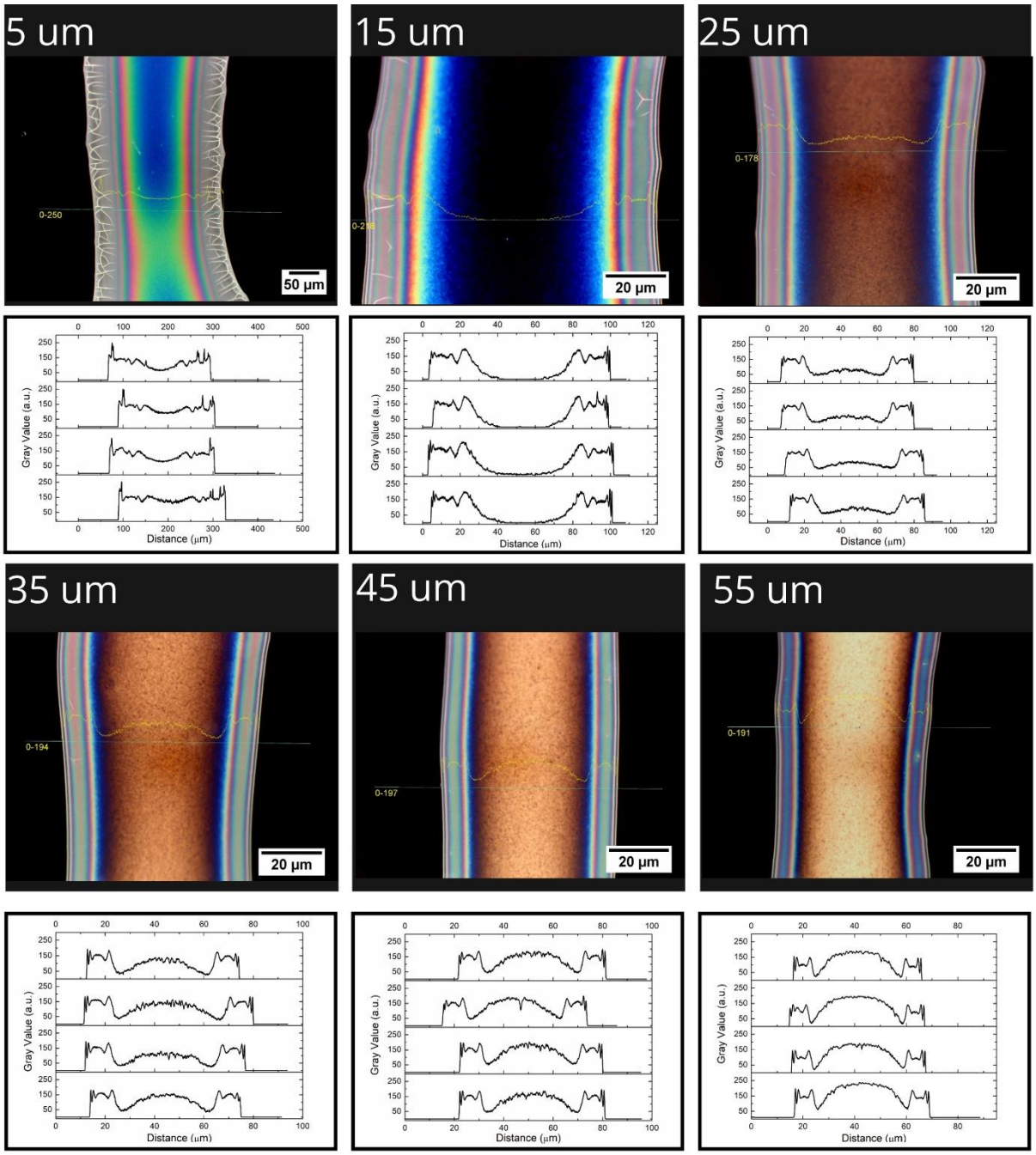

Figure C 14: *Optical micrographs and width profiles of ink concentration 6.57 % $_{w/w,}$ printed on UV treated 10 nm alumina coated silicon wafer substrates.*

Table C 7: *Calculations for coffee ring height measurements via AFM, width measurements via optical microscopy and the resulting volume measurements for inks printed for a length of 1 µm.*

Droplet Spacing (µm)	***2.19 %$_{w/w}$ Untreated***	***2.19 %$_{w/w}$ UV Treated***	***6.57 %$_{w/w}$ Untreated***	***6.57 %$_{w/w}$ UV Treated***
AFM Measured Height (µm)				
5	*1.546257*	*0.323888*	*2.842101877*	*0.535699722*
45	*0.4872*	*0.20721*	*0.828035*	*0.245966555*
60	*0.433597*	*0.228254*	*0.706764*	*0.280351041*
Optically measured width (µm)				
5	*46.74166667*	*23.503125*	*31.903875*	*39.13325*
45	*5.19475*	*4.7865*	*6.654*	*6.5775*
60	*3.71325*	*3.993125*	*5.60675*	*4.941*
Volume (µm^3)				
5	*72.27462928*	*7.61238015*	*90.67406302*	*20.96367116*
45	*2.5308822*	*0.991810665*	*5.50974489*	*1.617845014*
60	*1.61005406*	*0.911446754*	*3.962649057*	*1.385214496*

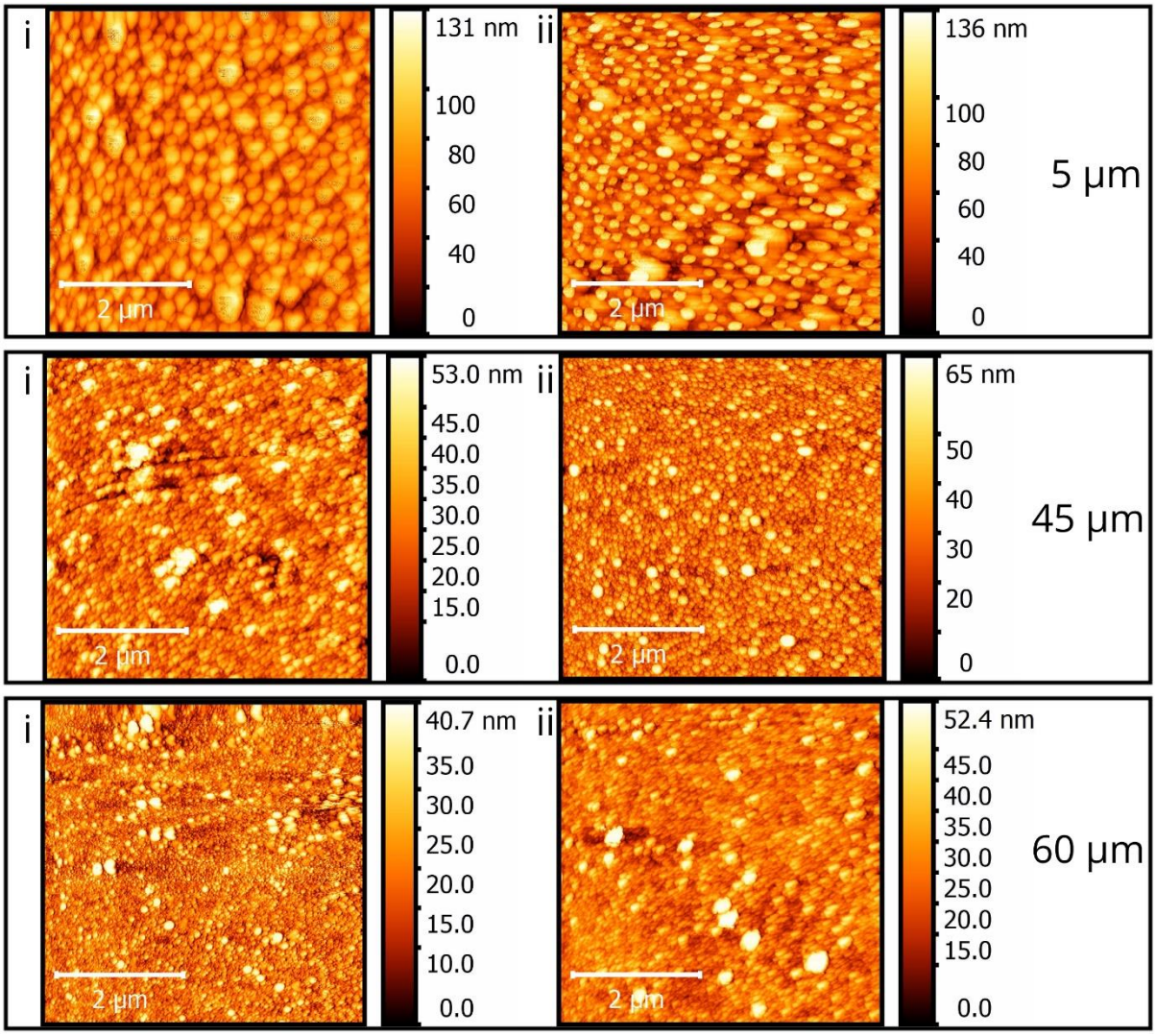

Figure C 15: *AFM micrographs showing nucleated catalyst islands in* ***i)*** *region 1 and* ***ii)*** *region 2 for ink concentration 2.19 %w/w printed on UV treated 10 nm alumina coated silicon substrates at droplet spacings 5 µm, 45 µm and 60 µm.*

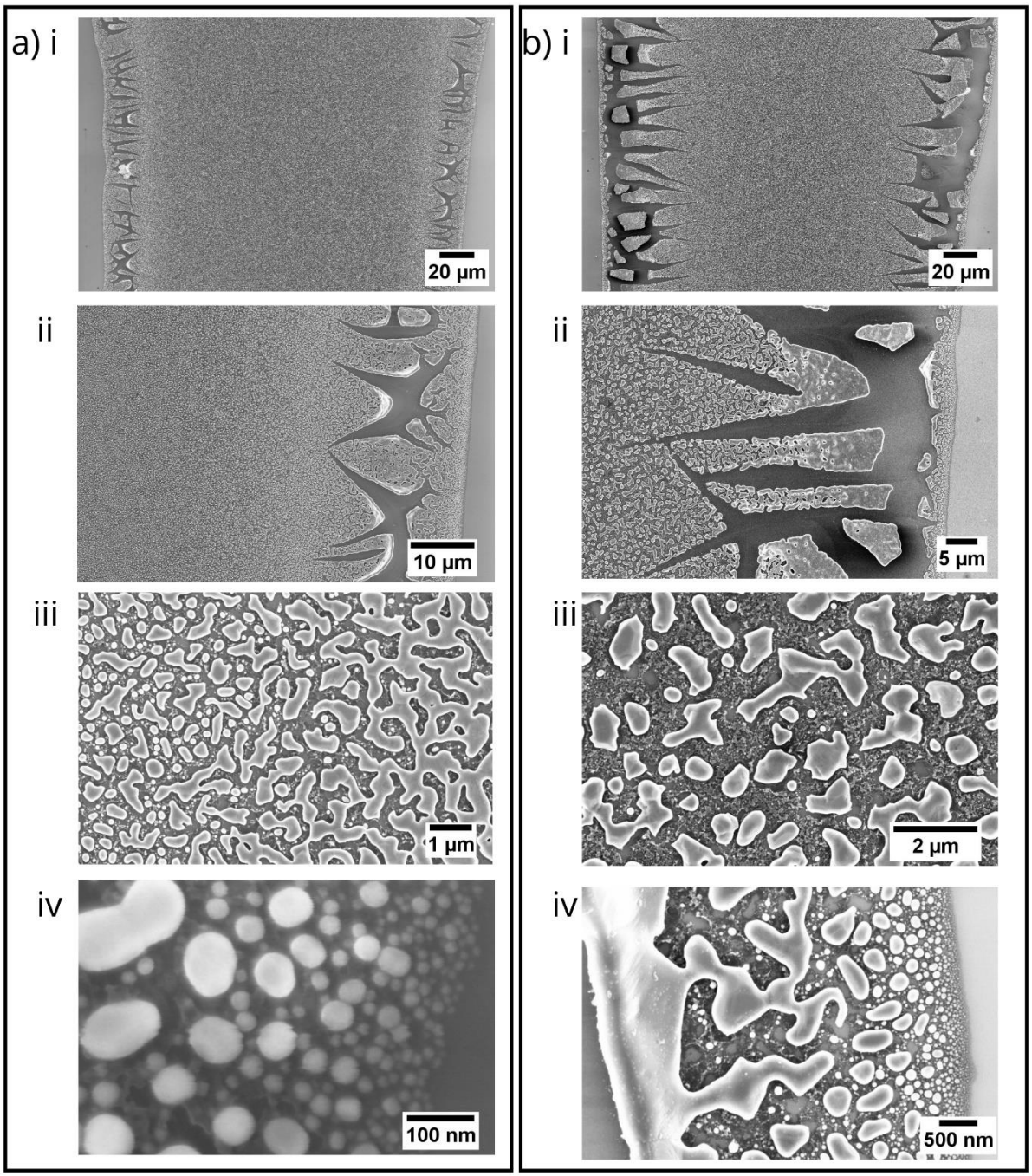

Figure C 16: *SEM micrographs of annealed films of ink concentrations* ***a)*** *2.19 %$_{w/w}$ and* ***b)*** *6.57 %$_{w/w}$ printed on UV treated 10 nm alumina coated silicon substrates at droplet spacings 5 µm.*

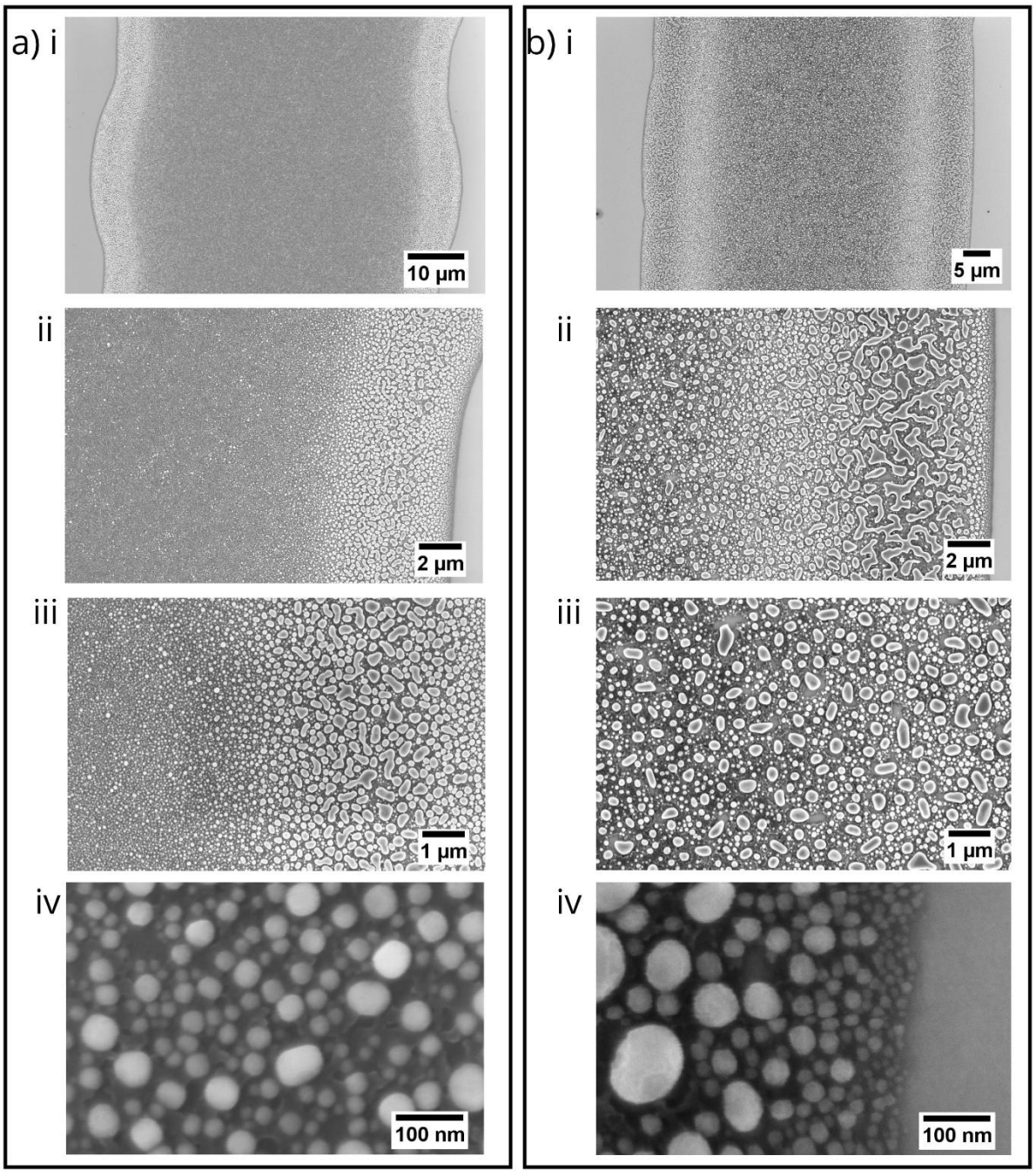

Figure C 17: *SEM micrographs of annealed films of ink concentrations* ***a)*** *2.19 %$_{w/w}$ and* ***b)*** *6.57 %$_{w/w}$ printed on UV treated 10 nm alumina coated silicon substrates at droplet spacings 45 µm.*

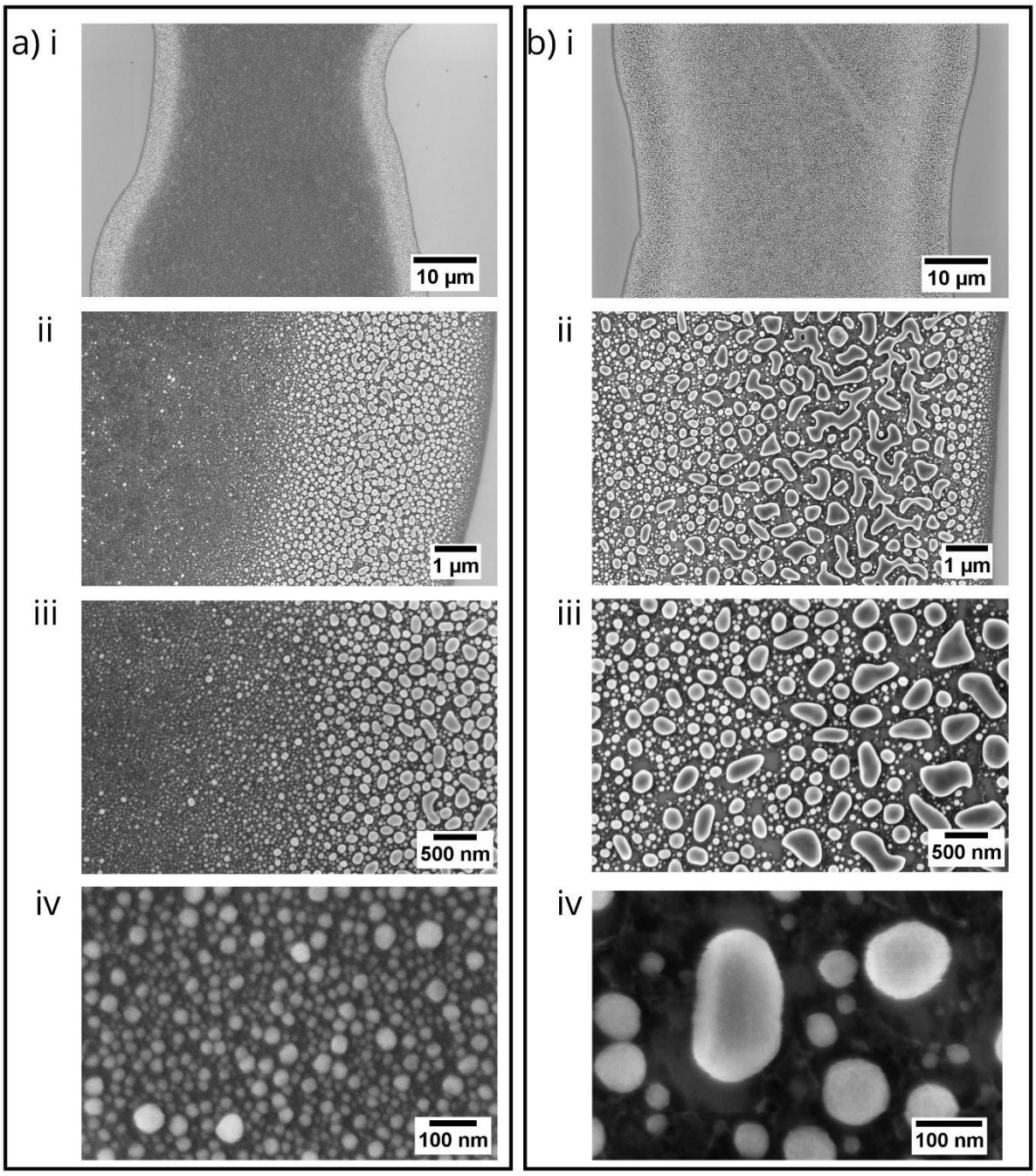

Figure C 18: *SEM micrographs of annealed films of ink concentrations* ***a)*** *2.19 %$_{w/w}$ and* ***b) 6.57 %$_{w/w}$*** *printed on UV treated 10 nm alumina coated silicon substrates at droplet spacings 60 µm.*

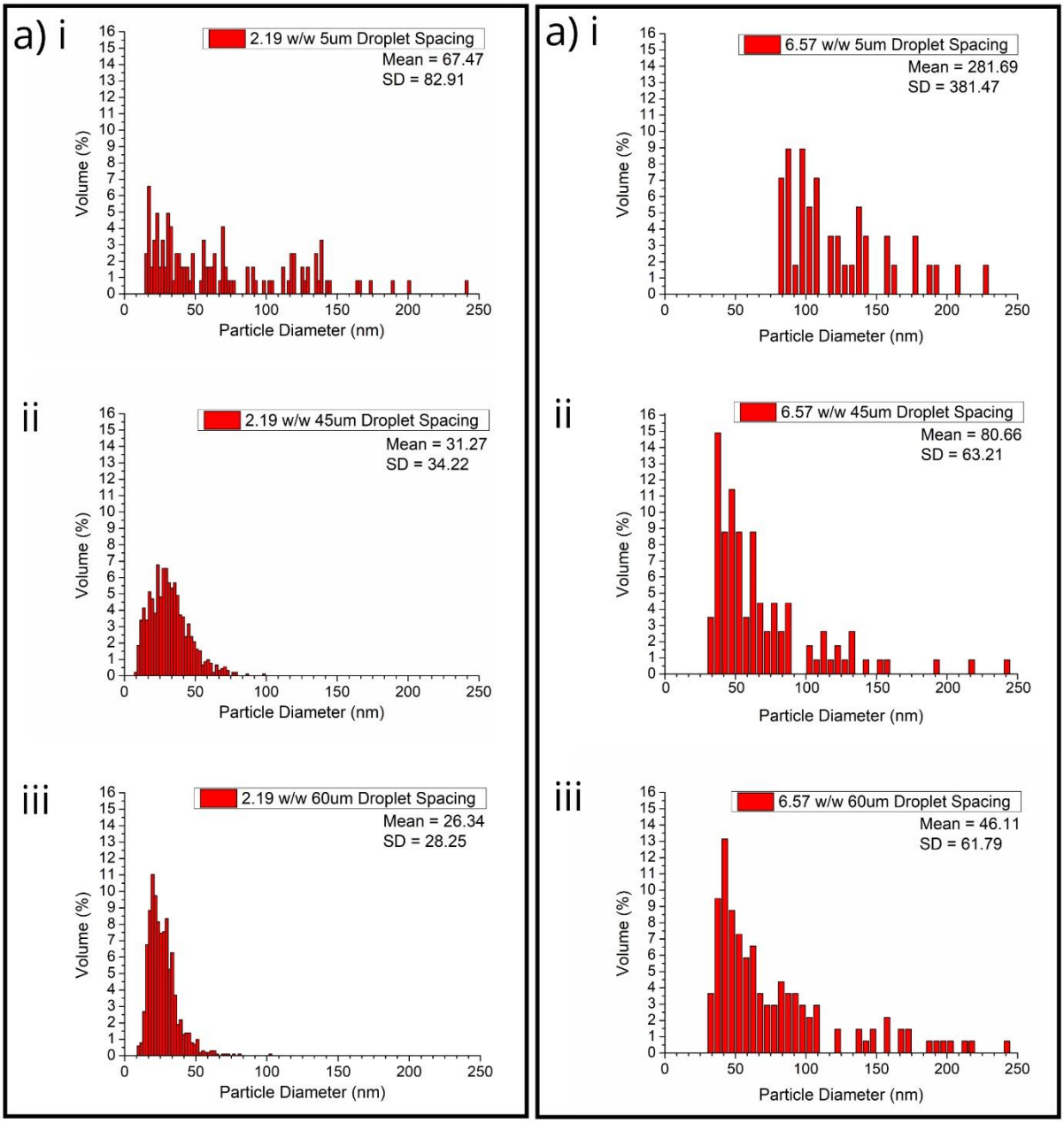

Figure C 19: *Graphical representation of particle size distribution for ink concentrations* ***a)*** *2.19 %$_{w/w}$ and* ***b) 6.57 %$_{w/w}$*** *printed on UV treated 10 nm alumina coated silicon substrates at droplet spacings 5 µm, 45 µm and 60 µm.*

Appendix D

Table D 1: *Fluence calculations for varying modulation efficiencies and attenuation wheel positions used.*

		2014 – 2015	2015 - 2016	2016 - 2017
Modulation efficiency %	**Attenuation Wheel Position**	**Fluence ± 0.005 (J/cm²)**	**Fluence ± 0.005 (J/cm²)**	**Fluence ± 0.005 (J/cm²)**
25	2	0.20	0.15	0.13
26	2	0.28	0.21	0.18
27	2	0.39	0.30	0.26
28	2	0.52	0.40	0.35
28	12	0.45	-	-
28	13	0.41	-	-
28	14	0.37	-	-
28	15	0.34	-	-
28	16	0.30	-	-
28	17	0.27	-	-
28	18	0.23	-	-
28	19	0.20	-	-
29	2	0.68	0.53	0.48
30	2	0.87	0.68	0.61
30	3	0.91	0.67	0.61
30	4	0.85	0.61	0.57
30	5	0.79	0.57	0.53
30	6	0.74	0.54	0.50
30	7	0.70	0.51	0.45
30	8	0.65	0.48	0.44
30	9	0.61	0.45	0.39
30	10	0.57	0.42	0.37
30	11	0.52	0.39	0.34
30	12	0.48	0.36	0.31
30	13	0.45	0.33	0.28
30	14	0.41	0.30	0.25
30	15	0.37	0.27	0.23
30	16	0.33	0.24	0.20
30	17	0.30	0.21	0.18
30	18	0.26	0.19	0.15
30	19	0.23	0.16	0.13
30	20	0.20	0.14	0.12
31	2	1.27	0.88	0.73
32	2	1.54	1.09	0.95
33	2	1.85	1.58	1.17
34	2	2.18	1.59	1.43
35	2	2.57	1.87	1.68
36	2	2.98	2.17	1.95
37	2	3.43	2.50	2.25

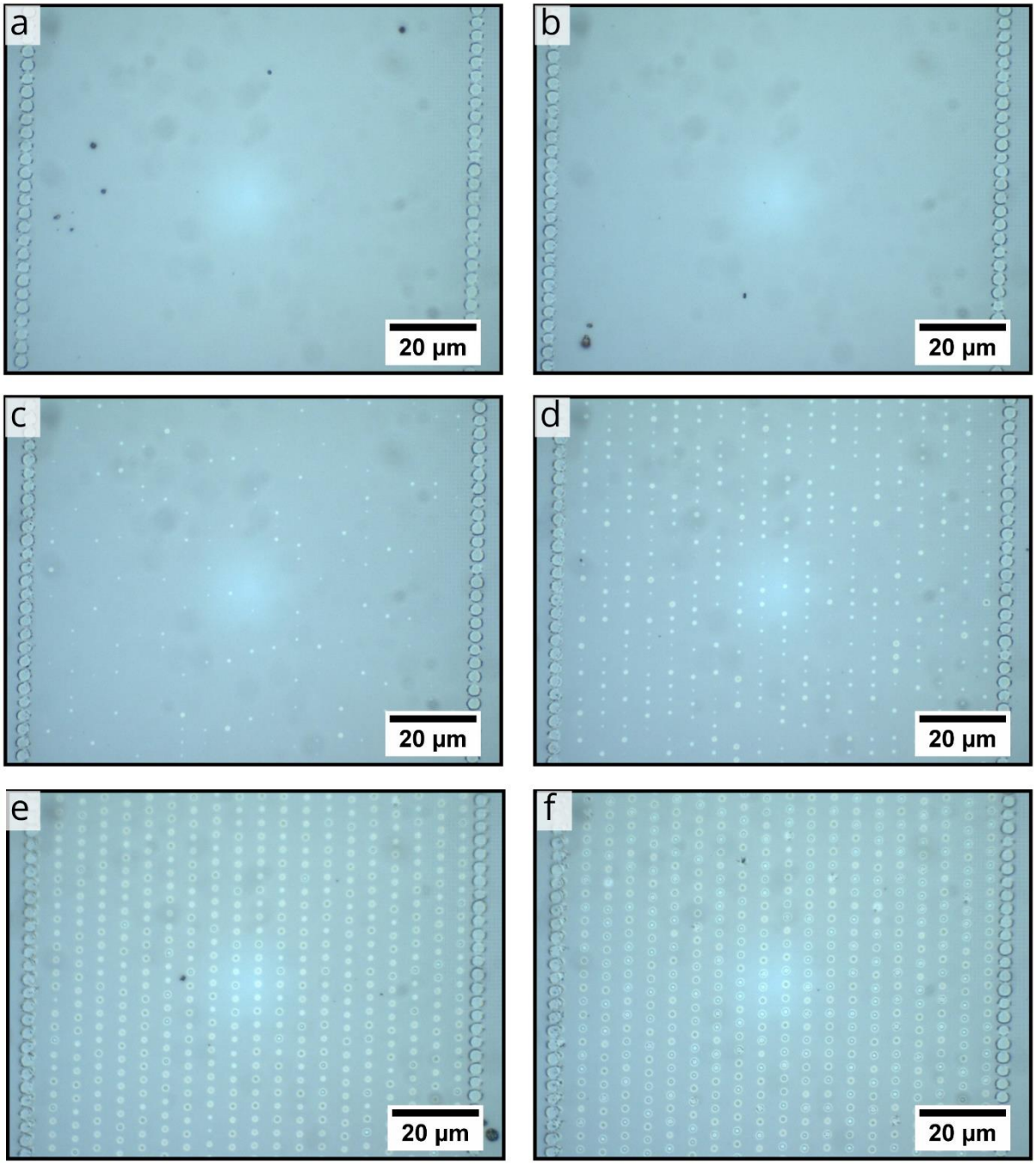

Figure D 1: *Optical micrographs of 1 nm iron coated 10ASW substrates with a) no laser exposure and lines patterned at fluence* ***b)*** *0.20 J/cm², **c)** 0.27 J/cm², **d)** 0.30 J/cm², **e)** 0.37 J/cm² and **f)** 0.41 J/cm².*

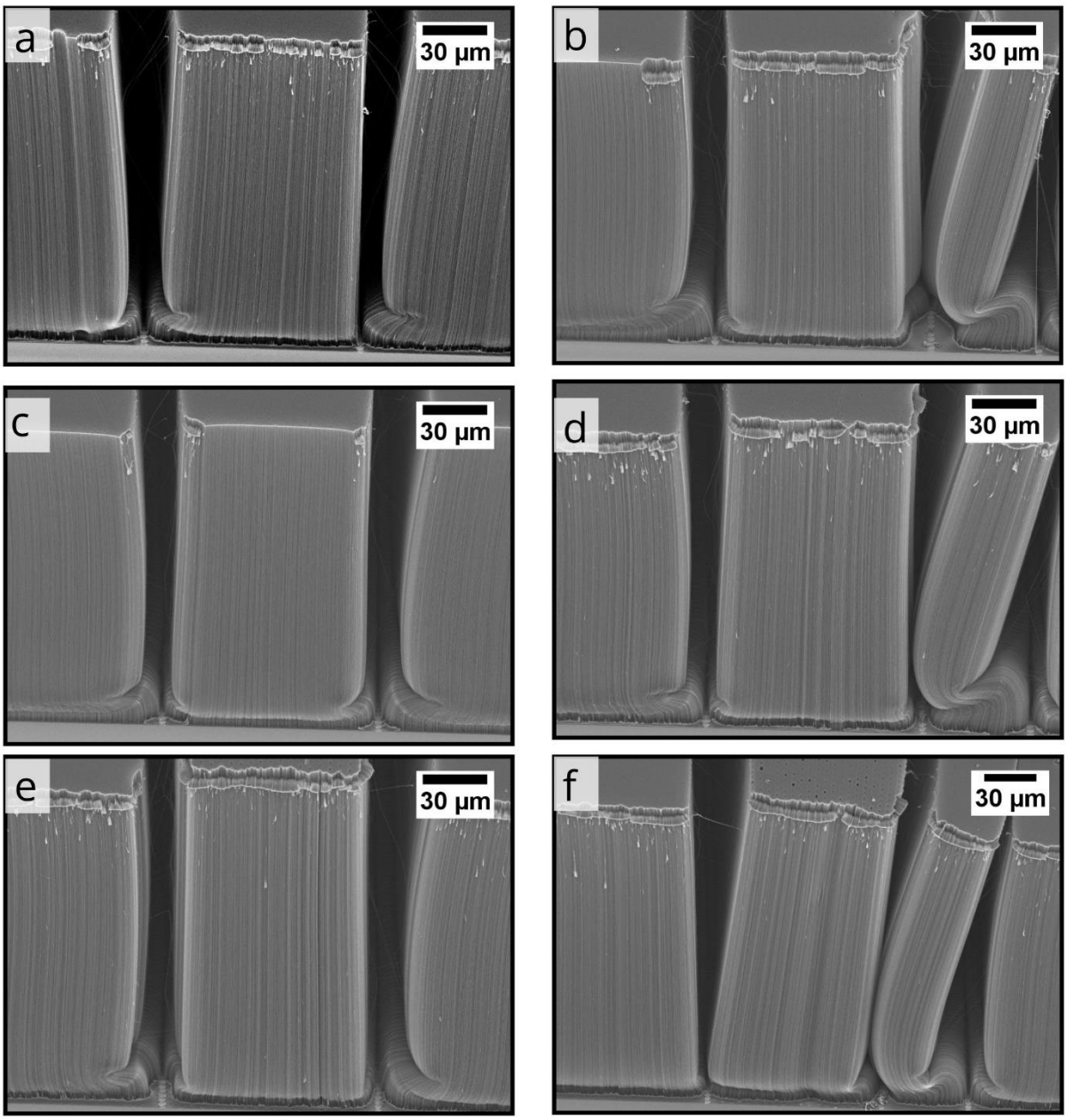

Figure D 2: *SEM micrographs showing side view of VA-CNTs grown from* ***a)*** *unpatterned and laser patterned 1 nm alumina coated 10ASW substrates at fluence* ***b)*** *0.20 J/cm² **c)** 0.27 J/cm², **d)** 0.30 J/cm², **e)** 0.37 J/cm² and **f)** 0.41 J/cm².*

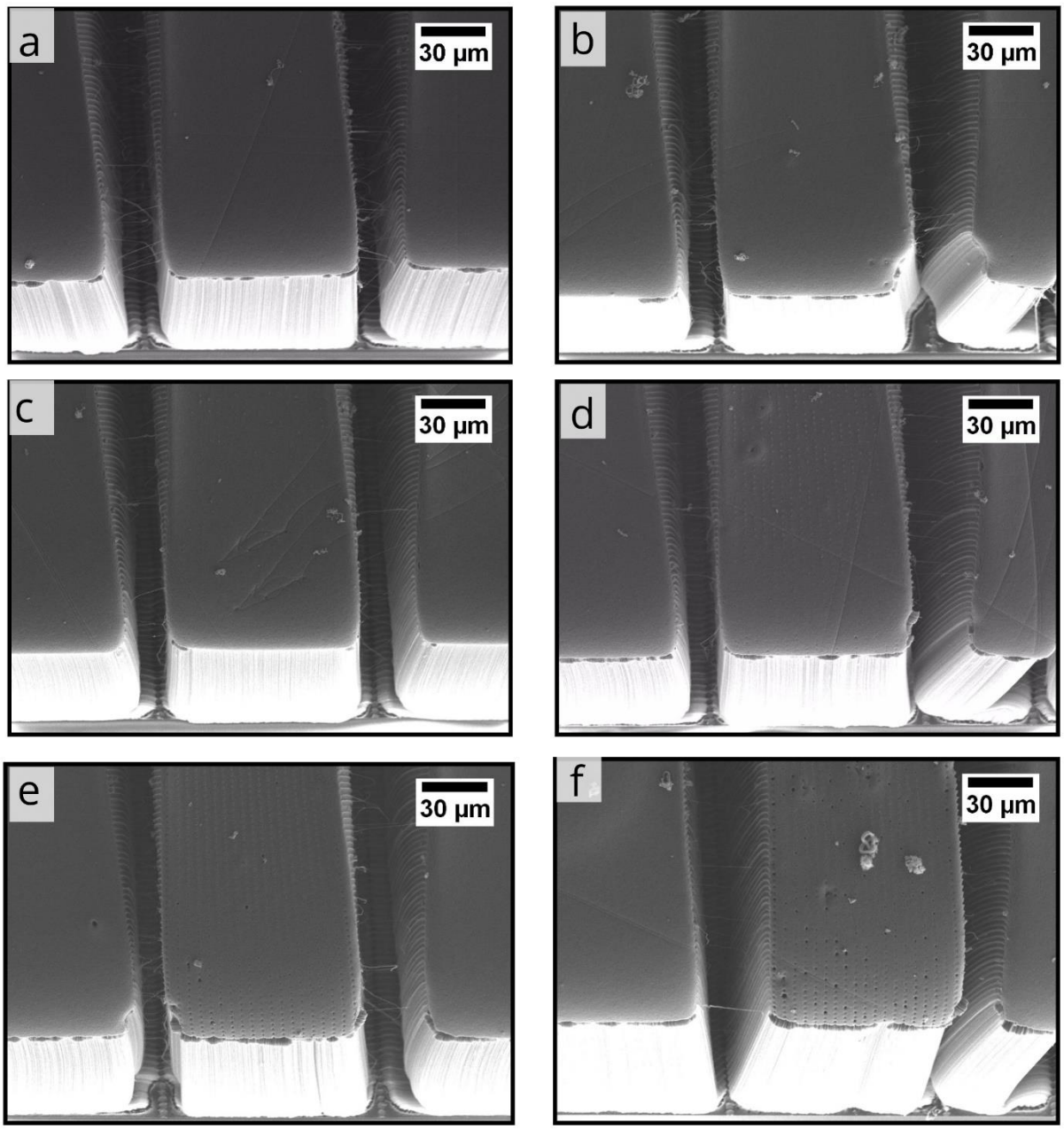

Figure D 3: *SEM micrographs showing top view of VA-CNTs grown from* ***a)*** *unpatterned and laser patterned 1 nm alumina coated 10ASW substrates at fluence* ***b)*** *0.20 J/cm² **c)** 0.27 J/cm², **d)** 0.30 J/cm², **e)** 0.37 J/cm² and **f)** 0.41 J/cm².*

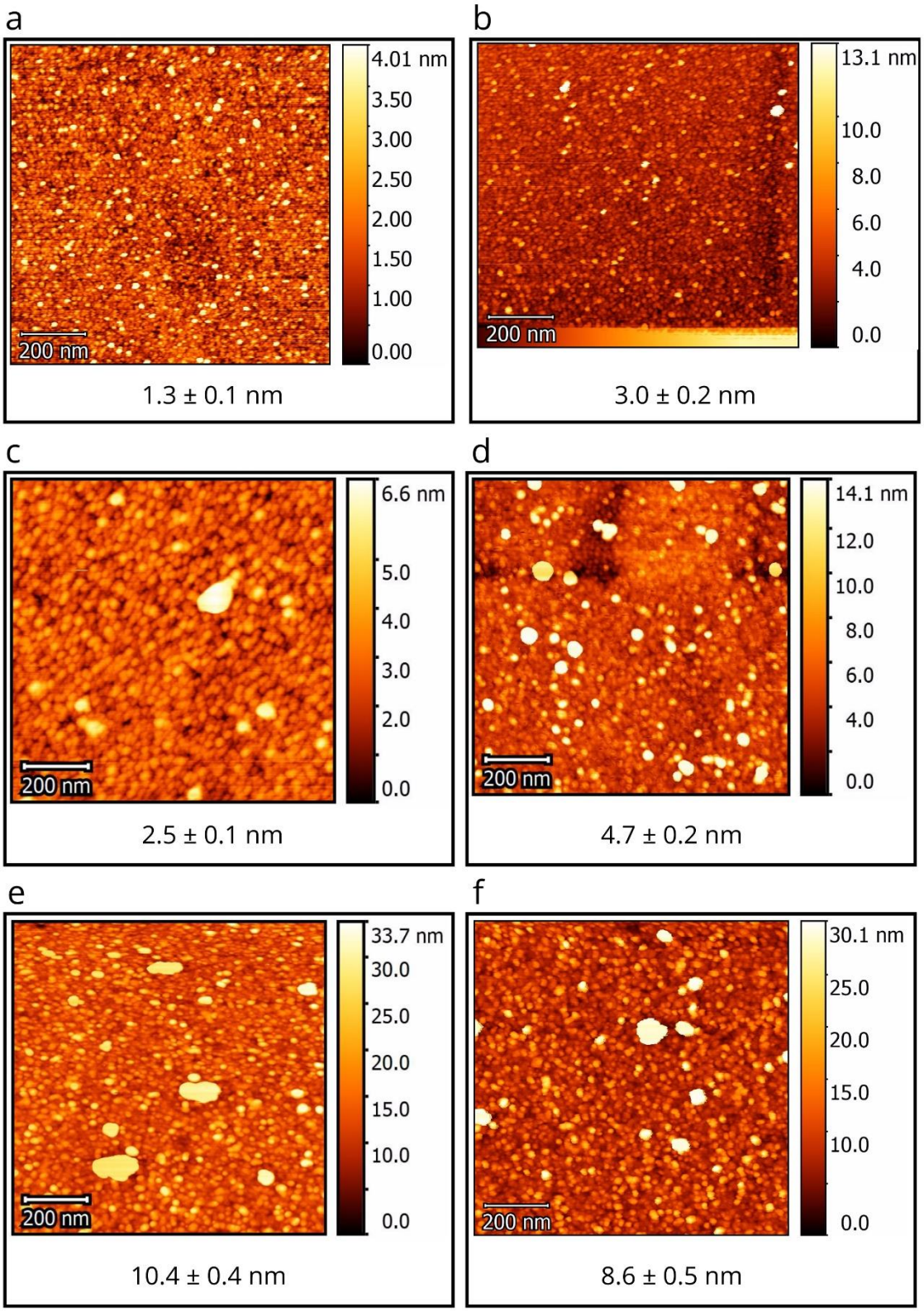

Figure D 4: *AFM micrographs of laser paths patterned on annealed 1 nm iron coated 10ASW substrates at fluence* ***a)*** *0.28 J/cm², **b)** 0.52 J/cm· **c)** 0.79 J/cm², **d)** 2.18 J/cm², **e)** 2.57 J/cm² and **f)** 2.98 J/cm². All errors represent the standard error calculated.*

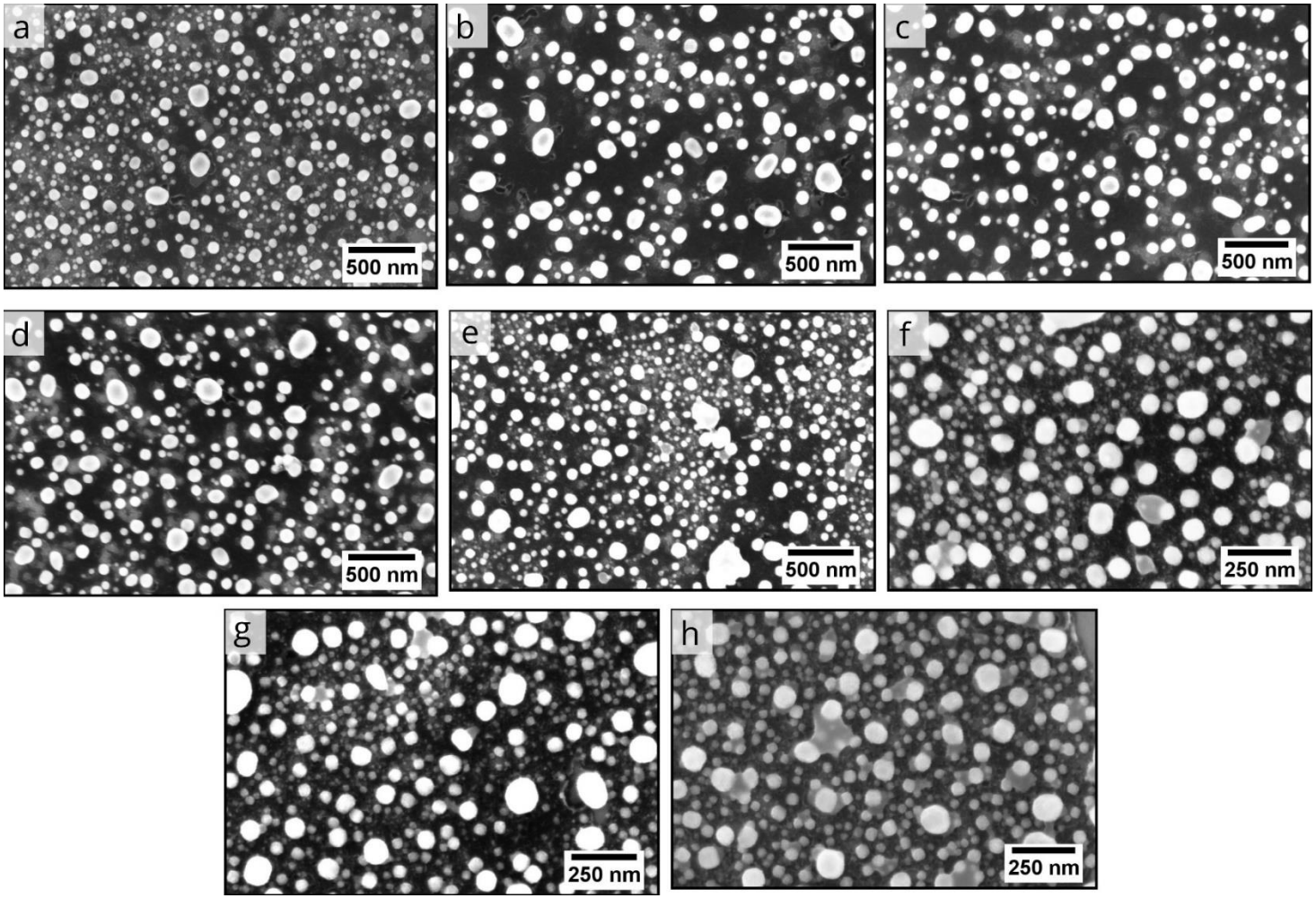

Figure D 5: *Post annealing SEM micrographs of ink concentration 2.19 %w/w printed at droplet spacing 5 µm on 10ASW substrates* ***a)*** *before patterning and after laser patterning at fluence* ***b)*** *0.35 J/cm², **c)** 0.48 J/cm² **d)** 0.63 J/cm², **e)** 0.95 J/cm² **f)** 1.43 J/cm² **g)** 1.17 J/cm² and **h)** 1.95 J/cm².*

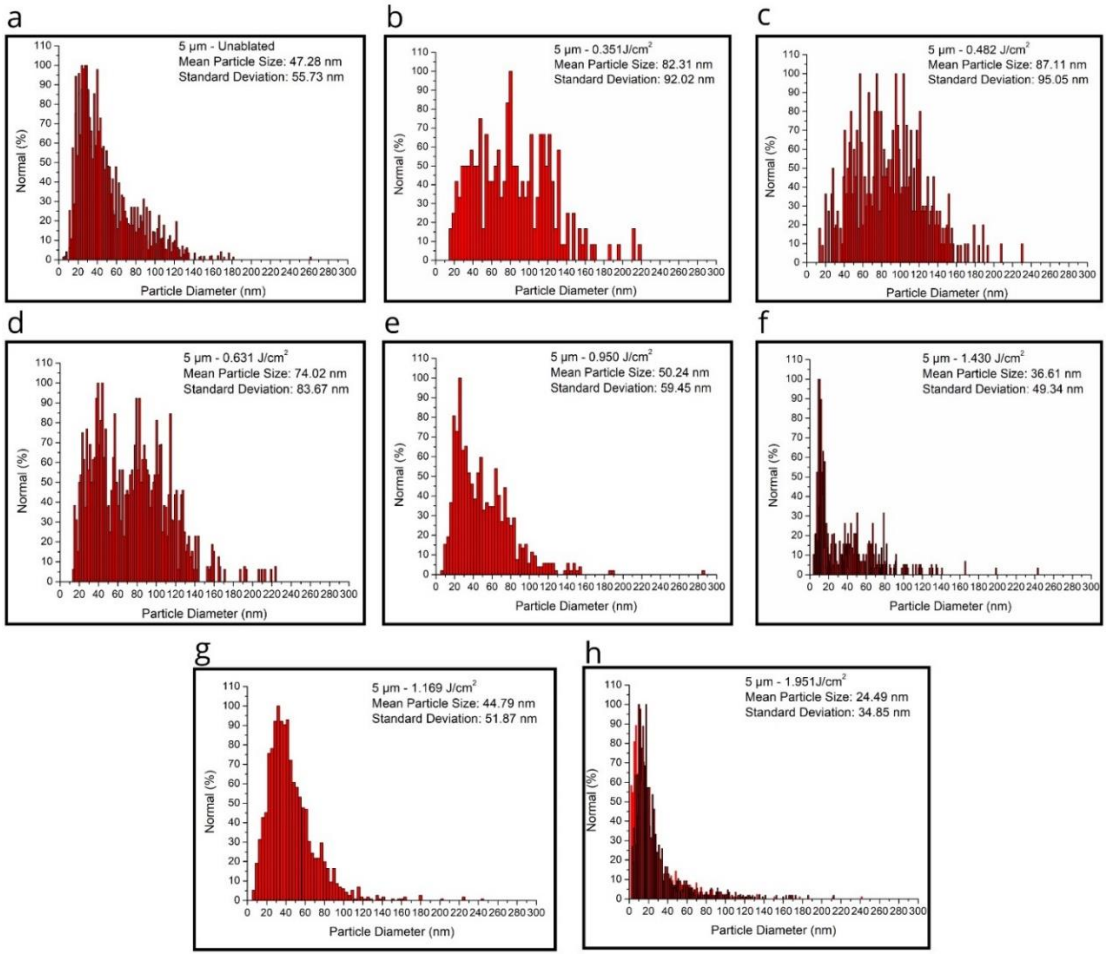

Figure D 6: *Post annealing SEM micrographs of ink concentration 2.19 %w/w printed at droplet spacing 5 µm on 10ASW substrates* ***a)*** *before patterning and after laser patterning at fluence* ***b)*** *0.35 J/cm², **c)** 0.48 J/cm² **d)** 0.63 J/cm², **e)** 0.95 J/cm² **f)** 1.43 J/cm² **g)** 1.17 J/cm² and **h)** 1.95 J/cm².*

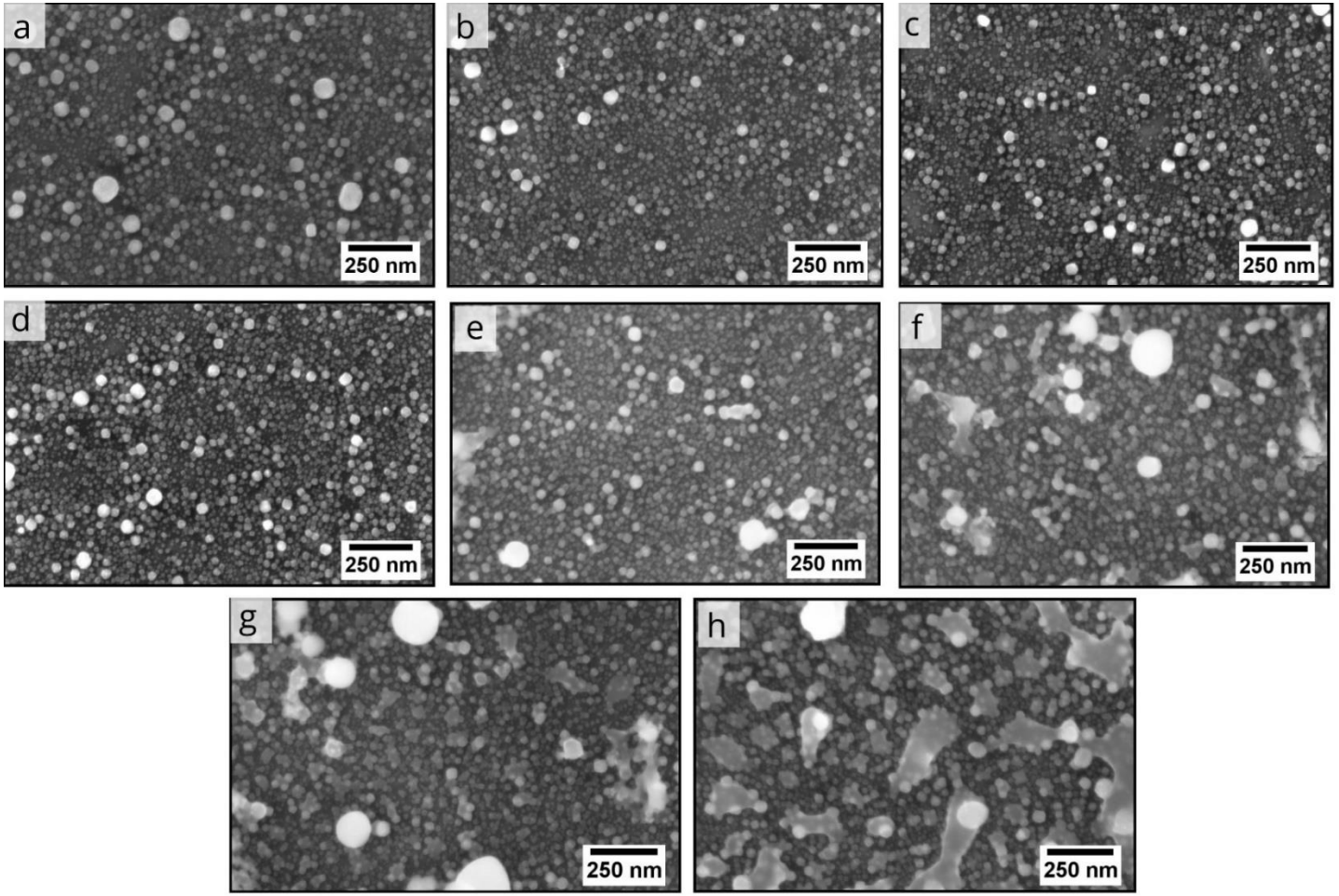

Figure D 7: *Post annealing SEM micrographs of ink concentration 2.19 %w/w printed at droplet spacing 45 µm on 10ASW substrates* ***a)*** *before patterning and after laser patterning at fluence* ***b)*** *0.35 J/cm², **c)** 0.48 J/cm² **d)** 0.63 J/cm², **e)** 0.95 J/cm² **f)** 1.43 J/cm² **g)** 1.17 J/cm² and **h)** 1.95 J/cm².*

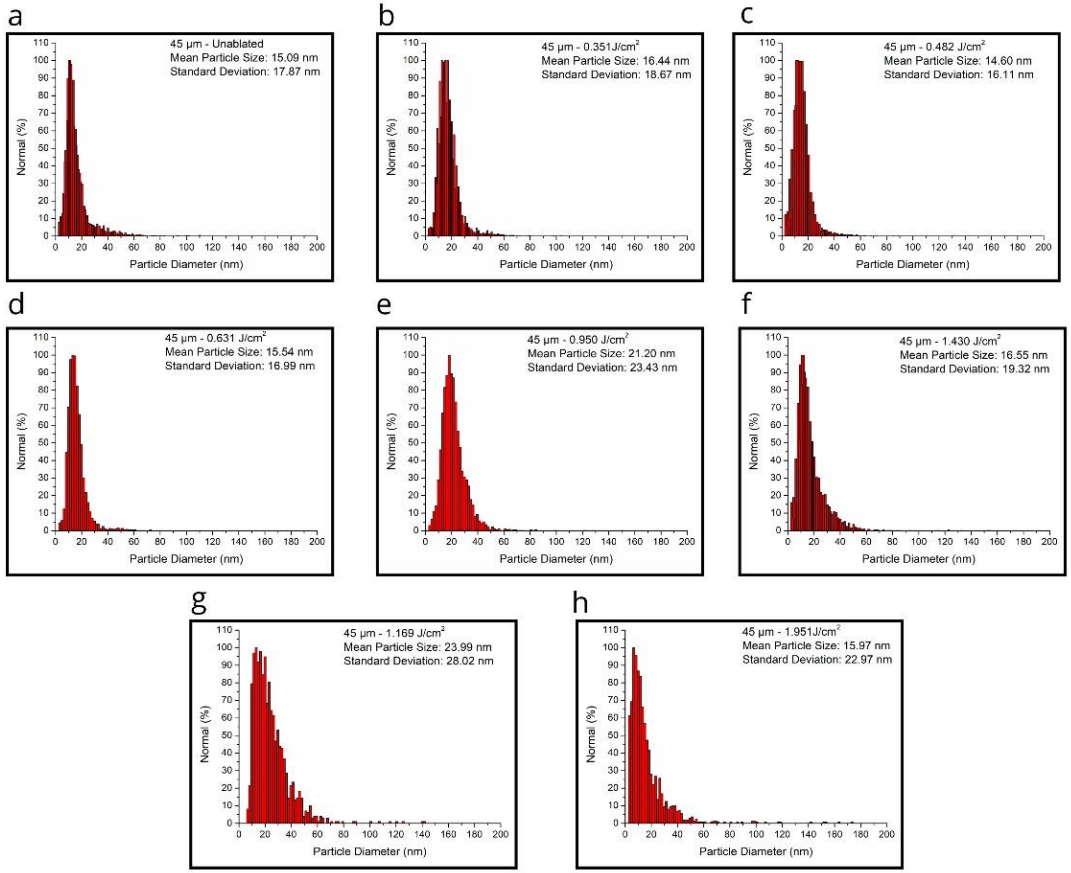

Figure D 8: *Post annealing SEM micrographs of ink concentration 2.19 %w/w printed at droplet spacing 45 µm on 10ASW substrates* ***a)*** *before patterning and after laser patterning at fluence* ***b)*** *0.35 J/cm², **c)** 0.48 J/cm² **d)** 0.63 J/cm², **e)** 0.95 J/cm² **f)** 1.43 J/cm² **g)** 1.17 J/cm² and **h)** 1.95 J/cm².*

Appendix E

Table E 1: *Dimensions of resolution test pattern.*

Feature Number	**Dimension Details**
1	100 µm lines patterned at a pitch of 200 µm
2	75 µm lines patterned at a pitch of 15. µm
3	50 µm lines patterned at a pitch of 100 µm
4	40 µm lines patterned at a pitch of 80 µm
5	30 µm lines patterned at a pitch of 60 µm
6	20 µm lines patterned at a pitch of 40 µm
7	10 µm lines patterned at a pitch of 20 µm
8	8 µm lines patterned at a pitch of 16 µm
9	5 µm lines patterned at a pitch of 10 µm
10	3 µm lines patterned at a pitch of 6 µm
11	2 µm lines patterned at a pitch of 4 µm
12	15 µm lines at 15 °rotation 1mm long
13	8 µm lines at 15 °rotation 1mm long
14	Large single block – 2x2 mm

Table E 2: *Recipe for sensing relative humidity.*

Gas Type	Step No.	Step Description	Flow Rate (sccm)	Step Duration (min)	Voltage (V)
Relative Humidity	1	Evacuate	0	10	0.01
	2	0%	0	5	0.01
	3	25%	124	5	0.01
	4	0%	0	5	0.01
	5	50%	249	5	0.01
	6	0%	0	5	0.01
	7	75%	374	5	0.01
	8	0%	0	5	0.01
	9	100%	499	5	0.01
	10	0%	0	5	0.01

Table E 3: *Recipe for sensing NO_2 and NH_3.*

Gas Type	Step No.	Step Description	Flow Rate (sccm)	Step Duration (min)	Voltage (V)
NO_2 and NH_3	1	Evacuate	0	10	0.01
	2	0 ppm	0	5	0.01
	3	25 ppm	124	5	0.01
	4	0 ppm	0	5	0.01
	5	50 ppm	249	5	0.01
	6	0 ppm	0	5	0.01
	7	75 ppm	374	5	0.01
	8	0 ppm	0	5	0.01
	9	100 ppm	499	5	0.01
	10	0 ppm	0	5	0.01

Table E 4: *Recipe for sensing CO_2.*

Gas Type	Step No.	Step Description	Flow Rate (sccm)	Step Duration (min)	Voltage (V)
CO_2	1	Evacuate	0	10	0.01
	2	0 ppm	0	10	0.01
	3	25000 ppm	13	5	0.01
	4	0 ppm	0	5	0.01
	5	50000 ppm	25	5	0.01
	6	0 ppm	0	5	0.01
	7	100000 ppm	50	5	0.01
	8	0 ppm	0	5	0.01
	9	250000 ppm	124	5	0.01
	10	0 ppm	0	5	0.01

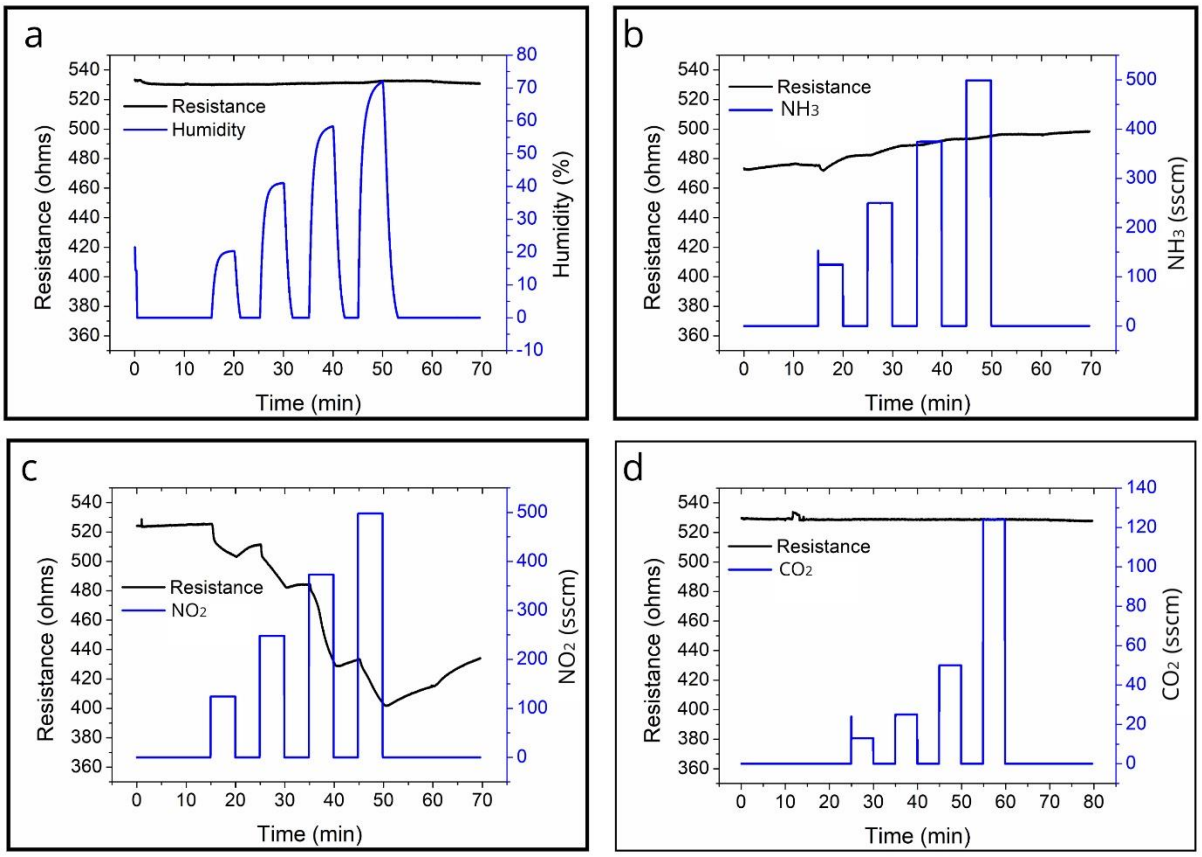

Figure E 1: *Graphical representation of resistance chage (Ohms) vs time (min) and gas flow rate (sccm) vs time (min) when varying* ***a)*** *humidity* ***b)*** *NH_3,* ***c)*** *NO_2 and* ***d)*** *CO_2 for sensor 2.*

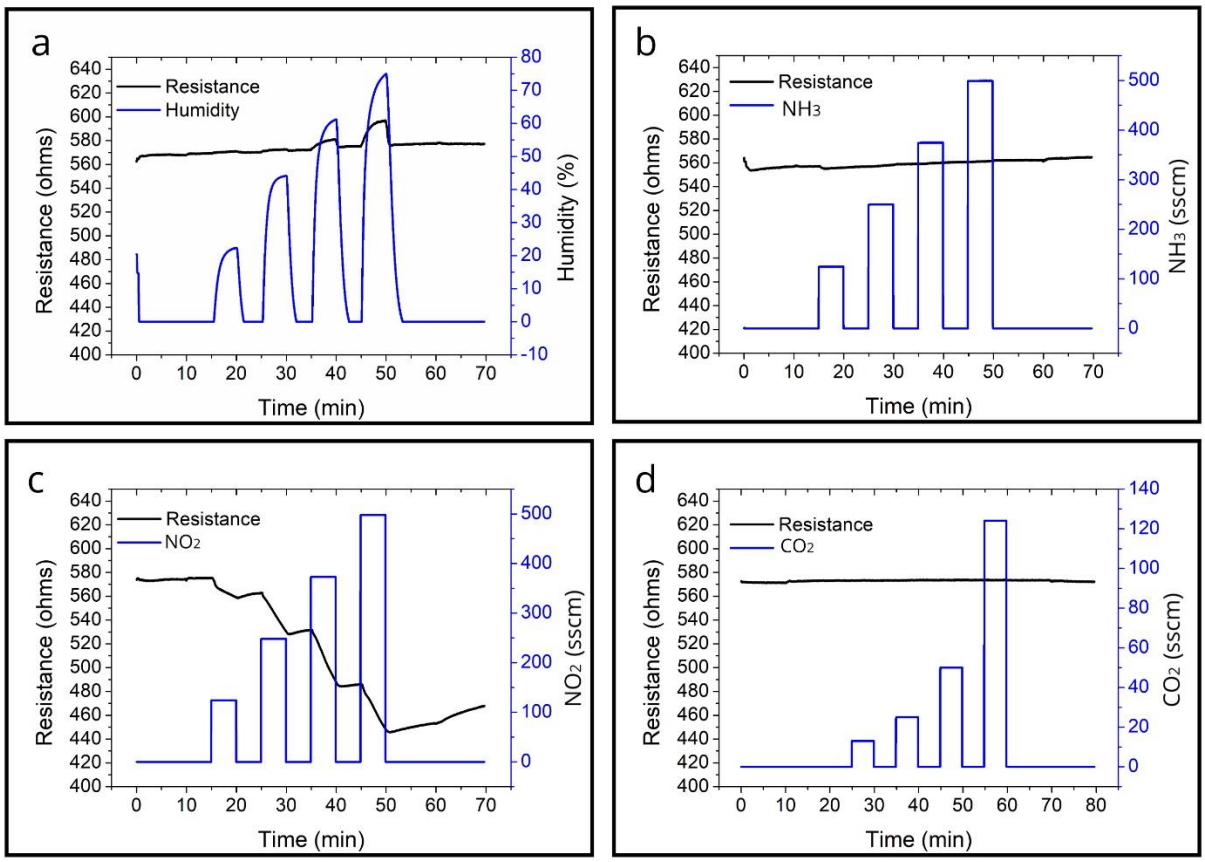

Figure E 2: *Graphical representation of resistance chage (Ohms) vs time (min) and gas flow rate (sccm) vs time (min) when varying* ***a)*** *humidity* ***b)*** *NH_3,* ***c)*** *NO_2 and* ***d)*** *CO_2 for sensor 3.*

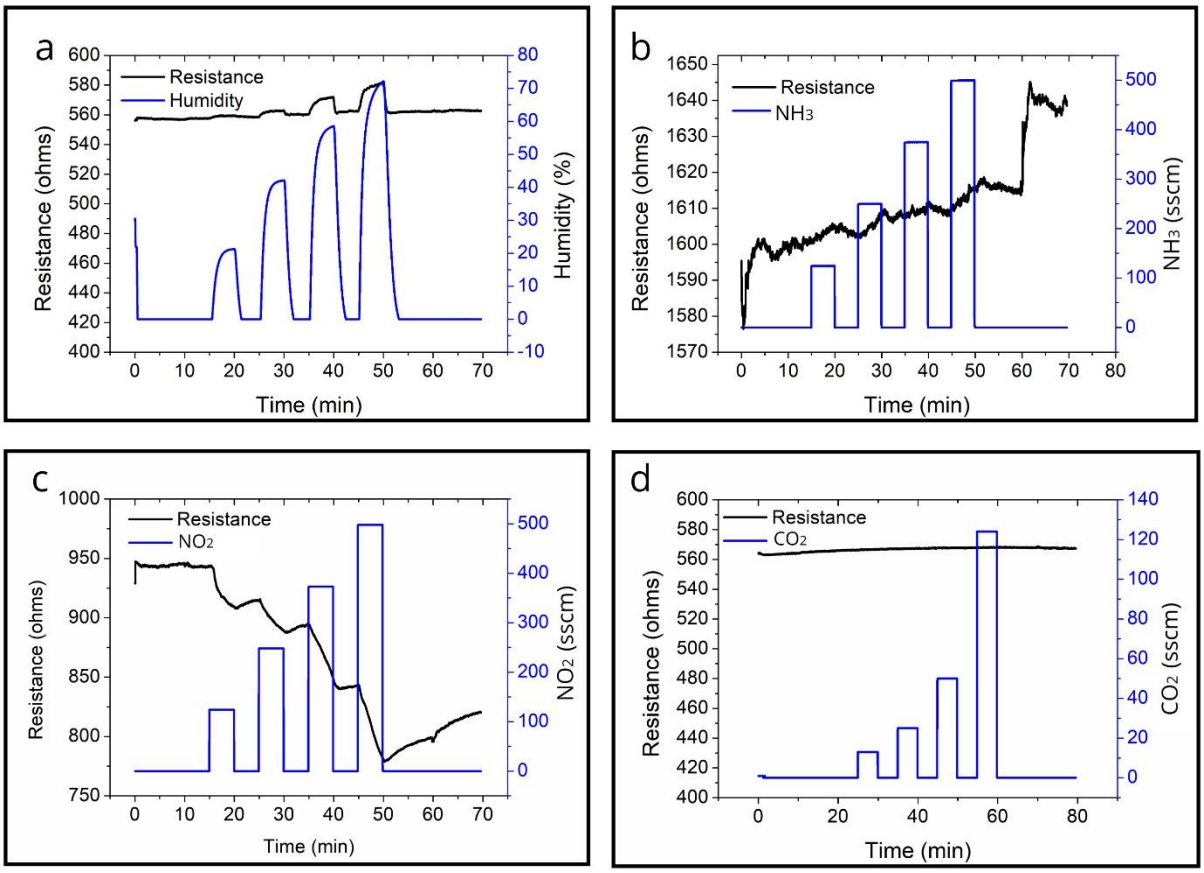

Figure E 3: *Graphical representation of resistance chage (Ohms) vs time (min) and gas flow rate (sccm) vs time (min) when varying* ***a)*** *humidity* ***b)*** *NH_3,* ***c)*** *NO_2 and* ***d)*** *CO_2 for sensor 4.*